UNIVERSITY OF OKLAHOMA

GRADUATE COLLEGE

VARIATIONAL PSEUDO MULTIPLE-DOPPLER ANALYSES OF A DRYLINE UTILIZING VERY-HIGH RESOLUTION MOBILE DOPPLER RADAR DATA

A Dissertation

SUBMITTED TO THE GRADUATE FACULTY

in partial fulfillment of the requirements for the

degree of

Doctor of Philosophy

By

CHRISTOPHER C. WEISS

Norman, Oklahoma

2004

VARIATIONAL PSEUDO MULTIPLE-DOPPLER ANALYSES OF A DRYLINE UTILIZING VERY-HIGH RESOLUTION MOBILE DOPPLER RADAR DATA

A Dissertation APPROVED FOR THE

SCHOOL OF METEOROLOGY

BY

Howard B. Bluestein
Dr. Howard Bluestein, chair

Dr. Evgeni Fedorovich

Dr. Alan Shapiro

Dr. Baxter Vieux

Carl E. Hane
Dr. Carl Hane

Dr. David Stensrud

Conrad L. Ziegler
Dr. Conrad Ziegler

ACKNOWLEDGMENTS

First, I would like to thank my advisor, Howie Bluestein, for his able guidance and support through my years at the University of Oklahoma. Also, many thanks to my committee members for many useful conversations: Howie, Evgeni Fedorovich, Carl Hane, Alan Shapiro, David Stensrud, Baxter Vieux and Conrad Ziegler.

There are many others I wish to acknowledge, without whom this work would have been very difficult. Bart Geerts and Dave Leon at the University of Wyoming were instrumental in the UWKA intercomparison efforts. David Dowell provided useful insight on variational radar processing techniques. Curtis Alexander, Nettie Arnott, Mike Buban, Josh Wurman and Yvette Richardson all assisted in providing DOW and SMART-R radar data from the 22 May 2002 case. Paul Markowski provided guidance on the GIS applications. Brendan Fennell drove the UMass vehicle for the 22 May 2002 data collection. I also need to thank our department computer coordinator, Mark Laufersweiler, for the ample computer support.

I wish to express my love and gratitude to my entire family, without whom none of this would have been possible. Especially, thank you Mom and Dad for supporting me every step of the way in my career choice. My thanks also goes out to my friends that have seen me through the good times and bad during my graduate school experience.

Finally, my love goes to my wife, Stephanie. Thank you for being my rock.

This research was supported by NSF research grants ATM-9912097 and ATM-0241037.

TABLE OF CONTENTS

ABSTRACT

The dryline has long been associated with the development of severe thunderstorms in the southern Plains during the spring and early summer months. The propagation and structure of the dryline are closely tied to surface processes that are neither well-understood nor well-resolved with current observational capabilities. As a result, there are often large errors in forecasts of dryline position and structure.

Improvements in radar technology have allowed for better observations of the dryline in recent years. Here, very-fine scale radar observations taken with the mobile UMass W-band radar during a double-dryline IHOP event on 22 May 2002 in the Oklahoma panhandle are presented. The observations are placed in the context of the dryline secondary circulation, which describes flow in a plane normal to the dryline. The narrow half-power beamwidth of the antenna on the W-band (0.18 deg) permitted the measurements of channels of upward (10 m s^{-1} over a horizontal distance of 50-100 m) and downward (-6 m s^{-1} over a horizontal distance of 1 km) vertical velocity, greater in absolute magnitude than that previously reported in dryline field studies.

A ground-based variational pseudo-multiple Doppler processing technique is introduced, which is used to decompose time series of RHI velocity data into horizontal and vertical wind components. Results of observation system simulation experiments (OSSEs) with both an analytic and LES data set indicate the technique very accurately retrieves the individual components of motion. Further, the OSSE results highlight shortcomings of the technique. Finally, the technique is applied to a

retrograding dryline from 22 May 2002. Fine-scale structure of the retreating dryline interface is presented.

VARIATIONAL PSEUDO MULTIPLE-DOPPLER ANALYSES OF A DRYLINE UTILIZING VERY-HIGH RESOLUTION MOBILE DOPPLER RADAR DATA

CHAPTER 1: INTRODUCTION

1.1 Introduction to problem

The dryline has long been identified as a region favorable for the development of deep convection. The feature is prevalent during the spring months (Rhea 1966 identified dryline occurrence on 40% of spring days) over the southern and central U.S. Plains. Owing to the strong vertical wind shear that is often characteristic of the dryline environment, storms that form on the dryline often attain supercellular attributes, thereby carrying the attendant threat of large hail, damaging winds and tornadoes.

The dryline can be thought of as the intersection of the top of a surface-based layer of virtually cool, moist air originating over the Gulf of Mexico and the sloping terrain east of the Rocky Mountains. The axis of the dryline represents a three-dimensional region of enhanced low-level convergence. Therefore it also denotes a zone in which upward vertical motion is relatively strong.

For convective initiation to occur, air parcels that ascend in the dryline convergence zone (DCZ) must attain the level of free convection (LFC) prior to exiting the DCZ (Ziegler and Rasmussen 1998). However, the amount of negative buoyancy that air parcels must overcome (i.e., the "capping inversion") to achieve the LFC is often substantial. Ascending air parcels in the DCZ are influenced by the air mass characteristics on either side of the boundary, and the relative contribution from each of these air masses determines: 1) the amount of negative buoyancy parcels ascending in the DCZ experience, 2) the amount of moisture contained within the ascending air parcels, 3) the residence time of the air parcels in the DCZ and 4) the amount of moisture detrained to the environment during ascent. All four of these factors directly affect the success or failure of deep convective initiation. Unfortunately, all four of these factors are largely indeterminable in operational practice. Proximity soundings (and model forecasts derived from these soundings) are about the only reliable tools available for determination of positive (CAPE) and negative (CIN) buoyancy, but these soundings largely fail to capture the true three-dimensional kinematic and thermodynamic environment of the DCZ. The determination of air parcel characteristics, particularly the parcel moisture, is well beyond our present operational measurement capabilities. Furthermore, the mesoscale and microscale processes governing all of the aforementioned factors are largely unknown due to the limited number of thorough investigations that have been carried out.

During the spring of 2002, an ambitious multi-agency field experiment, the International H_2O Project (IHOP) was conducted over the central and southern Plains. The primary goal of this project was the "improved characterization of the four-dimensional distribution of water vapor and its application to improving the understanding and prediction of convection" (UCAR/ATD 2002). The convection initiation (CI) component of this project was focused on resolving the kinematics of surface boundaries, particularly heterogeneities that would yield clues to the preferential development of convection (e.g., triple points[1]). Multiple ground-based and aircraft-based measurement platforms were employed for this purpose.

As part of this cooperative effort, the W-band (3 mm wavelength) radar from the University of Massachusetts (Bluestein and Pazmany 2000) gathered data on several IHOP case days. Since the quality of the data on 22 May 2002 was superior to that obtained on the rest of the operations days, this date has been chosen as a focus for this study. Owing to the very fine beamwidth of the radar (0.18 degrees), previously unresolved dryline spatial structure was observed. Considering the multitude of available measurement platforms, this dryline was one of the most intensively observed in history.

The primary scientific objective of this research is to *resolve previously unseen finescale motions of the dryline.* Knowing these motions will help us better visualize the contribution of each individual air mass at the dryline interface, and will perhaps lead to better conceptual models of modes of success and failure of CI in the DCZ.

1.2 Background on dryline research

The history of dryline study is broad and extensive. Contributions to the study of the dryline have primarily involved either observational case studies or numerical modeling. The dryline was first mentioned by Fujita (1958), who discussed the

---

[1] The term "triple point" is colloquially used to denote the intersection point of three distinctly different air masses. The intersection of a dryline and a baroclinic boundary (front, outflow boundary) is often referred to in such a manner.

concept of a "dry front" and associated thunderstorm development. This analysis followed from the Tornado Research Airplane Project, which gathered the earliest observations of the dryline. During 1961-1962, the National Severe Storm Project (NSSP) staff (1963) carried out more detailed analyses. In these studies, dewpoint gradients on the order of 18 ^{o}C/1-10 km of horizontal extent were found. Furthermore, surface convergence values on the order of 10^{-3} s^{-1} were documented.

Rhea (1966) performed a climatological study of the dryline over the southern Plains covering the spring months (April-June) of 1959-1962. He found that the dryline (defined as a >= 10 ^{o}F dewpoint discontinuity between adjacent surface stations) was present during approximately 45% of days in the study. Even more significant was the finding that, of these dryline days, 70% exhibited some form of radar echo development within 200 nautical miles of the boundary (Fig. 1). It appears that owing to the limitations of the available data, the methodology for dryline case selection may have admitted large dewpoint gradients associated with cold fronts as well; hence, the reported rate of convective initiation was erroneously large. Rhea also noted that "there was some suggestion...of a mechanical lifting and/or thermal effect on echo development from the Wichita Mountains..." (p.59) These words were perhaps the first to hint at the dependence of storm initiation at the dryline on characteristics of the terrain.

Rhea made the astute observation that there was likely some degree of lateral mixing between the dry and moist air masses at the dryline interface. The typical proportion of this mixture is still largely unknown today. In his paper, he assumed that there was an equal mixing of dry and moist air masses (his equations (2) and (3)). Using this equally mixed parcel, Rhea concluded that "thunderstorm formation appears feasible at the dryline in essentially all cases…even without the aid of any destabilizing convergence between the two air masses". This statement suggested the prevalence of CAPE over the dryline. Indeed, this often-extreme conditional instability plagues forecasters today, and necessarily biases forecasts such that there is a high false alarm rate.

Schaefer (1974), using several years of data, developed a conceptual model of the typical life cycle of the dryline. In this study, he closely related the concept of the dryline to the vertical distributions of temperature and moisture on either side of the boundary. As stated in this paper, "Once a dryline forms, it is very intimately related to the low-level inversion or stable layer" (p.448). Furthermore, Schaefer documented the presence of high-frequency waves on the capping inversion east of the dryline (e.g., structure of isentropes and isohumes in Fig. 2).

Ogura and Chen (1977) and Sun and Ogura (1979) introduced the "inland sea breeze" hypothesis for the intensification of the moisture gradient associated with the dryline (Fig. 3). This hypothesis drew an analog to the coastal sea breeze, in which a diurnal variation in non-homogeneous surface heating induces a vertical circulation in the plane normal to a sea breeze boundary. They found in their two-dimensional planetary boundary layer (PBL) model that vertical motions along the boundary were sufficient for the development of moist convection.

Parsons et al. (1991) performed a detailed case study of a retrograding dryline in west Texas using a Doppler lidar and rawinsonde observations. In contrast to its radar counterpart, the lidar had certain advantages as it afforded increased azimuthal and range resolution, no side lobes and no ground clutter. However, it was rather limited in its range (<10 km maximum range). The dryline in their case exhibited numerous horizontal inflections, including a general bending to the west over the southern portion of the boundary (near Midland, Texas), an attribute closely tied to the topography of the region. Rawinsonde ascents showed clearly that the potential temperature in the mixed layer above the capping inversion east of the dryline was equal to that in the mixed convective boundary layer west of the dryline. Using conservation principles, this observation confirmed that virtually warm air parcels in the dry air ascended over the virtually cool boundary layer to the east of the dryline (Fig. 4). These rawinsondes ascents further suggested that the moist air was deepest within 5 km of the leading edge of the dryline, indicative of an upward "bulge" in specific humidity. The strongest upward vertical motion was found to be just on the dry side of the boundary. Evidence was also given for the existence of gravity waves, as spatial virtual potential temperature fluctuations were 90 degrees out of phase with the vertical motion field. The magnitude of the measured horizontal pressure gradient and the observed speed of dryline retrogression in their case were consistent with that expected from density current theory.

Sun and Wu (1992) used a two-dimensional mesoscale model with soil physics to assess the relative importance of meteorological and topographic factors in the formation of the dryline. They found that low-level wind shear and terrain slope were critical to the development of their simulated dryline, while horizontal gradients in soil moisture played an important, though secondary, role. Interestingly, they demonstrated that an initial moisture gradient was not necessary for the development of a dryline: simply superimposing a prescribed convergent wind field on sloping terrain (with no initial horizontal gradient in specific humidity) developed a dryline within 36 hours of simulation time. The structure of the vertical motion in their simulated dryline was similar to that shown in previous research, in that the maximum in upward motion was located on the western edge of the baroclinic zone.

Hane et al. (1993) (hereafter H93) presented results from the Cooperative Oklahoma Profiler Studies-1991 (COPS-91). In this study, multiple airborne-based and ground-based observing systems were deployed to study the dryline. The peak convergence in the DCZ was found to be at an altitude of 1.1 km MSL (~several hundred m AGL). This finding highlighted the importance of the *integrated* vertical divergence in the determination of success or failure of convective initiation. Also of interest was the identification of an elevated maximum in mixing ratio just above the convective boundary layer (CBL) to the east of the dryline. This maximum was speculated to be moisture transported vertically at the DCZ, then advected eastward at inversion level. It was suggested that this layer of moisture could entrain into developing storm east of the dryline. H93 also documented the motion of the dryline as a series of discrete "steps," the cause of which may have been subsidence east of the dryline. On one of the case days there was a double fineline structure indicative of two convergence zones/moisture gradients (Fig. 5). It was hypothesized that the region between these finelines represented a third distinct air mass, that of a broad mixing zone. Finally, aircraft traverses revealed that moisture gradients were much sharper along certain sections of the dryline than others, presumably highlighting specific regions as being more favorable for the initiation of convection. This finding added emphasis to the concept of along-dryline variability, a topic which is actively studied today (e.g., during IHOP).

Ziegler et al. (1995) documented the first attempt at explicitly modeling the dryline. Using a non-hydrostatic two-dimensional mesoscale model, the authors demonstrated the sensitivity of the dryline to east-west gradients in soil moisture. In regions with high soil moisture content, less incoming solar radiation was partitioned to sensible heating, especially in comparison to the strong sensible heating of the relatively barren terrain west of the dryline. Consequently, hydrostatic horizontal pressure gradients developed and accelerated the easterly subgeostrophic flow in the plane normal to the dryline. In numerical experiments with horizontally homogeneous soil moisture, no dryline was produced. The modeling effort also confirmed many of the observed dryline properties in previous studies (e.g., θ_v gradients on the order of >4 g kg^{-1} per 10 km, upward bulges of moisture above the surface dryline location, eastward advection of vertically transported moisture)

Crawford and Bluestein (1997) (hereafter CB97) further analyzed selected COPS-91 case days to obtain characteristics of various dryline passages, primarily based upon surface mesonetwork data. For some eastward moving drylines, oscillations in dewpoint and wind direction and speed with a period of ~ 90 minutes were noted after dryline passage (Fig. 6). The explanation posed by CB97 was that gravity waves in the mid and upper troposphere caused periodic mixing down of high zonal momentum from that level. The authors also identified three modes of dryline passage: gradual (slow decrease in surface dewpoint), immediate (quick dewpoint drop, relatively co-located with a wind shift, continuous dryline motion) and step-wise (discrete "jumps" in dryline location). For westward moving drylines, the authors presented evidence that refuted the density-current theory, as no surface pressure response was noted with retrogression in most cases. Furthermore, the observed virtual temperature decrease was less than that which would have been dynamically consistent with the observed retrogression speed.

CB97 suggested two hypotheses to explain the apparent "stepped" nature of some of the drylines. The first was the "mixing zone" hypothesis, after Ziegler and Hane (1993). The basis of this theory was that the airmass between two separate moisture discontinuities (e.g., double dryline in Hane et al. 1993) was itself a separate third airmass type, a mixture of volumes of air from either side of the dryline. This intermediate airmass was termed the "mixing zone". CB97 also suggested the "downdraft hypothesis" in which descent (e.g., due to turbulent kinetic energy from the return branch of the dryline secondary circulation) to the east of the dryline ascent caused drier air to be transported to the surface in a series of steps.

Hane et al. (1997) analyzed a case from COPS-91 to document the finescale dryline structure and address the topic of along-dryline variability. They found that irrigation processes could have acted to retard dryline advancement by decreasing sensible heat flux from the surface. Also, soundings revealed that the time of cumulus cloud development was coincident with the time of most rapid increase in the depth of the CBL east of the dryline. The location of maximum upward vertical motion was found to be towards the dry side of the boundary, consistent with that found by other investigators (e.g., Parsons et al. 1991, Sun and Wu 1992). Some of the observed along-dryline variability of cumulus convection was obvious (e.g., local maxima in moisture advection due to heterogeneities in the surface wind). However, other more subtle features were discovered. For example, a secondary convergent/cloud line was observed that formed an angle with the dryline boundary (Fig. 7). It was hypothesized by the authors that this cloud line was the result of spatial differences in vertical momentum mixing, which were suggested to be due to strong heterogeneities in land use. A mesoscale circulation could have developed at an arbitrary orientation with respect to the dryline. The initiation of deep convection was found to occur at the intersection of this secondary convergence line with the dryline (Fig. 7).

Atkins et al. (1998) used National Center for Atmospheric Research (NCAR) Electra Doppler Radar (ELDORA) data from the Verification of the Origins of Rotation in Tornadoes Experiment (VORTEX-95) (Rasmussen et al. 1994) to investigate along-dryline variability in relation to horizontal convective rolls (HCRs) (e.g., Lemone 1973, Weckwerth et al. 1997). The intersection points of the dryline and these HCRs were shown to have enhanced ascent (i.e., the upward motion in the

DCZ lifted the HCR axes) and resulted in horizontally periodic cumulus cloud development. The dryline secondary circulation was well resolved by the ELDORA, including the rotor at the head of the circulation (Fig. 8). The observations in the paper supported density current theory (Simpson 1969) as the dynamical model governing the retrograding dryline, though it was found to be valid only on the leading edge of the dryline circulation (2-5 km). The authors argue that on larger scales the Coriolis force also must be accounted for in the flow-force balance.

Ziegler and Rasmussen (1998) delved into the details of the convective initiation question utilizing data gathered in COPS-91, VORTEX-94 and VORTEX-95. They found that moisture convergence (calculated from ELDORA wind analyses and in-situ specific humidity measurements taken aboard the NOAA P-3 aircraft) exponentially decreased with height in the DCZ above a constant boundary layer value (Fig. 9). The strongest upward vertical motion was found at and above 1 km AGL in the DCZ. Throughout the paper, emphasis was placed on the importance of deep layer convergence in the development of convection. Even with deep convergence and no convective inhibition (CIN), convective initiation often failed to occur due to dry, stable layers above the moist boundary layer. In situations with weak mesoscale lift, rising air parcels could achieve LCL without reaching LFC, at which point the mixing with the ambient air mass affected the moisture content of the parcel. The fundamental conclusion from this work was that *for deep convection to initiate, air parcels must achieve their LFC prior to leaving the mesoscale updraft of the dryline* (Fig. 10). Following this line of thought, the authors attempted to quantify the likelihood of initiation by computing ratios (h_{wmax}/h_{LCL}, h_{wmax}/h_{LFC}) relating the height of maximum vertical motion in the DCZ (h_{wmax}) to the height of the LCL (h_{LCL}) and LFC (h_{LFC}). For convective initiation, it was found that the vertical flux of moist air from the mesoscale updraft must dominate the horizontal flux of dry air from west of the dryline. The contribution from each air mass is largely tied to the tilt of the dryline secondary circulation. For example, strong positive westerly vertical wind shear would suggest a largely tilted secondary circulation, which is prohibitive for convective initiation. This conclusion was similar to that found by Peckham and Wicker (2000). They showed in an idealized numerical simulation that a strong westerly wind reduced the magnitude of upward vertical motion in the DCZ.

Weiss and Bluestein (2002) used ELDORA data from a case during VORTEX-95 to synthesize the boundary layer circulations associated with the near-dryline environment. The analyses revealed a tilted dryline secondary circulation, with maximum horizontal convergence (nearly constant in the lowest 1 km AGL as indicated by Ziegler and Rasmussen (1998)) tilted to the east with height in the boundary layer (Fig. 11). Maximum upward and downward vertical motions in the dryline region were found to be 2 m s^{-1} and 2-3 m s^{-1}, respectively[2]. The downward motion was located approximately 5 km to the east of the ascending motion in the DCZ, similar in location to that suggested by the "downdraft hypothesis" in H93 and CB97, and shown by the analyses of Atkins et al. (1998). The couplet of vertical motion defined a rotor circulation (on the head of the mesoscale secondary

[2] For an LFC of ~ 2 km, a parcel ascending at 2 m s^{-1} would need to reside in the DCZ for ~ 15 min to reach the LFC.

circulation[3]) which may have been a visible effect of a frontogenetical process acting to further increase surface convergence, and hence the gradients of moisture and potential temperature, at the dryline interface. The authors also demonstrated evidence of a residual form of the dryline secondary circulation (RDSC) that may have existed on the cool side of the intersection point of the dryline with an outflow boundary (residing above the cold pool) (Fig. 12). Theories about the mode of convective initiation in a triple point regime were posed. One such theory drew an analog between the outflow boundary and the secondary convergence line discovered in Hane et al. (1997).

Jones and Bannon (2002) used a mixed layer model to analyze the diurnal behavior of the dryline. They found that dryline advancement was most sensitive to the amount of surface heat flux (relative to the depth of the mixed layer and strength of the capping inversion). Vertical entrainment increased the slope of the dryline, but did not affect its eastward advancement significantly. Boundary layer heating, therefore, was found to be the primary mechanism for dryline propagation. The authors also found a spike in inversion height when the dryline ceased its eastward movement in the late afternoon. It was speculated that this spike was due to both vertical entrainment and horizontal convergence in the CBL. This spike in inversion height was significant as it often coincided with the time of convective initiation.

[3] The mesoscale secondary circulation is defined by the (easterly) low-level inflow of virtually cool air near the surface and the (westerly) return flow of virtually warm air near the capping inversion level. The horizontal scale of this circulation is O~10-100 km.

1.3 Background on Doppler data processing

The primary tool of research used in the study of many atmospheric phenomena, including drylines, is Doppler radar, owing to its ability to sense remotely radial wind velocity over a large region of space in a short period of time. However, the processing of Doppler data is non-trivial, limited by the designs of both the instrument and the collection method.

Doppler radars provide only the radial component of motion along the line of sight of the radar beam. Therefore, no information on the wind component normal to the line of sight is available. However, for multiple radar systems that observe a region of space simultaneously (at some distance apart), it is possible over a limited domain to calculate wind components in non-radial planes. This process is often referred to as *dual-Doppler synthesis* or in general for more than one radar, *multiple-Doppler synthesis*. These techniques can generally be classified as either traditional or variational (or a hybrid of both). Traditional techniques are generally iterative, and involve iterations between diagnostic equations for the dependent variables. Therefore, the unknown analysis variables are found in a non-simultaneous manner. Variational techniques incorporate all dependent analysis variables into one minimized functional, and these variables are usually solved simultaneously.

1.3.1 Traditional techniques

The most basic experimental design is the dual-Doppler configuration (Fig. 13), in which there are two radar platforms (ideally of similar characteristics) separated by some distance (often referred to as the *baseline*). Using geometry, one can write an expression for the radial wind velocity for each of the radars as a function of the Cartesian wind components u, v, and w:[4]

$$V_{r1} = [x_1 u + y_1 v + z w]/R_1 \tag{1a}$$

$$V_{r2} = [x_2 u + y_2 v + z w]/R_2 \tag{1b}$$

where the subscripts 1 and 2 denote the radar number, V_{rn} denotes the radial velocity measurement from radar n; x, y and z represent the location of the sampled data point relative to the radar, u, v and w are the Cartesian wind velocity components, and R is the slant range from the radar to the sampled data point [$R=(x^2+y^2+z^2)^{1/2}$]. As this system stands, it is an underdetermined problem with two equations ((1a), (1b)) describing the relation between three unknowns (u, v, w). However, we can introduce a kinematic constraint to close the system. For example, one can use the anelastic mass continuity equation:

$$\frac{\partial w}{\partial z} = -\left(\frac{\partial u}{\partial x} + \frac{\partial v}{\partial y}\right) + \kappa w \tag{2a}$$

$$\kappa = -\left(\frac{\partial(\ln \rho)}{\partial z}\right) \tag{2b}$$

[4] If considering precipitation particles, one must also account for the terminal fall speed of these particles in the calculation of w.

where $\rho(z)$ is a base-state horizontally averaged density and κ denotes the vertical density stratification (assumed constant here).

The solution of the individual Cartesian wind velocities is usually found using an iterative process between the radial wind expressions ((1a), (1b)) and the mass continuity equation ((2a), (2b)). A boundary condition must be imposed to carry out this process, either at the upper boundary (e.g., w=0 at the top of a thunderstorm) or at the lower boundary (e.g., w=0 at the surface (impermeability)). The direct integration of mass continuity makes it a strong constraint, one that incurs error due to the vertical density stratification of the atmosphere.

Armijo (1969) was the first to develop the above theory for determining the true three-dimensional wind field. He reduced the three-equation system ((1a),(1b),(2a),(2b)) to a single partial differential equation (pde) in w with coefficients involving known data (radial velocity data and geometrical factors). Armijo also realized that the geometry of the problem lent itself well to a cylindrical coordinate system, with the central axis of the cylinder aligned along the radar baseline. Using a transformation from Cartesian to cylindrical coordinates, he derived a simpler pde for w, from which u and v could be calculated. Armijo further developed his theory for the case of three non-collinear Doppler radars (Fig. 14), demonstrating that radial velocity data from three radars and the equation of mass continuity were sufficient to determine the full three-dimensional wind field. However, he further noted that analysis errors were quite likely due to both radial velocity observation error and the transformation of data from the coordinate system in which it was gathered (e.g., interpolation).

Brandes (1977) applied the technique of Armijo (1969) to dual-Doppler observations of a severe thunderstorm. The reflectivity and radial velocity data were first interpolated to horizontal planes using an asymmetric Barnes weighting function (an oblate spheroid). With this technique, Brandes was able to create a plausible analysis of the storm flow structure.

Many other dual-Doppler analyses in the literature have used traditional dual-Doppler techniques to recover the three-dimensional wind field, but will not be elaborated on further as the focus of this work will be on variational techniques.

1.3.2 Variational techniques

The framework of the variational problem is really that of static data assimilation (e.g., 3D-VAR). In other words, at a fixed time, we seek an analysis that best satisfies all of the data given. In this case, the analyzed field sought is a set of three-dimensional wind vectors at all of the gridpoints in a solution domain. The input to the problem are the radial wind velocities from all of the observing radars. As will be shown below, variational techniques offer many advantages over the traditional techniques. For example, the types and strength of the constraints are flexible, the radial nature of the observations can be preserved, and there are no elevation angle restrictions on the analysis[5].

For dual-Doppler analysis, the system of radial velocity equations ((1a) and (1b)) represent an underdetermined problem. In other words, if n denotes the number of unknowns in the system and m denotes the number of equations relating these unknowns, then there are n-m degrees of freedom to our solution space, and therefore infinitely many solutions exist. To make the problem well posed (and to obtain a unique solution), we must impose additional constraints. The number and types of these constraints make each variational technique distinct. The designs of the problem dictate the proper formulation. For each technique[6], a cost function J is defined similar to the following:

$$J = \Sigma_{\text{domain}} (\Sigma_{\text{obs}} (\text{departure from observations})^2 + (\Sigma_{\text{constraints}} \text{ departure from constraints})^2) \tag{3}$$

The final solution (e.g., the analysis) is therefore the one that minimizes the variance of the departure from all observations and all constraints, summed over the whole domain. A wide variety of variational problems can be defined based on the types (and number) of observations and choice of constraints.

[5] Traditional iterative techniques suffer from mathematical instability in regions with high-elevation angle radial velocity data (Dowell and Shapiro 2003)

[6] Specifically, weak constraint techniques in this example

If background information is available (e.g., a previous model forecast, climatology), then the assimilation problem includes this information as a constraint. An example of this is optimal or statistical interpolation, where a cost function similar to the following is developed (Lorenc (1986)):

$$J(\vec{x}) = \tfrac{1}{2}(\vec{x} - \vec{x}_b)^T B^{-1}(\vec{x} - \vec{x}_b) + \tfrac{1}{2}(\vec{y}_o - H(\vec{x}))^T R^{-1}(\vec{y}_o - H(\vec{x})) \qquad (4)$$

where $\vec{x}$ is the analyzed field, $\vec{x}_b$ is the background field, $\vec{y}_o$ is a vector of observations, H is an operator that transforms variables between observational space and gridpoint space, and B and R are the background and observation covariance matrices[7], respectively. This technique is very powerful, and is widely used in model initialization today (e.g., ECMWF).

In the event that no background information is available, then other constraints must be introduced. Most often these constraints take the form of dynamical balance relations. Sasaki (1970) was the first to develop the variational technique for this type of problem. He introduced three strategies for variational minimization:

Timewise localized:

$$\delta J = \delta \sum_{\Omega} \sum_{i} \left\{ \widetilde{\alpha}_i (\varphi_i - \widetilde{\varphi}_i)^2 + \alpha_i (\nabla_t \varphi_i)^2 \right\} = 0 \qquad (5a)$$

[7] These covariance matrices express the variance (on-diagonal) and spatial correlation (off-diagonal) of background and observation error, respectively.

Strong dynamical constraint:

$$\delta J = \delta \sum_{\Omega} \sum_{i} \left\{ \widetilde{\alpha}_i (\varphi_i - \widetilde{\varphi}_i)^2 + \lambda_i G_i \left(\varphi_i, \varphi_j, \nabla_t \varphi_i, \nabla_{xk} \varphi_i, \nabla_{xk} \varphi_j \right) \right\} = 0 \tag{5b}$$

Weak dynamical constraint:

$$\delta J = \delta \sum_{\Omega} \sum_{i} \left\{ \widetilde{\alpha}_i (\varphi_i - \widetilde{\varphi}_i)^2 + \alpha_i G_i \left(\varphi_i, \varphi_j, \nabla_t \varphi_i, \nabla_{xk} \varphi_i, \nabla_{xk} \varphi_j \right)^2 \right\} = 0 \tag{5c}$$

In the above equations, δJ represents the incremental form of the cost function, α_i and $\widetilde{\alpha}_i$ are weighting coefficients for the weak constraints, φ_i and φ_j are the analysis values, $\widetilde{\varphi}_i$ are the observations, ∇_t is the local change, ∇_{xk} is the spatial derivative in the x_k direction (k=1, 2, 3), G_i denotes a prognostic or diagnostic equation (described below), and λ_i is the Lagrange multiplier.

The dynamical or kinematic constraint $\alpha_i (\nabla_t \varphi_i)^2$ in the first formulation (5a) acts as a low-pass filter; that is, high frequency scales of motion are damped. This variational procedure produces an analysis field identical to the observational field in phase, but reduced in amplitude. The second formulation (5b) will find a solution that *exactly* satisfies the dynamical or kinematic constraint $G_i \left(\varphi_i, \varphi_j, \nabla_t \varphi_i, \nabla_{xk} \varphi_i, \nabla_{xk} \varphi_j \right)$ and *approximately* satisfies the observations $\widetilde{\varphi}_i$. Examples of G include the primitive horizontal and vertical momentum equations (and approximations thereof), mass continuity and the thermodynamic equation. To use such a framework, one must be confident in the validity of the dynamical constraint (e.g., is it appropriate for the scale of motion considered?) relative to the accuracy of the data. In such a situation where the validity of the constraint is in question and/or the data are believed to be very accurate, then the weak constraint formalism (5c) may be the best choice[8]. In this formulation, the constant α_i can be altered according to this relative characteristic accuracy. It can be shown that in the limit of $\alpha \to \infty$, the weak constraint solution converges to that of the strong constraint solution.

1.3.3 Application of variational techniques in dual/multiple Doppler studies

Since their introduction into the meteorological literature in the late 1950's[9], variational techniques have been used in a number of dual and multiple-Doppler analyses of convection.

Ray et al. (1980) (hereafter R80) tested a number of traditional and hybrid traditional/variational techniques in the wind retrieval of a tornadic thunderstorm. The traditional techniques involved either upward integration of the standard equation set (e.g., (1a), (1b), (2a), (2b)) with a boundary condition of w=0 at ground, or a downward integration with w=0 at the top of the storm (which required data to extend to the top of the storm). The hybrid techniques utilized a variational adjustment

[8] As will be demonstrated later, it may even be appropriate to remove the dynamic constraint altogether if enough observations are present.

[9] Originally, the techniques were developed for objective analysis.

applied *after* the synthesis of the three-dimensional winds with the traditional equation set (e.g., (1a), (1b), (2a), (2b)). The cost function for the two-radar case was as follows:

$$E = \iint \left\{ \int \left[\alpha^2 (u - u_{obs})^2 + \beta^2 (v - v_{obs})^2 \right] dz + \lambda \left[\int \left(\frac{\partial u}{\partial x} + \frac{\partial v}{\partial y} \right) dz + C \right] \right\} dxdy = \text{minimum} \tag{6}$$

where α and β were weak constraint weighting coefficients (inversely proportional to the observational error covariance), u and v were analyzed velocities, u_{obs} and v_{obs} were the observed velocities, λ was the Lagrange multiplier, and C was a constant representing the integrated horizontal divergence such that the term multiplying λ equaled zero.

R80 also presented techniques for three sets of radial velocity measurements. For the three radar system, a unique "direct" solution of the three wind components can be obtained if the measurements are error-free and non-collinear, e.g. three equations of form (1a) and (1b) with no kinematic constraint. However, measurement error makes an exact direct solution impossible, particularly for the w component, where measurement error is a significant percentage of the typical magnitude. Therefore, a least-squares solution was the only possible way to find u, v and w in this direct manner. R80 concluded that the best analysis technique for the three-radar case was one that took u, v and w from the direct solution mentioned above, followed by application of a variational minimization with a strong mass continuity constraint (Fig. 15). The triple-Doppler analysis was found to have less variance in the divergence fields compared to its dual-Doppler counterpart. Therefore, divergence-derived fields (e.g., *w*) were more robust. R80 generalized this thought: "*As more information is used, the quality of a properly designed analysis improves and the error variance is reduced.*" (p. 1619).

Chong and Campos (1996) presented the extended overdetermined dual-Doppler variational (EODD) technique. EODD performed a variational adjustment of the horizontal velocity components given a specified estimate of w^0. The cost function minimized for EODD was:

$$F(u,v)=\int_s\left\{\sum_i\left[\alpha_i u+\beta_i v+\gamma_i(w^0+V_t)-V_i\right]^2+\mu_1\left[\frac{\partial u}{\partial x}+\frac{\partial v}{\partial y}+\frac{\partial w^0}{\partial z}-\kappa w^0\right]^2+\mu_2\left[J_2(u)+J_2(v)\right]\right\}dxdy \tag{7}$$

where α, β and γ were the geometrical coefficients relating radial velocity and Cartesian velocity components, u and v were the analyzed horizontal winds, w^0 was the fixed guess of vertical velocity, V_t was the terminal fall speed of precipitation, V_i was the observation of radial wind, μ_1 and μ_2 were the weighting coefficients of the constraints and J_2 was a second order derivative acting as a filter. The first term in (7) defined the fit of the analysis to the observations, the second term was a weak mass continuity constraint, and the third term was a low-pass filter. The analysis values of horizontal velocity resulting from the minimization of F: [10]

$$\frac{\partial F}{\partial u} = 0 \text{ and } \frac{\partial F}{\partial v} = 0 \tag{8}$$

were then used in the anelastic mass continuity equation ((2a), (2b)) to obtain a new estimate of w^0, which was replaced in (7) to calculate new horizontal velocities. This iterative procedure was repeated until convergence was achieved.

One can immediately see a major benefit of such a formalism, namely that the radial nature of the observations was preserved. In other words, the minimization was performed directly on the departure from V_i, and not on a previously synthesized wind component (e.g., as in R80).

Bousquet and Chong (1998) (hereafter BC98) presented the multiple-Doppler synthesis and continuity adjustment technique (MUSCAT) to improve upon EODD. The cost functional was very similar to the EODD case (7), except that the first term describing the fit to the data was:

$$\frac{1}{N}\sum_{p=1}^{n_p}\sum_{q=1}^{n_q(p)}\omega_q\left[\alpha_q u + \beta_q v + \gamma_q (w + V_T) - V_q\right]^2 \tag{9}$$

[10] The minimization equations $\frac{\partial F}{\partial u} = 0$ and $\frac{\partial F}{\partial v} = 0$ are referred to as the Euler-Lagrange equations.

Here, n_p was the number of radars, $n_q(p)$ was the total number of measurements inside an ellipsoid of influence for each radar, N was the total number of measurements for all radars, ω_q was a distance-dependent weight function (e.g., Cressman), w was the analyzed vertical velocity, and all other variables were as in (7). BC98 noted that one limitation of the EODD technique was the interpolation of polar coordinate radial velocity data to a Cartesian grid prior to application of EODD. This interpolation was necessary to get a value of V_i for each radar observing the point in space. For regions close to the radar, the angular orientation of the outgoing radial changed quickly for small displacements. Therefore, averaging induced a large amount of error close to the radar, which was demonstrated clearly by the case studies of BC98 (Fig. 16). The MUSCAT formulation incorporated the interpolation procedure directly into the least-squares minimization. As a result, all observations (in their pure radial form) within the ellipsoid of influence were included in the analysis, rather than a single representative average.

BC98 also noted that due to the iterative nature of EODD, residuals in the analyzed velocity values led to inconsistent horizontal and vertical velocities. MUSCAT was developed as a simultaneous method of solution (note the presence of w rather than w^0 in (9) compared to (7)).

Shapiro and Mewes (1999) furthered this work by presenting a series of variational techniques in coplanar coordinates. These techniques combined the radial wind relations and mass continuity equation as weak and strong constraints for the minimization. They found that the transformation from Cartesian to cylindrical coordinates greatly reduced the complexity of the analysis (for the two-radar system). The formulations were shown to be well-posed mathematically when, for each point in the analysis domain, radial velocity data were available along the entire coplane azimuthal line running through that point to the upper and lower boundaries (with w specified on these boundaries). The authors stressed the importance of the simultaneous analysis of all unknowns. For hybrid techniques (e.g., R80) where variational adjustment is performed on already-synthesized Cartesian winds, the radial wind relationships (e.g., (1a), (1b)) are no longer satisfied. Furthermore, they found a constraint for the stability of traditional iterative methods (later corrected by Dowell and Shapiro (2003)).

Gao et al. (1999) (hereafter G99) presented a comprehensive outline of the framework of the variational problem. Only one interpolation step was required for their analysis, that being the conversion of velocities in gridpoint space to the locations of the radial velocity measurements. As above, the radial nature of the observations was preserved with such a formulation. This variational problem included the fit to a background field (an ARPS model forecast) as a constraint. The cost function minimized was as follows:

$$J = J_O + J_B + J_D + J_S \tag{10a}$$

$$J_O = \frac{1}{2}\sum_{m,n}\left(CV_r^{m,n} - V_{r,ob}^{m,n}\right)^2 \tag{10b}$$

$$J_B = \frac{1}{2}\left[\sum_{i,j,k}\alpha_{ub}\left(\vec{u} - \vec{u}_b\right)^2 + \sum_{i,j,k}\alpha_{vb}\left(\vec{v} - \vec{v}_b\right)^2 + \sum_{i,j,k}\alpha_{wb}\left(\vec{w} - \vec{w}_b\right)^2\right] \tag{10c}$$

$$J_D = \frac{1}{2}\sum_{i,j,k}\alpha_D\left(\frac{\partial\bar{\rho}u}{\partial x}+\frac{\partial\bar{\rho}v}{\partial y}+\frac{\partial\bar{\rho}w}{\partial z}\right)^2 \tag{10d}$$

$$J_S = \frac{1}{2}\left[\sum_{i,j,k}\alpha_{us}\left(\nabla^2\vec{u}\right)^2+\sum_{i,j,k}\alpha_{vs}\left(\nabla^2\vec{v}\right)^2+\sum_{i,j,k}\alpha_{ws}\left(\nabla^2\vec{w}\right)^2\right] \tag{10e}$$

J_O, J_B, J_D, J_S denote the following constraints on the analysis in minimization: fit to observations, fit to background, mass continuity, and smoothness, respectively. The variables *m* and *n* denote the number of radars and number of observations, respectively, *i*, *j* and *k* are the indices of the gridpoints, *C* is a linear interpolator from gridpoint to observation space, V_r is the measured radial velocity, α is the weight for each constraint, $\vec{u},\vec{v},\vec{w}$ are the analyzed wind components, and $\vec{u}_b,\vec{v}_b,\vec{w}_b$ are the background wind components. The authors found that their analyses were predominantly insensitive to the precise choice of α, and therefore were treated as "tuning parameters."

The procedure for solution was as follows. First, an initial guess of the control variable vector Z was made (e.g., $\vec{Z} = (\vec{u},\vec{v},\vec{w})^T$). The cost function was then calculated for each of the four components (J_O, J_B, J_D, J_S) separately. The values of ∇J were then computed with respect to the control variable $\left(\frac{\partial J}{\partial\vec{u}},\frac{\partial J}{\partial\vec{v}},\frac{\partial J}{\partial\vec{w}}\right)$. Using these gradient values, the control variables were updated by the conjugate gradient method:

$$Z_{i,j,k}^{n} = Z_{i,j,k}^{n-1} + \left(\alpha \cdot f\left(\frac{\partial J}{\partial \bar{Z}} \right)_{i,j,k} \right) \tag{11}$$

where the superscript referred to the iteration number. The change in the control variable was that which effected the maximum decrease in the cost function *J*. After the update, the norm of *J* (or of ∇J) was calculated. If this value was found to be less than some tolerance, it was assumed that the global minimum in *J* (the optimal solution) was found. Otherwise, the process was repeated until convergence was achieved. The authors found that the number of iterations required for a suitable retrieval of *w* was considerably larger than that for *u* and *v*. It was posed that errors in *u* and *v* contributed more to the cost function during early iterations, and that the mass continuity constraint and errors in *w* were more prominent in later iterations.

G99 tested the importance of the mass continuity and smoothness constraints by selectively removing them from some of the analyses. When mass continuity was removed, the horizontal winds were still properly retrieved. However, the solution for *w* was very poor. In fact, there was no coherent structure in the analyzed *w* below about 4 km AGL (since *w* was not observed close to the ground with horizontal radar scans). The solution also deteriorated rapidly when the smoothness constraint was removed.

In conclusion, G99 summarized some of the advantages of the variational technique. In addition to some of the advantages listed above, it was also noted that the mass continuity equation was not explicitly integrated. This integration (especially upwards from a lower boundary) is a large source of error in the traditional analysis methods, as biases in analyzed divergence accumulate with height.

Mewes and Shapiro (2002) demonstrated the utility of using the vorticity equation in determining proper boundary conditions for w when integrating mass continuity between an upper and lower boundary. They minimized the cost function

$$J = \int_V \left\{ \alpha^2 \left[\frac{\partial \zeta}{\partial t} + u\frac{\partial \zeta}{\partial x} + v\frac{\partial \zeta}{\partial y} + w\frac{\partial \zeta}{\partial z} + (\zeta + f)\left(\frac{\partial u}{\partial x} + \frac{\partial v}{\partial y}\right) + \left(\frac{\partial w}{\partial x}\frac{\partial v}{\partial z} - \frac{\partial w}{\partial y}\frac{\partial u}{\partial z}\right)\right]^2 + \left(\frac{\partial \rho u}{\partial x} + \frac{\partial \rho v}{\partial y} + \frac{\partial \rho w}{\partial z}\right)^2 \right\} dV' \tag{12}$$

where α is a weighting coefficient, u and v are the analyzed horizontal wind components, ζ is the relative vorticity, w is the vertical velocity (control variable) and f is the Coriolis acceleration. Minimizing this cost function with respect to w_{top} and w_{bottom} provided the optimal solution for w with height. Mass continuity acted as a weak constraint in this analysis. Mewes and Shapiro also posed a strong mass continuity constraint form of this problem, which was found to be inferior to the weak constraint method due to the accumulation of integrated divergence errors (as mentioned above). Based on tests with numerically simulated data, they found that the vorticity equation method provided the most accurate retrieval of vertical velocity when beam blockage was present (e.g, when the boundaries of the domain were in a data-void region). The vorticity equation method outperformed other methods for determining boundary conditions in such a situation (e.g., for a lower boundary condition: imposing impermeability (w=0) at the lowest data level, extrapolating divergence to the ground from lowest data level). However, the impermeability condition was still found to be superior if data were present all the way to the boundaries.

Dowell and Bluestein (2002) used a weak constraint pseudo dual-Doppler variational procedure on airborne radar data from a cyclic tornadic supercell during VORTEX-95. One of the major assumptions that goes into the pseudo-dual Doppler synthesis technique is that of stationarity (e.g., for ELDORA a sampled region of space does not change between scans from the fore and aft radar on the NCAR Electra). Obviously, this assumption is violated if the feature of interest is translating. Dowell and Bluestein developed a technique to determine the optimal storm motion, minimizing the penalty function:

$$J = \int_{R^{(4)}} \left[\left(\frac{\partial u'}{\partial t} \right)^2 + \left(\frac{\partial v'}{\partial t} \right)^2 + \left(\frac{\partial w'}{\partial t} \right)^2 \right] dR^{(4)} \tag{13}$$

where u', v' and w' were the analyzed Cartesian wind components, and

$\frac{\partial'}{\partial t} = \frac{\partial}{\partial t} + U_s \frac{\partial}{\partial x} + V_s \frac{\partial}{\partial y}$ was the Lagrangian time derivative (U_s and V_s are the advective speeds). By minimizing J with respect to U_s and V_s, the optimal storm motion was calculated. Subtracting this velocity from the time series of data allowed the principle of stationarity to be applied properly. The remainder of the analysis was similar to that in Gao et al. (1999), less the background and smoothness constraints.

CHAPTER 2: THE 22 MAY 2002 DRYLINE

2.1 Synoptic and mesoscale overview

The synoptic pattern for 22 May 2002 was characteristic of many days with a dryline present in the southern Plains. A negatively-tilted longwave 500 mb trough extended over the western United States at 1200 UTC (Fig. 17a). The trough was progressive, moving eastward through the day (e.g., the 500 mb temperature dropped 9 °C over 12 hours at Aberdeen, SD in advance of the trough (Figs. 17a, 17b)). A weak 500 mb jet (35 kts) extended across central and southern Colorado in association with this wave. To the south and east of the wave, 500 mb winds were very light over most of Oklahoma and Texas.

At 700 mb, winds over the Oklahoma and Texas panhandles (hereafter, the "target region") were considerably veered[11]. For example, the 1200 UTC 700 mb wind at Amarillo (AMA) was from 230 degrees at 15 knots (Figs. 18a, 18b). Therefore, very warm air from the elevated terrain of New Mexico was advected northeastward to establish a moderately strong capping inversion at 750 mb (e.g., 1200 UTC sounding from AMA (Fig. 19a)).

At 850 mb (near the surface), winds were south-southwesterly over the target region at 1200 UTC (Fig. 20a). Modest moisture was transported from the western Gulf of Mexico during the previous 48 hours, and was present near the surface (e.g., AMA dewpoint was 10 °C). Moisture rapidly advected northward at 850 mb over

[11] The term "veered" is used colloquially to indicate a strong westerly wind component (e.g., *veered* to southwesterly from southerly).

most of Texas and Oklahoma during the afternoon of 22 May[12] (e.g., OUN 850 mb dewpoint increased 14 °C from 1200 UTC to 0000 UTC (Figs. 20a, 20b)).

The 1200 UTC AMA sounding (Fig. 19a) showed a strong inversion from the surface to just below 750 mb, due to a combination of nocturnal radiational cooling at the surface and advection of the high-terrain mixed layer by the veered 700 mb winds (AMA T_{700}=10 °C). Ample potential instability existed above this level. The convective temperature was judged to be approximately 30 °C. The Dodge City, Kansas (DDC) 1200 UTC sounding (Fig. 21a) showed a very similar thermodynamic profile.

At 1500 UTC, the dryline was located near the Texas/New Mexico border (Figs. 22a, 22b). With the surface winds veered to the east of the boundary, very little convergence was apparent at the dryline at this time. By 1800 UTC (Figs. 23a, 23b), the dryline had mixed eastward through the central Oklahoma panhandle and southwestern Kansas; sharp decreases in dewpoint were noted at Elkhart, KS (EHA) and Liberal, KS (LBL). Hardly any wind shift occurred with the dryline passage, largely because winds had already veered to the east of the boundary. Farther to the south, surface dewpoints fell gradually (e.g., at AMA), less indicative of a distinct dryline passage. This region will later be shown to be in an intermediate zone between two sharp moisture gradients/drylines.

At 2100 UTC, the dryline was still located in the eastern OK panhandle, near the border of Texas and Beaver counties (Fig. 24). The dewpoint changed by 32 °F

[12] This moisture return in part contributed to a severe thunderstorm outbreak over Texas and Oklahoma on 23 May 2002.

(17.8 °C) over 60 km between Beaver, OK and Hooker, OK. A wind shift was also evident across the dryline, from which it may be inferred that there was convergence (assuming there was limited confluence). There were very gusty winds on both sides of the dryline. The dewpoint at AMA decreased in a more steady manner until 2300 UTC, when there was a sharp decrease (Fig. 25).

Surface winds generally backed to the east of the dryline during the late afternoon and early evening (Fig. 25). This diurnal effect has been attributed to heating of the elevated high terrain and troughs in the lee of the Rocky Mountains, both of which increase easterly ageostrophic flow in the late afternoon and early evening hours to the east of the dryline (Benjamin and Carlson 1986). Deep convection initiated along the dryline over northwestern Kansas and eastern Nebraska by late in the afternoon (Fig. 26). This region was more directly influenced by the western longwave trough (Figs. 17a, 17b), which likely produced vertical motion and mid-level cooling that aided in the development of the convection. Farther to the south, the vertical thermodynamic profile was largely unaffected by the trough (Figs. 21a, 21b). It can be seen in the 0000 UTC DDC sounding (Fig. 21b) that convective temperature had been achieved at this time, yet no deep convection was observed. Also evident on the sounding was a subsidence inversion at about 600 mb. This feature was likely tied to the position of DDC on the anticyclonic shear side of the 500 mb jet (Figs. 17a, 17b). The weak subsidence in response to differential anticyclonic vorticity advection (AVA) over this portion of the dryline may have been in part responsible for the suppression of deep convection. Farther south, based on an

Atmospheric Emitted Radiance Interferometer (AERIplus)[13] sounding from Vici, OK, the capping inversion was still established (Fig. 27), limiting convective development.

A comparison of AMA soundings at 1200 UTC and 0000 UTC (Figs. 19a, 19b) show the effects of the (eastern) dryline passage. The sharp increase in mixing ratio at 600 mb and decrease in mixing ratio at the surface from 1200 UTC to 0000 UTC highlighted the strong vertical turbulent mixing associated with dryline "passage." The top of the convective boundary layer had risen to approximately 550 mb by 0000 UTC. Horizontal momentum also mixed vertically such that there was very little vertical wind shear in this environment.

It is seen in WSR-88D radar reflectivity data from KAMA at 2300 UTC and 0000 UTC (Fig. 28a, 28b) that there was a double-fineline structure over the northern Texas panhandle. The passage of the westernmost fineline coincided with the sharp dewpoint decrease observed at AMA at 2300 UTC. Earlier in the afternoon, AMA was between the finelines and observed gradual decreases in dewpoint. This behavior was in accord with the "mixing zone" hypothesis presented by Ziegler and Hane (1993), and observed in other studies (e.g., Hane et al. (1997) and Crawford and Bluestein (1997)). In other words, the region between the finelines may have had a combination of thermodynamic properties outside of the finelines. The two finelines were oriented such that they converged just to the north of the SPOL radar at Homestead, OK (Fig. 29). Visible satellite imagery (Fig. 30) showed clearly a wedge-shaped area of cumulus cloud cover in the region between the radar finelines

[13] The AERIplus is an interferometer that creates vertical profiles of temperature and moisture based on downwelling infrared radiation (Feltz et al. 2003).

(Figs. 28a, 28b, 29). A time series of in-situ dewpoint taken aboard the University of Wyoming King Air (UWKA) further supported the existence of two moisture gradients (Fig. 29b). It is noted that the domain of UMass operations (white box in Fig. 29a) on this day was to the south of the intersection point. Therefore, the data collection encompassed both drylines. Both dryline boundaries were beginning their diurnal retrogression by 0000 UTC (Figs. 28a, 28b)

2.2 UMass W-band data collection

2.2.1 W-band radar characteristics

The primary data sets used for this study were collected with the W-band radar from the University of Massachusetts (Fig. 31). The characteristics of the radar are listed below:

Transmitter:

Operating frequency	95.04 GHz (λ=3 mm)
Transmitter power	1.2 kW, 1% duty
Transmit pulse length	100 ns – 1 μs (228 ns for 5/22/02)
Pulse repetition frequency	15 kHz (on 5/22/02, others available)
Polarization	H or V

Receiver:

Sample resolution	30 m (on 5/22/02, others available)
Maximum range	15 km (precipitation), ~3 km (clear-air)
Unambiguous velocity	+/- 15.8 m s^{-1} (5/22/02, others available)

Antenna:

Type	Cassegrain dish
Diameter	4 ft
Beamwidth (3 dB)	0.18 degrees
Gain	59 dB
dB down (E field)	19.2,22 dB (left,right) @ 0.39 deg

The utility of the UMass radar can be demonstrated by considering the radar equation for a point target (derived from Rinehart 1997):

$$\overline{P}_r = \frac{c}{1024\pi^2 \ln 2}\left[P_t \tau \lambda^2 G_o{}^2 \theta\varphi\right]\frac{\eta_{av}}{r^2} \tag{14}$$

where $\overline{P}_r$ is the power returned (averaged over multiple samples), c is the speed of light, P_t is the transmitted power, τ is the pulse length, λ is the wavelength, G_o is the maximum gain of the antenna's main lobe, θ and ϕ are the horizontal and vertical beamwidths, respectively, η_{av} is the average backscatter cross-sectional area of the target, and r is the slant range to the target.

The UMass radar has been used as a tool for investigating the finescale structure of tornadoes and their parent severe thunderstorms (e.g., Bluestein et al. 2003, Bluestein et al. 2004). However, it has demonstrated significant capability of clear-air detection as well (e.g., Bluestein and Pazmany 2000). The radar has a wavelength of 3 mm, an order of magnitude smaller than most operational and research radar platforms. From (14) we see that $\overline{P}_r \propto \lambda^2 G_o{}^2 \propto \lambda^{-2}$, so the short wavelength of the W-band allows for much greater sensitivity than conventional mobile X-band radars (assuming all other parameters in (14) are similar between the platforms). Furthermore, the shorter wavelength allows a very small beamwidth (a half-power beamwidth of 0.18 degrees). Again from (14), it is seen that a smaller beamwidth yields greater returned power ($\overline{P}_r \propto G_o^2\theta\varphi \propto \pi^4\theta^{-1}\varphi^{-1}$). At a typical range of 1 km from the radar, the azimuthal/vertical resolution is 3.14 m. Since the power of return for clear-air targets is relatively low, the returned power spectra are rather noisy. Therefore, one must average multiple samples to obtain reliable reflectivity and velocity estimates.

Three different pulse lengths were used during the course of IHOP operations in 2002. Increasing the pulse length yields greater sensitivity (from (14) $\overline{P}_r \propto \tau$) at the expense of along-radial resolution by:

$$\Delta R = \frac{c\tau}{2} \tag{15}$$

where ΔR is the slant range length of the return pulse contributing volume (i.e., the along-radial resolution). For data obtained on 22 May 2002, a pulse length of 228 ns was used, which was equivalent to 30 m along-radial resolution (note: this value is independent of the displayed resolution, which is determined by the signal processor).

The primary scatterering source for the power returned to the W-band radar were most likely insects (Wilson and Schreiber 1986, Martin 2003). Since the wavelength was comparable to the size of the targets, Mie scattering was the dominant source of returned power. The stated minimum detectable signal for the W-band radar was –35 dBZ_e at a range of 1 km from the radar. The average reflectivity in convergence zones at this range (shown later) was about –20 dBZ_e, representing a returned power over 30 times the minimum detectable signal.

2.2.2 Methods of data collection

During IHOP, the UMass radar gathered clear-air data on the following dates: 22 May, 3 June, 9 June and 10 June (Fig. 32) A number of different deployment strategies were utilized in the data collection and were as follows:

1) Velocity Azimuth Display (VAD) (Rabin and Zrnic 1980) – stationary collection of data taken at ~45 degrees elevation (Fig. 33). The antenna was rotated horizontally through ~ 220 degree portion of a cone (limited by the hardware of the positioner). The horizontal wind could be calculated as a function of height AGL assuming that the vertical profile was horizontally homogeneous over the volume of data collection.

2) Vertical antenna – antenna pointed at 86 degrees (maximum elevation allowed by the positioner) and driven across the boundary (Fig. 34). The result was a time series of vertical velocity data, which was converted to a spatial profile using recorded GPS data[14].

[14] According to the manufacturer, the position of the Garmin GPS receiver is accurate to within 15 m on average.

3) Stationary RHI (SRHI) – stationary data collection in which the antenna was rotated from ~0-86 degrees (Figs. 35, 36). Multiple vertical sectors of radial velocity data were obtained in this manner. Although useful for tracking reflectivity and diagnosing radial velocity, the u and w components could not be retrieved independently with such a collection strategy.

4) Rolling RHI (RRHI) – 0-86 degree RHIs collected with the platform in motion (Fig. 37). The radial velocity was adjusted for platform motion (section 3.1). As will be discussed later, the principles of pseudo-dual Doppler analysis (e.g., Hildebrand et al. 1996) could be applied to data taken in such a manner to retrieve the individual u and w wind components.

2.3 Results from vertical antenna deployment (leg 3, 2221-2235 UTC)

From 2221-2235 UTC, the UMass W-band executed a westward-moving vertical antenna deployment across the double dryline along US Highway 270 near Elmwood, OK (Fig. 38). The objective of this deployment was to obtain a time series of vertical velocity in the near-dryline environment. The vehicle maintained a nearly constant speed of 60 mph (26.8 m s^{-1}) during the traverse, along which gentle undulations in the terrain were noted. Though the position of radial velocity measurements was adjusted for the pitch of the platform (discussed in section 3.1), it was impossible to avoid the inclusion of the horizontal wind component into the measurement. However, the effect was very small owing to the shallow terrain slope[15].

The Shared Mobile Atmospheric Research and Training Radar (SMART-R) (Fig. 39a, 39b[16]) (Biggerstaff and Guynes 2000) and NCAR S-band Polarimetric Radar (SPOL) (Fig. 29) (http://www.atd.ucar.edu/rsf/spol/spol.html) both indicated a fineline associated with the eastern DCZ. This boundary was oriented north-northeast to south-southwest. Therefore, the traverses were not precisely normal, but rather formed a small angle from normal, to the boundary. As mentioned in section 2.1, a secondary fineline was evident to the west of the "primary" (i.e., targeted) dryline. Though not recognized at the time of data collection, the UMass W-band transected this secondary feature just before the termination of leg 3 (Figs. 38, 39a, 39b).

The time section of reflectivity from leg 3 (Fig. 40) shows clearly the eastern DCZ as an area of reflectivity in excess of -15 dBZ_e. The reflectivity maxima was associated with a local concentration of boundary-layer scatterers, primarily insects (Wilson and Schreiber 1986, Martin 2003). To a first approximation, these insects are treated as passive and are therefore representative of the wind that is transporting them. Convergence regions, like the one in Fig. 40, therefore represent areas with a higher density of insects (assuming the insect size distribution was the same everywhere). The plume of highest reflectivity was nearly vertical, consistent with previous observations of a nearly vertical dryline interface (e.g., Crawford and

[15] As a worst-case scenario, a 20 m s^{-1} wind with a 2 degree platform pitch would erroneously add 0.7 m s^{-1} to the vertical velocity measurement

[16] The refractivity field in Fig. 39b is derived by using the delay in return from known ground targets to assess the index of refraction (mostly a function of moisture).

Bluestein 1997). A mobile mesonet traverse of the eastern dryline revealed a 6 °C increase in dewpoint over approximately 1 km as the probe headed eastward (Fig. 41). Coincident with the dewpoint rise was a sharp pressure increase of 4 mb. A portion of this pressure rise was due to an elevation drop (calculated from the hypsometric equation to be 2.6 mb), but there was a residual pressure increase that was in part due to the virtual temperature decrease. Assuming that the horizontal changes in temperature and dewpoint measured at the surface were also constant through the lowest 1 km AGL, the hydrostatic pressure increase was 0.2 mb. Thus, a residual pressure increase of 1.2 mb remained, possibly due to non-hydrostatic effects.

Approximately 9 km to the west of the primary (eastern) dryline was the secondary (western) dryline. The feature, though quite subtle in PPI reflectivity imagery from SPOL (Fig. 29) and SR1 (Fig. 39), was very distinct in the UMass W-band cross section (Fig. 40). Both the eastern and western convergence zones were nearly vertical in the lowest 1-1.5 km AGL, above which a considerable tilt to the east with height was evident. DCZs with a larger downshear tilt with height have been identified as being less favorable for the development of deep convection as ascending parcels have a greater chance of advecting out of the DCZ before reaching the LCL and LFC (Ziegler and Rasmussen 1998, Peckham and Wicker 2000).

Minima in reflectivity were observed in the dryline interface at approximately 1.5 km AGL. One of these areas ("D_1" in Fig. 40) was immediately to the east of the surface position of the eastern DCZ. The other position ("D_2" in Fig. 40) was about 4 km to the east of the DCZ. The vertical velocity data from the same leg (Fig. 42) showed a correlation between these low reflectivity intrusions and subsiding air motion (considering the fringe vertical velocity values on the border of these reflectivity-void regions and others to the west of the eastern DCZ). Since the source for the scatterers (i.e., insects) is the surface, the scatterer concentration is nearly zero at higher altitudes (e.g., above the boundary layer). Therefore, downward motion represents transport from a region where there is a dearth of insects, and is therefore associated lack of radar reflectivity (D. Leon, University of Wyoming, 2004, personal communication).

To confirm further the presence of downward motion in these reflectivity-void regions, observations from the University of Wyoming King Air (UWKA) were considered. The flight leg (Fig. 38) crossed directly over the path of the UMass W band, and ended approximately ten minutes before the completion of UMass leg 3. Note that the flight leg was performed normal to the primary dryline, and therefore formed an angle to the UMass ground leg.[17] The UWKA radar showed the presence of downward motion (Fig. 43a) in the regions marked by reflectivity voids to the east of the primary DCZ in Fig. 40. The downward motion (generally -2 to -4 m s^{-1}) immediately to the east of the surface position of the DCZ ("D_1" in Figs. 43a and 43b) may have represented an impediment to the ascent of air parcels in the DCZ. If this downward motion were a characteristic of the DCZ over a large region of space and substantial periods of time then it may have played a role in precluding convective initiation for this case day.

[17] The distance scale in Fig. 43a is the east-west component of total flight leg distance and can therefore be compared to UMass data directly.

The region of subsiding air approximately 4 km to the east of the dryline ("D_2" in Figs. 43a and 43b) was much broader (~ 3 km wide). Vertical velocity values in excess of –4 m s^{-1} were observed in this corridor. The position of this descending air was consistent with that found in the airborne radar study of Weiss and Bluestein (2002). The lowered maximum altitude of returned power in this region (~ 1 km AGL) suggested that the source region for this downward moving air was at least in part from above the CBL. One can therefore infer that this air had lower specific humidity. In-situ measurements taken aboard the UWKA at 700 m AGL (Fig. 43c) confirm a small local decrease in dewpoint in this area, with other decreases in descending regions farther to the east (Fig. 44). The downward transport of air from above the CBL may have assisted in the eastward propagation of the dryline through the late morning and early afternoon hours.

UMass W-band measurements of the primary DCZ indicated a maximum upward vertical velocity of 8 to 9 m s^{-1} (Fig. 43b). This intense upward motion was evident only over a very narrow region, however, approximately 50-100 m wide. The UWKA measured a maximum w of 7.1 m s^{-1} (Fig. 43a). Although there were small differences in the exact location the DCZ was crossed between the ground and flight tracks (Fig. 38), the difference in maximum w was at least partly attributable to the larger beamwidth (UMass - 0.18 degrees, UWKA - 0.7 degrees) and faster cross-track platform motion (UMass - 26.8 m s^{-1}, UWKA - ~ 62.0 m s^{-1}). Both of these factors ultimately increased the effective size of the beam by increasing the size of the resolution volume. A crude representation of this effect was achieved by a running multiple-point average through the UMass vertical velocity data. For example, a three-point average (very roughly equivalent to a 0.6 degree beamwidth[18]) decreased maximum *w* in the DCZ to 7 m s^{-1} (Fig. 45). For a five-point average (roughly equivalent to a 1.0 degree beamwidth such as that on a typical mobile X-band radar), maximum *w* further decreased to 6 m s^{-1} (Fig. 46).

Both the UMass and UWKA radars detected upward vertical velocity associated with the convergence zone of the western dryline. However, the magnitude of the upward motion again varied between the platforms. The UWKA indicated relatively weak ascent of ~ 2 m s^{-1}, while UMass showed a maximum *w* of ~ 5 m s^{-1} in narrow regions. Again, the effective beamwidth may have contributed to this difference. The larger tilt and decreased distance between the primary and secondary drylines[19] (compared to UMass) suggest that the UWKA measurements may have been made on a distinctly different portion of the secondary dryline. Regardless, both platforms showed a wide region of descent approximately 3-4 km wide centered about 4-5 km east of the secondary dryline. A decrease in dewpoint of 1 °C was seen here as well in UWKA in-situ data (Fig. 44b).

A boresighted video camera was mounted on the W-band dish to assist the radar operator in the proper placement of the narrow beam during field operations. At times when the antenna was pointed vertically, the video served to identify regions of cloud cover directly above the instrument. Three such regions were found during the leg 3 deployment. The first (labeled "A" in Figs. 40, 42) area was immediately to

---

[18] To find the exact equivalency, the gain pattern of the respective antennae must be considered.
[19] Recall that the UWKA intercepted the secondary dryline north of the UMass intercept (Fig. 38)

the west of the primary DCZ, and contained a very shallow cumulus cloud (Fig. 40). The second area was likely associated with the ascending branch of a HCR and was found halfway between the primary and secondary DCZ (labeled "B" in Figs. 40, 42) and contained more vigorous convection (Fig. 40). The third area of cloud cover was by far the widest (~2 km) and was associated with the DCZ of the secondary dryline (labeled "C" in Figs. 40, 42). No cumulus cloud cover was seen above or east of the primary DCZ, nor was any seen west of the secondary DCZ[20]. This observation was consistent with the "wedge" shape of cumulus convection seen on satellite (Fig. 30). It is possible that this zone represented an optimal blend of the highest specific humidity to the east of the primary dryline and the deepest CBL to the west of the secondary dryline (Fig. 47).

[20] Cirrus cloud cover was seen, however.

CHAPTER 3: WEAK-CONSTRAINT VARIATIONAL DOPPLER WIND SYNTHESIS

3.1 Methodology of data processing

The raw UMass data were subjected to pre-analysis processing to remove known errors. First, data associated with weak power return were removed. The assigned velocity for a range bin is calculated with a power-density function (Doviak and Zrnic 1984):

$$\overline{V} = \frac{\int_{-Nyquist}^{+Nyquist} V\, S(V)\, dV}{\int_{-Nyquist}^{+Nyquist} S(V)\, dV} \tag{16}$$

where $\overline{V}$ is the assigned velocity, V is a velocity within the Nyquist interval and $S(V)$ is the spectral power associated with the velocity V. Weak-return data produce biased velocity estimates such that the absolute magnitude of velocity is underestimated (Fig. 48). Instrument noise in the spectrum has a profound impact on the assigned velocity in cases of weak return. If the true meteorological signal has a power close to the instrument noise, then the noise has a relatively significant impact in the integration to determine the assigned velocity estimate (from (16)). Since instrument noise contributes random power to the velocity spectrum, the end result is a very noisy velocity field in weak-return regions. For this reason, SOLO software from NCAR (Oye et al. 1995) was used to remove all data associated with a reflectivity < -30 dBZe[21]. This threshold was subjectively chosen as one that appropriately removed the most erroneously variant velocity data. The remaining velocity data were then unfolded around the Nyquist velocity of $^{+}/_{-}$ 15.8 m s^{-1}.

At this point, the velocity data were deemed reliable (owing to the high signal to noise ratio). However, the data were still platform-relative. To transform the data to a ground-relative reference frame, both the magnitude and position of the velocity values had to be altered. GPS measurements of position (latitude/longitude) and velocity (mph) were recorded at 1 s intervals during the data collection. The recorded translational velocity was subtracted from each ray in the velocity time series to make the magnitudes ground-relative.

Using the recorded GPS position and radar elevation, each range cell of each ray in the time series was mapped to a specific point in *x-z* space using the following geometric formulae (Fig. 49):

$$x = x_{start} + (n * 15\,m)\cos(\alpha) - 7.5\,m \tag{17}$$

$$z = z_{start} + \delta_{elevation} + (n * 15\,m)\sin(\alpha) - 7.5\,m \tag{18}$$

where n was the range gate number, α was the platform-relative elevation and $\delta_{elevation}$ was the correction for the platform's elevation above the reference height (z_{start}). The

[21] Ideally, one should apply the threshold based on power returned. However, the UMass W-band processor did not record actual power of return. A mock returned power field was created by applying a range correction to reflectivity. The thresholds for this mock field and reflectivity were found to be about the same.

decimal result from (17) and (18) was rounded to yield the x and z location of the gridpoint.

Since the elevation angles were platform-relative, a correction factor had to be included to account for the pitch angle of the platform (i.e., if the platform were pointed uphill or downhill). GPS elevation data were initially considered to compute a correction factor. The pitch was calculated in the following manner for every second of GPS data:

$$\text{Platform pitch} = \tan^{-1}\left(\frac{\Delta z}{\Delta x}\right) \tag{19}$$

where Δz was the change in elevation and Δx was the change in horizontal position. The GPS elevation data were very noisy, and were noted to drift when the platform was stationary. Since the GPS used atmospheric pressure to calculate elevation, it was not surprising that the calculation was suspect in the dryline environment, since pressure can vary in the horizontal on the order of 1-2 mb (Parsons et al. 1991). In an attempt to find a more reliable measure of pitch, 30 meter digital elevation models (DEMs) from the USGS were employed (Fig. 50a). Values of GPS and DEM elevation were compared for an early leg of data collection on 22 May 2002 (Fig. 50b). It was evident that the GPS systematically underestimated the pressure by about 10 mb on average, undoubtedly due to an inaccurate hydrostatic reduction of the observed pressure to the surface. A comparison of pitch calculated from the DEM and GPS data (using (19)) (Fig. 50c) reveals a much smoother and realistic pitch calculation for the case of the DEM data.

Once the proper pitch was determined, the x and z gridpoint values for each ray of velocity data were altered (Fig. 51). For a westward pointed truck:

$$\Delta X_{\text{adjustment}} = -\Delta X_{\text{uncorrected}} \sin\theta \quad (\text{for } +\theta) \qquad (20a)$$
$$= \Delta X_{\text{uncorrected}} \sin\theta \quad (\text{for } -\theta)$$

$$\Delta Z_{\text{adjustment}} = -\Delta Z_{\text{uncorrected}} \sin\theta \qquad (20b)$$

Likewise, for an eastward pointed truck:

$$\Delta X_{\text{adjustment}} = \Delta X_{\text{uncorrected}} \sin\theta \quad (\text{for } +\theta) \qquad (21a)$$
$$= -\Delta X_{\text{uncorrected}} \sin\theta \quad (\text{for } -\theta)$$

$$\Delta Z_{\text{adjustment}} = \Delta Z_{\text{uncorrected}} \sin\theta \qquad (21b)$$

where θ was the pitch angle (positive θ denoted an uphill pitch for a westward moving radar).

A dynamically-allocated linked list[22] was introduced to store the gridded reflectivity and radial velocity values. For each cell of each ray, reflectivity, radial velocity and the *look angle* (i.e., the pitch-adjusted elevation angle of the platform) were stored. As might be expected, many gridpoints in the domain had a very large number of data stored, especially near the ground. In fact, some points in leg 6 had

[22] A dynamically-allocated linked list allocates memory as needed (i.e., as an observation is processed), as opposed to arrays, which allocate memory at initialization. Since the number of observations varied considerably across the domain, arrays (which required the same number of observation records for each gridpoint) were not a proper choice as most of the memory allocated was unused. In fact, the memory requirements for the arrays exceeded that of the machine!

well over 300 records (Fig. 52)! This overlapping of radial-velocity data presented an over-determined analysis problem, which was exploited in the pseudo-multiple Doppler analysis technique (explained in section 3.2).

3.2 Derivation of weak-constraint formulation

When designing the variational analysis for this problem, it was important first to determine what measure(s) would be used to define the "best" analysis. There were many ways to approach this. For example, if dynamical imbalances were intolerable, then an analysis was desired that satisfied the balance exactly at the expense of all other possible constraints (e.g., observations, smoothness) Another approach to the analysis was to seek a solution that did not satisfy any condition specifically, rather, to satisfy one or more multiple conditions in the best manner possible. A common example of this approach is regression (finding an analysis (e.g., line, quadratic curve, n^{th} order polynomial) that fits all data points by minimizing the square of the departure of each data point from the analysis).

Much the same, variational analyses can be constructed to prioritize different constraints. Possible constraints considered for these analyses included: radial velocity observations, anelastic mass continuity and smoothness. The smoothness constraint was eliminated for several reasons. First, extra smoothing would reduce the primary benefit of the UMass W-band radar: very high spatial resolution. In other words, a smoothness constraint would potentially eliminate small scales of motion that were real and resolvable. Furthermore, some smoothing was already included in the variational analysis procedure through the mass continuity constraint, where uncoupled errors in u and w were diminished. Lastly, there was no physical basis for the smoothing. The mass continuity constraint, on the other hand, is based on an approximation to a physical law.

For this project, a strict constraint on mass continuity was deemed unnecessary as: 1) the observations were deemed highly reliable owing to the significant amount of overlap (therefore, random observational error approximately canceled), 2) weak constraint formulations have been found to be more accurate than strong constraint formulations in pseudo-dual Doppler analyses of thunderstorms (Dowell and Bluestein 2002), 3) the chosen continuity relation was an approximation to exact mass conservation and 4) the analyses were not to be used for model initialization, where an imbalance might shock the beginning time steps of a simulation.

Following the specifications above, the cost function to be minimized was:

$$J = J_{obs} + \beta J_{continuity} \tag{22a}$$

$$J_{obs} = \sum_{n=1}^{m(x,z)} \left(c_1^n u + c_2^n w - V_r^n \right)^2 \tag{22b}$$

$$J_{continuity} = \left(\partial u / \partial x + \partial w / \partial z + \kappa w \right)^2 \tag{22c}$$

$$c_1 = \cos(\alpha) \tag{22d}$$

$$c_2 = \sin(\alpha) \tag{22e}$$

where (22b) represented the contribution to the cost function from observational discrepancy and (22c) denoted the contribution to the cost function from anelastic mass continuity violation. In equations (22a) - (22e) u and w were the analysis values, V_r was the observed radial velocity, c_1 and c_2 represented geometric coefficients mapping velocities from Cartesian space to that of the radial velocity vectors, κ was the correction to mass continuity for vertical density stratification, m was the total number of observations per gridpoint of which n was a specific observation, and α was the look angle for each observation. The formulation was similar to that developed by Gao et. al (1999) (less a background and smoothness constraint) and Dowell and Bluestein (2002) (neglecting variations in the y direction).

The β term in (22a) represents the relative weight given to mass continuity violation and observation increments (differences between the analysis and observations) in the calculation of the cost function. It is similar in many ways to the ratio of the B^{-1} and R^{-1} error matrices in the statistical interpolation algorithm of (4). In this case, however, we did not know the spatial error characteristics of the W-band radar. Therefore, the β term was a rather arbitrary assignment of the relative accuracy of the observations compared to the kinematic constraint. A higher value of β denotes a larger penalty for anelastic mass continuity violation, which may be desired when using observations with larger errors. Likewise, a smaller value of β introduces a larger penalty for analysis gridpoints that deviate from the observations of radial velocity. For the units of J_{obs} and $J_{continuity}$ to be consistent (m^2 s^{-2}), it was necessary for β to have units of m^2. A logical choice of length scale was the grid spacing of the analysis. It was therefore deemed appropriate to assign:

$$\beta = (\Delta x)^2 = (\Delta z)^2 \tag{23}$$

Since the grid spacing used for this analysis was $\Delta x = \Delta z = 30$ m, β was chosen to be 900 m^2.

The anelastic mass continuity equation has the implicit assumption that density variations in the horizontal are negligible compared to the vertical variations in the base state. The κw term reflects the consideration for vertical variations in density where:

$$\kappa = \frac{1}{\rho} \partial\rho / \partial z \tag{24}$$

Starting with the ideal gas law and the hydrostatic equation,

$$P = \rho RT$$

$$\partial P / \partial z = -\rho g \tag{25}$$

the κ term can be expressed as:

$$\kappa = \frac{1}{\rho}\frac{\partial \rho}{\partial z} = -\frac{g}{RT} - \frac{1}{T}\frac{\partial T}{\partial z} \tag{26}$$

For the lowest 3 km of the atmosphere (which is the extent of vertical sampling with the W-band radar), the lapse rate was dry adiabatic (Figs. 19b, 21b). Therefore, using:

$$\frac{\partial T}{\partial z} = -10\ {}^{\circ}C/km$$

$$T_{sfc} = 300\ {}^{o}K$$

$$T_{3\ km\ AGL} = 270\ {}^{o}K$$

the following values of κ were calculated:

$$\kappa_{sfc} = -8.05 \times 10^{-5}\ m^{-1}$$

$$\kappa_{3\ km\ AGL} = -8.9 \times 10^{-5}\ m^{-1}$$

κ was linearly interpolated between these bounds for altitudes between the surface and 3 km AGL.

The derivation of the weak constraint variational formulation follows. We start with the statement of the cost function (from (22a)-(22e)) as follows:

$$J = \iint_{xz}\left[\sum_{n=1}^{m(x,z)}\left(c_1^n u + c_2^n w - V_r^n\right)^2 + \beta\left(\frac{\partial u}{\partial x} + \frac{\partial w}{\partial z} + \kappa w\right)^2\right]dxdz \tag{27}$$

We then take the variation with respect to u to get:

$$\delta_u J = \iint_{xz}\left[2\sum_{n=1}^{m(x,z)}\left(c_1^n u + c_2^n w - V_r^n\right)c_1^n \delta u + 2\beta\left(\partial u/_{\partial x} + \partial w/_{\partial z} + \kappa w\right)\partial/_{\partial x}(\delta u)\right] dxdz \tag{28}$$

The above is a statement of how the cost function changes for incremental changes of analysis u over the entire domain. Since the second variation of J is positive definite, the task of finding the minimum of J is straightforward. The minimum of J (i.e., the ideal analysis) will occur when:

$$\delta_u J = 0 \tag{29}$$

We divide (28) by two, distribute the integration and set the expression equal to zero so that:

$$\begin{aligned}\delta_u J &= \iint_{xz}\sum_{n=1}^{m(x,z)}\left(c_1^n u + c_2^n w - V_r^n\right)c_1^n \delta u \; dxdz \\ &\quad + \iint_{xz}\beta\left(\partial u/_{\partial x} + \partial w/_{\partial z} + \kappa w\right)\partial/_{\partial x}(\delta u)dxdz \\ &= 0\end{aligned} \tag{30}$$

The second term on the right hand side of (30) contains an undesired derivative of δu (as we wish to collect the δu terms later in the derivation). To remove this derivative, the term is integrated by parts. This term then becomes:

$$\int_z \beta\left(\partial u/\partial x + \partial w/\partial z + \kappa w\right)\delta u \Big|_{x_{west}}^{x_{east}} dz - \iint_{xz} \delta u\, \partial/\partial x \left[\beta\left(\partial u/\partial x + \partial w/\partial z + \kappa w\right)\right] dxdz \qquad (31)$$

The first term of (31) requires specific information at the boundaries. We can arbitrarily eliminate this term by either: 1) satisfying anelastic mass continuity exactly on the lateral boundaries or 2) setting boundary conditions on the analysis (not allowing the analysis to vary such that $\delta u = 0$). Condition #1 was chosen for both the east and west boundaries. Incorporating the reduced version of (31) into (30), we find that:

$$\delta_u J = \iint_{xz} \sum_{n=1}^{m(x,z)} \left(c_1^n u + c_2^n w - V_r^n\right) c_1^n \delta u \; dxdz$$

$$- \iint_{xz} \beta \delta u\, \partial/\partial x \left(\partial u/\partial x + \partial w/\partial z + \kappa w\right) dxdz$$

$$= 0 \qquad (32)$$

Rewriting the expression, we find that:

$$\iint_{xz}\left[\sum_{n=1}^{m(x,z)}\left(c_1^n u + c_2^n w - V_r^n\right)c_1^n - \beta \partial/_{\partial x}\left(\partial u/_{\partial x} + \partial w/_{\partial z} + \kappa w\right)\right]\delta u\, dxdz = 0 \quad (33)$$

Distributing the summation, we see that:

$$\iint_{xz}\left[\sum_{n=1}^{m(x,z)}\left(c_1^n\right)^2 u + \sum_{n=1}^{m(x,z)}\left(c_1^n c_2^n\right) w - \sum_{n=1}^{m(x,z)}\left(c_1^n V_r^n\right) - \beta \partial/_{\partial x}\left(\partial u/_{\partial x} + \partial w/_{\partial z} + \kappa w\right)\right]\delta u dxdz = 0$$

(34)

Discounting the trivial solution of $\delta u = 0$, (34) can only be true if the bracketed term equals zero, or:

$$\boxed{\sum_{n=1}^{m(x,z)}\left(c_1^n\right)^2 u + \sum_{n=1}^{m(x,z)}\left(c_1^n c_2^n\right) w - \sum_{n=1}^{m(x,z)}\left(c_1^n V_r^n\right) = \beta \partial/_{\partial x}\left(\partial u/_{\partial x} + \partial w/_{\partial z} + \kappa w\right)} \quad (35)$$

Equation (35) represents the first Euler-Lagrange equation.

To derive the second Euler-Lagrange equation, the variation of (27) with respect to w is taken:

$$\delta_w J = \iint_{xz} 2\sum_{n=1}^{m(x,z)}\left(c_1^n u + c_2^n w - V_r^n\right)c_2^n \delta w dxdz$$

$$+ \iint_{xz} 2\beta\left(\partial u/_{\partial x} + \partial w/_{\partial z} + \kappa w\right)\left[\partial/_{\partial z}(\delta w) + \kappa(\delta w)\right]dxdz\Big] \quad (36)$$

Distributing the second term on the RHS of (36), this second term becomes:

$$\iint_{xz} 2\beta\left(\partial u/\partial x + \partial w/\partial z + \kappa w\right)\partial/\partial z\,(\delta w)\,dxdz + \iint_{xz} 2\beta\left(\partial u/\partial x + \partial w/\partial z + \kappa w\right)\kappa(\delta w)\,dxdz \quad (37)$$

As before, the solution requires removal of the derivative of δw in the first term of (37). Integrating the first term of (37) by parts yields:

$$\int_{x} 2\beta\left(\partial u/\partial x + \partial w/\partial z + \kappa w\right)\delta w\Big|_{z_{bottom}}^{z_{top}} dx - \iint_{xz} 2\delta w \beta\,\partial/\partial z\left(\partial u/\partial x + \partial w/\partial z + \kappa w\right)dxdz \quad (38)$$

The leftmost term can be eliminated by either: 1) satisfying anelastic mass continuity exactly or 2) prescribing a boundary condition on w (not allowing w to vary) at the top and bottom boundary. The natural boundary condition for the ground is one of impermeability (w=0). In analyses using large-beamwidth data or obstacle-blocked flow near the ground (e.g., Mewes and Shapiro 2000), the lowest level of available radar data is far enough above the surface that the impermeability condition is invalid. However, in this case the narrow beamwidth of the W-band permitted observation sufficiently near the surface such that w=0 could be applied as a prescribed lower boundary condition (the beamwidth is 9 m at a range of 3 km from the radar). Unlike in thunderstorm cases, where the top of the domain is the tropopause (e.g., Dowell and Bluestein 2002), impermeability cannot be applied safely as a top boundary condition in this case. At 3 km AGL, vertical motion O~(1 m/s) can easily be found (e.g., from convection penetrating upward from the boundary layer, lift from synoptic-scale features) (Bluestein 1993, Geerts and Miao 2003). Consequently, anelastic mass continuity was enforced as a top boundary condition.

With the first term of (38) eliminated, (38) can be combined with (37) to give:

$$\iint_{xz} 2\beta\delta w\left[-\frac{\partial}{\partial z}\left(\frac{\partial u}{\partial x}+\frac{\partial w}{\partial z}+\kappa w\right)+\kappa\left(\frac{\partial u}{\partial x}+\frac{\partial w}{\partial z}+\kappa w\right)\right]dxdz \tag{39}$$

Combining (39) with (36) yields the expression for the first variation of the cost function with respect to w:

$$\delta_w J = \iint_{xz} 2\sum_{n=1}^{m(x,z)}\left(c_1^n u + c_2^n w - V_r^n\right)c_2^n\delta w$$
$$+ 2\beta\delta w\left(\kappa-\frac{\partial}{\partial z}\right)\left(\frac{\partial u}{\partial x}+\frac{\partial w}{\partial z}+\kappa w\right)dxdz \tag{40}$$

Again, the condition where (40) is equal to zero is desired, yielding the ideal minimized solution. Dividing (40) by two and collecting the δw terms:

$$\iint_{xz}\left[\sum_{n=1}^{m(x,z)}\left(c_1^n u + c_2^n w - V_r^n\right)c_2^n + \beta\left(\kappa-\frac{\partial}{\partial z}\right)\left(\frac{\partial u}{\partial x}+\frac{\partial w}{\partial z}+\kappa w\right)\right]\delta w dxdz = 0 \tag{41}$$

Discounting the trivial solution of $\delta w = 0$, (41) can only be true if the bracketed term equals zero; that is:

$$\sum_{n=1}^{m(x,z)} \left(c_1^n u + c_2^n w - V_r^n\right) c_2^n = \beta\left(-\kappa + \partial/\partial z\right)\left(\partial u/\partial x + \partial w/\partial z + \kappa w\right) \tag{42}$$

Distributing the summation on the left hand side of (42):

$$\boxed{\sum_{n=1}^{m(x,z)} \left(c_1^n c_2^n\right) u + \sum_{n=1}^{m(x,z)} \left(c_2^n\right)^2 w - \sum_{n=1}^{m(x,z)} c_2^n V_r^n = \beta\left(-\kappa + \partial/\partial z\right)\left(\partial u/\partial x + \partial w/\partial z + \kappa w\right)} \tag{43}$$

Equation (43) is the second Euler-Lagrange equation.

As discussed in section 1.3.3, there are a number of different methods for finding the optimal solution with knowledge of $\nabla_{u,w} J$ (e.g., steepest descent, conjugate gradient). The preferred method for solution here (after Dowell and Bluestein 2002) is a numerical iteration of the two Euler-Lagrange equations. It is noted that the two Euler-Lagrange equations (35) and (43) are coupled in the unknown analysis variables u and w. Therefore, the system is complete and can be solved iteratively for the optimal analysis values.

Before the analysis can be computed, the Euler-Lagrange equations must be discretized. Isolating u on the left hand side of (35):

$$u = \frac{\sum_{n=1}^{m(x,z)} \left(c_1^n V_r^n\right) - \sum_{n=1}^{m(x,z)} \left(c_1^n c_2^n\right) w + \beta \frac{\partial}{\partial x}\left(\frac{\partial u}{\partial x} + \frac{\partial w}{\partial z} + \kappa w\right)}{\sum_{n=1}^{m(x,z)} \left(c_1^n\right)^2} \tag{44}$$

Distributing the derivative, the last term of the numerator becomes:

$$\beta \frac{\partial^2 u}{\partial x^2} + \beta \frac{\partial}{\partial x}\left(\frac{\partial w}{\partial z} + \kappa w\right) \tag{45}$$

Discretizing equation (45) in u:

$$\beta \frac{u_{i+1,j} - 2u_{i,j} + u_{i-1}}{(\Delta x)^2} + \beta \frac{\partial}{\partial x}\left(\frac{\partial w}{\partial z} + \kappa w\right) \tag{46}$$

Combining (46) with the discretized form of (43) yields:

$$u_{i,j} = \frac{\sum_{n=1}^{m(x,z)} \left(c_1^n V_r^n\right) - \sum_{n=1}^{m(x,z)} \left(c_1^n c_2^n\right) w + \beta \left(\frac{u_{i+1,j} - 2u_{i,j} + u_{i-1,j}}{(\Delta x)^2}\right) + \beta \frac{\partial}{\partial x}\left(\frac{\partial w}{\partial z} + \kappa w\right)}{\sum_{n=1}^{m(x,z)} \left(c_1^n\right)^2} \tag{47}$$

Collecting the u_i terms:

$$u_{i,j}\left(1+\frac{\frac{2\beta}{(\Delta x)^2}}{\sum_{n=1}^{m(x,z)}\left(c_1^n\right)^2}\right)=\frac{\sum_{n=1}^{m(x,z)}\left(c_1^n V_r^n\right)-\sum_{n=1}^{m(x,z)}\left(c_1^n c_2^n\right)w+\beta\left(\frac{u_{i+1,j}+u_{i-1,j}}{(\Delta x)^2}\right)+\beta\,\partial\!\left/\partial x\right.\left(\partial w\!\left/\partial z\right.+\kappa w\right)}{\sum_{n=1}^{m(x,z)}\left(c_1^n\right)^2} \tag{48}$$

Rewriting (48) and discretizing the remainder of the expression:

$$\boxed{u_{i,j}=\frac{\sum_{n=1}^{m(x,z)}\left(c_1^n V_r^n\right)-\sum_{n=1}^{m(x,z)}\left(c_1^n c_2^n\right)w_{i,j}+\beta\left(\frac{u_{i+1,j}+u_{i-1,j}}{(\Delta x)^2}\right)+\beta\left(\frac{w_{i+1,j+1}-w_{i+1,j-1}-w_{i-1,j+1}+w_{i-1,j-1}}{4\Delta x\Delta z}\right)+\beta\kappa\left(\frac{w_{i+1,j}+w_{i-1,j}}{2\Delta x}\right)}{\sum_{n=1}^{m(x,z)}\left(c_1^n\right)^2+\frac{2\beta}{(\Delta x)^2}}} \tag{49}$$

In a similar manner, the second Euler-Lagrange equation (43) can be discretized. Solving (43) for w:

$$w_{i,j}=\frac{\sum_{n=1}^{m(x,z)}c_2^n V_r^n-\sum_{n=1}^{m(x,z)}\left(c_1^n c_2^n\right)u+\beta\left(-\kappa+\partial\!\left/\partial z\right.\right)\left(\partial u\!\left/\partial x\right.+\partial w\!\left/\partial z\right.+\kappa w\right)}{\sum_{n=1}^{m(x,z)}\left(c_2^n\right)^2} \tag{50}$$

Distributing the last term of the numerator and discretizing all derivatives:

$$w_{i,j}=\frac{\sum_{n=1}^{m(x,z)} c_2^n V_r^n-\sum_{n=1}^{m(x,z)}\left(c_1^n c_2^n\right)u+\beta\left(\frac{u_{i+1,j+1}-u_{i-1,j+1}-u_{i+1,j-1}+u_{i-1,j-1}}{4\Delta x\Delta z}\right)-\beta\kappa^2 w_{i,j}+ +\beta w_i \,{\partial\kappa}/{\partial z}+\beta\left(\frac{w_{i,j+1}-2w_{i,j}+w_{i,j-1}}{(\Delta z)^2}\right)}{\sum_{n=1}^{m(x,z)}\left(c_2^n\right)^2}$$

(51)

Collecting all $w_{i,j}$ terms, we arrive at the final discretized expression of Euler-Lagrange equation #2:

$$\boxed{w_{i,j}=\frac{\sum_{n=1}^{m(x,z)} c_2^n V_r^n-\sum_{n=1}^{m(x,z)}\left(c_1^n c_2^n\right)u+\beta\left(\frac{u_{i+1,j+1}-u_{i-1,j+1}-u_{i+1,j-1}+u_{i-1,j-1}}{4\Delta x\Delta z}\right)+\beta\left(\frac{w_{i,j+1}+w_{i,j-1}}{(\Delta z)^2}\right)}{\sum_{n=1}^{m(x,z)}\left(c_2^n\right)^2+\beta\kappa^2+\frac{2\beta}{(\Delta z)^2}-\beta\,{\partial\kappa}/{\partial z}}}$$

(52)

The centered differencing employed above introduces a problem at the boundaries of the domain. When calculations were made at a boundary point, centered first-order derivatives were approximated by one-sided derivatives. To handle the second-order derivatives, a layer of extra gridpoints was added outside the domain (Fig. 53). Only values of u (w) were needed at these exterior side (top) gridpoints to accommodate the calculations of $\partial^2 u/\partial x^2$ ($\partial^2 w/\partial z^2$) in (35) and (43).

During each iteration of the solution process, the exterior gridpoints had to be updated to enforce the boundary conditions. Along the lower boundary, the impermeability condition was applied such that w=0 for all points along z=0 and z=-1 (exterior gridpoints). For the rest of the boundaries, mass continuity was required to be satisfied exactly. For each point along these boundaries, the anelastic mass continuity equation was used to update the exterior gridpoint value. For example, along the top row of exterior gridpoints, the following equation was used for the updates:

$$w_{i,j+1} = -2\kappa\Delta z\, w_{i,j} - \left(\frac{\Delta z}{\Delta x}\right)\left(u_{i+1,j} - u_{i-1,j}\right) + w_{i,j-1} \qquad (53)$$

Similar equations were used for u on the lateral boundaries. Again, one-sided derivatives were used when required (i.e., in the corner regions).

The optimal solution was found in the following manner:

1) The domain was initialized with a first guess of the analysis (u=w=0 for all of the analyses in this dissertation).

2) Equation (49) was applied to update the analysis value u for the entire domain, from left to right, and from bottom to top.

3) Equation (52) was used in a similar manner to update the analysis value for w.

4) The top and side boundary conditions were updated.

5) The cost function J was calculated for the analysis values found from steps 2 and 3.

6) If the reduction in cost function from the iteration (e.g., Fig. 54) was not below a prescribed tolerance, steps 2 through 5 were repeated.

The above procedure allowed for convergence to the optimal solution, regardless of the choice of first guess in step 1[23]. Once the optimal solution was reached, the analysis values were output to graphics packages (ZXPLOT (http://www.caps.ou.edu/ZXPLOT/) and NCAR graphics (http://ngwww.ucar.edu/)) to generate plots.

3.3 Homogeneous flow test case

To test the analysis technique developed above, a series of observational system simulation experiments (OSSEs) were developed. For each OSSE, model output was sampled in a manner similar to that of the 22 May 2002 data collection. The result of this operation was a time series of radial velocity data, which was then used in conjunction with the variational analysis technique. Since the "truth" was already known (i.e., the model state from which the radial velocity was sampled), exact error statistics could be generated. These statistics revealed the accuracy of the synthesis techniques and allowed for the determination of optimal scanning strategies.

[23] Portions of the domain with small look angle difference amongst the observations did show a small dependence on the first guess as the analyzed velocity values tended to be slightly closer to the first guess.

The first OSSE developed was an analytical constant horizontal flow field of 10 m s^{-1} (i.e., u=10 m s^{-1}) over the entire domain. This flow was sampled using a rolling RHI technique similar to that of the traverse of leg 6 on 22 May 2002 (section 3.5) (Fig. 55), using a constant platform velocity of 30 mph (13.33 m s^{-1}) and vertical antenna rotation rate (hereafter scan rate) of 1.6 degrees s^{-1}. Data were "processed" at 10 Hz in accordance with the signal processor in the W-band radar system. As in all cases, a first guess of u=w=0 was introduced as a first guess to the variational synthesis procedure.

The results from this experiment (Fig. 56) show that the technique was successful at reproducing the horizontal flow with very little error. The RMS error for the domain:

$$RMS = \sqrt{\frac{1}{N}\left[\sum_{i=1}^{N}\left(x_i - x_{truth}\right)^2 + \sum_{i=1}^{N}\left(z_i - z_{truth}\right)^2\right]} \tag{54}$$

was calculated to be 0.28 m s^{-1}.

Multiple simulations were performed to test the sensitivity of the analysis RMS error to the scanning strategy of the hypothetical UMass radar (Table A)[24]. The first series of experiments varied the platform velocity from 1 mph (0.44 m s^{-1}) to 70 mph (31.11 m s^{-1}) while holding the scan rate fixed at 2.0 degrees s^{-1}. The resulting

[24] The "X"s in Table A are scan strategies that yielded at least one hole (i.e., data-void point) in the analysis domain. Such a situation requires an artificial hole-filling algorithm using bogus analysis values, which was undesirable.

plot of RMS error (Fig. 57) showed clearly an increase in RMS error as the platform velocity was increased (e.g., RMS = 0.014 m s^{-1} for a platform velocity of 10 mph (4.44 m s^{-1}), and RMS = 0.416 m s^{-1} for a platform velocity of 45 mph (20.00 m s^{-1}). The increase in RMS error was attributed largely to sub-critical look angle differences[25] over portions of the domain (Figs. 58a, 58b). The analyses for these high-RMS cases (e.g., Figs. 59a, 59b) showed the largest error near the top of the domain, where look angle differences were in the range of zero to 10 degrees (e.g., Fig. 58b). In these sub-critical regions, the radial velocity observations were nearly collinear. Therefore, the accuracy of the retrieval of the individual components of motion (u/w) was less certain. The resulting analysis had a u component that was too weak compared to the real u component in the sub-critical regions (Fig. 56). If the first guess for the analysis was changed to u=20.0 m s^{-1} (from u=0 m s^{-1}) the analysis u component error had identical magnitude, but was of opposite sign (i.e., the u-component was too strong). Therefore, it is apparent, that the innovation (the departure of observations from the analysis in each iteration) was under-applied in regions with sub-critical look angle differences, and the resulting analysis was therefore closer to the first guess. In the real atmosphere, the radial velocity error arises from instrument error. In these OSSEs, the error was due to the truncation of radial velocities and assignment of radial velocity to grid using a nearest-neighbor approach.

[25] The generally accepted (though seemingly undocumented) threshold for independence of radial velocity observations in dual-Doppler analyses is 30 degrees.

The second series of simulations varied the scan rate as platform velocity was held constant at 30 mph (13.33 m s^{-1}). RMS decreased sharply initially (Fig. 60) as the scan rate increased. The minimum RMS error (0.026 m s^{-1}) was found with a scan rate of 6.0 degrees s^{-1}. As in the previous discussion, the decrease in RMS error was largely due to the reduction in area covered by sub-critical maximum look angle differences (Figs. 61, 62). As the scan rate was increased beyond 3.0 degrees s^{-1}, the RMS error did not change appreciably.

Comparing the "optimal" scan strategies (defined here by RMS less than 0.02 m s^{-1}) to that used by the UMass W-band on 22 May 2002 (Figs. 56, 58, 62b), an important conclusion is obvious. *The scan rate should have been increased, possibly a substantial amount, over that actually used for the data collection.* The major concern about a fast scan rate (entering this period of collection) was an inadequate look count over portions of the domain. It was feared that a fast scan rate would introduce data-void holes into the analysis. A natural trade-off exists between radar coverage and look angle separation. A faster scan rate allows for more independent looks at points in the domain – at the expense of overlapping ray coverage. However, it is evident that more than sufficient radar coverage existed for a scan rate of 5-10 degrees s^{-1}, possibly even higher[26]. Nonetheless, the chosen scan strategy still allowed for a very accurate analysis, with a characteristic error of 3% of the velocity magnitude.

[26] The upper limit of a useful scan rate is dictated by the number of samples averaged to produce the velocity value. If too many samples are averaged, then the resolution volume is widened considerably for a fast scan rate.

3.4 LES test case

The above experiments have proven that the variational synthesis technique performs well over a homogeneous domain. However, it was desirable to test how the technique performed in regions with strong gradients in wind direction and velocity, similar to the environment near atmospheric boundaries. To this end, an OSSE was developed using output from a Large Eddy Simulation (LES) (Fedorovich and Conzemius, 2003, personal communication). The LES was not designed to simulate the dryline, but rather the thermal structure of a highly-sheared, strongly-heated convective boundary layer.

The LES was initialized with winds from radiosonde observations (RAOBS) taken at Dodge City, Kansas (DDC) and Amarillo, TX (AMA) at 0000 UTC on the evening of 22 May 2003 (Figs. 19b, 21b). The simulation was carried out for an 11 hour period[27], from a 1230 UTC start time. At the end of this simulation (2330 UTC), fields of the *u*, *v*, and *w* wind components were saved to test the OSSE.

Plan views of *u* at 90 m AGL and *w* at 900 m AGL (Fig. 63) show clearly a southwest-to-northeast-oriented axis of convergence and upward motion in the center of the domain. The two-dimensional nature of this convection and the orientation of the axis parallel to the mean BL wind (Fig. 19b) suggest that this feature was a horizontal convective roll (HCR) (Lemone 1973, Weckwerth 1997, Atkins et al. 1998). It is noted that this feature had a very similar orientation to the dryline of 22

[27] The LES was programmed to end when the boundary layer depth reached a pre-specified value.

May 2002. Maximum upward motion was slightly over 6 m s^{-1} along the southern section of this HCR.

An east-west vertical cross section was plotted across the LES domain to show the vertical structure of the HCR (Fig. 64). Upward motion in the HCR extended to approximately 1.5 km AGL, and was about 1 km wide. Weaker regions of generally subsiding air extended over the remainder of the domain. As it was for the analytical cases in section 3.3, the model output was sampled by the UMass pseudo-radar. The radar platform was assumed to be moving westward with a velocity of 30 mph (13.33 m s^{-1}) and a scan rate of 1.5 degrees s^{-1}.

The time series of radial velocity was analyzed using the variational analysis discussed in sections 3.2 and 3.3. Iterations were repeated until the reduction of cost function was within the prescribed tolerance of 1 m^2 s^{-2} (Fig. 54). When measured against the actual LES output (the "truth"), an RMS error of 0.568 m s^{-1} was calculated. The analysis qualitatively reproduced all of the features, even those very small in scale (Figs. 65, 66). Most of the RMS error accrued in the upper portion of the domain, near and above 2 km AGL. As demonstrated in the analytical cases in section 3.3 (e.g., Fig. 56b), this region had sub-critical look angle differences, and therefore collinearity amongst the radial velocity observations. The analysis was biased towards the first guess in these regions, again representing the under-application of the innovation in each iteration of the analysis technique.

Series of experiments were designed to test the sensitivity of the analysis to the platform motion and scan rate. The design of the experiments was identical to that of the constant-flow OSSE in section 3.3. In the first set of experiments, the platform velocity was varied while maintaining a fixed scan rate of 2.0 degrees s^{-1}. As in the analytical cases, RMS error did increase with increasing platform velocity (Fig. 67), but at a slower rate (RMS = 0.507 m s^{-1} for a platform velocity of 10 mph (4.44 m s^{-1}) , and RMS = 0.649 m s^{-1} for a platform velocity of 45 mph (20.0 m s^{-1})). The cause of this increase was again likely due to sub-critical look angle differences over the upper portion of the domain (Fig. 58).

In the next set of experiments, the platform velocity was held constant at 30 mph (13.33 m s^{-1}) while varying the scan rate from 1.5 degrees s^{-1} to 10.0 degrees s^{-1}. The RMS error, as expected, did decrease as scan rate was increased (such that adjacent RHI scans being to overlap) (Fig. 68). Once the scan rate was increased beyond 2.5 degrees, however, there was very little further reduction in the RMS error.

The experiments were repeated for a wide combination of scanning parameters (Table B). The lowest RMS values for the suite of experiments were about 0.4 m s^{-1} higher than in the analytic (constant velocity) cases. The reason for greater error is speculated to be in the assignment of radial velocity observations to the analysis grid. In this regard, the analysis procedure did suffer from strong heterogeneities in wind direction and speed. However, since RMS error was still very small, the technique still yielded a very high quality analysis.

To test the dependence of the simulations on the specific coverage pattern of the antenna (e.g., did direct measurement of *w* in the areas of strong upward motion matter?), the LES OSSE was repeated with an antenna descending from a start angle of 85.0 degrees (the control case started with a rising antenna pointed at 0 degrees). The resulting antenna coverage was therefore the inverse of the control run (i.e., the antenna was horizontal where it was vertical in the control run and vice versa). The RMS did not change appreciably (Tables C, D), on average by about 1%.

To this point, it was assumed that the UMass pseudo-radar was a perfect instrument. In other words, the data were assumed to contain no observational error. In reality, observational error is present in all measurement platforms. Sources of error include: instrument noise (from the receiver), representativeness (e.g., beam spreading, ducting) and others. To simulate the effect of the instrument error, a Gaussian (i.e., random normal) error was added to the observations. In the first experiment there was an error standard deviation of 1.0 m s^{-1}, which was equivalent to the stated error characteristics of the UMass radar (A. Pazmany, 2003, personal communication). As in the previous cases, an increase in platform velocity resulted in higher RMS error for slow scan rates (Table E) as the look angle differences fell below the critical level for pseudo-multiple-Doppler processing. However, in contrast to the error-free case (Table B), an increase in RMS was also noted for scan rates where the look angle differences were sufficient for all platform velocities (e.g., RMS = 0.671 m s^{-1} for platform velocity of 10 mph (4.44 m s^{-1}) and scan rate of 5.0 degrees s^{-1}; RMS = 0.718 m s^{-1} for platform velocity of 55 mph (24.4 m s^{-1}) and scan rate of 5.0 degrees s^{-1}). This increase in RMS error was attributed to the decrease in look count over the domain in fast-platform motion cases (Fig. 69). In these cases, there were fewer samples at each point in the domain, and the random instrument error was more likely to exert a bias for the smaller sample population.

As expected, the magnitude of the RMS error was higher than the perfect-observation control run, but still small in comparison to the wind velocity. A comparison of the OSSE output with the LES output ("truth") for the control platform velocity of 30 mph (13.33 m s^{-1}), scan rate of 1.6 deg s^{-1} and observational error standard deviations of 1.0 m s^{-1} and 2.0 m s^{-1} (Fig. 70) showed that the variational analysis technique did a very good job at reproducing all of the features in the domain (RMS error = 0.751 m s^{-1} and 1.093 m s^{-1} for error standard deviations of 1.0 m s^{-1} and 2.0 m s^{-1}, respectively). As before, performance was worst in the upper portion of the analysis domain where radar coverage was not sufficient.

3.5 Application to 22 May 2002 UMass W-band data

The tests in the previous sections demonstrate the robustness of the variational analysis technique for controlled experiments. They also highlight the major weakness of the technique: larger error variance in regions of sub-critical look angle difference.

The variational analysis was applied to rolling RHI data taken on the (primary) 22 May 2002 dryline as it retrograded back towards the west in the early evening hours (leg 6, 0007-0036 UTC (23 May 2002)). The retrogression (Fig. 71) was not uniform as there was evidence of wave activity along the dryline interface. Data from various radar platforms permitted an estimated retrogression speed between 2 and 5 m

s^{-1} during the period of the leg 6 traverse. The platform traveled at a nearly constant velocity of 30 mph (13.33 m s^{-1}) towards the west as RHI sweeps were taken from the rear horizon up through ~86 degrees above the rear horizon (Fig. 37). The raw time series of data were post-processed as described in section 3.1 before the analysis was performed.

A composite reflectivity image[28] for the traverse (Fig. 72) showed the pronounced eastward tilt of the dryline interface with height during retrogression. As in leg 3, the DCZ appeared as a maximum in reflectivity, presumably due to the local increase in insect concentration in this region. The domain chosen for analysis was the lowest 1 km AGL, where there were no holes in the data.

Due to the retrogression of the dryline, the stationarity assumption was compromised. As a result, regions with large time intervals between looks produced erroneous large vertical velocity values. To mitigate the effect of dryline propagation, a cutoff time window of 60 s (from first observation) was imposed. This cutoff did decrease maximum look angle differences in the domain, but the observed improvements (by increasing the accuracy of the stationarity approximation) were deemed greater than the potentially larger error variance (due to collinearity of the radial velocity observations).

The tolerance of the iterative minimization was set to 1.0 m^2 s^{-2} for the leg 6 analysis, and a first guess of u=w=0 m s^{-1} was applied for the entire domain. For the early iterations of the analysis (Fig. 54), there was a very sharp decrease in the cost

---

[28] The reflectivity at each point in the domain is that of the last look with the radar.

function. Since the cost function was quadratic, this evolution of *J* was expected. As the analysis approached the optimal solution, the decrease in cost function decelerated considerably. The decrease of the observation component of the cost function (22b) was somewhat offset by the increase in the mass continuity component (22c), which exhibited a substantial increase in the early iterations (expected since the first guess field of u=w=0 satisfied mass continuity exactly over the entire domain). A more cost-efficient technique would result for a higher tolerance, in which case a decent solution could have been found in as few as twenty iterations. For this case, the analysis ran for 244 iterations before ultimately converging.

The u-component of the optimal analysis (Fig. 73) reveals the upper and lower branches of the dryline secondary circulation quite clearly. The near-surface inflow to the DCZ from the east approached u=-6 m s^{-1} in some areas of the CBL. Above the CBL, strong westerly component winds (i.e., the return flow) were seen, a combination of air parcels from the moist CBL that had ascended in the DCZ (Hane et al. 1997) and parcels from the dry side that had advected up and over the moist CBL. Westerly winds upward of u=15-20 m s^{-1} were seen in the upper portion of the domain (just above 1 km AGL). The altitude of the boundary between easterly and westerly component winds varied between 500 m AGL and over 1 km AGL over the domain, with the lowest altitude seen near x=128 (~3 km east of the dryline) and x=400 (~12 km east of the dryline). Both of these areas were also coincident with subsiding air.

The DCZ showed up clearly in the *w*-component field (Fig. 74) as a maximum *w* of 8-10 m s^{-1} (over a very narrow region of ~100 m as in leg 3). The eastward tilt of the DCZ with height was again present. A small area of descent was evident at ~500 m AGL approximately 4 km to the east of the surface position of the DCZ. The position of this descending motion was similar to that shown for leg 3 earlier and the airborne Doppler case study of Weiss and Bluestein (2002), but lacked the vertical continuity present in the latter case. More vertically continuous areas of subsidence were apparent farther to the east of the DCZ, at and around x=180 (~5 km east of the dryline), x=270 (~8 km east of the dryline) and x=420 (~13 km east of the dryline).

UWKA data were again compared to UMass data (Fig. 75a) to determine if consistent vertical velocity features were observed from both platforms. Though the flight track of the UWKA was 5-15 km to the north of UMass leg 6 (Fig. 55) and more than 30 minutes had elapsed between the periods of UWKA and UMass data collection, similar areas of ascent and descent were present in data from both platforms. The upward motion in the DCZ was again lesser than that measured by UMass (as in leg 3). Subsiding regions in UMass data to the east of the DCZ (grey lines in Figs. 75a and 75b) were very much present in the UWKA field as well. To the best of the author's knowledge the magnitude and structure of these areas of ascent and descent have not been documented previously in a dryline environment.[29]

[29] Stepped aircraft traverses have shown broad descending areas previously (e.g., Ziegler and Hane 1993, Hane et al. 1997, Hane et al. 2001), but this study provides a more detailed look at the structure and magnitude of these areas.

3.6 Impact of the β parameter

Up to this point, little attention has been given to the β parameter in (27). In a dual-Doppler or pseudo-dual Doppler scheme (e.g., Dowell and Bluestein 2002), this term represents the relative weight that analysis deviations from mass continuity are given to the analysis deviations from each pair of observations when computing the cost function for each gridpoint in the analysis domain. In the dual-Doppler case, there are two observations for each of these points (e.g., the fore and aft antenna looks of the ELDORA). Therefore the value of β, a constant, solely determines the relative weight of observational and continuity constraints. However, in this pseudo-*multiple* Doppler case, any number of observations may exist at each gridpoint (as noted earlier, upwards of a few hundred). Therefore, in (27), β <u>and *m*</u> control the relative weights for the constraints. Consequently, mass continuity receives almost no weight for high-observation gridpoints as it is effectively weighted as one observation. The optimal analysis, therefore, is effectively a solution based upon observations alone.

To increase the influence of continuity in the analysis, β was modified to scale with the number of observations:

$$\beta = \mathrm{m}\,(\Delta \mathrm{x})^2 \tag{55}$$

The incorporation of (55) into (27) effectively served as a low-pass filter, and the resulting analyses were expected to be smoother as a result.

The new minimization equation was first tested on the constant-flow OSSE from section 3.3 (u=10 m s^{-1}, w=0 m s^{-1} over the whole domain). A greatly exaggerated normal random error of σ_{error} = 6.0 m s^{-1} was added to the time series of radial velocity. The resulting analysis with the nominal mass continuity constraint ($\beta = (\Delta x)^2$) yielded an RMS error of 2.75 m s^{-1} (Fig. 76a). With the stronger mass continuity constraint, the RMS error decreased to 1.83 m s^{-1} (Fig. 76b). Further, most of the error was confined to the regions of very low look count (Fig. 56) and minimal look angle difference at the top of the domain. The decrease in RMS was expected, as uncorrelated errors in u and w were easily damped by the mass continuity constraint.

When applied to the data from leg 6, the new formulation also provided a much smoother result. The u-component (Fig. 77) and w-component wind fields (Fig. 78) maintained their qualitative structure, though absolute magnitudes of vertical velocity were lower (e.g., maximum w in the DCZ was 6-7 m s^{-1}). Zooming in on the DCZ, one can still see very clearly the discontinuity in the u-component (Fig. 79a) and w-component fields at the dryline interface (Fig. 79b). Also, the rotor circulation on the head of the DSC remained intact.

From Fig. 79 it is clear that the easterly component winds at the surface extended west of the area of maximum upward motion. Further, the easterly component flow appeared to narrow to a point (Fig. 80), with a surge of dust/insects in advance of the retrograding dryline.

CHAPTER 4: SUMMARY AND DISCUSSION

On the afternoon 22 May 2002, a unique data set was obtained on a double-dryline event in the Oklahoma panhandle. This data set was comprised of reflectivity and radial velocity measurements from the UMass 95 GHz W-band radar. The narrow beamwidth of the radar afforded very-fine azimuthal resolution of winds at and near the boundaries.

4.1 Dryline observations

With the antenna pointed vertically, the radar was driven westward across the primary dryline boundary from 2221-2235 UTC. The DCZ was well resolved, with maximum upward vertical velocity of $w \sim 8$ m s^{-1} measured in a narrow channel approximately 50-100 m wide. This magnitude was larger than that reported in earlier mobile Doppler dryline studies. For example, Atkins et al. (1998) reported upward motion on the order of 1-2 m s^{-1} using ELDORA data with a horizontal (along-track) resolution of 600 m. Parsons et al. (1991) used lidar technology (with horizontal resolution of 200 m) to measure a maximum positive vertical velocity of $w \sim 5$ m s^{-1} on a retrograding dryline in west Texas. As stated in Parsons et al. (1991):

"...results [from coarser-resolution studies] were obtained with grids too large to resolve the sharp gradients typically observed at the leading edge of the dryline and are therefore likely to grossly underestimate actual convergence." (p.1253)

Using the same line of reasoning, the larger magnitudes of vertical velocity seen in the current study were likely in part due to the narrow beamwidth of the antenna. With a larger-beamwidth radar, samples inside the narrow channel of maximum *w* were averaged with neighboring samples of lesser magnitude. The narrow azimuthal and range resolution of the W-band also allowed for better measurement of the convergence in the DCZ. Firstly, this improvement was due to the narrowing of the cross-dryline width over which the velocity discontinuities were measured in the DCZ. Secondly, the narrower beamwidth permitted measurements to be taken much closer to the surface without contamination. Therefore the depth of the convergence was more accurate in this analysis. Even though a large maximum in *w* was found in this study, it may be possible that the maximum upward vertical velocity in the DCZ was still underrepresented due to the resistance of insects to upward transport (Achtemeier 1991), violating the assumption that insects are passive tracers of the flow. However, a negative vertical velocity error bias also has been found recently by Geerts and Miao (2003), who claimed a bias of -0.5 m s^{-1} in UWKA data.

Areas of subsidence were noted away from the DCZ. One such area was found in both UMass W-band and UWKA data approximately 4-5 km east of the DCZ. This position was consistent with a similar finding by Hane et al. (1993), in which the area of descent coincided with a moisture gradient at the surface. Unfortunately in the current case, mobile mesonets did not travel far enough east of the DCZ to confirm if similar gradients were seen at the surface. However, in-situ data from the UWKA indicated a minor decrease in dewpoint (~ 1 ^{o}C) in the upper portion of CBL. Other decreases in dewpoint were evident with areas of descent farther to the east.

4.2 Dryline dynamics

The areas of concentrated subsidence discussed above are potentially significant for many matters related to the dryline. Double drylines, for example, may form in such a manner, similar to the observations of Hane et al. (1997) and Hane et al. (2001), and the modeled "microfronts" of Ziegler et al. (1995). Hane et al. (1993) state:

> "...vertical wind shear and compensating downdrafts to the east of the dryline may locally enhance vertical mixing driven by entrainment of dry air from aloft" (p. 2138)

The transport of dry air to the surface in the near-dryline environment can have substantial effects. In the cases presented by Hane et al. (1997), vertical mixing of westerly momentum down to the surface was shown to form a convergence line in the dry air west of the dryline. Severe thunderstorms later initiated at the intersection point of this convergence line and at the dryline.

Whether the descending motion is initiated from the surface (e.g., sensible heat flux "mixing out" the CBL) or aloft (e.g., gravity waves in the capping inversion), if the downward transport of dry air can remain established for a sufficient amount of time and cover a sufficient amount of space (such that a robust secondary circulation can be established), *then it is possible that the frontogenetic process that maintains/intensifies the solenoid of the primary dryline can do so for any of these ancillary boundaries as well* (Fig. 81). Local horizontal gradients of virtual temperature can develop as near-surface air warms in regions of descent (indicated by pink/red shading in Fig. 81). The increase in temperature can be either a cause of the descent (e.g., sensible heat flux forcing vertical mixing of CBL with dry air aloft) or a result of the descent (e.g., adiabatic warming). As the horizontal gradient of virtual temperature increases with time, a secondary circulation will develop in the manner of the "inland sea breeze" (Ogura and Chen 1977, Sun and Ogura 1979).

As we have increased our operational ability for clear-air detection through the years, more "boundaries of unknown origin" have been identified in base reflectivity scans. The 3 May 1999 supercell that spawned the Moore, OK tornado initiated on such a boundary, well east of the primary dryline (Thompson and Edwards 2000). Some of these boundaries may well be mixing lines/secondary drylines. Even if a distinct DSC does not develop in association with an area of vertical momentum transport, the resultant maximum in surface convergence can make conditions more favorable for convective initiation locally.

Some recent airborne studies of the dryline (e.g., Atkins et al. 1998, Weiss and Bluestein 2002) have shown descending motion immediately to the west of the dryline. The results from the UMass leg 3 traverse and the UWKA in this case also indicate weak areas of descent in this region. These observations are consistent with previous observations of westerly-component acceleration immediately to the west of the dryline (e.g., Danielsen 1974, Doswell 1976, Ogura and Chen 1977, McCarthy and Koch 1982). Atkins et al. (1998) document a similar increase from 0-1.5 km AGL west of the dryline with WSR-88D VAD data. The effects of this downward momentum transport are similar to that discussed in the previous paragraph. More data need to be gathered to assess how ubiquitous this downward motion is, but the effect on convective initiation (a precursor?) could be significant (Fig. 82).

There are many possible explanations for the descent to the west of the dryline. Koch (1979) suggested that evanescent gravity waves can propagate to the surface in this region. Another possibility may be related to a shear-updraft interaction at the DCZ (Fig. 83). Westerly ambient flow impinging on the updraft of the DCZ creates a non-hydrostatic positive pressure perturbation according to:

$$\nabla^2 P' = -2\bar{\rho}\, {\partial \vec{V}}/{\partial z} \bullet \nabla_z w' \qquad (56)$$

where P' is the pressure perturbation, $\bar{\rho}$ is the base state density, $\vec{V}$ is the wind velocity vector and w' is the perturbation vertical velocity. Since upward vertical velocity typically increases with height in the DCZ (Fig. 9), the horizontal gradient of vertical velocity also increases with height. Therefore, the positive pressure perturbation attributed to the interaction of the updraft with the ambient westerly wind shear is typically stronger aloft than at the surface. The resulting vertical perturbation pressure gradient force must therefore be directed downward immediately to the west of the dryline, hence perhaps explaining a portion of the subsidence observed.

4.3 Pseudo-multiple Doppler data processing

A new ground-based pseudo-multiple Doppler processing technique was developed to analyze the rolling RHI data taken with UMass W-band. The technique used variational calculus to find an "optimal" analysis that satisfied radial velocity observations and anelastic mass continuity in a least squares sense. Testing of this technique demonstrated its robustness, even for flows containing a large amount of variability (e.g., an LES). The procedure, as expected, demonstrated its worst results for situations in which radial velocities were collinear.

The variational minimization was applied to data taken from 0007 UTC – 0036 UTC on the primary 22 May 2002 dryline as it retrograded towards the west. Highly detailed analyses showed very strong ascent in the DCZ, upwards of 10 m s^{-1} over a narrow width. Descending motion about 3 km to the east of the surface dryline (seen in both the UMass and UWKA) completed a rotor circulation on the head of the DSC, as in leg 3. Areas of organized strong descent upwards of 2 km wide and –4 to –6 m s^{-1} in magnitude were again evident farther to the east of the dryline.

The dryline exhibited considerable tilt during the retrogression, as much as 1:3 by the time of UMass leg 6. In fact, radar observations showed easterly component winds narrowing to a point along the surface. From Margules' formula, this tilt was consistent with an increased gradient of virtual temperature across the boundary[30]. A surface virtual temperature gradient combined with observed (though minute) surface pressure increases from the mobile mesonets with dryline passage supported the notion that density current dynamics were at least in part driving the retrogression back towards the west (Parsons et al. 1991).

Much potential exists for the developed ground-based pseudo-multiple Doppler technique. The 22 May 2002 data set represented a first attempt at rolling RHI data collection with the W-band. From the testing in section 3.3 and 3.4 it is apparent that data should have been collected with a faster scan rate. An increase to 6.0 deg s^{-1} (from 1.6 deg s^{-1}) greatly decreased the RMS error in the retrieved test fields, primarily by reducing the domain area covered by sub-critical look angle differences. Plans to test the faster scan rate in 2003 were canceled after the W-band radar failed. Similar testing plans remain for the future.

[30] The work of Margules shows how rotation restricts a fluid of higher density from completely undercutting a (horizontally) neighboring fluid of lighter density. Instead, a steady solution is one of a sloped frontal surface between the two fluids. Applying Margules' formula here implies the assumption that time scales are large enough in the retreating dryline environment that the Coriolis acceleration f is important.

REFERENCES

Achtemeier, G. L., 1991: The use of insects as tracers for "clear-air" boundary-layer studies by Doppler radar. *J. Atmos. Oceanic Technol.*, **8**, 746-765.

Armijo, L., 1969: A theory for the determination of wind and precipitation velocities with Doppler radars. *J. Atmos. Sci.*, **26**, 570-573.

Atkins, N. T., R. M. Wakimoto, and C. L. Ziegler, 1998: Observations of the finescale structure of a dryline during VORTEX 95: *Mon. Wea. Rev.*, **126**, 525-550.

Benjamin, S. G., and T. N. Carlson, 1986: Some effects of surface heating and topography on the regional severe storms environment, Part I: 3-D simulations. *Mon. Wea. Rev.*, **114**, 307-329.

Biggerstaff, M. I., and J. Guynes, 2000: A new tool for atmospheric research. Preprints, *20th Conf. on Severe Local Storms*, Orlando, FL, Amer. Meteor. Soc., 277-280.

Bluestein, H. B., 1993: *Synoptic-Dynamic Meteorology in Midlatitudes: Volume II Observations and Theory of Weather Systems.* Oxford University Press, New York, 594 pp.

———, and A. L. Pazmany, 2000: Observations of tornadoes and other convective phenomena with a mobile, 3–mm wavelength, Doppler radar: The spring 1999 field experiment. *Bull. Amer. Meteor. Soc.*, **81**, 2939–2952.

______, C. C. Weiss, and A. L. Pazmany, 2003: Mobile-Doppler-radar observations of a tornado in a supercell near Bassett, Nebraska on 5 June 1999. Part I: Tornadogenesis. *Mon. Wea. Rev.*, **131**, 2954 – 2967.

______, ______, ______, 2004: The vertical structure of a tornado near Happy, Texas on 5 May 2002: High-resolution, mobile, W-band, Doppler-radar observations. *Mon. Wea. Rev.* (accepted)

Bousquet, O., and M. Chong, 1998: A multiple-Doppler synthesis and continuity adjustment technique (MUSCAT) to recover wind components from Doppler radar measurements. *J. Atmos. Oceanic Technol*, **15**, 343-359.

Brandes, E. A., 1977: Flow in severe thunderstorms observed by dual-Doppler radar. *Mon. Wea. Rev.*, **105**, 113-120.

Chong, M., and C. Campos, 1996: Extended overdetermined dual-Doppler formalism in synthesizing airborne Doppler radar data. *J. Atmos. Oceanic Technol.*, **13**, 581-597.

Crawford, T. M., and H. B. Bluestein, 1997: Characteristics of dryline passage. *Mon. Wea. Rev.*, **125**, 463-477.

Danielsen, E., 1974: The relationship between severe weather, major duststorms, and rapid large-scale cyclogenesis, Part I: *Subsynoptic Extratropical Weather Systems*, M. Shapiro, Ed., National Center for Atmospheric Research, 215-241.

Doswell, C. A., III, 1976: Subsynoptic scale dynamics as revealed by use of filtered surface data. NOAA Tech. Memo. ERL NSSL-79 (NTIS#PB-265433/AS), 40 pp.

Doviak, R. J., and D. S. Zrnic, 1984: *Doppler Radar and Weather Observations, 2nd edition*. Academic Press, San Diego, 562 pp.

Dowell, D. C., and H. B. Bluestein, 2002: The 8 June 1995 McLean, Texas, Storm. Part I: Observations of cyclic tornadogenesis. *Mon. Wea. Rev.*, **130**, 2626-2648.

____, and A. Shapiro, 2003: Stability of an iterative dual-Doppler wind synthesis in Cartesian coordinates. *J. Atmos. Oceanic Technol.*, **20**, 1552-1559.

Feltz, W. F., W. L. Smith, H. B. Howell, R. O. Knuteson, H. Woolf and H. E. Revercomb, 2003: Near-continuous profiling of temperature, moisture, and atmospheric stability using the Atmospheric Emitted Radiance Interferometer (AERI). *J. Appl. Meteor.*, **42**, 584-597.

Fujita, T. T., 1958: Structure and movement of a dry front. *Bull. Amer. Meteor. Soc.*, **39**, 574-582.

Gao, J., M. Xue, A. Shapiro, and K. K. Droegemeier, 1999: A variational method for the analysis of three-dimensional wind fields from two Doppler radars. *Mon. Wea. Rev.*, **127**, 2128-2142.

Geerts, B., and Q. Miao, 2003: Vertical velocity and buoyancy characteristics of echo plumes detected by an airborne mm-wave radar in the convective boundary layer. Preprints, *31st Conf. on Radar Meteorology*, Seattle, WA, Amer. Meteor. Soc., 925-928.

Hane, C. E., C. L. Ziegler, and H. B. Bluestein, 1993: Investigation of the dryline and convective storms initiated along the dryline: Field experiments during COPS-91. *Bull. Amer. Meteor. Soc.*, **74,** 2133-2145.

——, M. E. Baldwin, H. B. Bluestein, T. M. Crawford, and R. M. Rabin, 2001: A case study of severe storm development along a dryline within a synoptically active environment. Part I: Dryline motion and an Eta model forecast. *Mon. Wea. Rev.*, **129,** 2183–2204.

——, H. B. Bluestein, T. M. Crawford, M. E. Baldwin, and R. M. Rabin, 1997: Severe thunderstorm development in relation to along-dryline variability: A case study. *Mon. Wea. Rev.*, **125,** 231-251.

Hildebrand, P. H., and Coauthors, 1996: The ELDORA/ASTRAIA airborne Doppler weather radar: High resolution observations from TOGA COARE. *Bull. Amer. Meteor. Soc.*, **77,** 213-232.

Jones, P. A., and P. R. Bannon, 2002: A mixed-layer model of the diurnal dryline. *J. Atmos. Sci.*, **59,** 2582-2593.

Koch, S. E., 1979: Mesoscale gravity waves as a possible trigger of severe convection along a dryline. Ph. D. dissertation, University of Oklahoma, 195 pp. [Available from School of Meteorology, University of Oklahoma, 100 East Boyd, Room 1310, Norman, OK 73019-0470]

Kuo, Y.-H., and Y.-R. Guo, 1989: Dynamic initialization using observations from a hypothetical network of profiler. *Mon. Wea. Rev.,* **117,** 1465–1481.

Lemone, M. A., 1973: The structure and dynamics of horizontal roll vortices in the planetary boundary layer. *J. Atmos. Sci.*, **30,** 1077-1091.

Lorenc, A. C., 1986: Analysis methods for numerical weather prediction. *Quart. J. R. Met. Soc.*, **112**, 1177-1194.

Martin, W. J., 2003: Measurements and modeling of the Great Plains low-level jet. Ph. D. Dissertation, University of Oklahoma, 242 pp. [Available at ftp://caps.ou.edu/wmartin]

McCarthy, J., and S. E. Koch, 1982: The evolution of an Oklahoma dryline. Part I: A meso- and subsynoptic-scale analysis. *J. Atmos. Sci.,* **39**, 225-236.

Mewes, J. J., and A. Shapiro, 2002: Use of the vorticity equation in dual-Doppler analysis of the vertical velocity field. *J. Atmos. Oceanic Technol.*, **19**, 543-567.

NSSP (National Severe Storms Project) Staff Members, 1963: Environmental and thunderstorm structures as shown by National Severe Storms Project observations in spring 1960 and 1961. *Mon. Wea. Rev.*, **91**, 271-292.

Ogura, Y., Y.-L. Chen, 1977: A life history of an intense mesoscale convective storm in Oklahoma. *J. Atmos. Sci.*, **34**, 1458-1476.

Oye, R., C. K. Mueller, and S. Smith, 1995: Software for radar translation, visualization, editing, and interpolation. *Preprints, 27th Conf. On Radar Met.*, Vail, CO, Amer. Meteor. Soc., 359-361.

Parsons, D. B., M. A. Shapiro, R. M. Hardesty, R. J. Zamora, and J. M. Intrieri, 1991: The finescale structure of a west Texas dryline. *Mon. Wea. Rev.*, **119**, 1283-1292.

Peckham, S. E., and L. J. Wicker, 2000: The influence of topography and lower-tropospheric winds on dryline morphology. *Mon. Wea. Rev.*, **128**, 2165-2189.

Rabin, R. M., and D. Zrnic, 1980: Subsynoptic-scale vertical wind revealed by dual Doppler radar and VAD analysis. *J. Atmos. Sci.,* **37,** 644–654.

Rasmussen, E. N., J. M. Straka, R. Davies-Jones, C. A. Doswell III, F. H. Carr, M. D. Eilts, and D. R. MacGorman, 1994: Verification of the Origins of Rotation in Tornadoes Experiment: VORTEX. *Bull. Amer. Meteor. Soc.*, **75**, 995-1006.

Ray, P. S., C. L. Ziegler, W. Bumgarner, and R. J. Serafin, 1980: Single and multiple-Doppler radar observations of tornadic storms. *Mon. Wea. Rev.*, **108**, 1607-1625.

Rhea, J. O., 1966: A study of thunderstorm formation along the dryline. *J. Appl. Meteor.*, **5**, 58-63.

Rinehart, R. E., 1997: *Radar for Meteorologists, Third Edition*. Knight, Fargo, 428 pp.

Sasaki, Y., 1970: Some basic formalisms in numerical variational analysis. *Mon. Wea. Rev.*, **98**, 875-883.

Schaefer, J. T., 1974: The life cycle of the dryline. *J. Appl. Meteor.*, **13**, 444-449.

Shapiro, A., and J. J. Mewes, 1999: New formulations of dual-Doppler wind analysis. *J. Atmos. Oceanic Technol.*, **16**, 782-792.

Simpson, J. E., 1969 : A comparison between laboratory and atmospheric density currents. *Quart. J. Roy. Meteor. Soc.*, **95**, 758-765.

Sun, W. Y., and Y. Ogura, 1979: Boundary layer forcing as a possible trigger to a squall line formation. *J. Atmos. Sci.,* **36**, 235-254.

——, and C.-Z. Chang, 1986: Diffusion model for a convective layer. Part I: Numerical simulation of convective boundary layer. *J. Climate Appl. Meteor.*, **25**, 1445-1453.

——, and C. C. Wu, 1992: Formation and diurnal variation of the dryline. *J. Atmos. Sci.,* **49**, 1606-1619.

Thompson, R. L., and R. Edwards, 2000: An overview of environmental conditions and forecast implications of the 3 May 1999 tornado outbreak. *Wea. Forecasting.,* **15**, 682–699.

UCAR/ATD, 2002: International H_2O Project (IHOP_2002): Operations Plan, 160 pp.

Weckwerth, T. M., J. W. Wilson, R. M. Wakimoto, and N. A. Crook, 1997: Horizontal convective rolls: Determining the environmental conditions supporting their existence and characteristics. *Mon. Wea. Rev.*, **125**, 505-526.

Weiss, C. C., 2000: Airborne Doppler analysis of a dryline-outflow boundary intersection and subsequent convection. M. S. thesis, University of Oklahoma, 163 pp. [Available from School of Meteorology, University of Oklahoma, 100 East Boyd, Room 1310, Norman, OK 73019-0470]

——, and H. B. Bluestein, 2002: Airborne pseudo-dual Doppler analysis of a dryline-outflow boundary intersection. *Mon. Wea. Rev.*, **130**, 1207-1226.

Wilson, J. W., and W. E. Schreiber, 1986: Initiation of convective storms by radar-observed boundary layer convergence lines. *Mon. Wea. Rev.*, **114**, 2516-2536.

Ziegler, C. L., and C. E. Hane, 1993: An observational study of the dryline. *Mon. Wea. Rev.*, **121**, 1134-1151.

——, W. J. Martin, R. A. Pielke, and R. L. Walko, 1995: A modeling study of the dryline. *J. Atmos. Sci.*, **52**, 263-285.

——, and E. N. Rasmussen, 1998: The initiation of moist convection at the dryline: Forecasting issues from a case study perspective. *Wea. Forecasting*, **13**, 1106-1131.

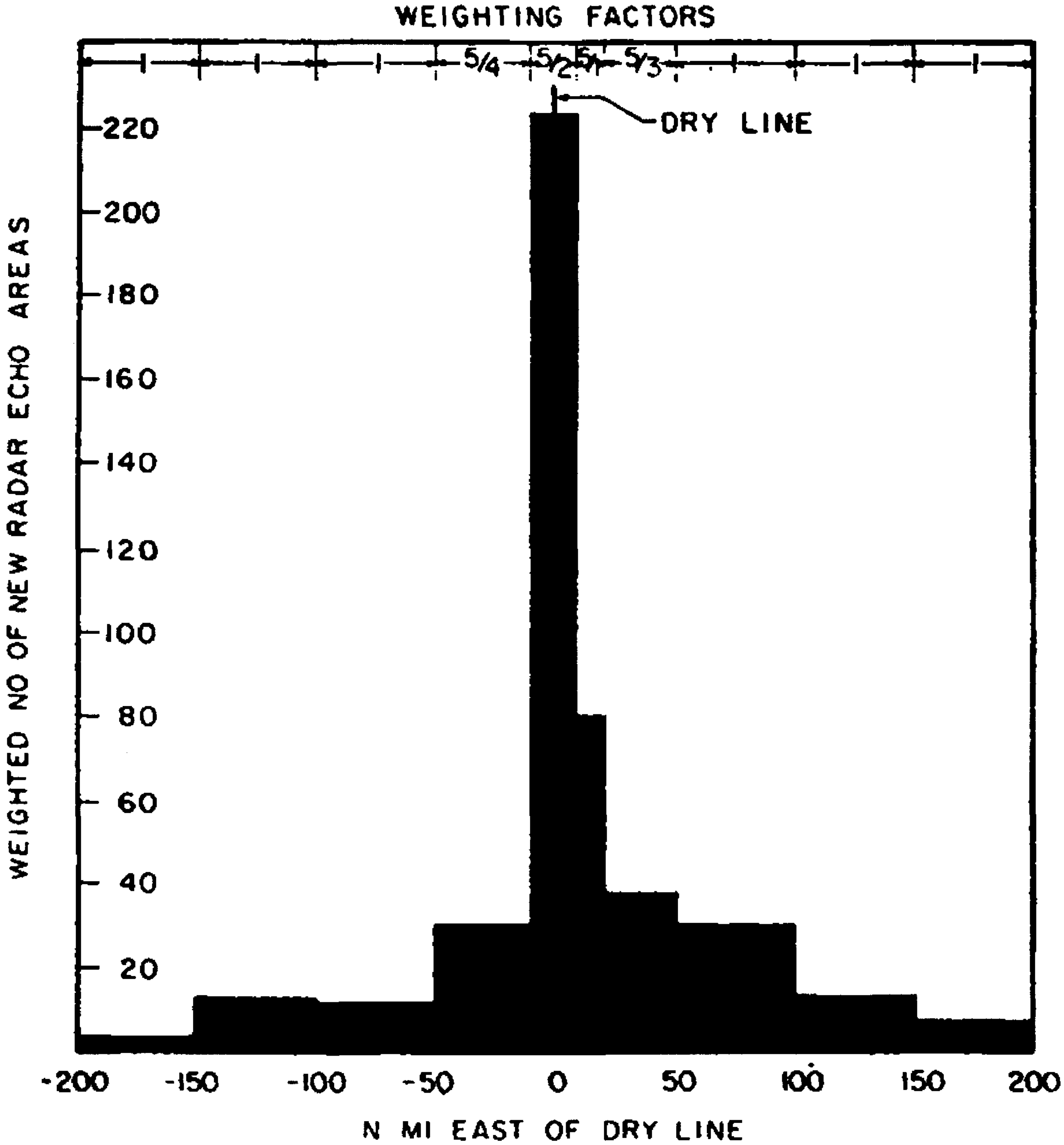

Figure 1 - (from Rhea et al. (1966), his Fig. 1) Frequency of new radar echo area development relative to surface position of the dryline for April, May and June, 1959 through 1962.

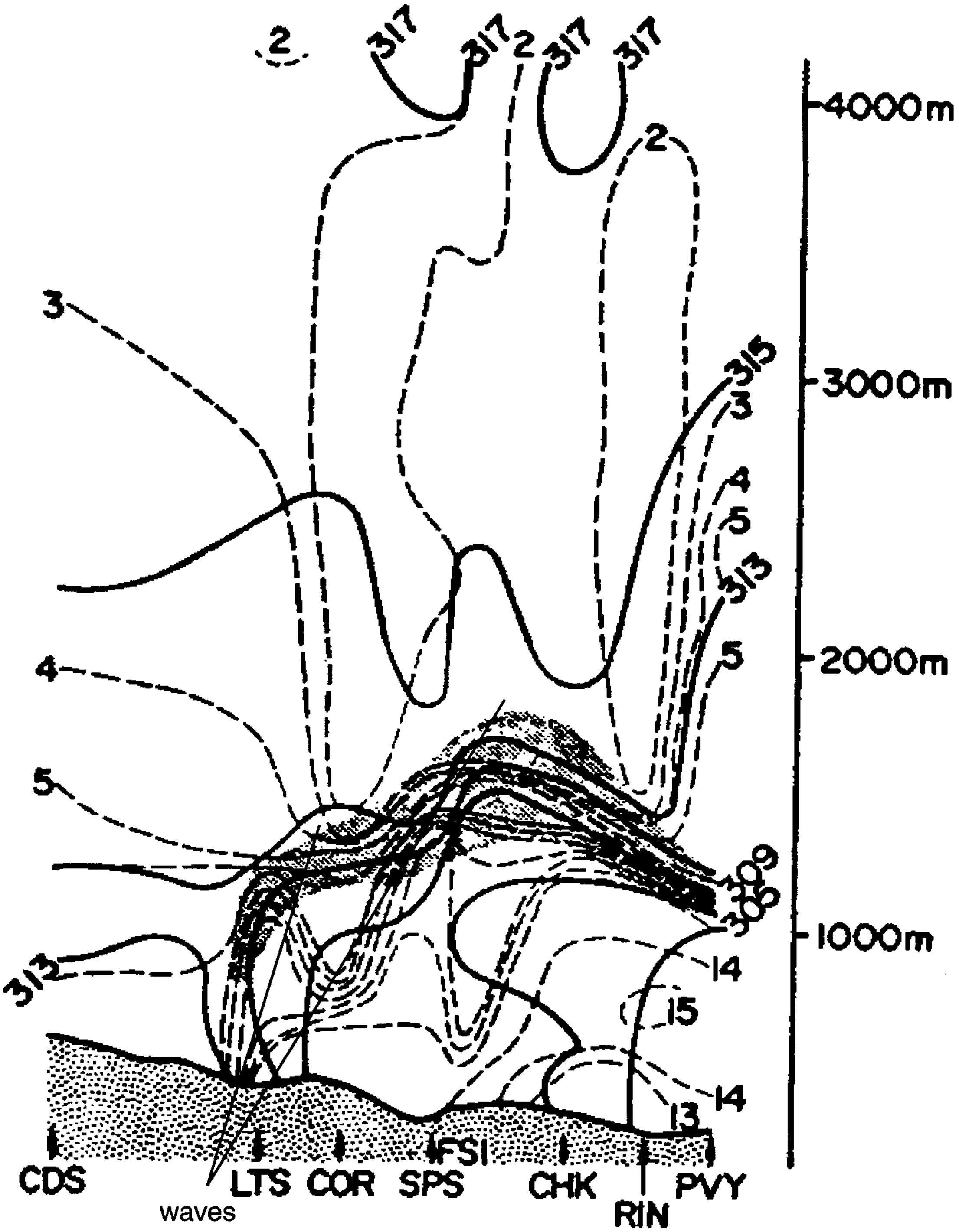

Figure 2 - (from Schaefer (1974), his Fig. 7) Cross section of a dryline at 1100 CST on 22 May 1966. Dark lines denote potential temperature (°K); dashed lines denote mixing ratio (g kg^{-1}). Shading denotes low-level inversion or markedly stable layer.

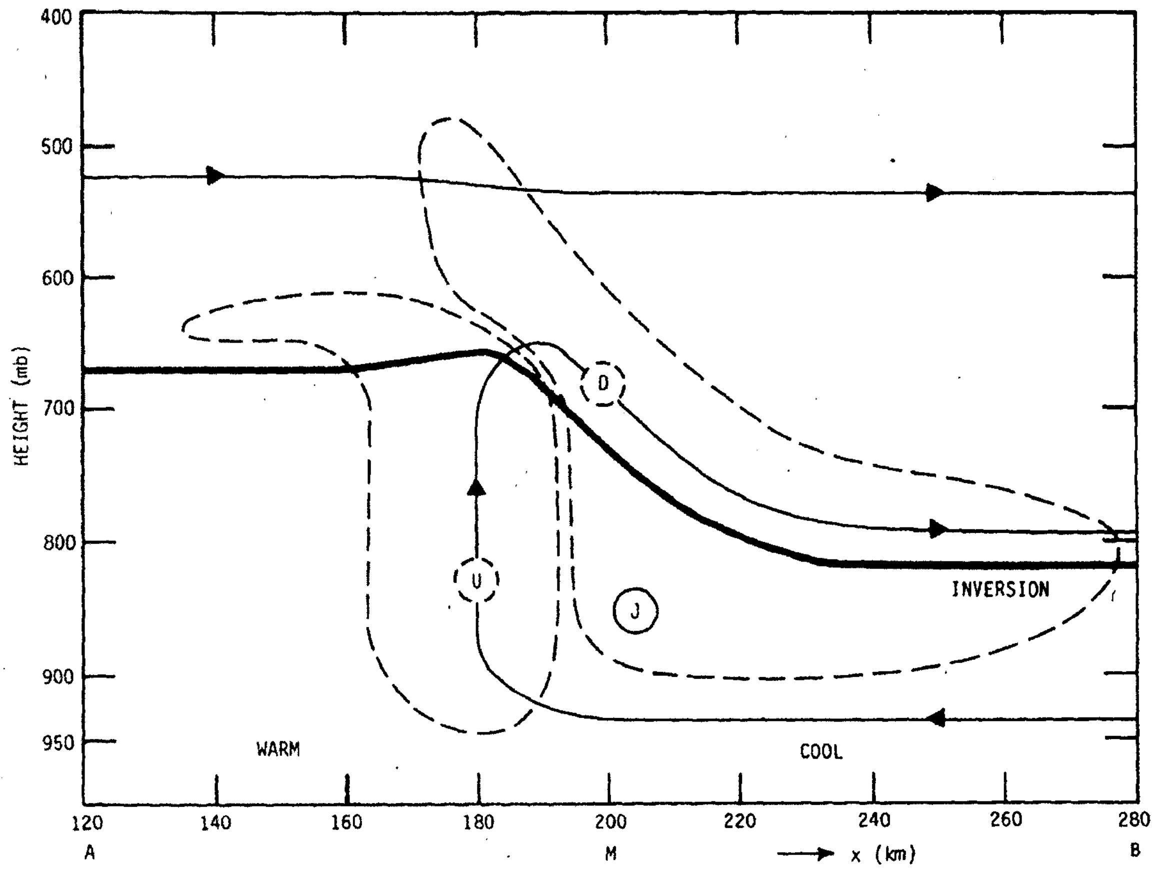

Figure 3 - (from Sun and Ogura (1979), their Fig. 12) Schematic vertical cross section across the dry line. J, U and D denote the locations of the cores of the jet in the y direction, the upward motion and the downward motion, respectively. The dashed lines are the contour lines of 2 cm s^{-1} for the vertical velocity.

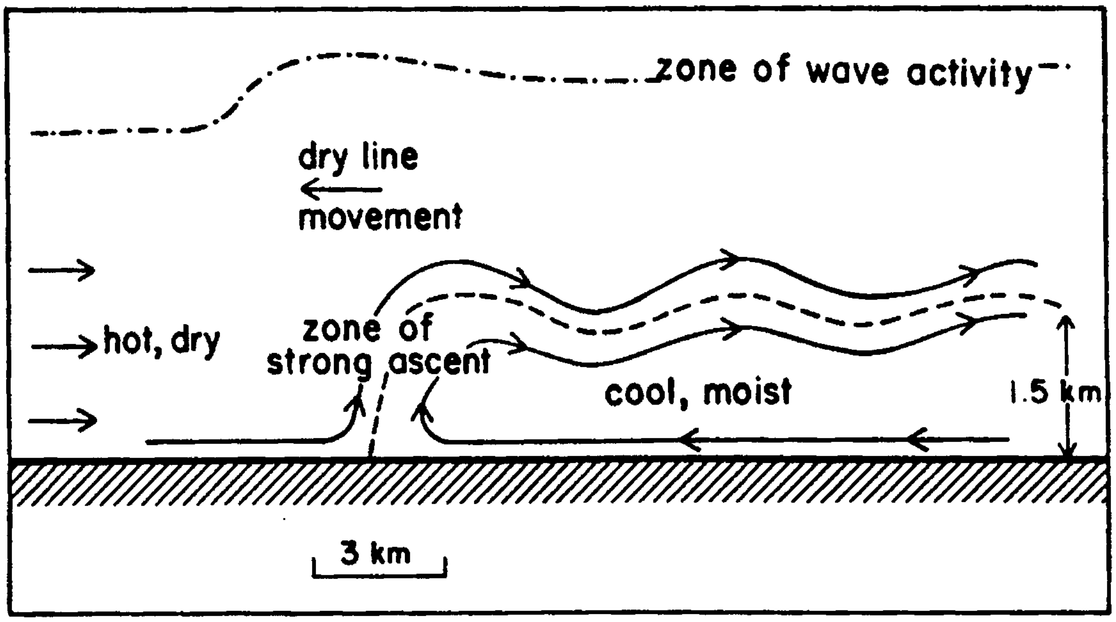

Figure 4 - (from Parsons et al. (1991), their Fig. 11) A schematic of the circulations associated in the vertical cross section perpendicular to the dryline for the late-afternoon and early-evening dryline with a significant density gradient. The dashed line is the boundary between the moist and dry air masses. The dash-dot line is the height of the boundary layer for the hot dry air mass.

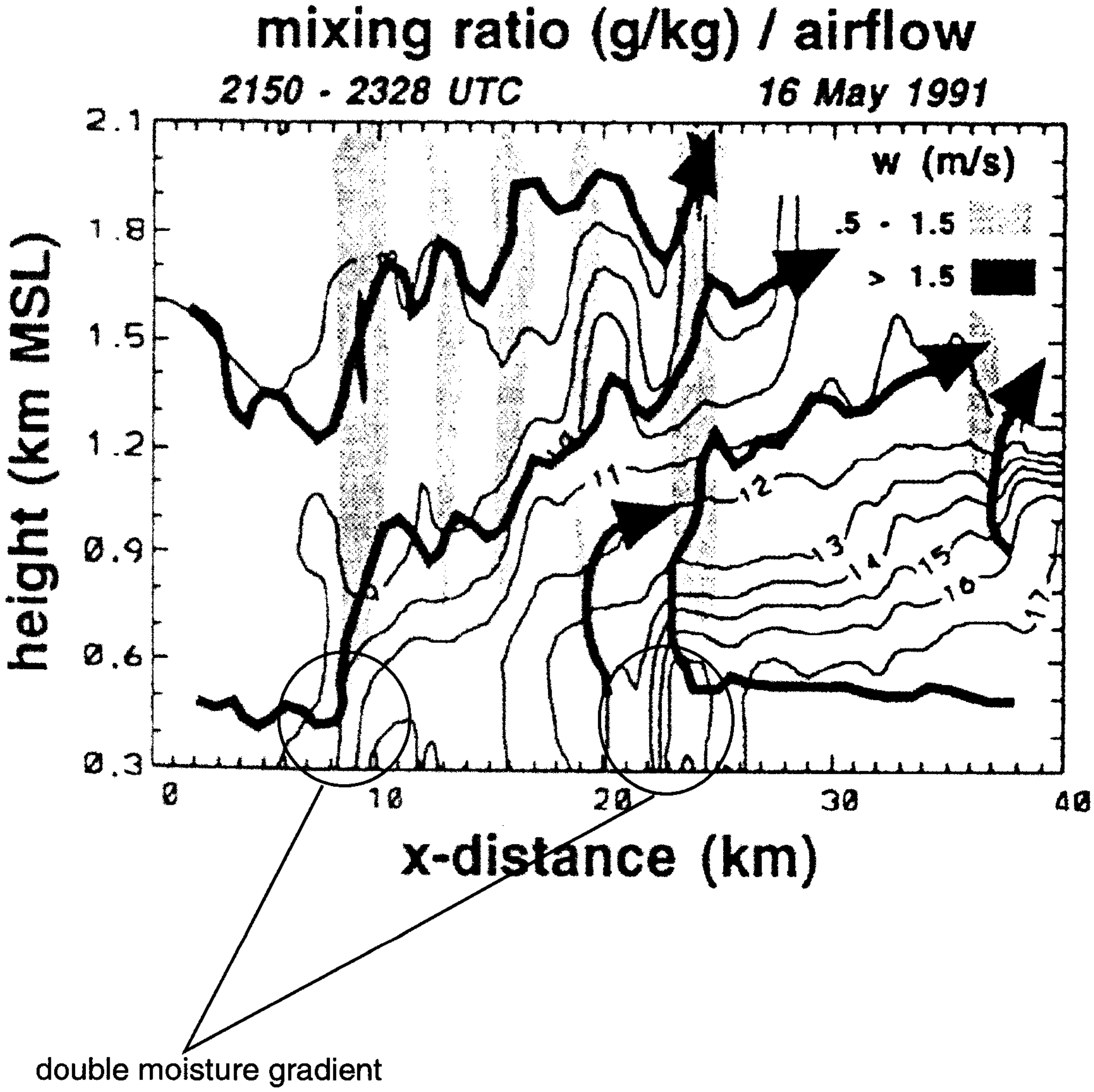

Figure 5 - (from Hane et al. (1993), their Fig. 10) Vertical cross section showing analysis of water vapor mixing ratio (g kg^{-1}) from aircraft traverses of the dryline of 16 May 1991. Selected streamlines are included and areas of upward motion shaded.

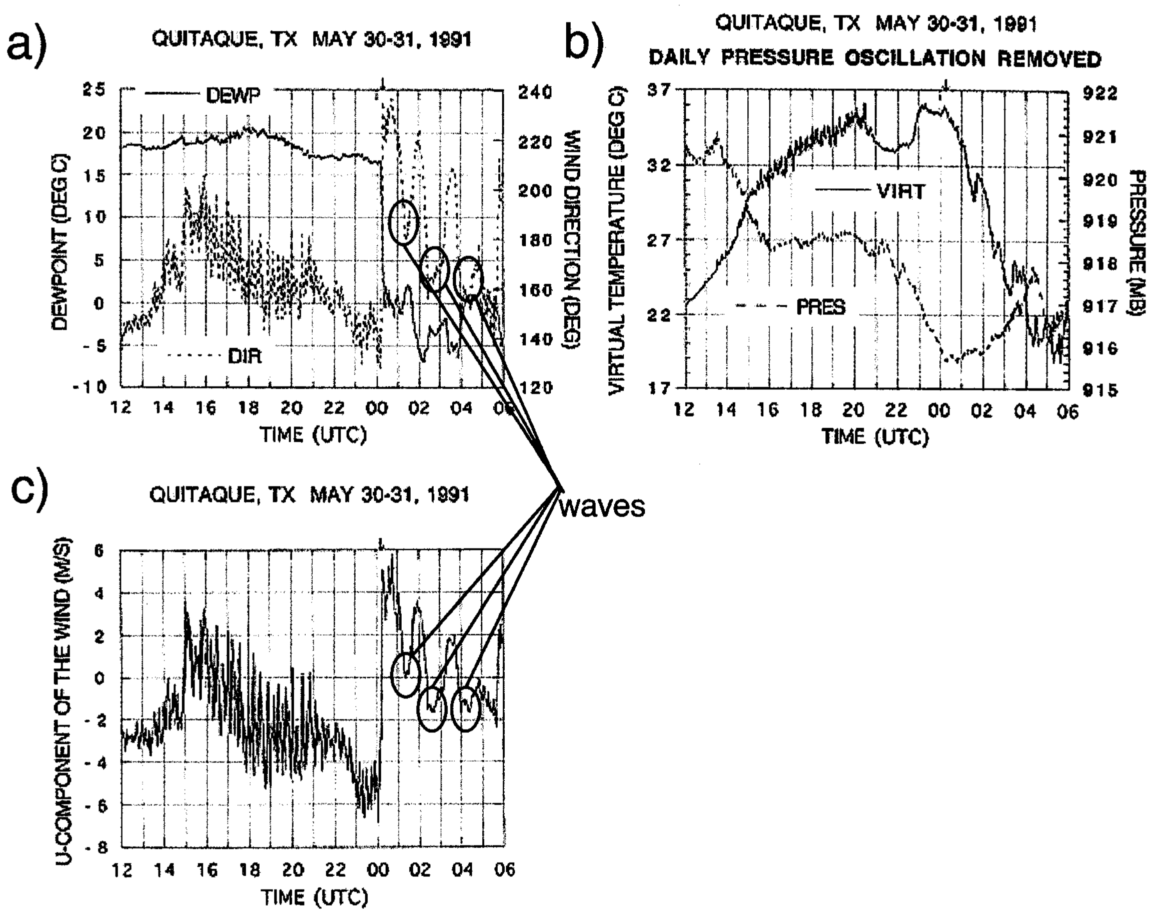

Figure 6 - (from Crawford and Bluestein (1997), their Fig. 4) Plots of (a) dewpoint (^{o}C, solid line) and wind direction (degrees, dashed line), (b) adjusted (i.e., the diurnal and semidiurnal waves have been removed) pressure (mb, dashed line) and virtual temperature (^{o}C, solid line), and (c) the zonal (u) component of the wind (m s^{-1}) as a function of time at the PAM-II mesonet site in Quitaque, Texas, on 30–31 May 1991. The dryline passed to the east of the site at the time indicated by the arrow at the top.

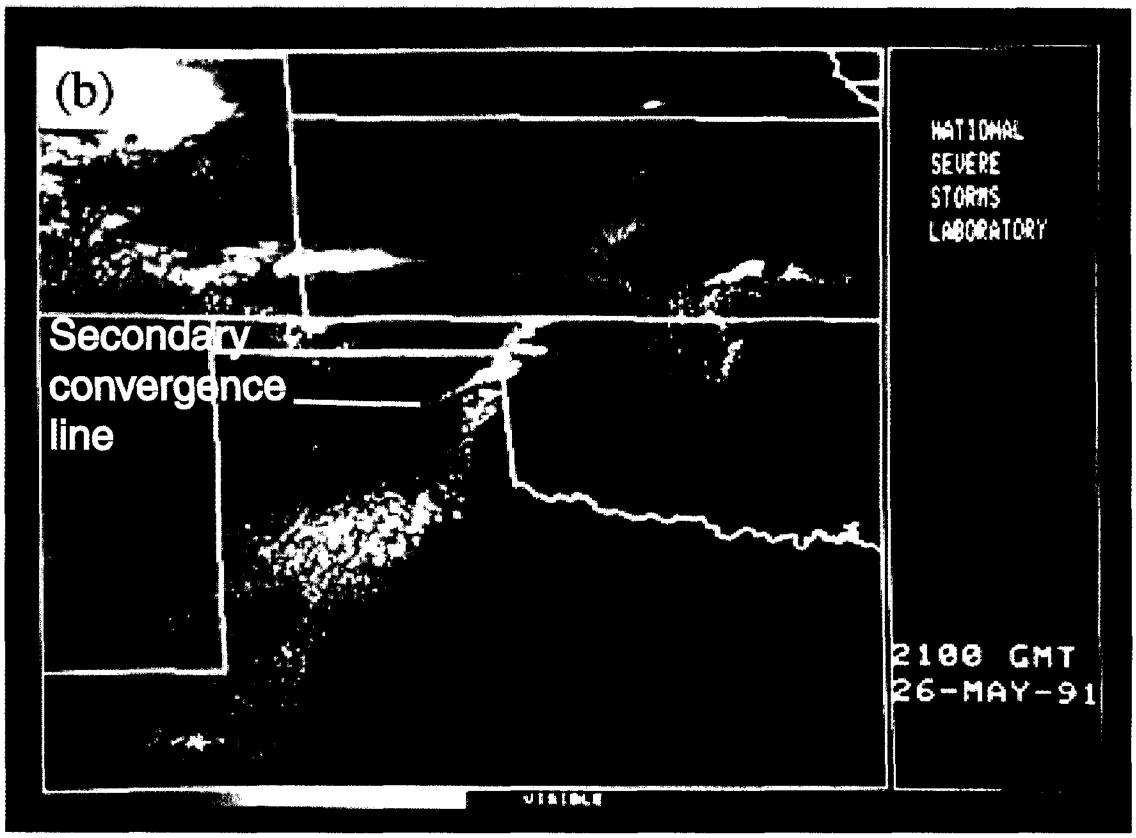

Figure 7 - (from Hane et al. (1997), their Fig. 8b) Visible image centered on the northeastern Texas panhandle from GOES-7 satellite on 26 May 1991 at 2101 UTC. Note the secondary convergence line.

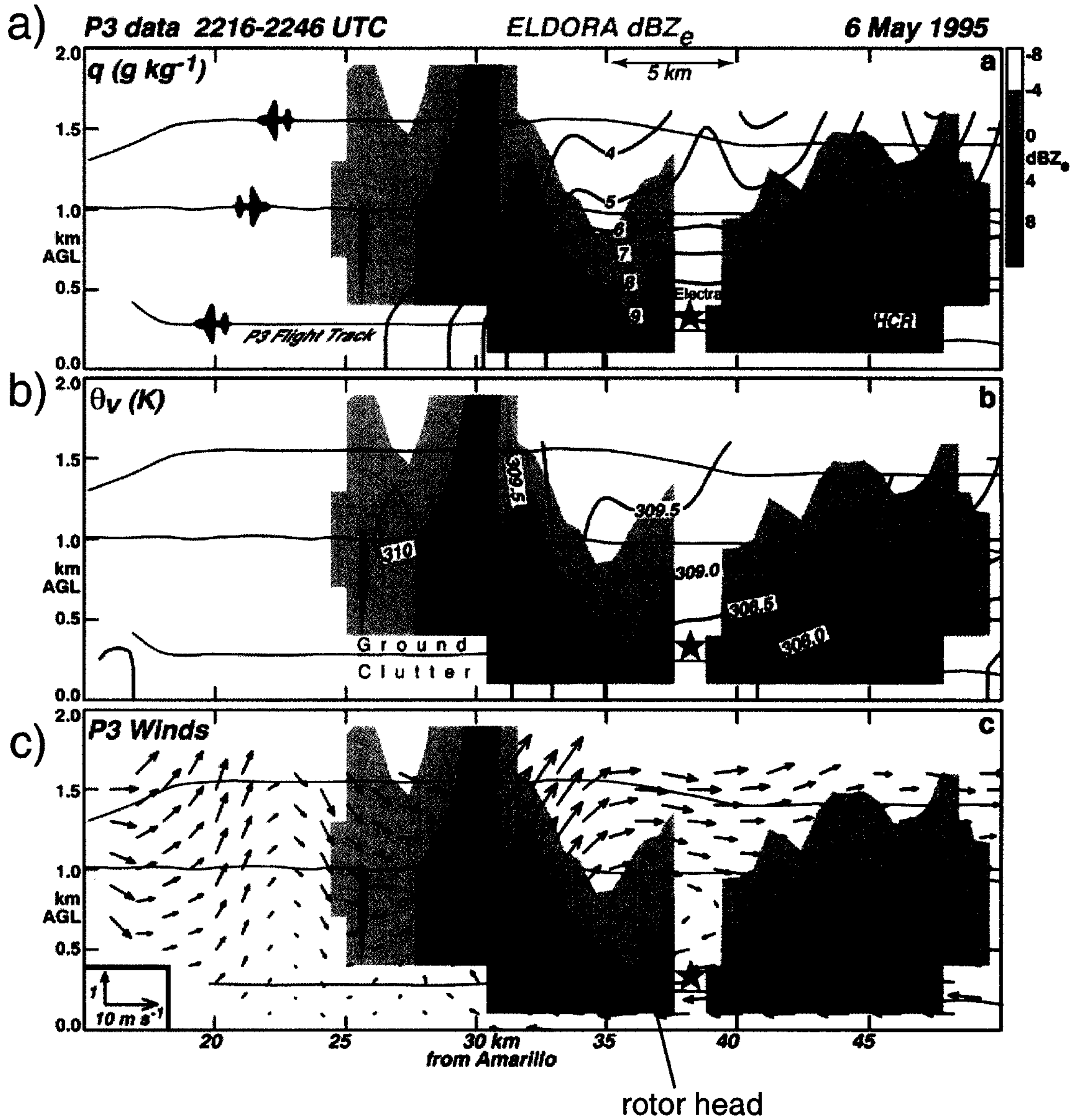

Figure 8 - (from Atkins et al. (1998), their Fig. 14) Vertical cross section of objectively analyzed P-3 data collected from 2216 to 2246 UTC [6 May 1995]. Plotted are (a) mixing ratio (g kg^{-1}), (b) virtual potential temperature (K), and (c) dryline relative winds (m s^{-1}) in the plane of the cross section. The gray field in all three panels is the ELDORA reflectivity field in the closest vertical cross section to the P-3 flight track. The thin black line is the P-3 flight track, while the star indicates the Electra position in the cross section.

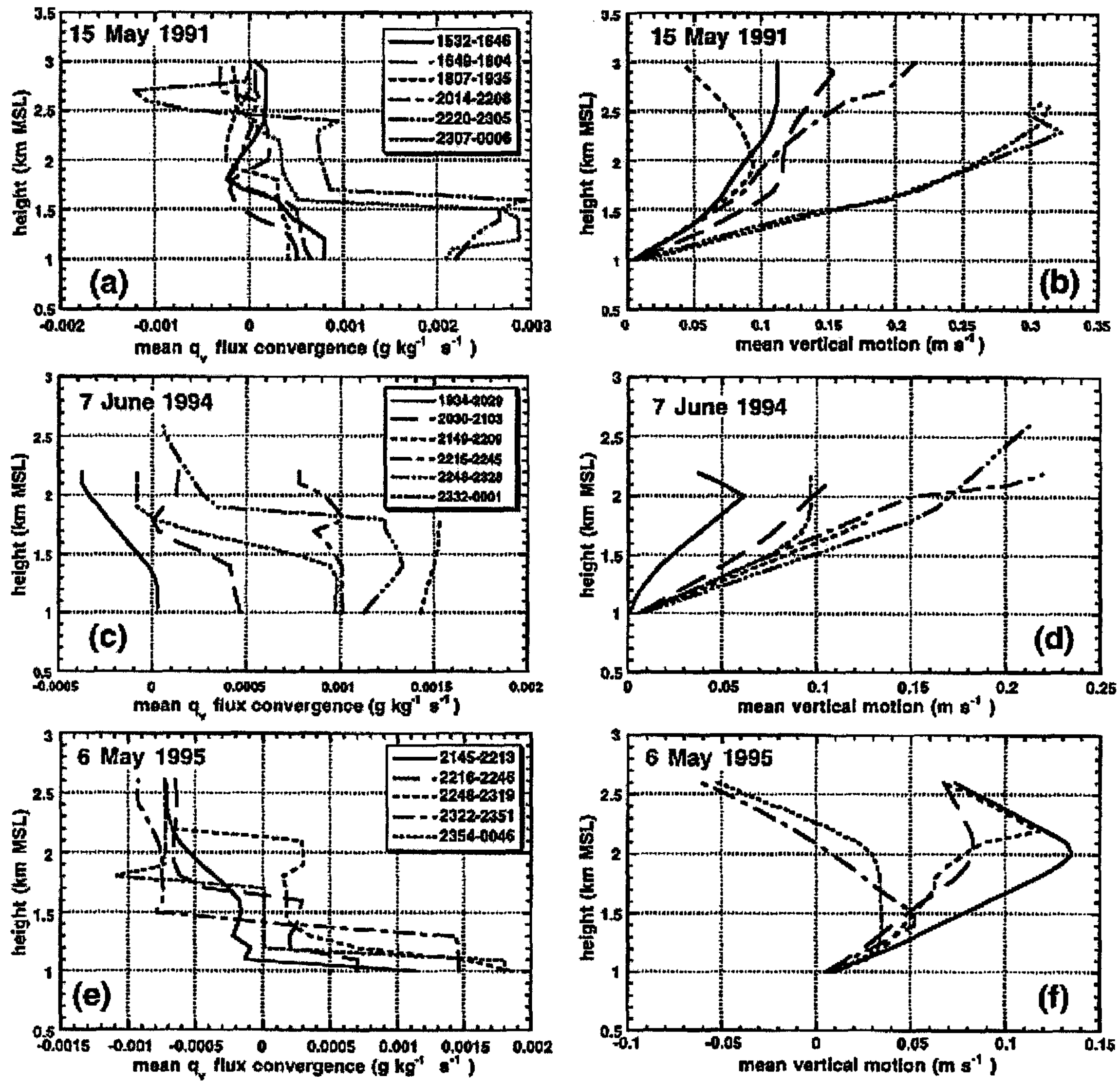

Figure 9 - (from Ziegler and Rasmussen (1998), their Fig. 16) Vertical profiles of horizontally averaged moisture flux convergence [(a), (c), (e)] and vertical velocity [(b), (d), (f)] over the cross-sectional analysis domains in the 15 May 1991 (row 1), 7 June 1994 (row 2), and 6 May 1995 (row 3) cases. Moisture flux convergence is the east–west component.

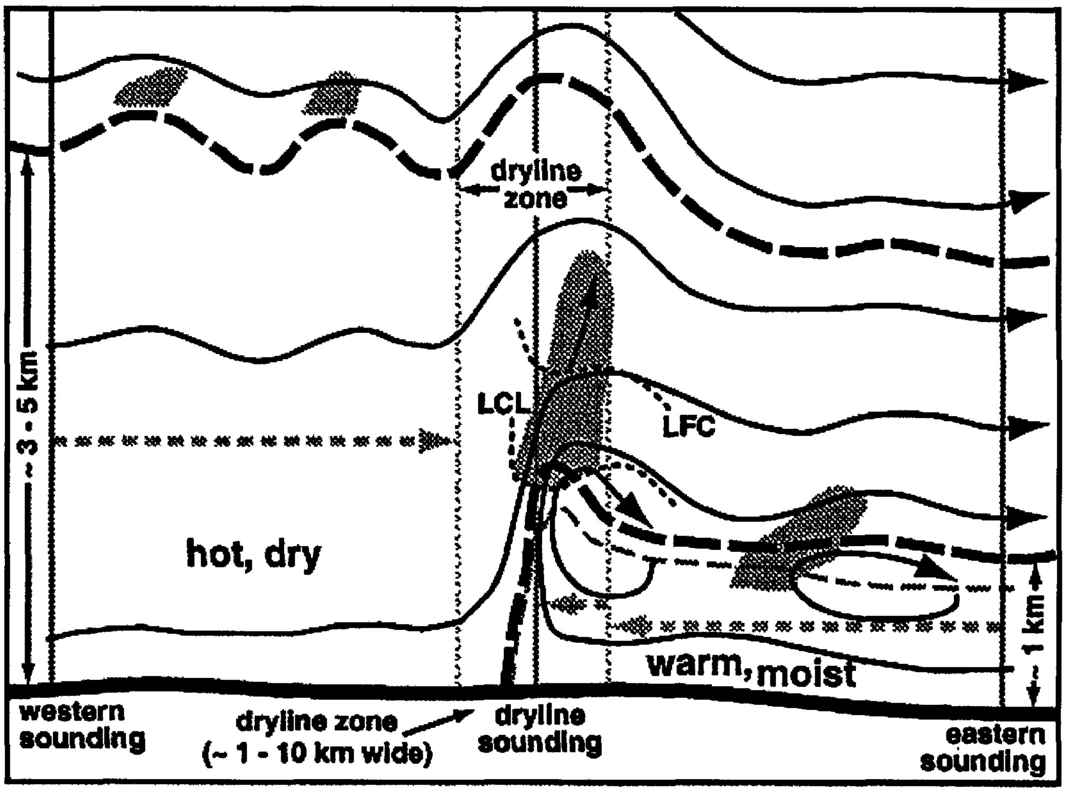

Figure 10 - (from Ziegler and Rasmussen (1998), their Fig. 17) Conceptual model of the dryline environment during afternoon and early evening, showing dryline position in relation to cumulus clouds and airflow streamlines. The lower heavy dashed curve denotes the extent of the moist convective boundary layer, while the upper heavy dashed curve locates the deep, dry convective boundary layer (west of dryline), and the elevated residual layer (east of dryline and above moist layer). The gray dashed curve locates the surface of zero westerly wind component. The heavy dashed streamline denotes a buoyantly accelerated cloudy air parcel trajectory.

Leg 7-8 Averaged Dryline Cross Section - Horizontal Divergence

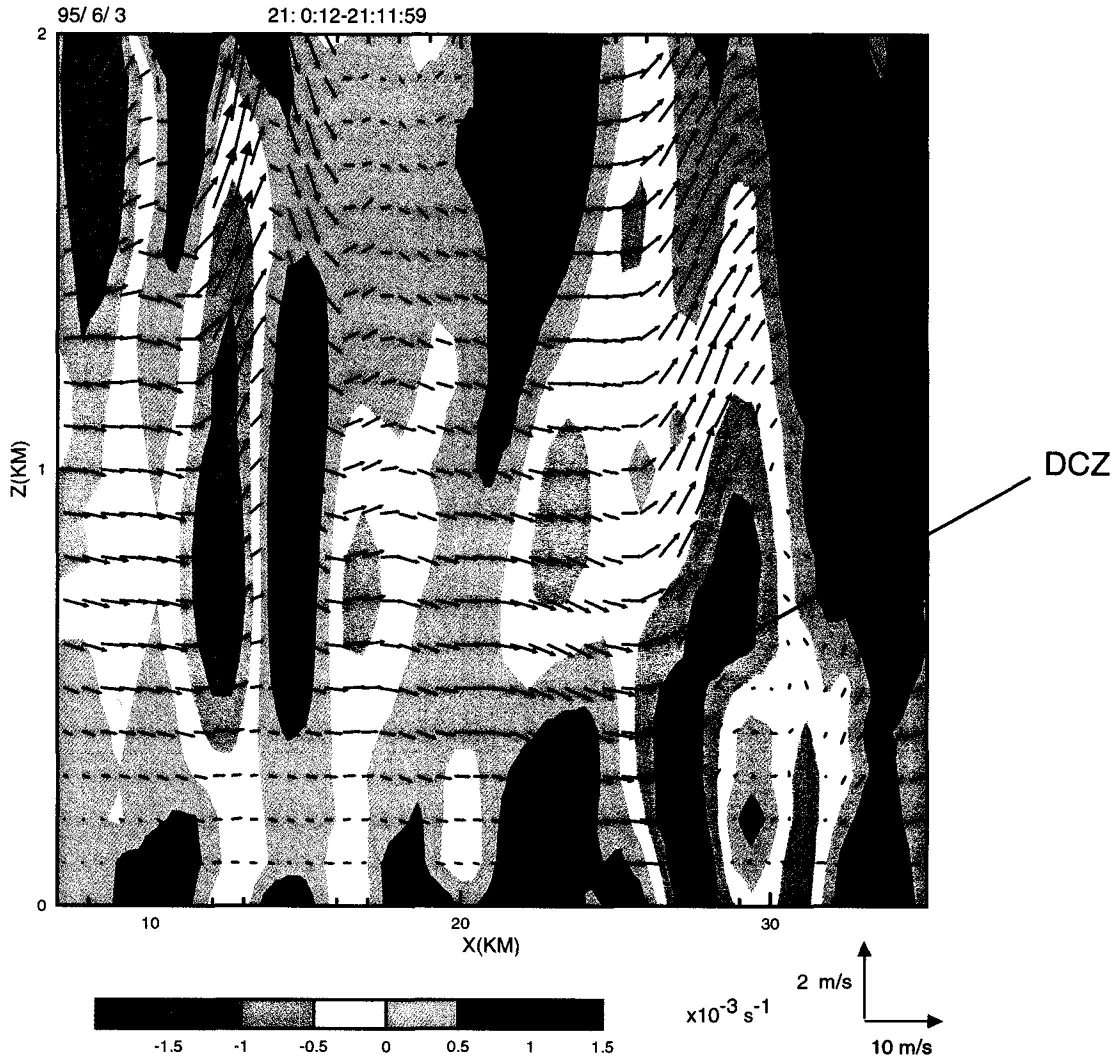

Figure 11 - (from Weiss and Bluestein (2002), their Fig. 12) Averaged ELDORA cross section across the 3 June 1995 dryline. Vectors represent average u and w winds (m s^{-1}; note different scales for u and w components). Shading represents average horizontal divergence (10^{-3} s^{-1}; scale at bottom). Blue colors indicate divergence, red colors indicate convergence.

Leg 11-12 Averaged Dryline Extension Cross Section (y=-5 to +1)

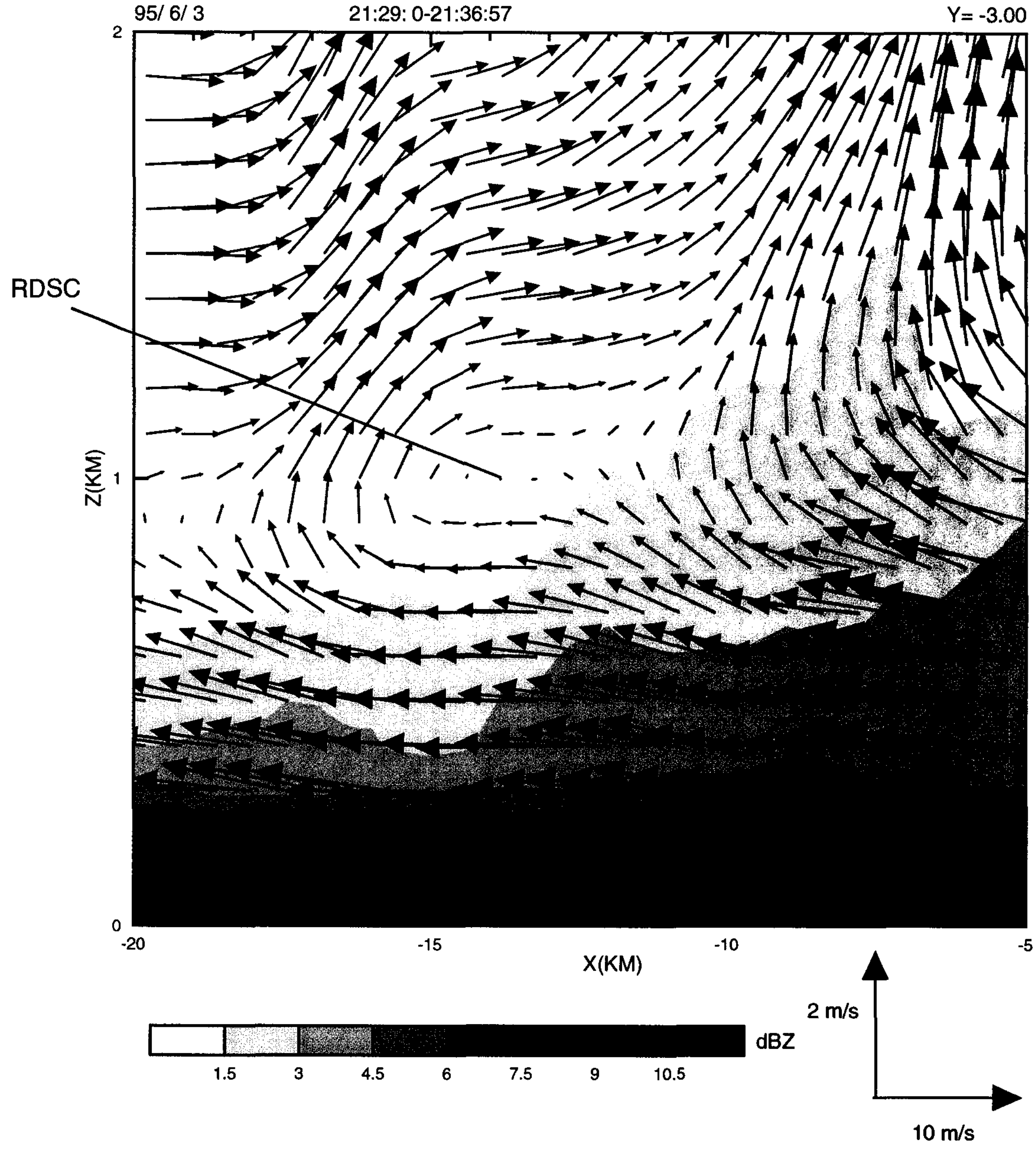

Figure 12 - (from Weiss and Bluestein (2002), their Fig. 16c) Averaged ELDORA cross section of a residual dryline secondary circulation (RDSC) north of an outflow boundary on 3 June 1995. Vectors represent average u and w winds (m s^{-1}, note different scales for u and w components). Average reflectivity indicated by shading (dBZ). RDSC position shown.

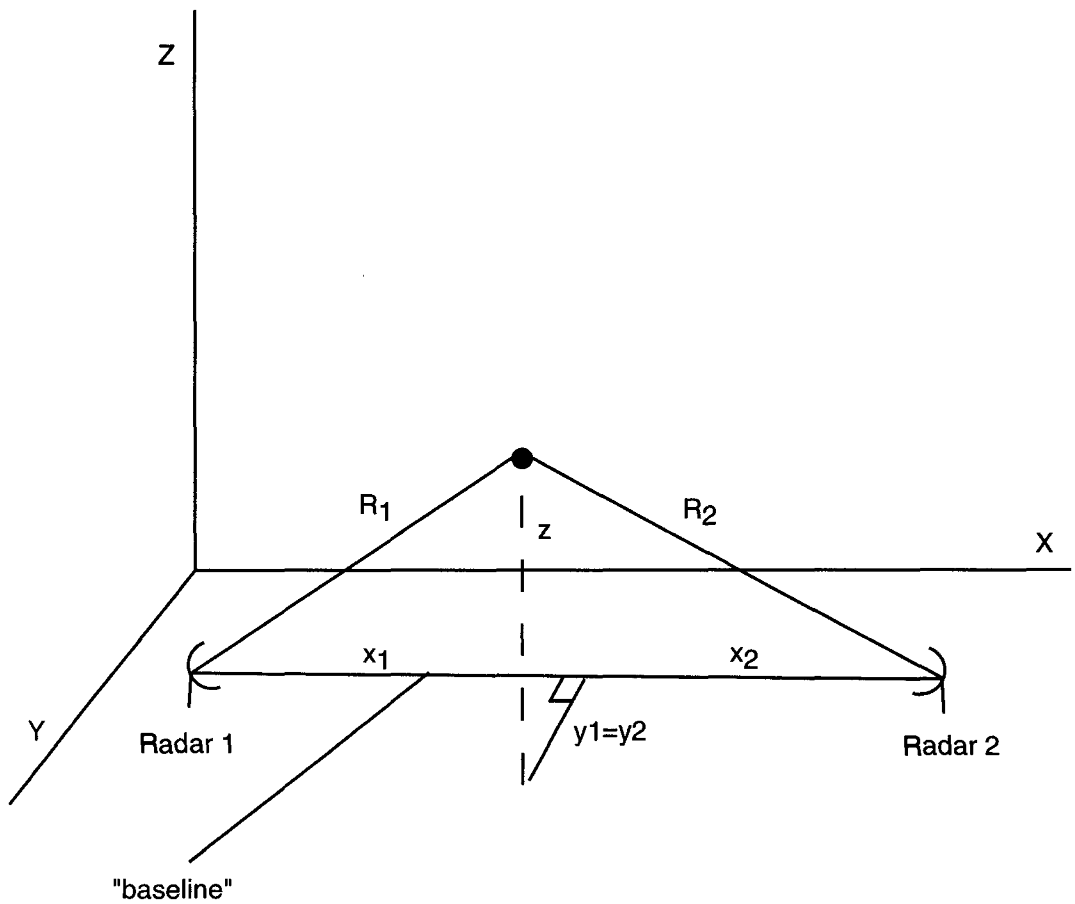

Figure 13 - The geometry of the traditional dual-Doppler problem for Eqns (1a) and (1b). Here, y_1=y_2 for the purposes of easy illustration.

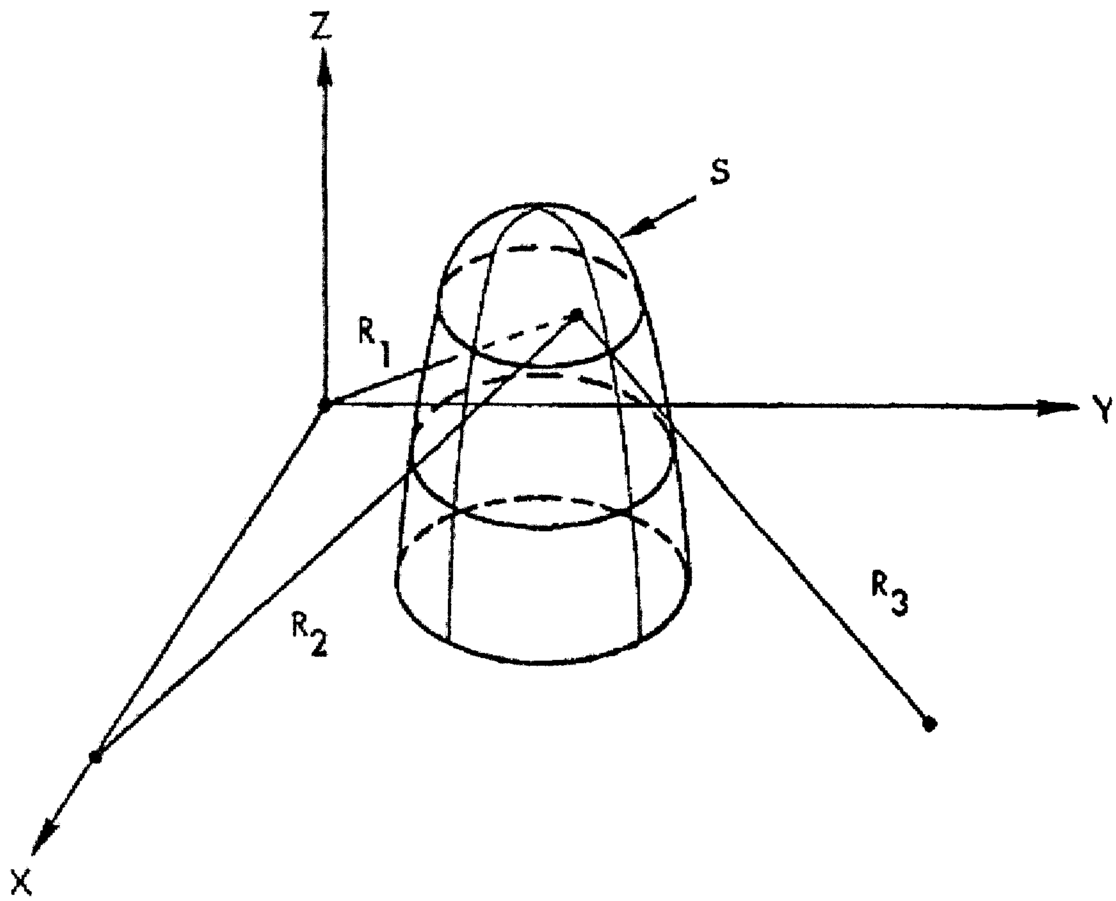

Figure 14 - (from Armijo (1969), his Fig. 1) Coordinate system conventions for three-radar problem.

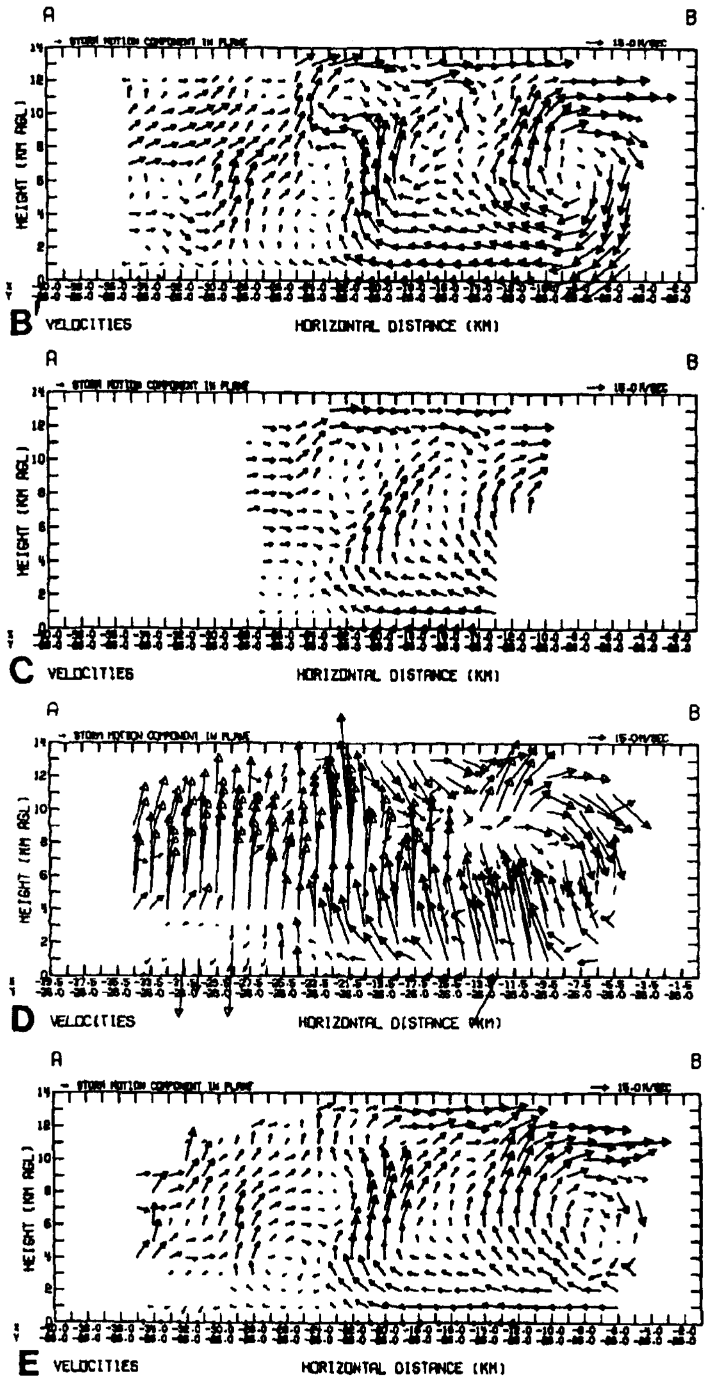

best analysis

Figure 15 - (from Ray et al. (1980), their Fig. 11) East-west cross sections of wind velocity through a thunderstorm using the following techniques (label in lower left corner of each panel): B' - integration downward from upper boundary, posterior variational adjustment to satisfy vertically integrated horizontal divergence; C - direct least squares estimation (3 radars); D - C with posterior variational adjustment as in B'; E - posterior variational adjustment of least squares estimation to satisfy mass continuity (best estimate).

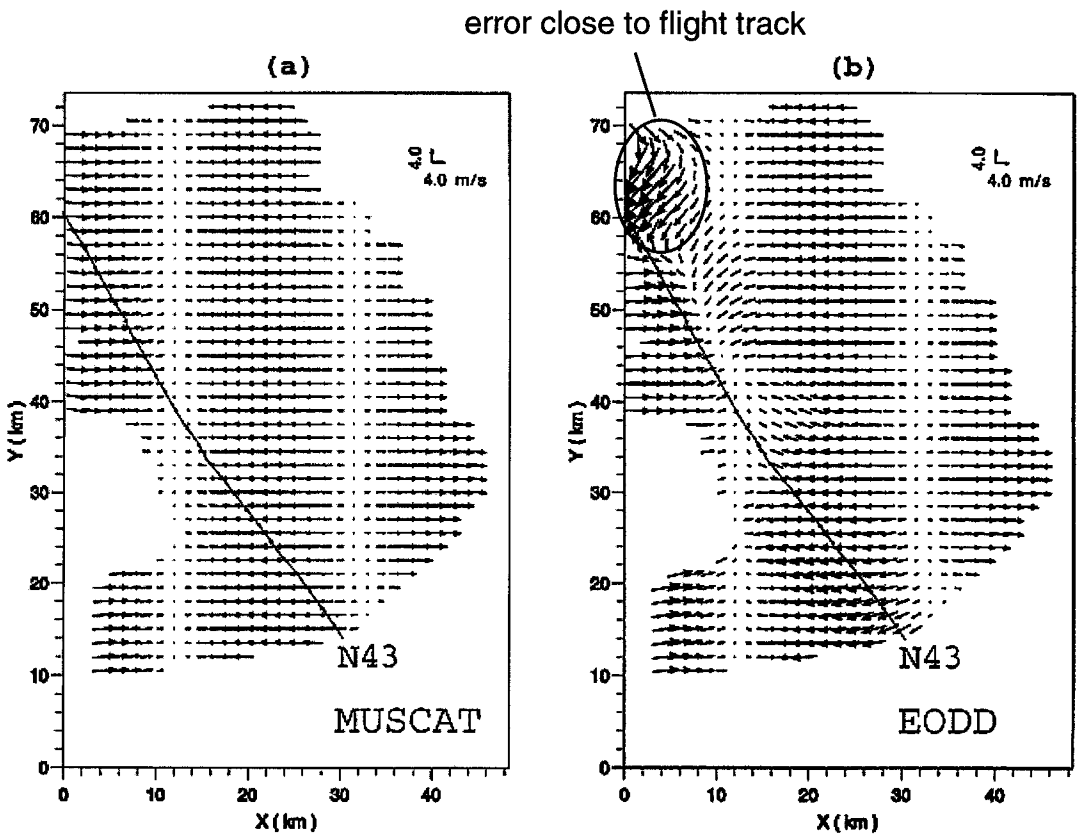

Figure 16 - (from Bousquet and Chong (1998), their Fig. 6) Retrieved horizontal flow at 5-km altitude from (a) MUSCAT and (b) EODD, as applied to simulated data. Oblique line refers to the flight track.

a)

b)

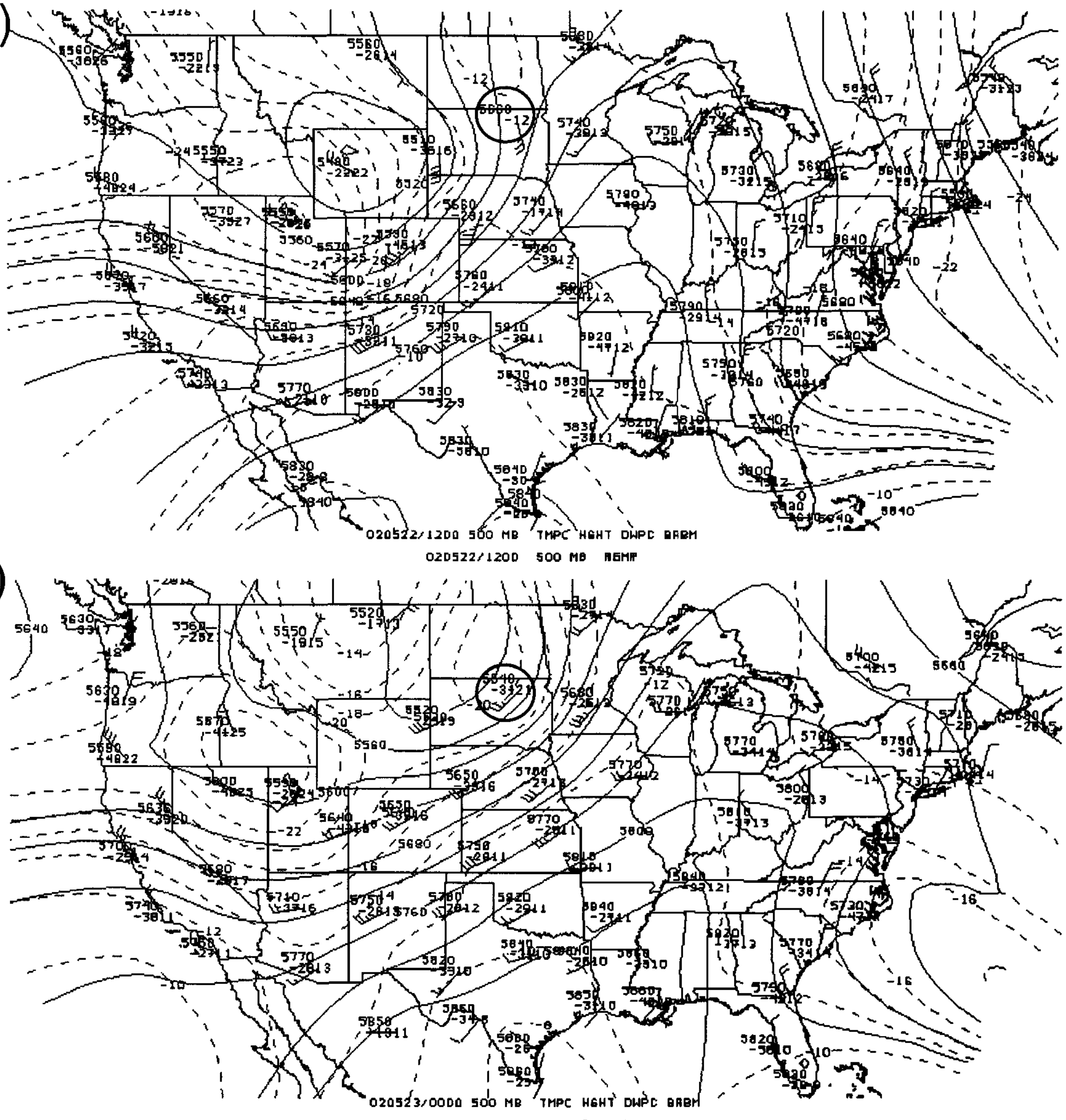

Figure 17 - 500 mb analyses valid on 22 May 2002 at a) 1200 UTC and b) 0000 UTC (23 May). Solid contours denote height (m, contoured every 40 m). Dashed lines denote temperature (deg C, contoured every 2 deg C). The Aberdeen, SD RAOB (referred to in the text) is circled.

a)

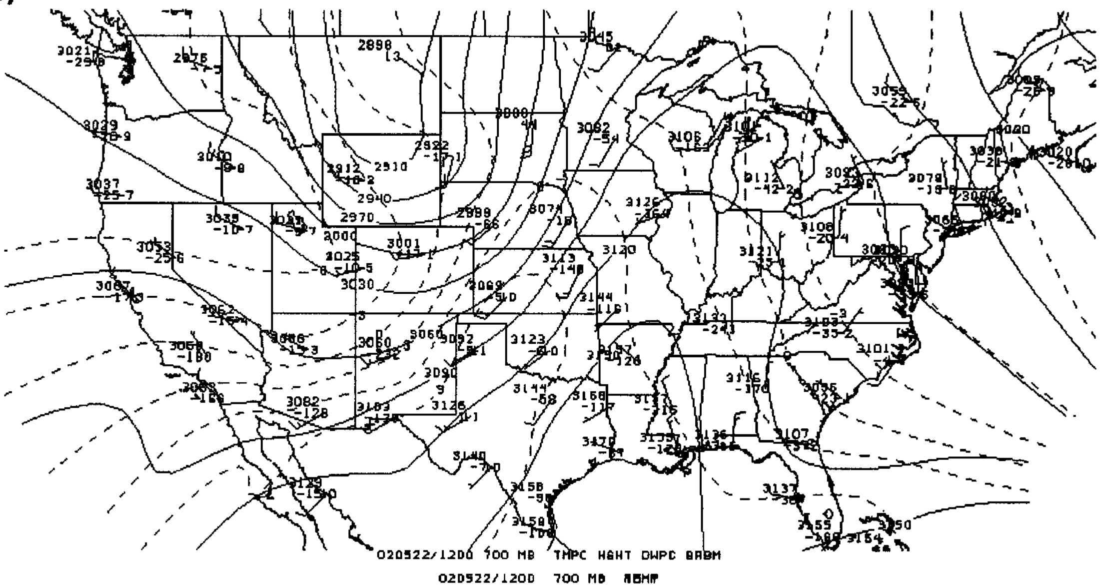

b)

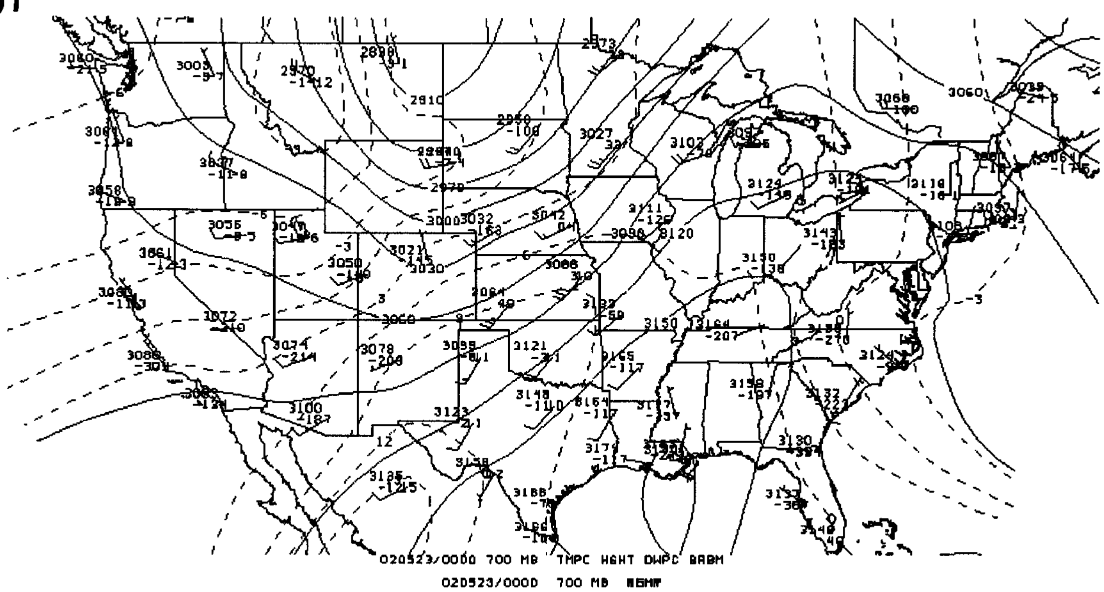

Figure 18 - 700 mb analyses valid on 22 May 2002 at a) 1200 UTC and b) 0000 UTC (23 May). Solid contours denote height (m, contoured every 30 m). Dashed lines denote temperature (deg C, contoured every 3 deg C).

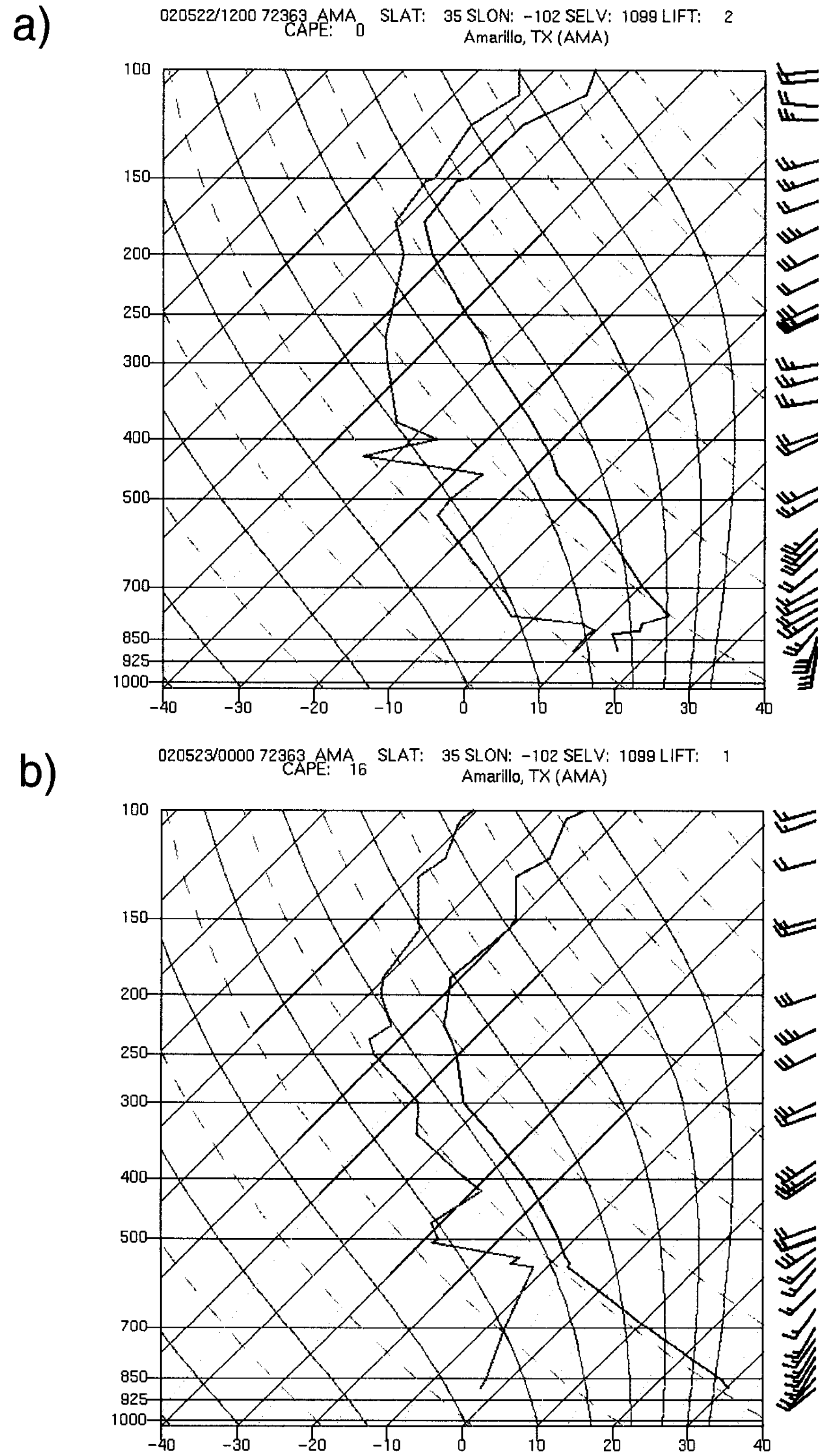

Figure 19 - Skew-T diagrams from RAOBS taken at Amarillo, TX, vaild on 22 May 2002 at a) 1200 UTC and b) 0000 UTC (23 May). Full (half) wind barbs represent 10 (5) knots.

a)

b)

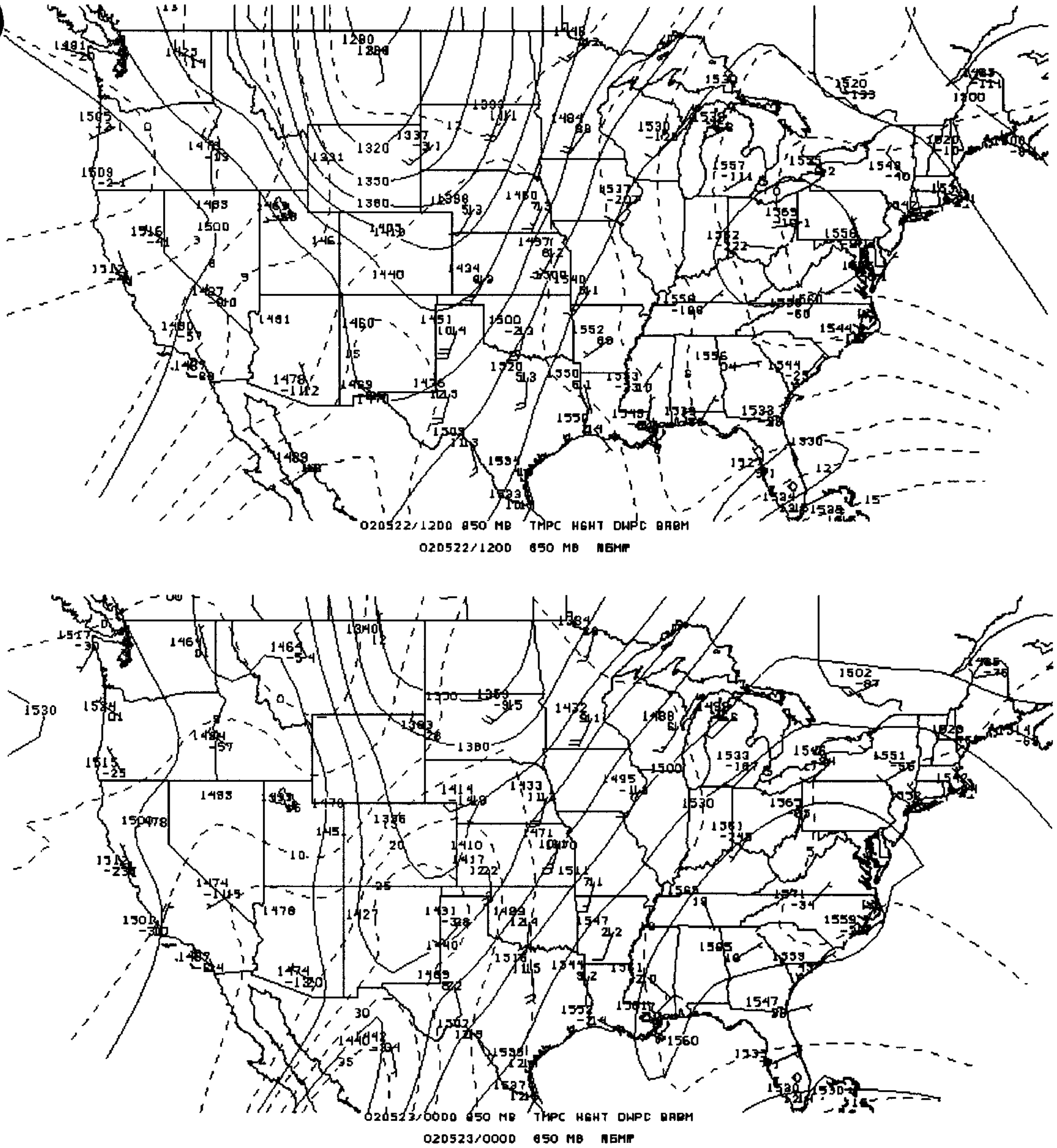

Figure 20 - 850 mb analyses valid on 22 May 2002 at a) 1200 UTC and b) 0000 UTC (23 May). Solid contours denote height (m, contoured every 30 m). Dashed lines denote temperature (deg C, contoured every 5 deg C).

a)

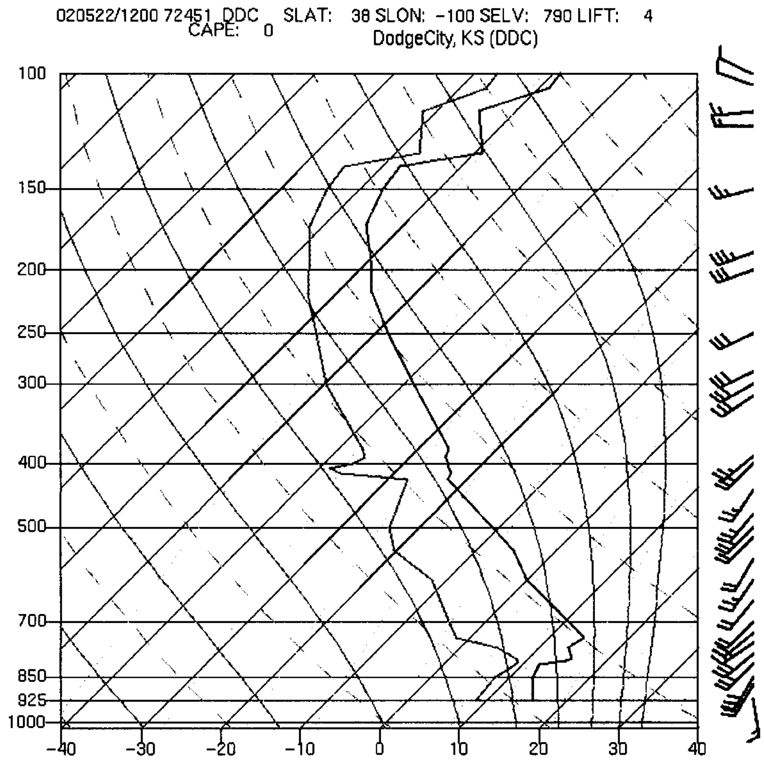

b)

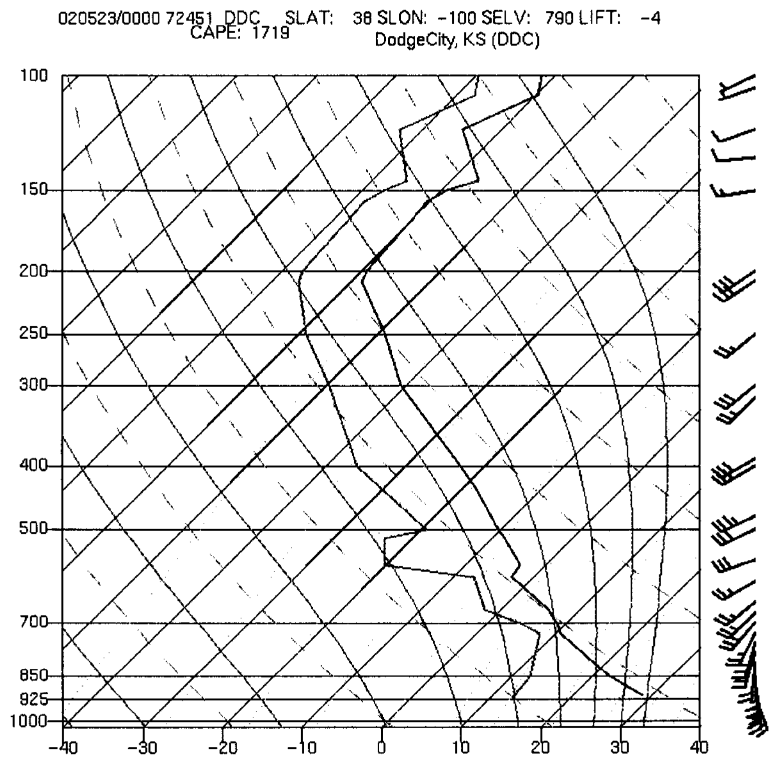

Figure 21 - Skew-T diagrams from RAOBS taken at Dodge City, KS valid on 22 May 2002 at a) 1200 UTC and b) 0000 UTC (23 May). Full (half) wind barbs represent 10 (5) knots.

a)

b)

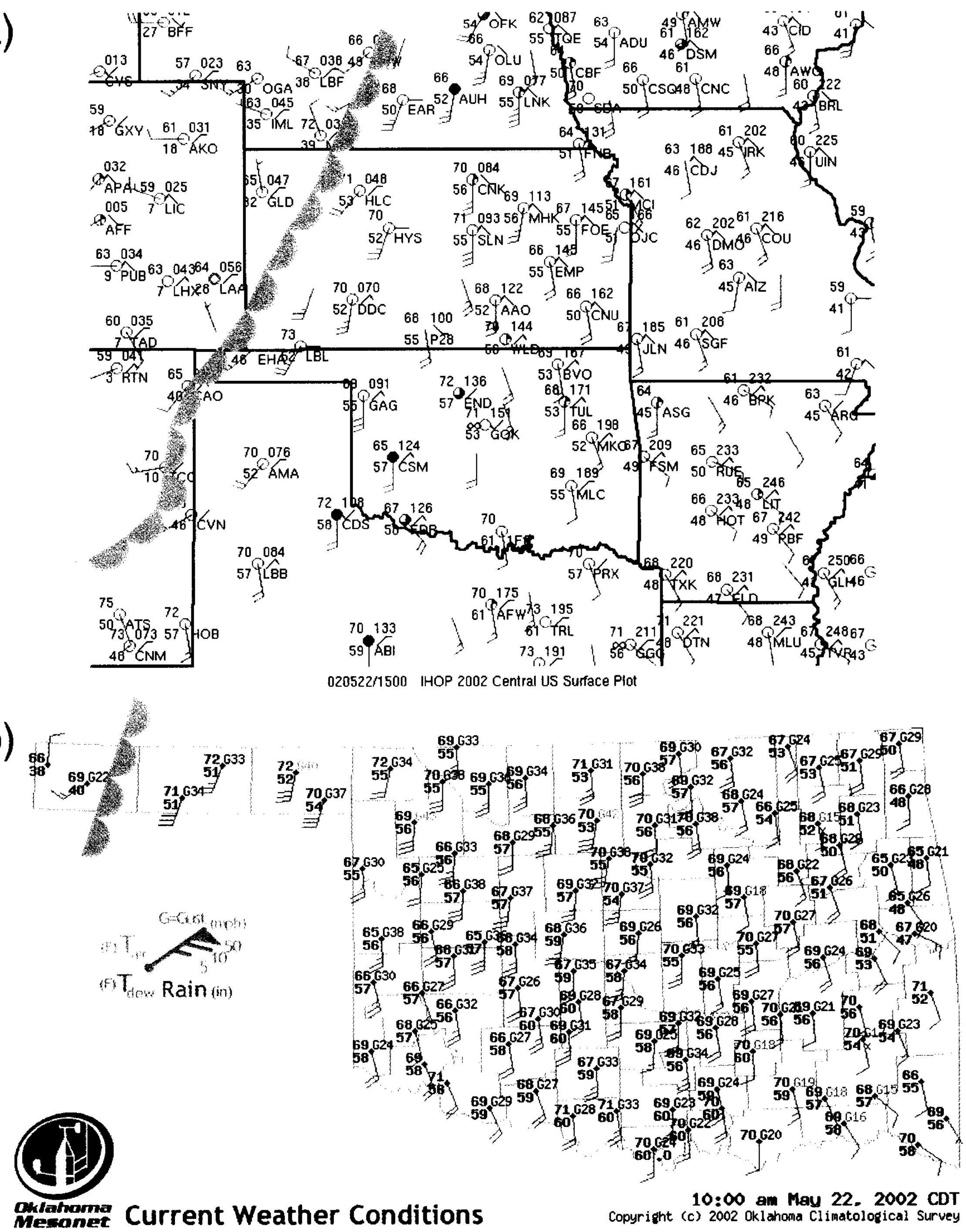

Figure 22 - a) Central Plains surface map and b) Oklahoma Mesonet surface map valid at 1500 UTC on 22 May 2002. Temperature and dewpoint for each station reported in deg F. The scalloped line in a) indicates the position of the dryline.

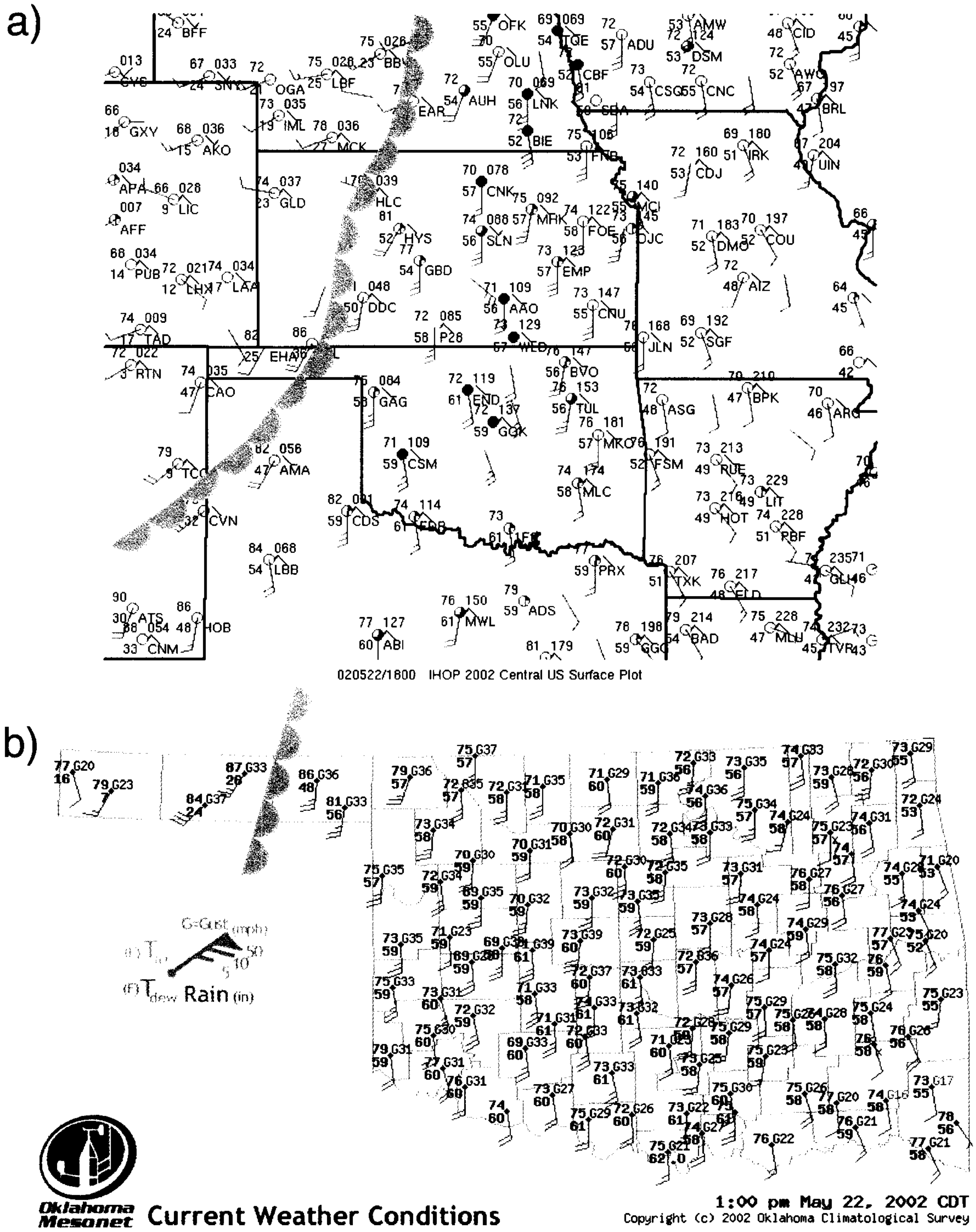

Figure 23 - a) Central Plains surface map and b) Oklahoma Mesonet surface map valid at 1800 UTC on 22 May 2002. Temperature and dewpoint for each station reported in deg F. The scalloped line in a) indicates the position of the dryline.

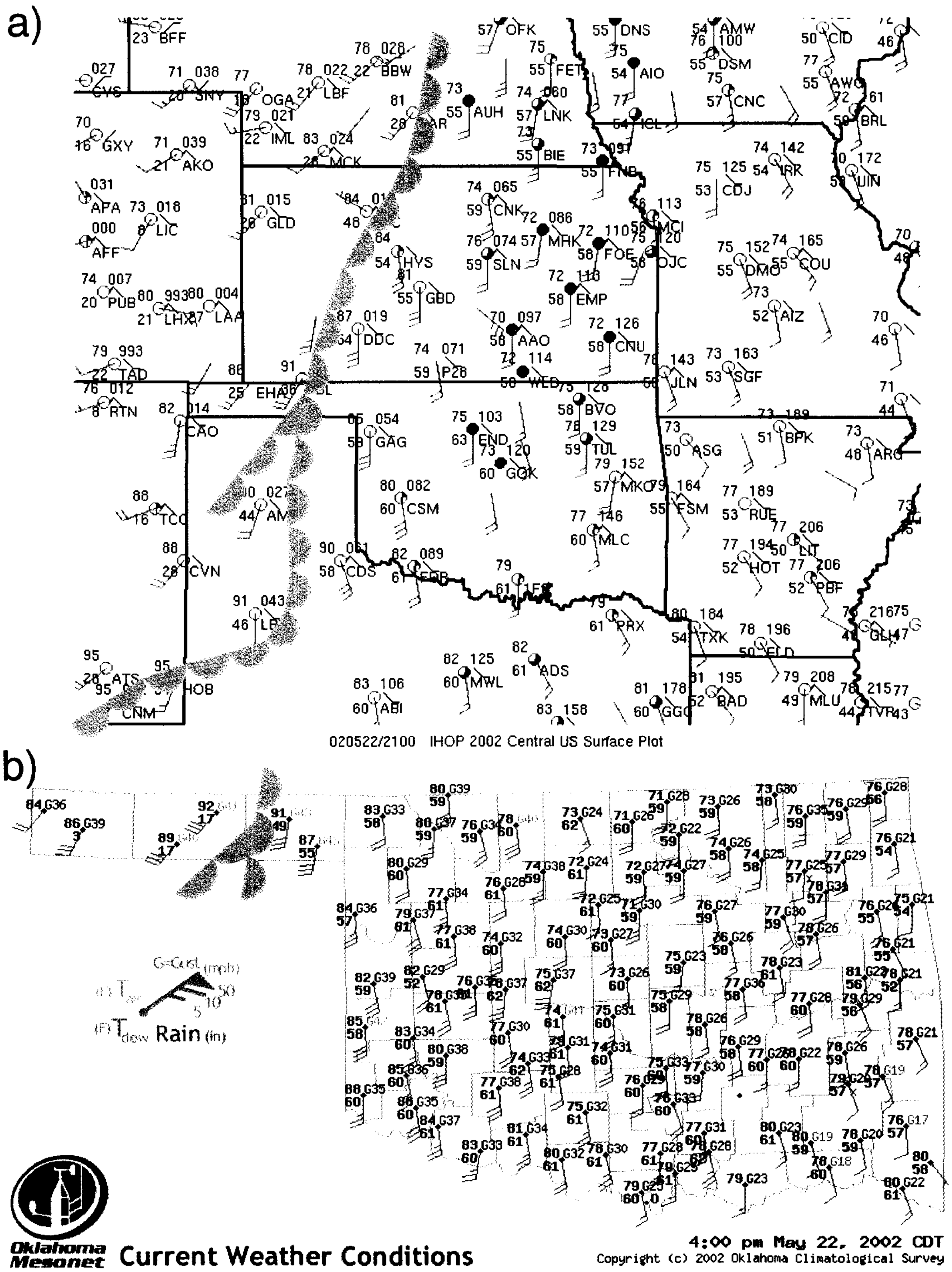

Figure 24 - a) Central Plains surface map and b) Oklahoma Mesonet surface map valid at 2100 UTC on 22 May 2002. Temperature and dewpoint for each station reported in deg F. The scalloped line in a) indicates the position of (known) drylines.

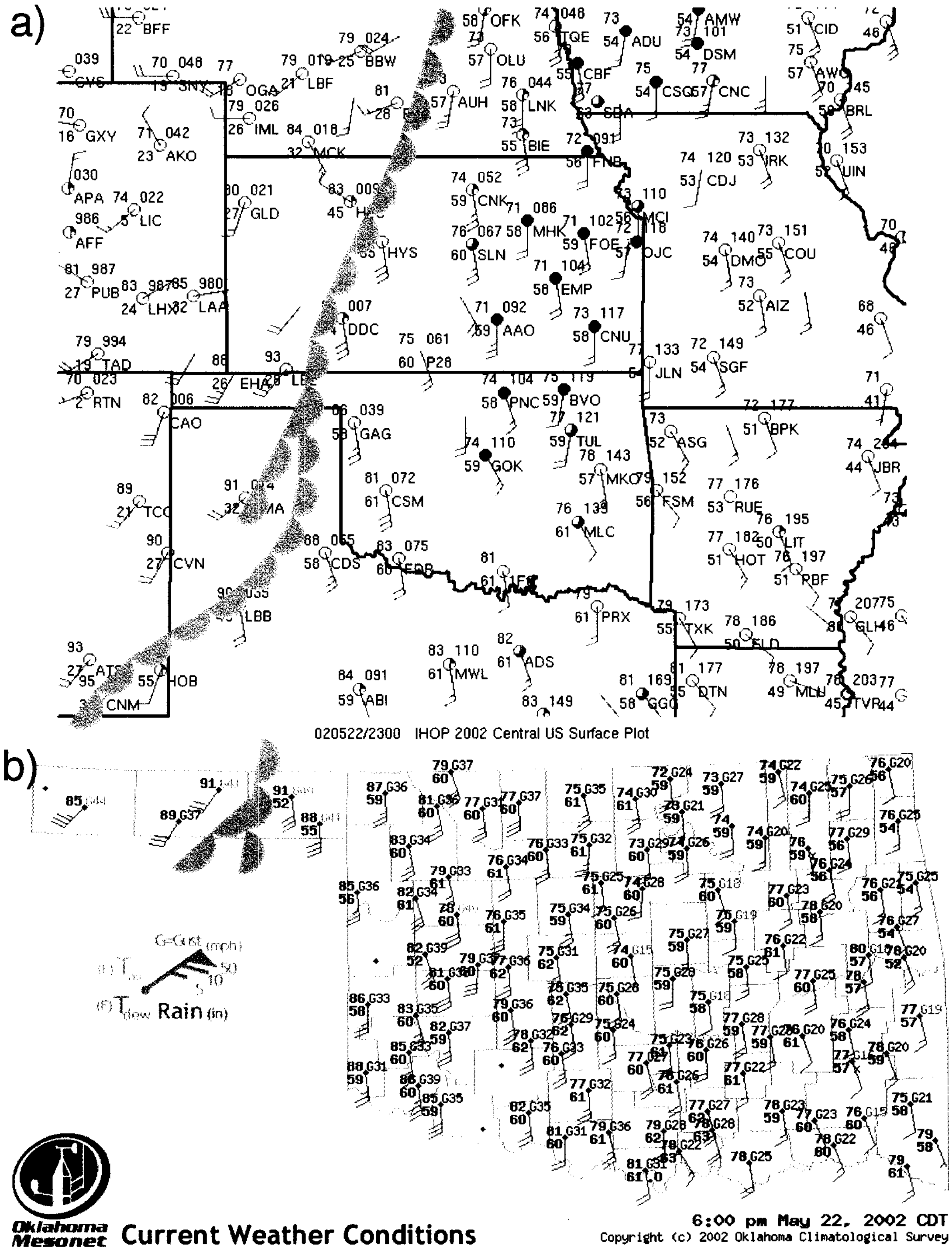

Figure 25 - a) Central Plains surface map and b) Oklahoma Mesonet surface map valid at 2300 UTC on 22 May 2002. Temperature and dewpoint for each station reported in deg F. The scalloped line in a) indicates the position of (known) drylines.

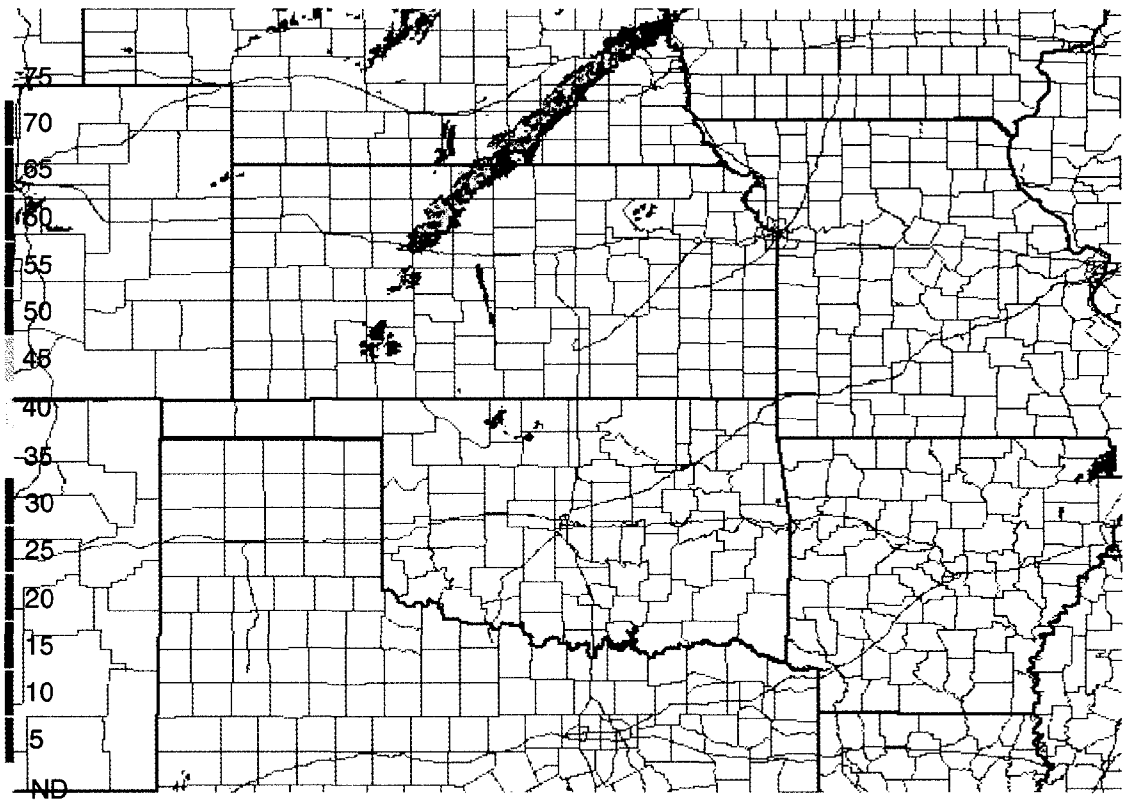

Figure 26 - NOWRAD composite reflectivity for 0000 UTC 23 May 2002. Reflectivity scale (dBZ) is provided on the left.

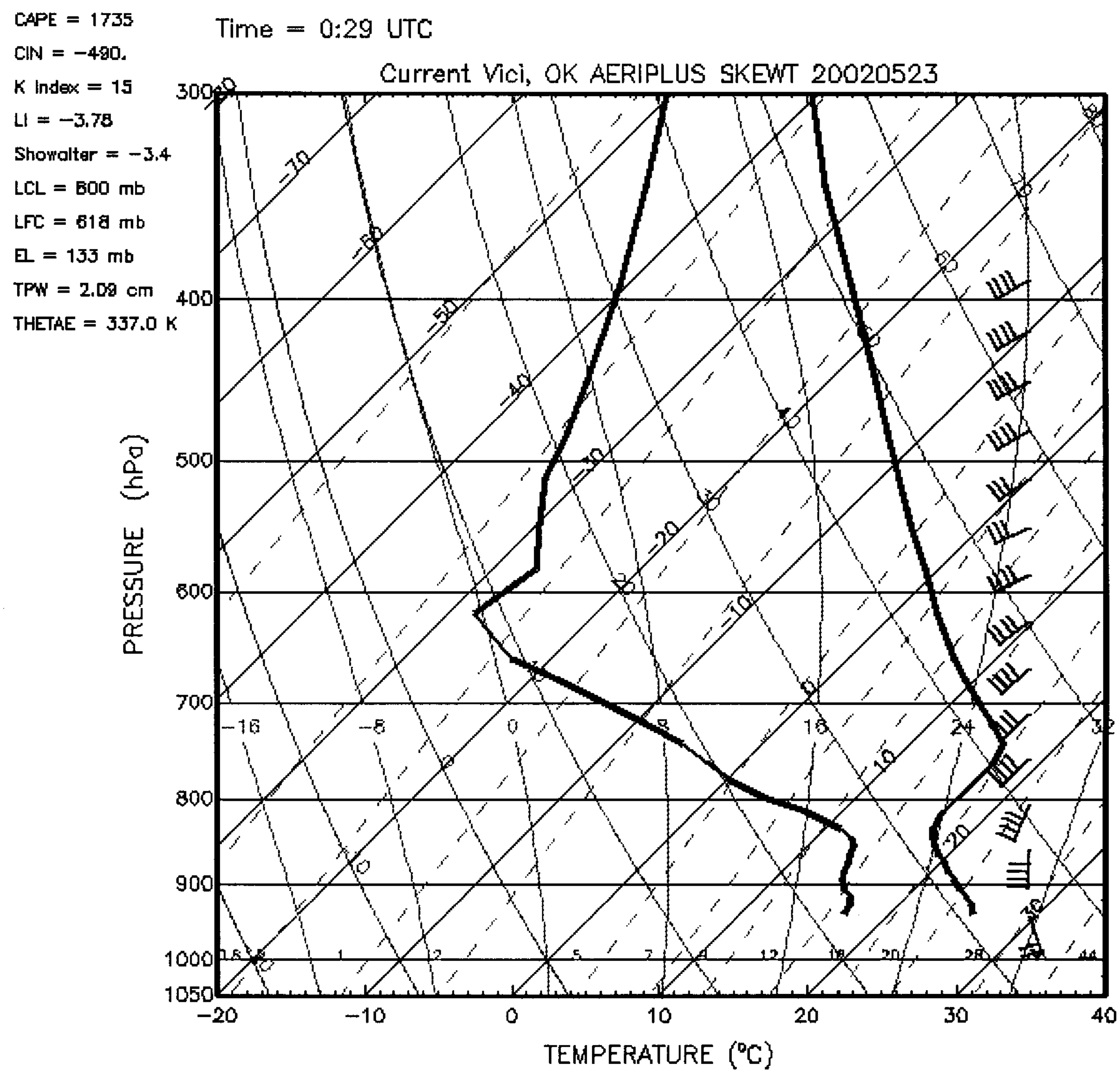

Figure 27 - Skew-T diagram from an Atmospheric Emitted Radiance Interferometer (AERIplus) sounding taken at Vici, OK valid 23 May 2002 at 0029 UTC. Full (half) wind barbs represent 10 (5) knots. The wind measurements are from a nearby profiler.

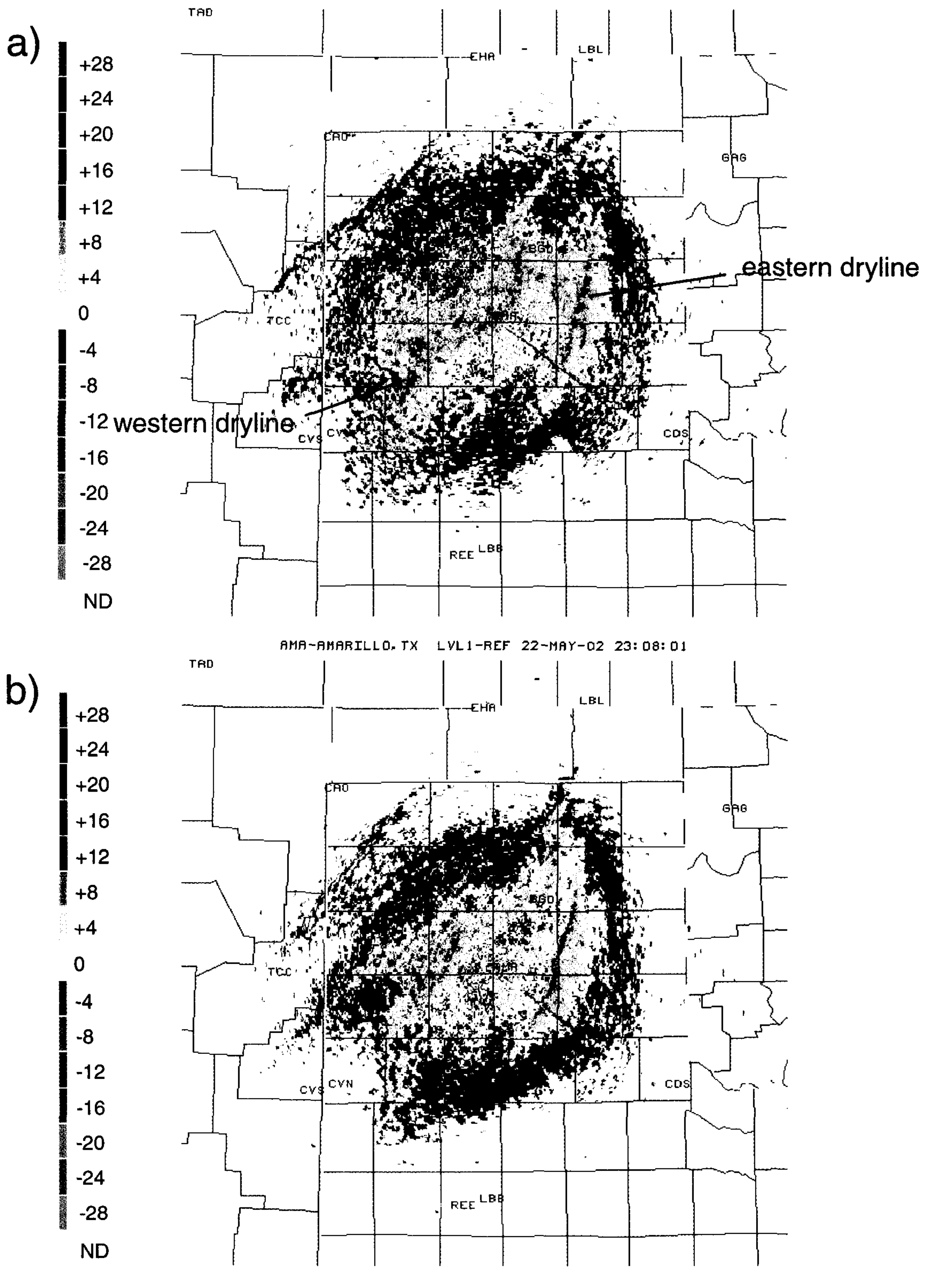

Figure 28 - WSR-88D 0.5 deg base reflectivity at Amarillo, TX valid a) 2308 UTC (22 May 2002) and b) 0007 UTC (23 May 2002). Reflectivity scale (dBZ) provided to the left. The locations of the eastern and western dryline are shown in a)

a)

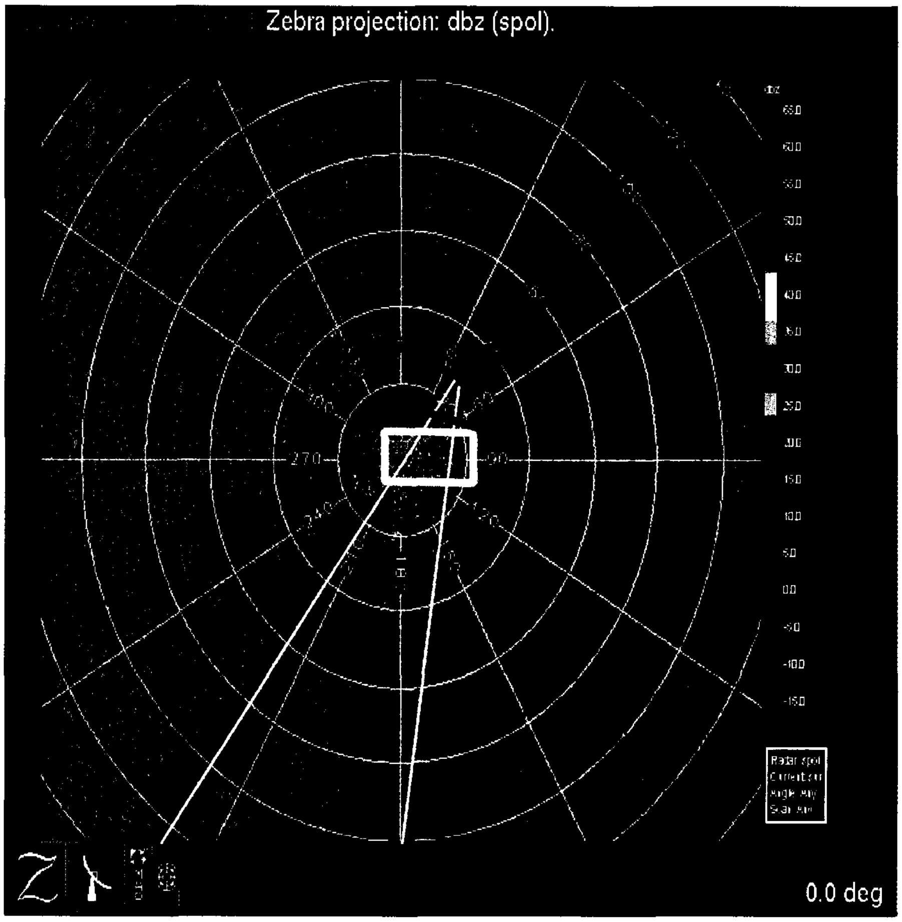

b)

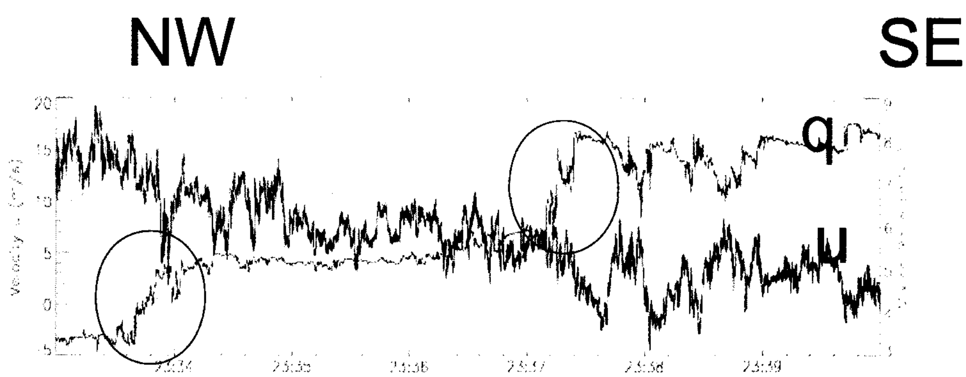

Figure 29 - a) Reflectivity from SPOL (location indicated in Fig. 30). Reflectivity scale (dBZ) indicated to the right. The straight white lines indicate the axes of two separate drylines. The white box represents the domain of operations for the UMass W-band radar. The red line denotes the flight track of the University of Wyoming King Air (UWKA) from 2233-2240 UTC. b) Traces of in-situ specific humidity (g kg^{-1}, magenta trace) and u-component wind (m s^{-1}, black trace) taken aboard the UWKA for the flight leg indicated in a). Time (UTC) is indicated along the bottom axis, scales for u-component wind and specific humidity are indicated on the left and right axes, respectively. The two regions of sharp moisture gradient are circled in green.

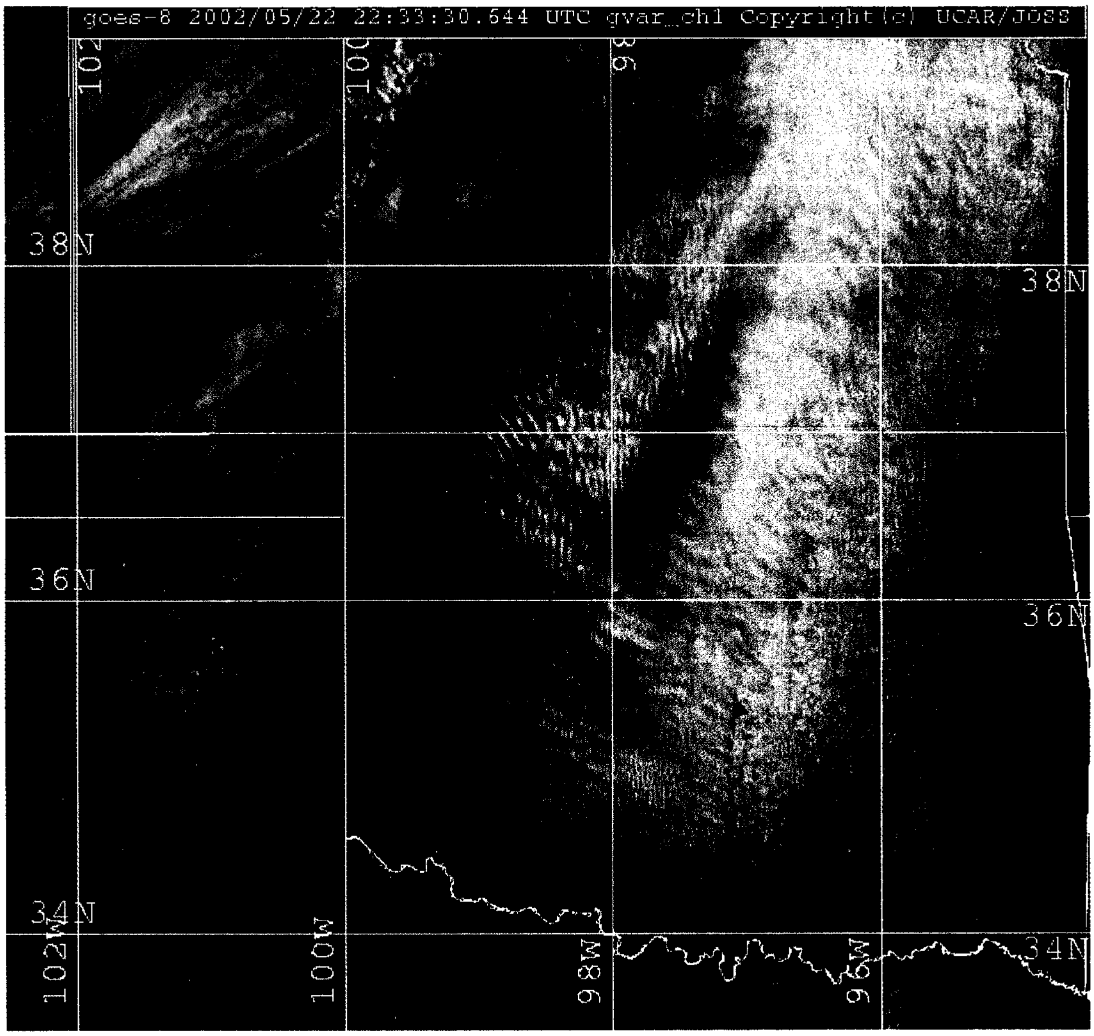

Figure 30 - GOES-8 visible satellite image taken at 2233 UTC on 22 May 2002. Yellow boundaries denote the state borders. The black dot indicates the location of SPOL.

Figure 31 - Photos of the University of Massachusetts W-band radar.

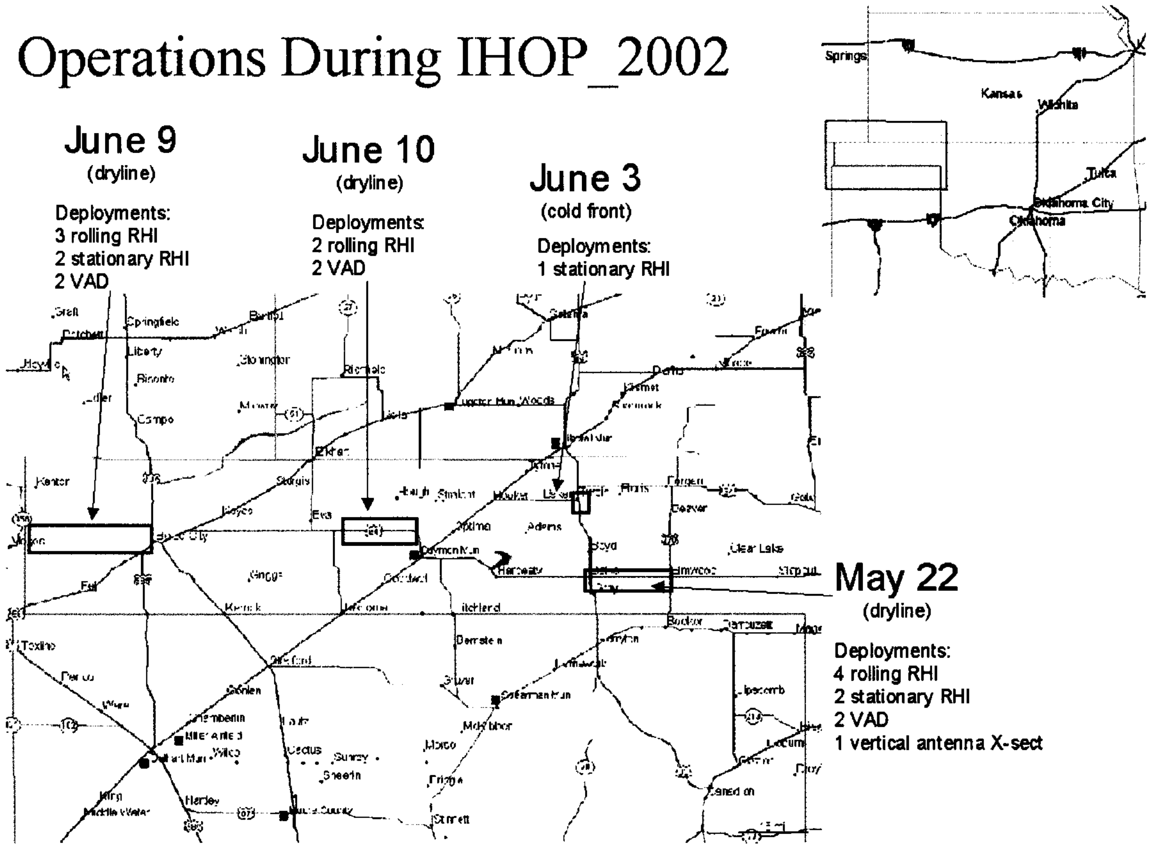

Figure 32 - An overview of IHOP operations days for the UMass radar.

Data Collection Strategies

Mode #1 - VAD

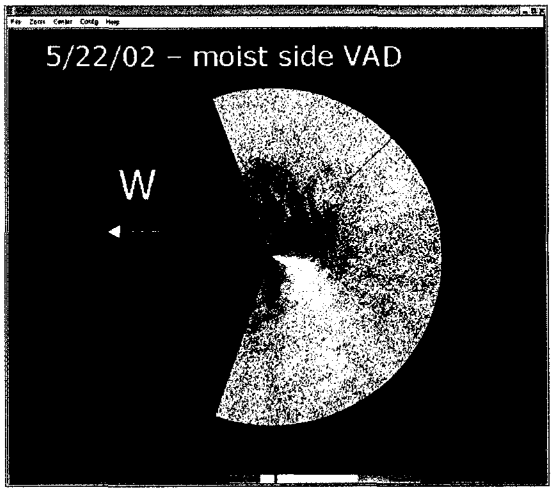

- Synthesize vertical wind profile from elevated sector scan (~ 220 degrees in azimuth, at 45 degrees elevation)
- Six VADs performed during IHOP, three on each side of the dryline.

Figure 33 - Schematic of VAD data collection with an example from 22 May 2002.

Data Collection Strategies

Mode #2 – Vertical Antenna

- Temporal/spatial profile of vertical velocity
- Performed on May 22 dryline

Figure 34 - A schematic of the vertical antenna method of data collection

Data Collection Strategies

Mode #3 – Stationary RHI

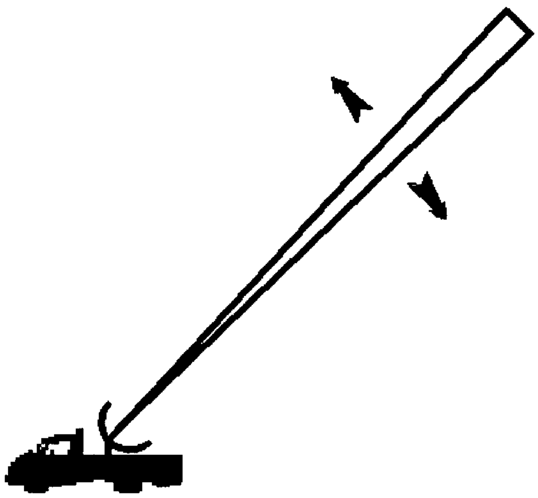

- Five such deployments during IHOP
- Drawback: No V_r decomposition into u/w
- Vertical sectors perpendicular to feature of interest

Figure 35 - Schematic of SRHI mode of data collection

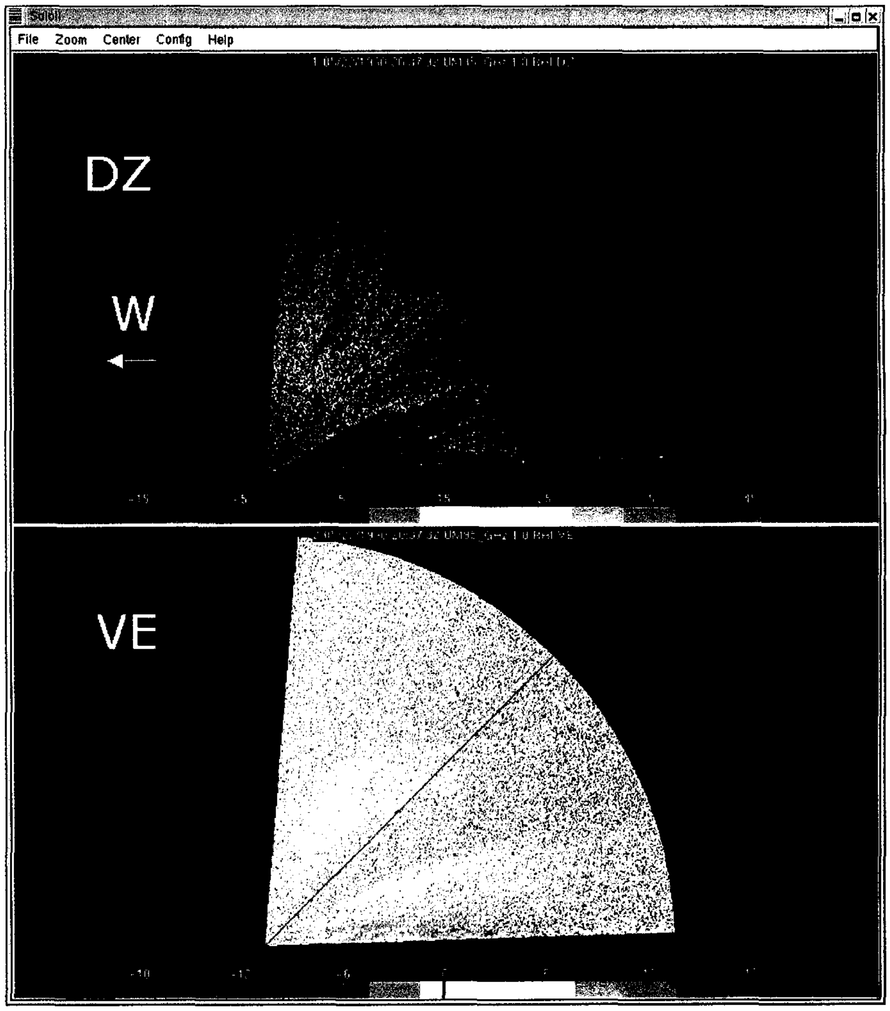

Figure 36 - An example of SRHI data collection from 22 May 2002. Pictured are reflectivity (dBZ_e, top panel) and radial velocity (m s^{-1}, bottom panel) for a retrograding dryline. Radar position is in the bottom left corner of the RHI sector. In the radial velocity panel, greens indicate motion towards the radar (easterly component), and yellows indicate motion away from the radar (westerly component). The motion of the dryline is to the left (west).

Data Collection Strategies
Mode #4 – Rolling RHI

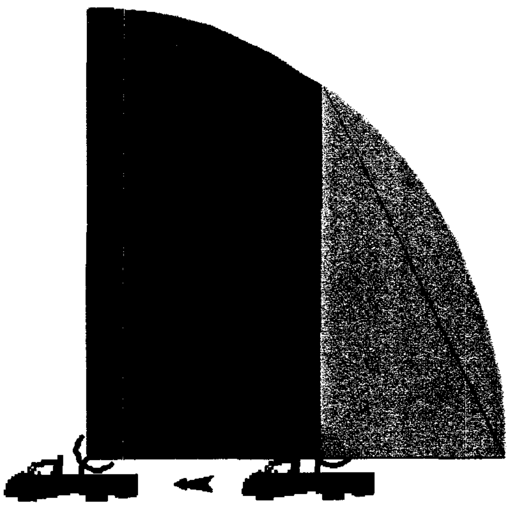

- Nine rolling RHIs during IHOP (all across drylines)
- GPS data critical
- Use pseudo-dual Doppler principles for u/w decomposition in lobe
  but...more complicated than airborne technique.

Figure 37 - Schematic of RRHI method of data collection.

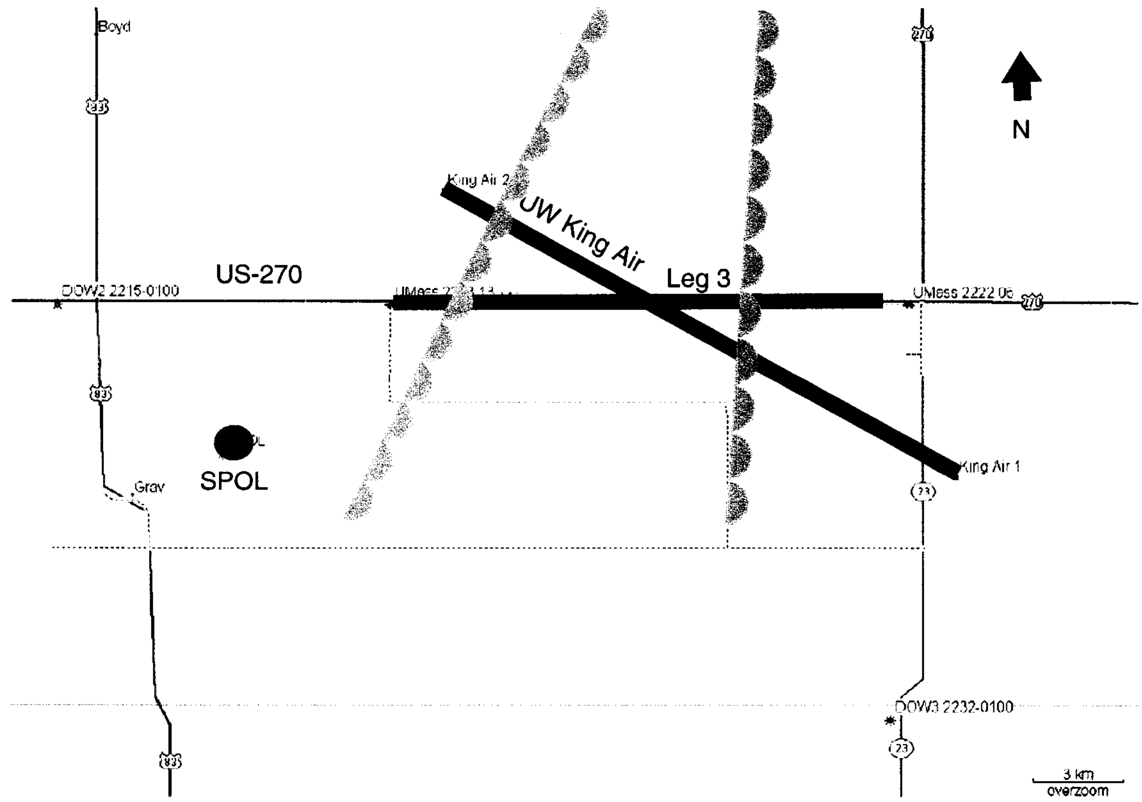

Figure 38 - A map of the leg 3 UMass W-band deployment. Distance scale located in the lower right hand corner. The thick red line denotes the path of the UMass vertical antenna deployment, from right to left (east to west). The thick blue line indicates the path of the UWKA radar from right to left (east-southeast to west-northwest). The scalloped lines indicate the position of known drylines. The red dot labeled (SPOL) denotes the position of the SPOL radar at Homestead, OK.

a)

SR1 0.5 deg
Reflectivity
5/22/02
2254 UTC

UMass Leg 3
(black track)
westward

b)

SR1 0.5 deg
Refractivity
5/22/02
2254 UTC

UMass Leg 3
(black track)
westward

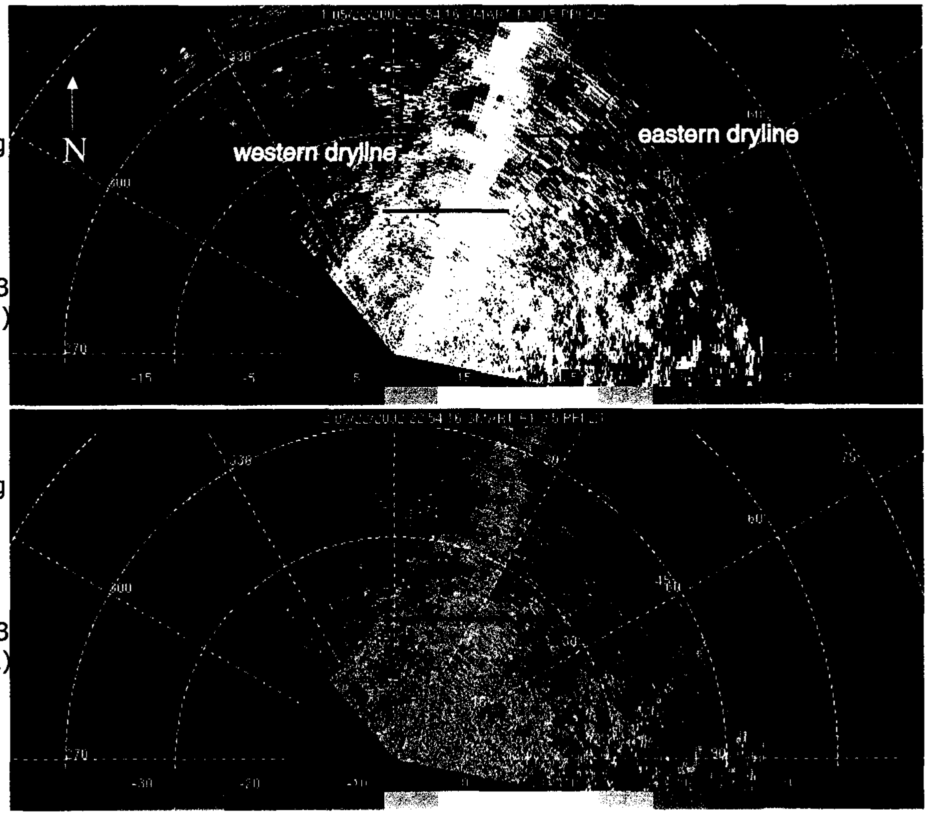

Figure 39 - 0.5 degree a) reflectivity and b) refractivity from the SMART-R at 2254 UTC on 22 May 2002. The black line indicates the path of UMass leg 3 (vertical antenna deployment). Note that these data were taken approximately 20 minutes after the termination of UMass leg 3. The locations of the eastern and western dryline are shown in a).

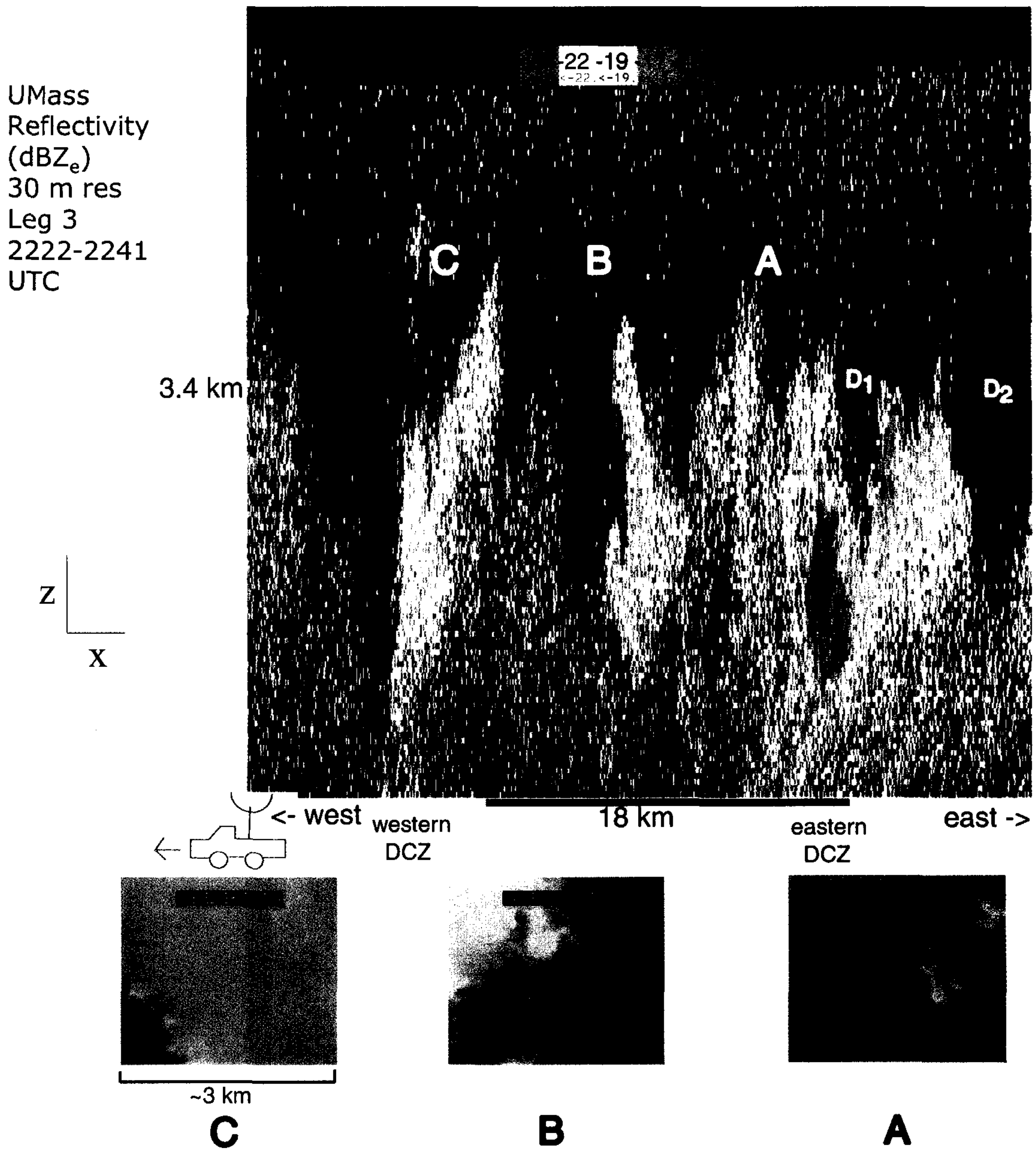

Figure 40 - East-west cross section of reflectivity from the leg 3 vertical antenna deployment. Reflectivity scale (dBZ_e) is shown at the top. 1 km scales for the horizontal and vertical direction are shown in the upper-right hand corner. Domain size is approximately 18 km wide (east-west) by 3.4 km high. Letters "A", "B" and "C" are the locations of cloud cover discussed in the text. The UMass vehicle was in motion towards the west (left). Labels "D_1" and "D_2" are referred to in the text. Images of video from the W-band boresighted video camera are shown. The blue bar at the base of the reflectivity image is the approximate track of the mobile mesonet probe in Fig. 41.

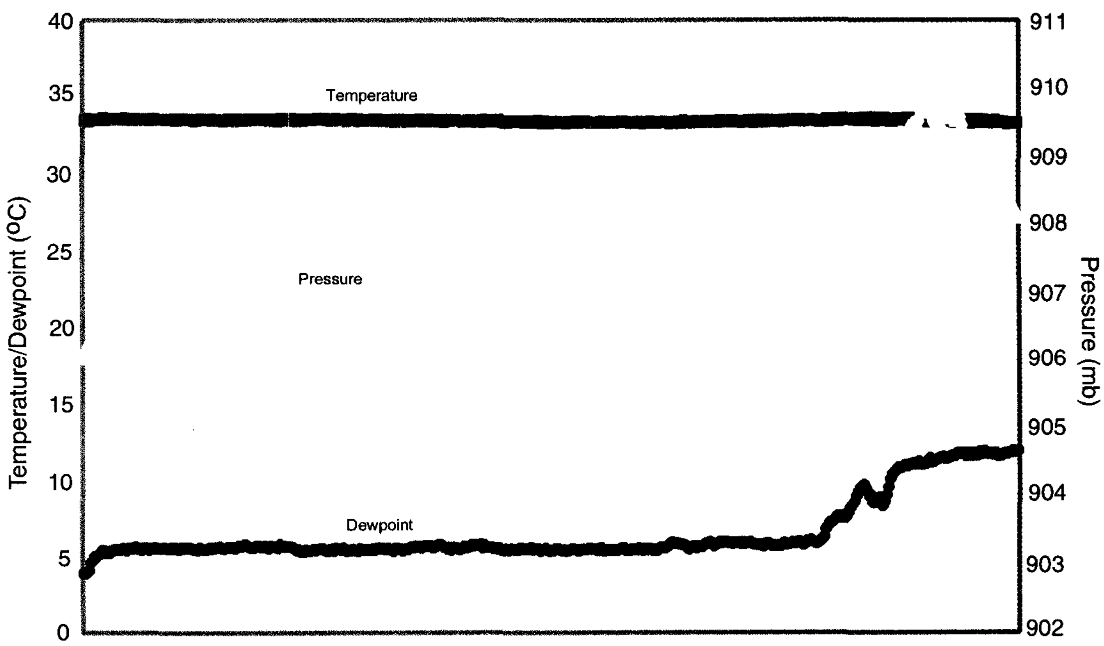

Figure 41 - Temperature, dewpoint (^{o} C, scale on left) and pressure (mb, scale on right) measured by a mobile mesonet probe from 2237-2245 UTC (approximate track denoted by blue line in Fig. 40).

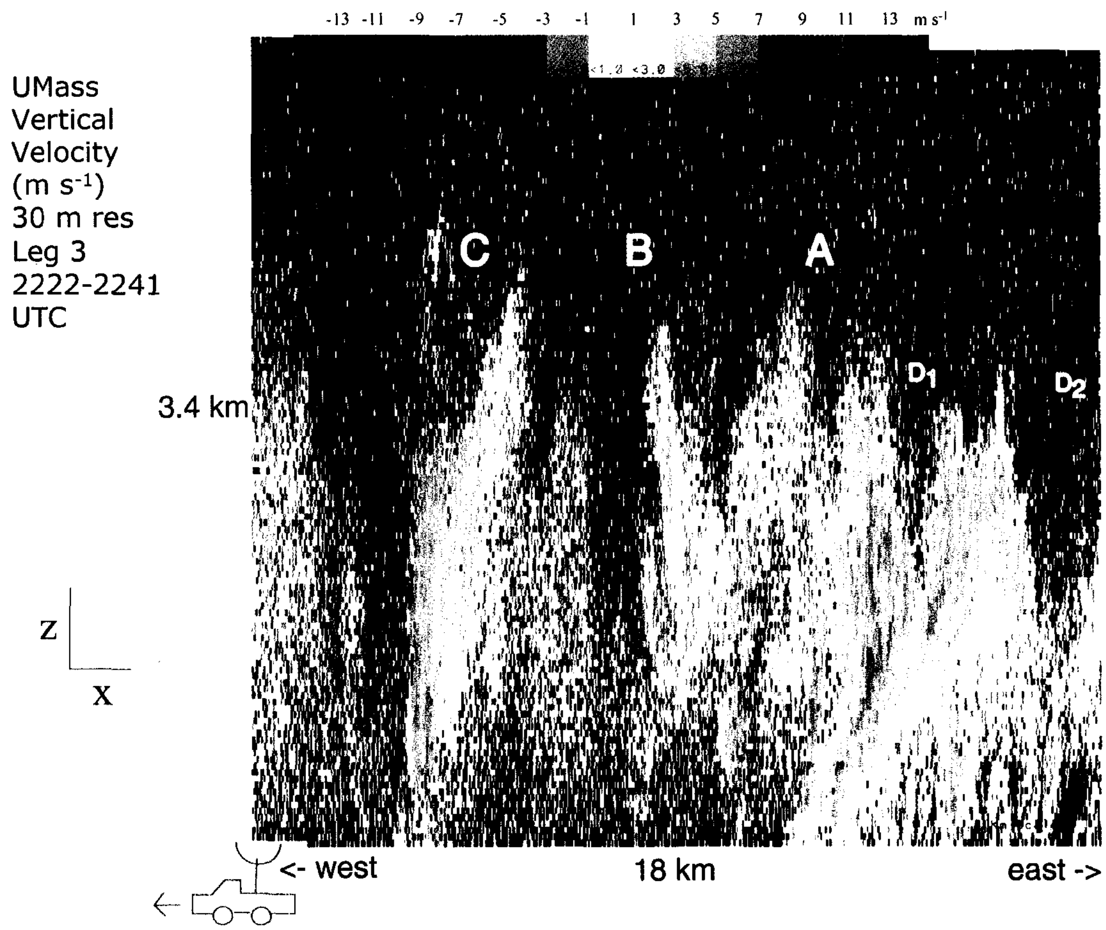

Figure 42 - as in Fig. 40, expect colors denote vertical velocity (m s^{-1}). Orange colors indicate upward motion, green colors indicate downward motion. Velocity scale is indicated at the top. Labels "D_1" and "D_2" are referred to in the text.

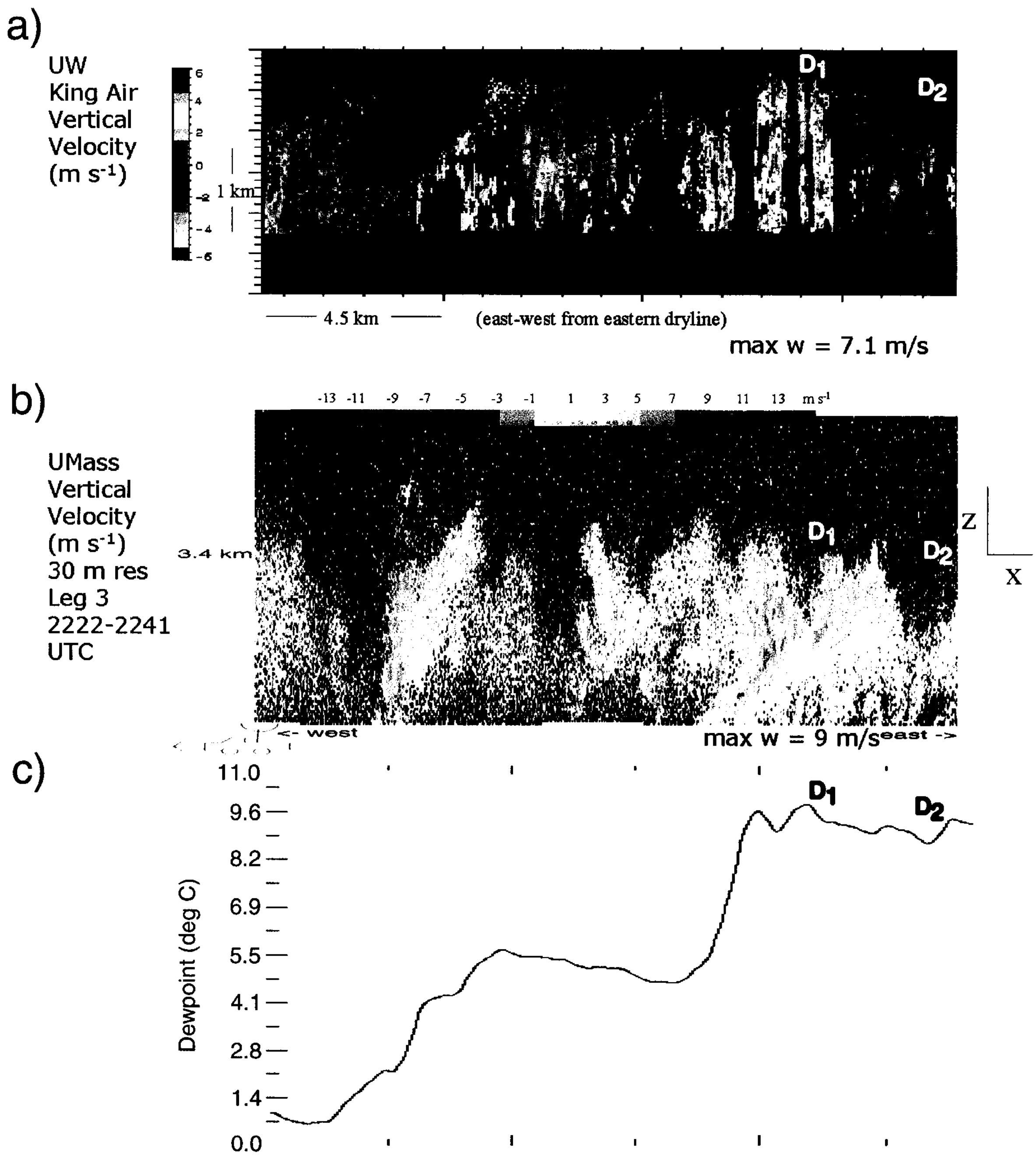

Figure 43 - a) UWKA vertical velocity (m s^{-1}, scale to left) from 2218-2224 UTC. b) UMass W-band vertical velocity as in Fig. 42. c) Trace of in-situ dewpoint measurements aboard the UWKA (deg C, scale indicated to left). All three images represent approximately the same distance east-west from the primary (eastern) dryline. Labels "D_1" and "D_2" are referred to in the text.

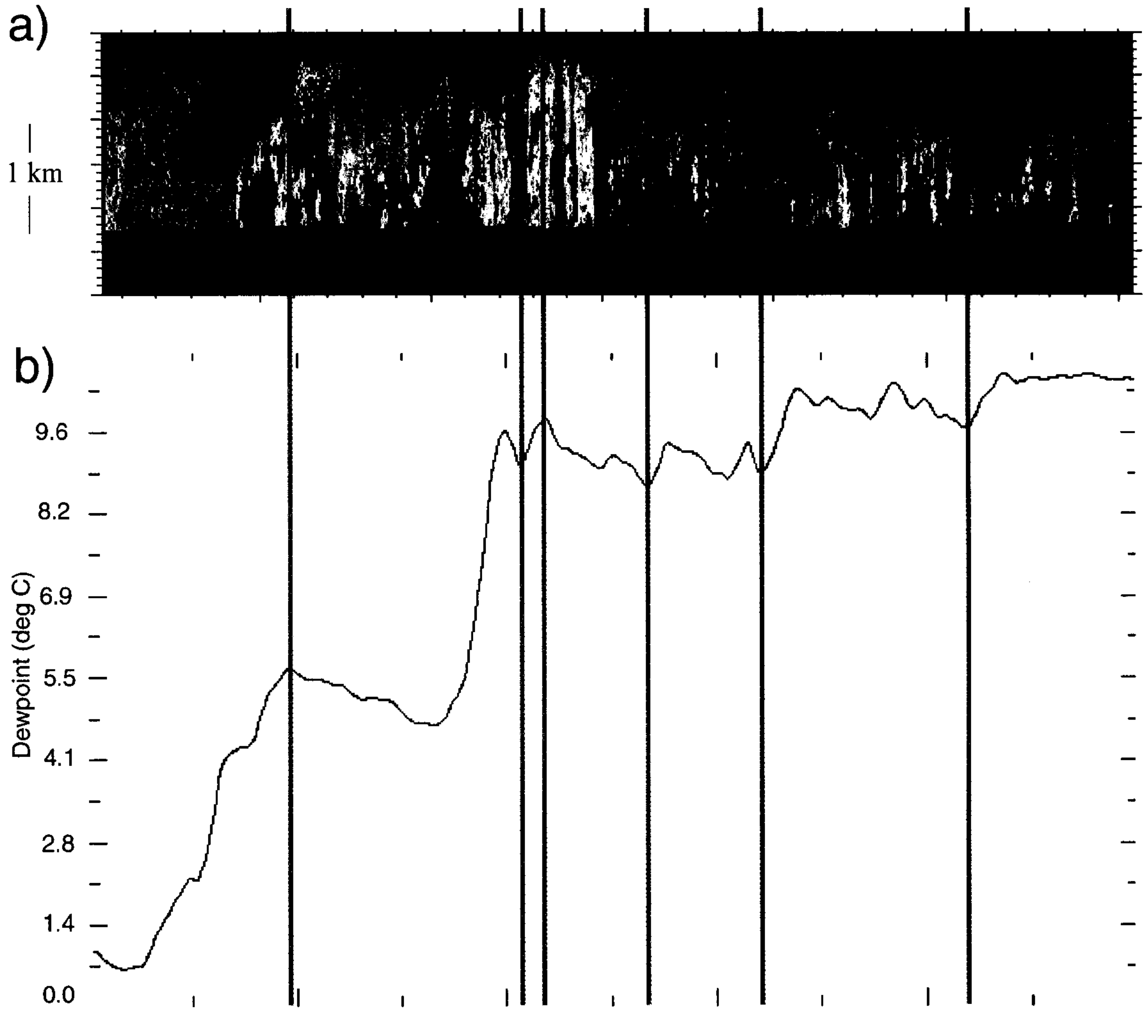

Figure 44 - a) UWKA vertical velocity (m s^{-1}, scale to left) from 2218-2224 UTC b) Trace of in-situ dewpoint measurements aboard the UWKA (^{o}C, scale indicated to left). The domain is wider than that of Fig. 43 (the full length of the UWKA track). The red lines are included as an aid to correlate the UWKA vertical velocity and dewpoint measurements.

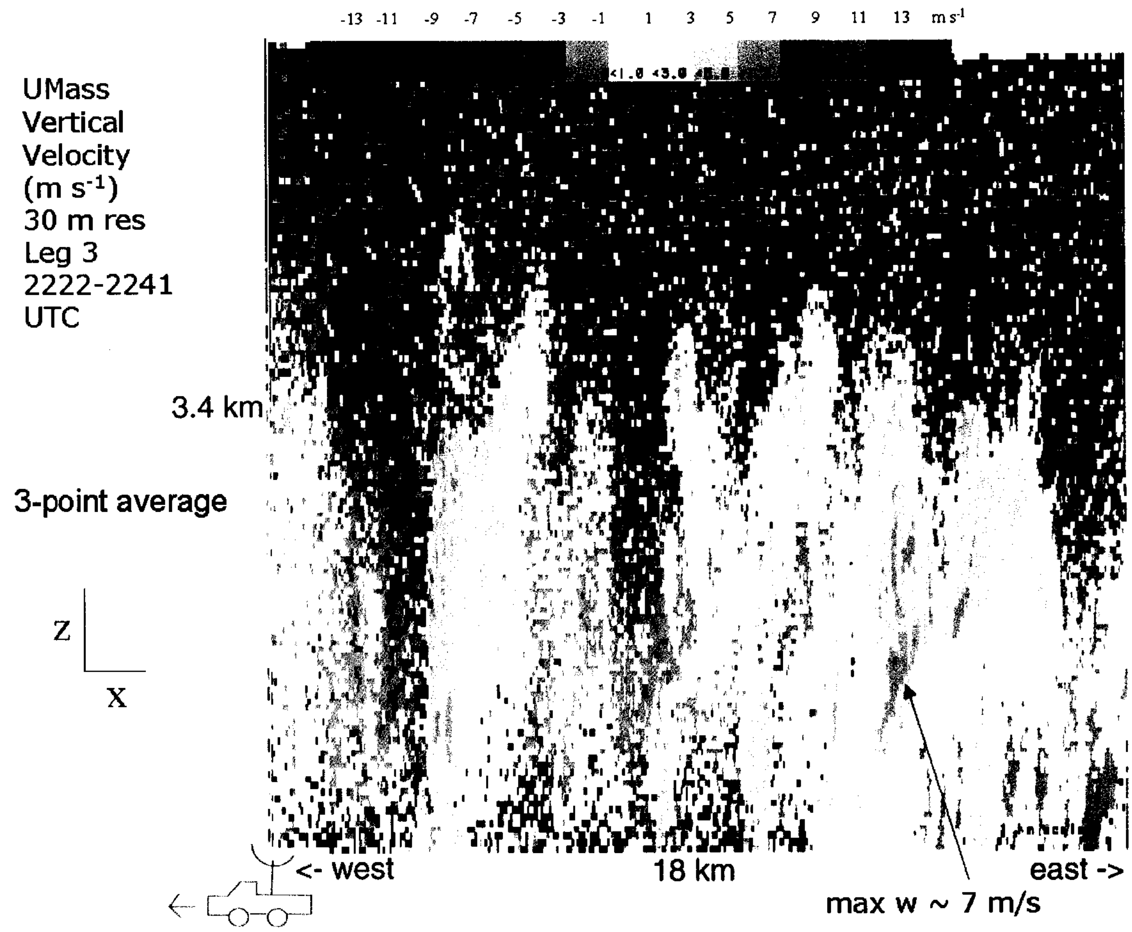

Figure 45 - as in Fig. 42, except with a three-point running average applied.

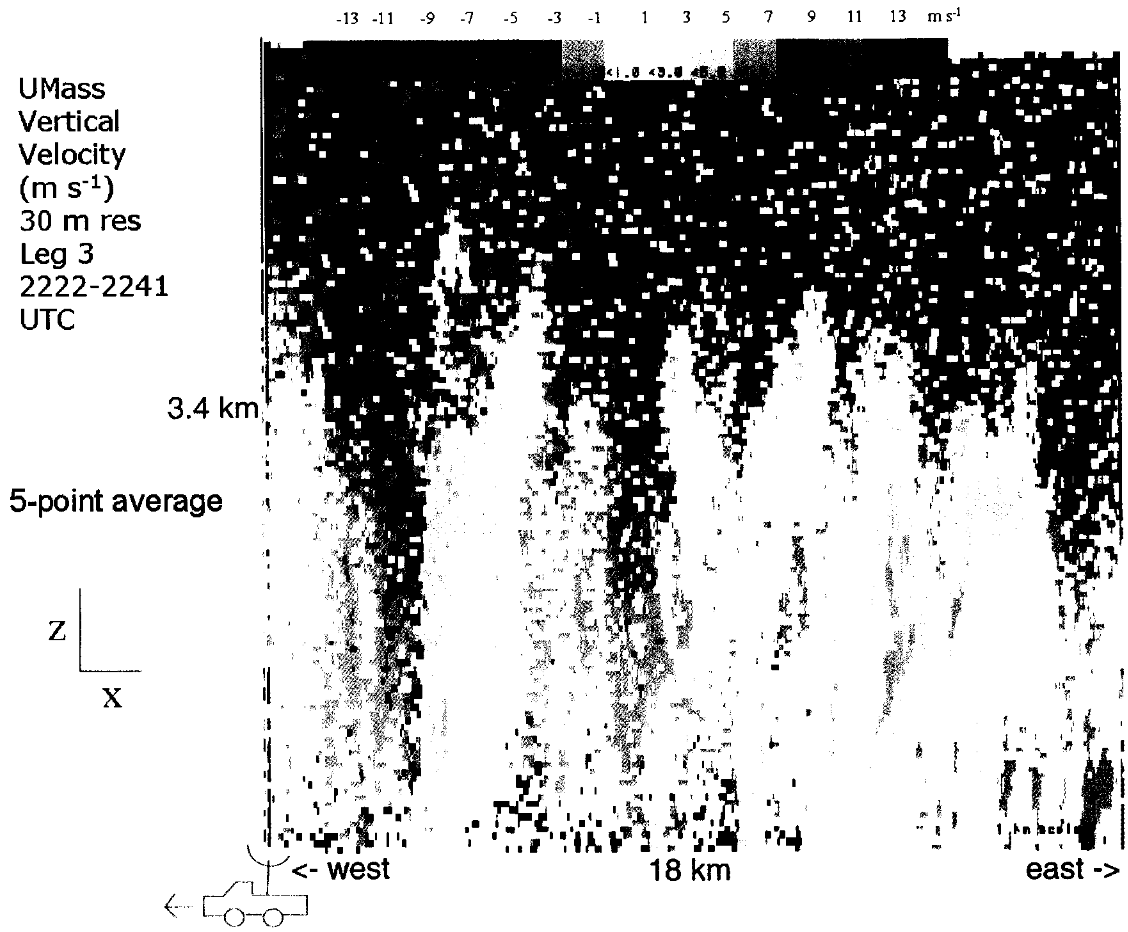

Figure 46 - as in Fig. 42, except with a five-point running average applied.

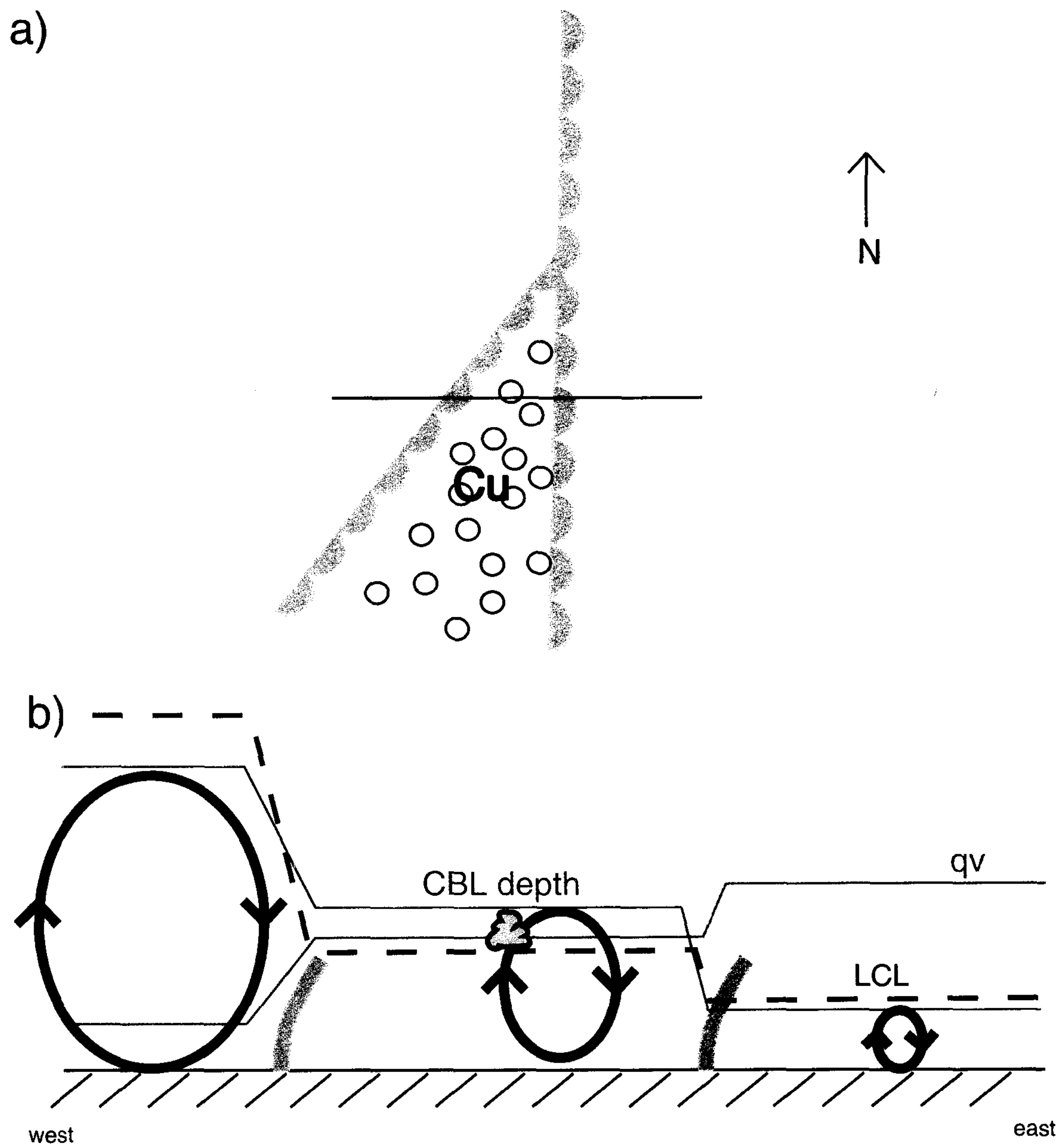

Figure 47 - A a) plan-view and b) east-west cross-section schematic of "wedge sector" cumulus. Circles in a) denote boundary layer convection. In b), the "qv" and "CBL depth" traces indicate the surface specific humidity and convective boundary layer depth, respectively. The dashed line denotes the location of the LCL.

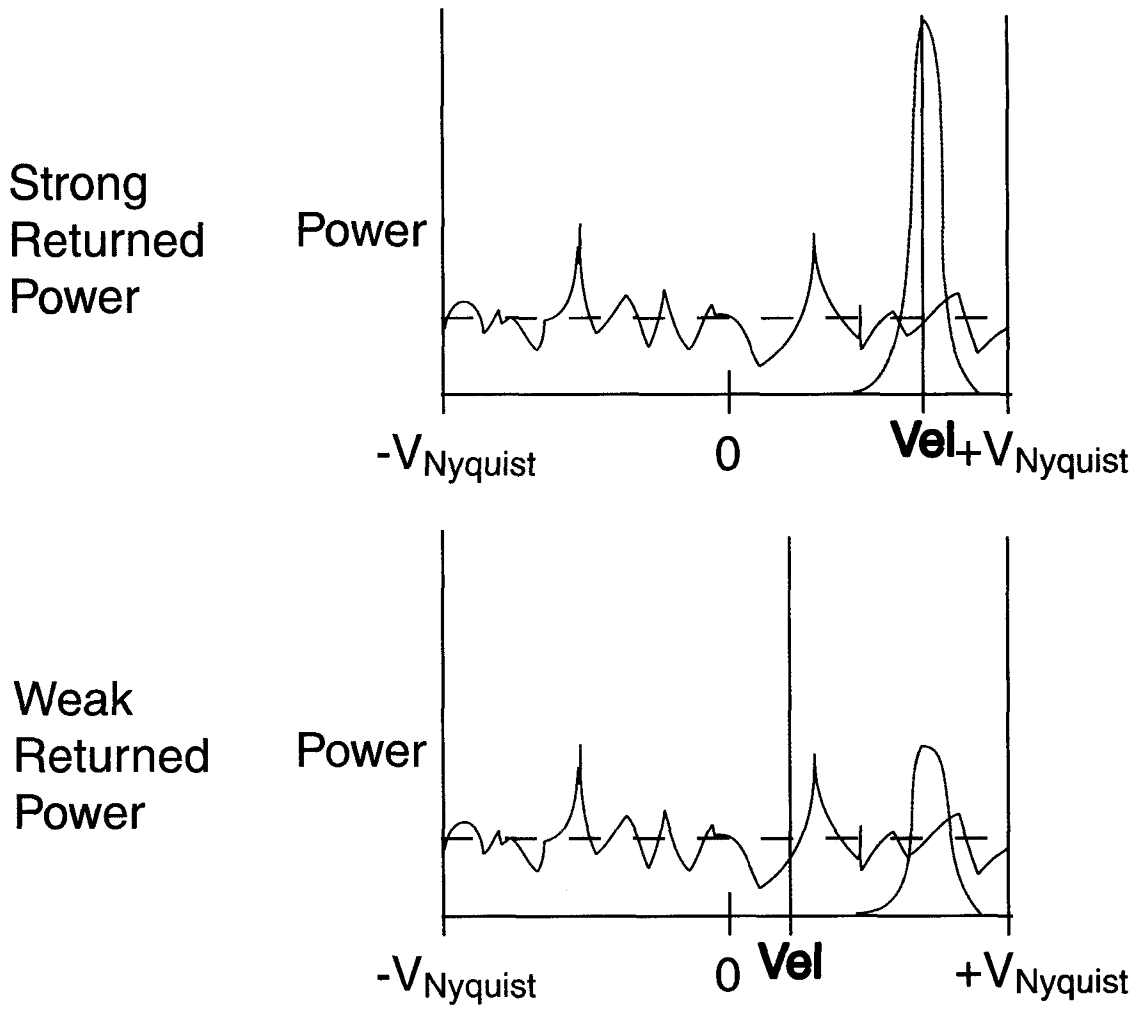

Figure 48 - Schematic of velocity assignment in strong- and weak-returned power cases. The red trace denotes spectral power attributed to radar noise. The green trace indicates the spectral power of the true target velocity. The blue line identifies the assigned velocity using a power-weighted mean.

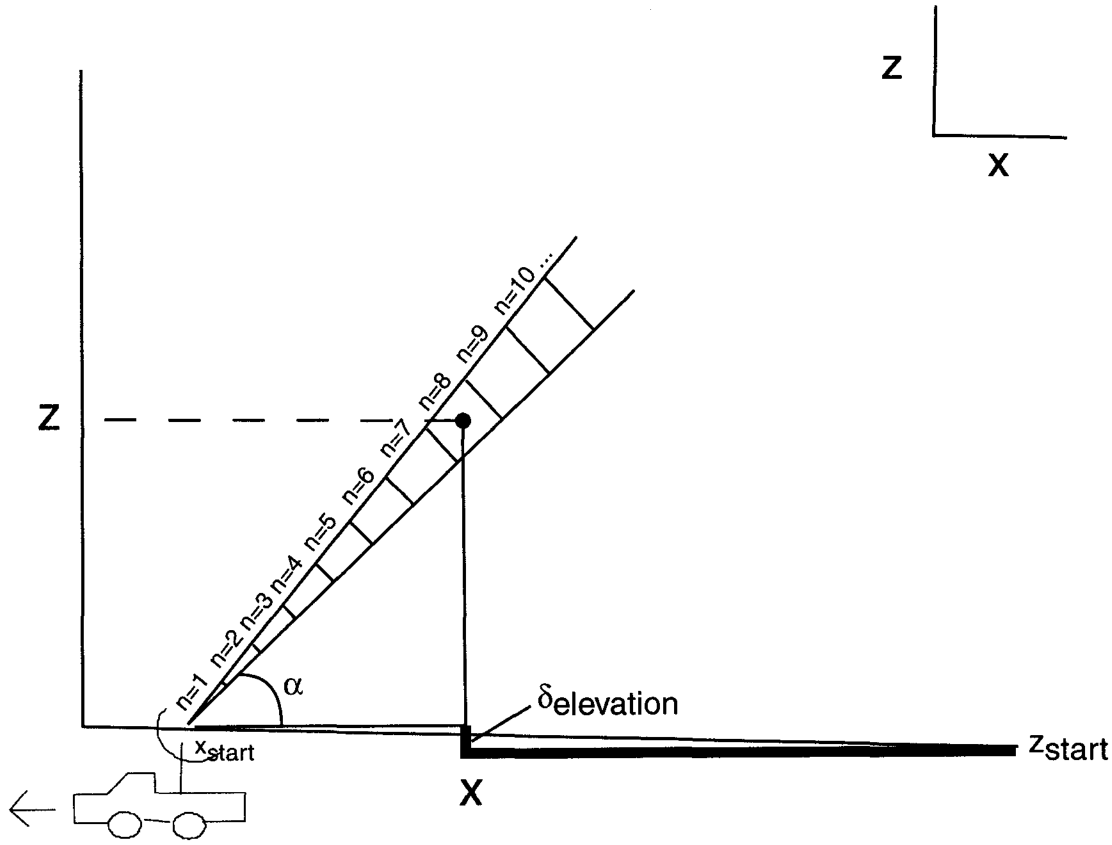

Figure 49 - A schematic illustrating the assignment of radial velocity observations to gridpoints in the domain (see equations (18) and (19) in the text).

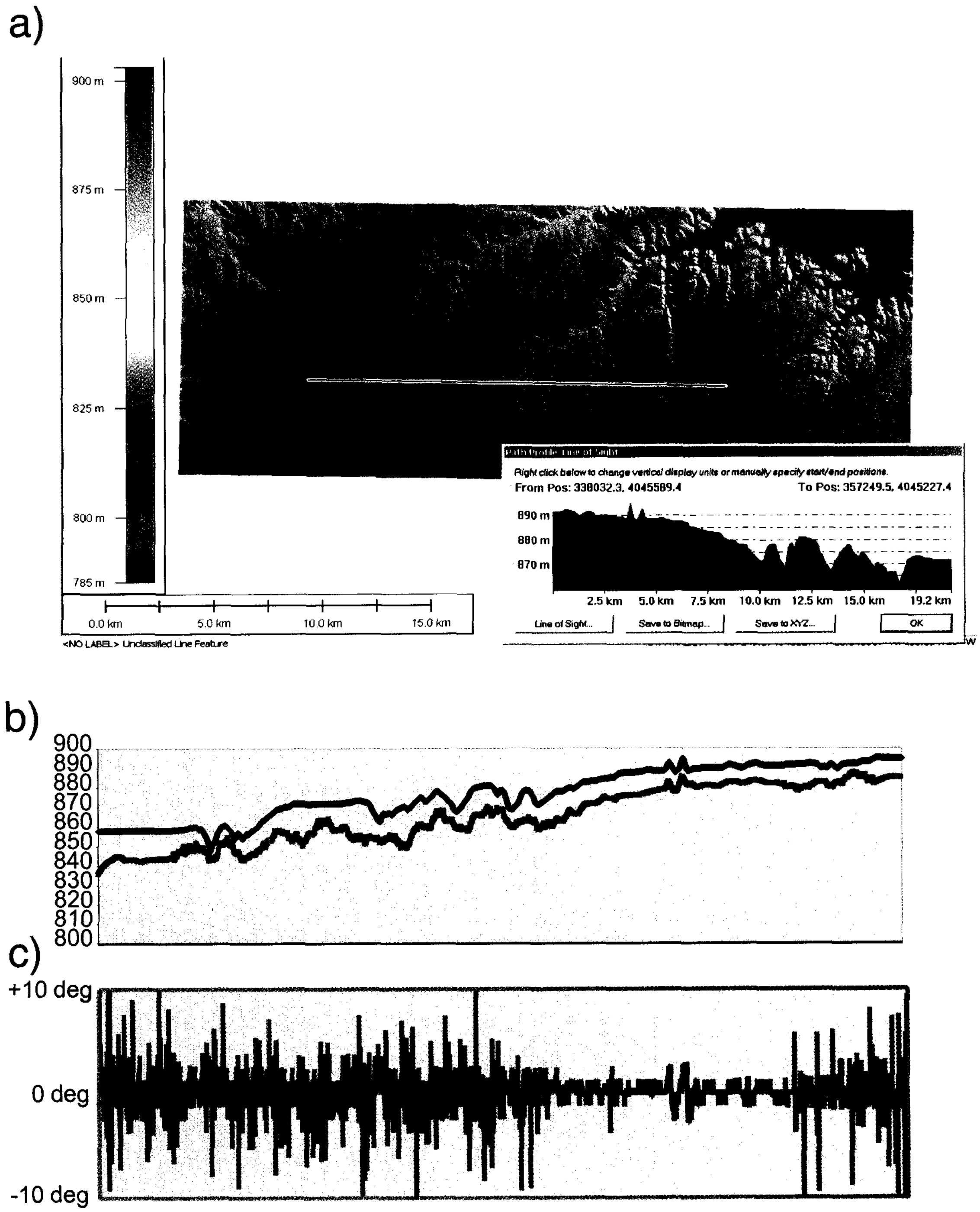

Figure 50 - a) Screen image of digital elevation model (DEM) data (30 m resolution) for UMass leg 6 (yellow line). A cross-section of terrain elevation is indicated in the lower right hand corner. b) Traces of elevation (m MSL, scale to left) from GPS (magenta line) and the DEM (blue line). c) Traces of pitch (degrees, scale to left) calculated from GPS (magenta line) and the DEM (blue line).

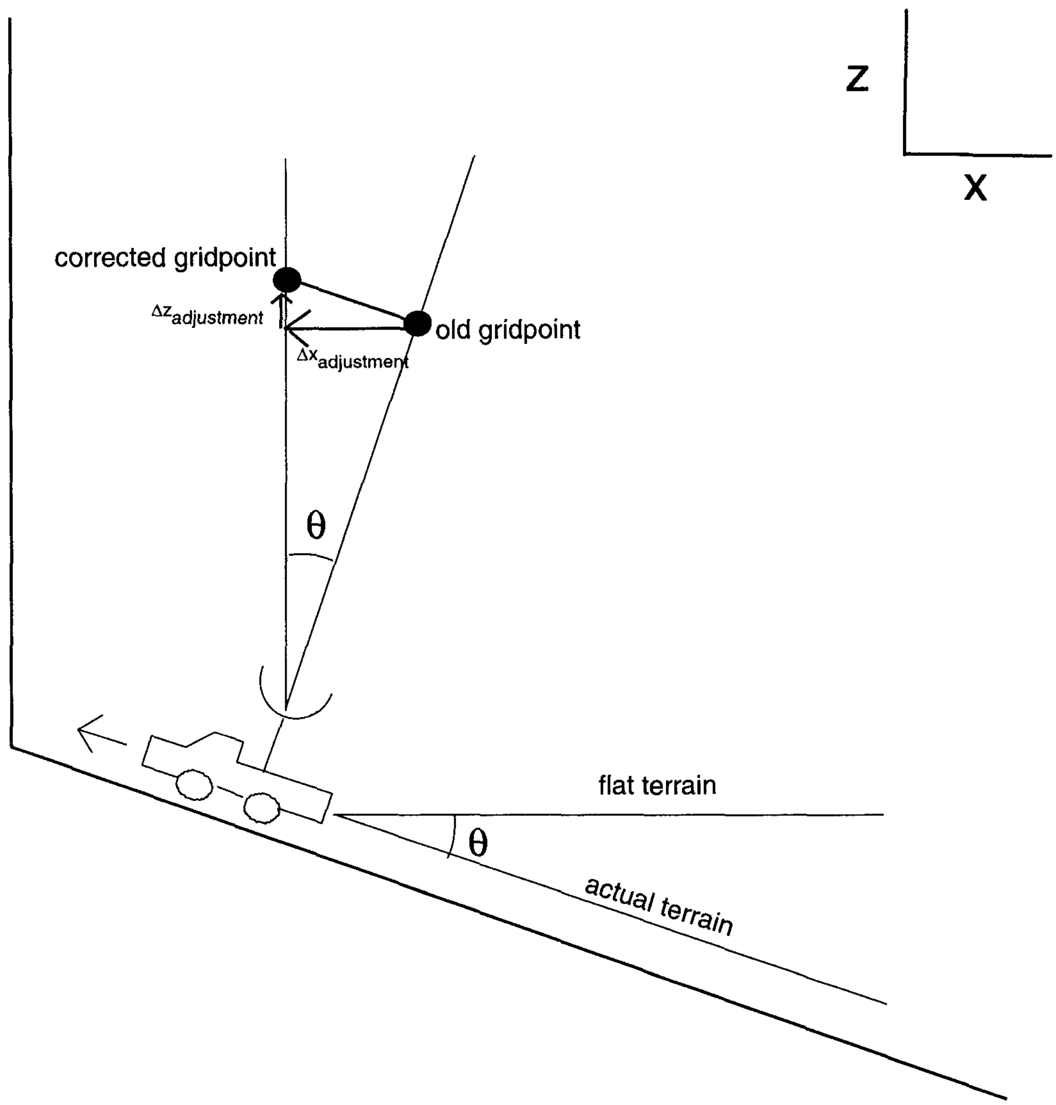

Figure 51 - A schematic illustrating the slope correction described in equations (21a) and (21b) in the text.

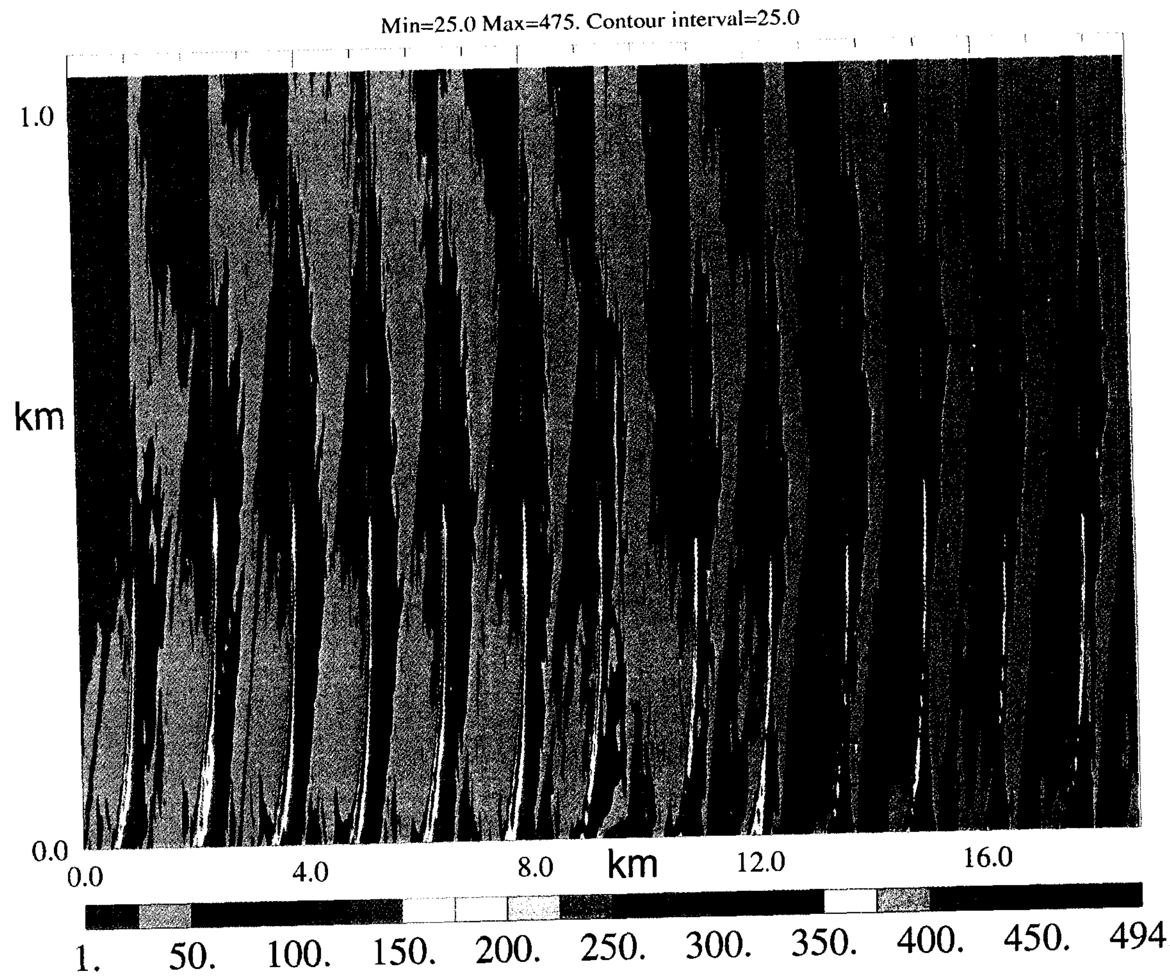

Figure 52 - An example of a look count composite, from UMass leg 6 (0007-0036 UTC). The scale is indicated at the bottom of the figure.

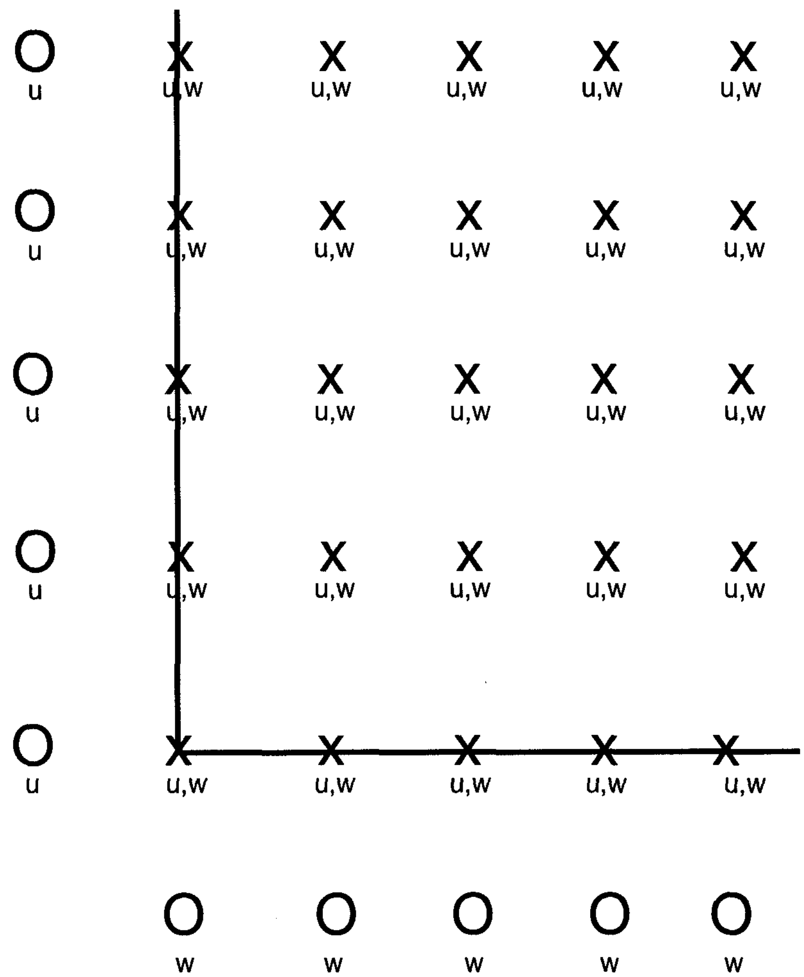

Figure 53 - A schematic of exterior gridpoints ("O"s) used in the update of boundary conditions. The lines indicate the physical edge of the domain boundary. The "X"s denote gridpoints contained within the domain. The variable values stored at each gridpoint (u and/or w) are indicated below the gridpoint.

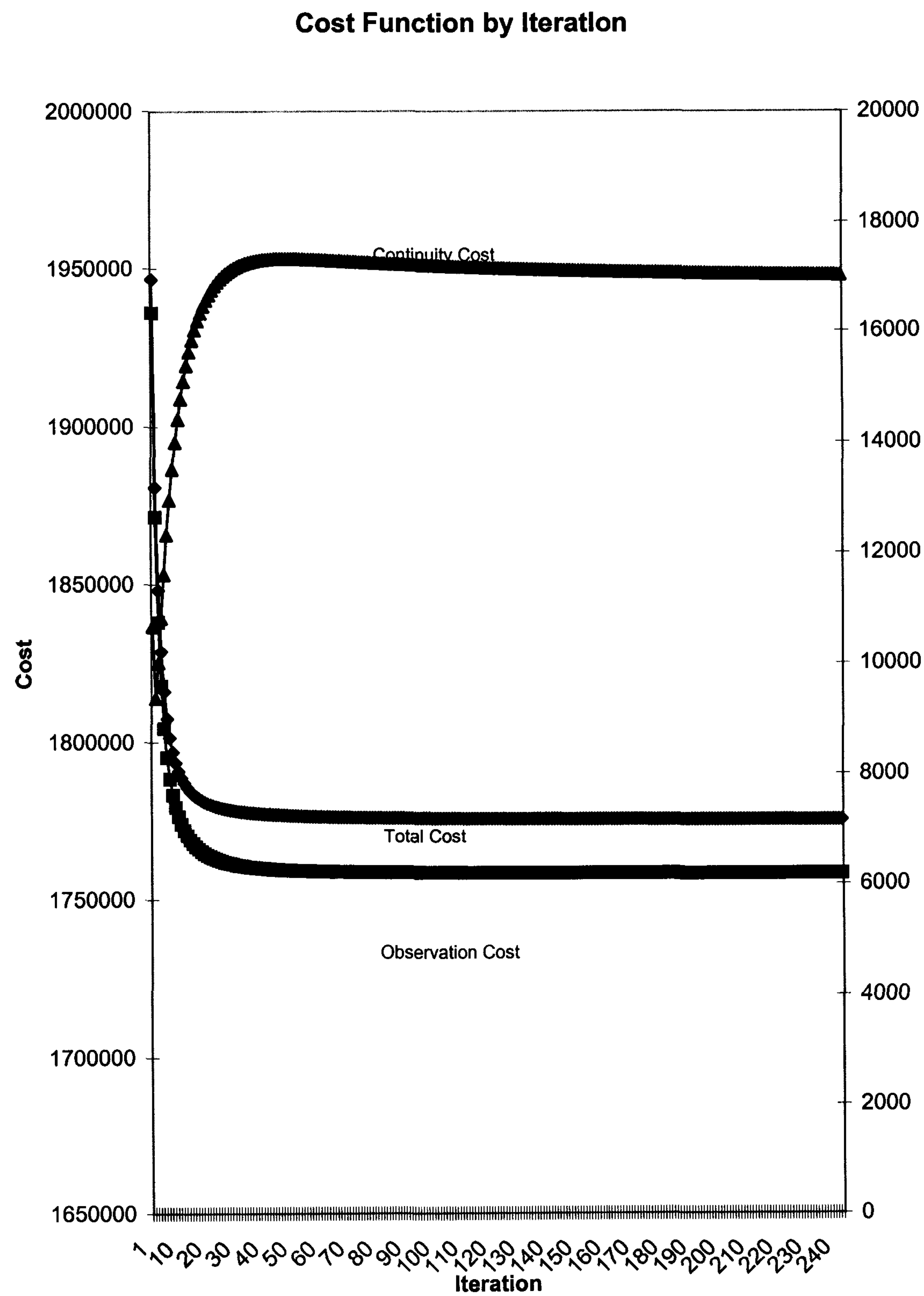

Figure 54 - Contributions to the cost function from observations (left scale) and mass continuity (right scale) by iteration. The total cost function (left scale) is also indicated.

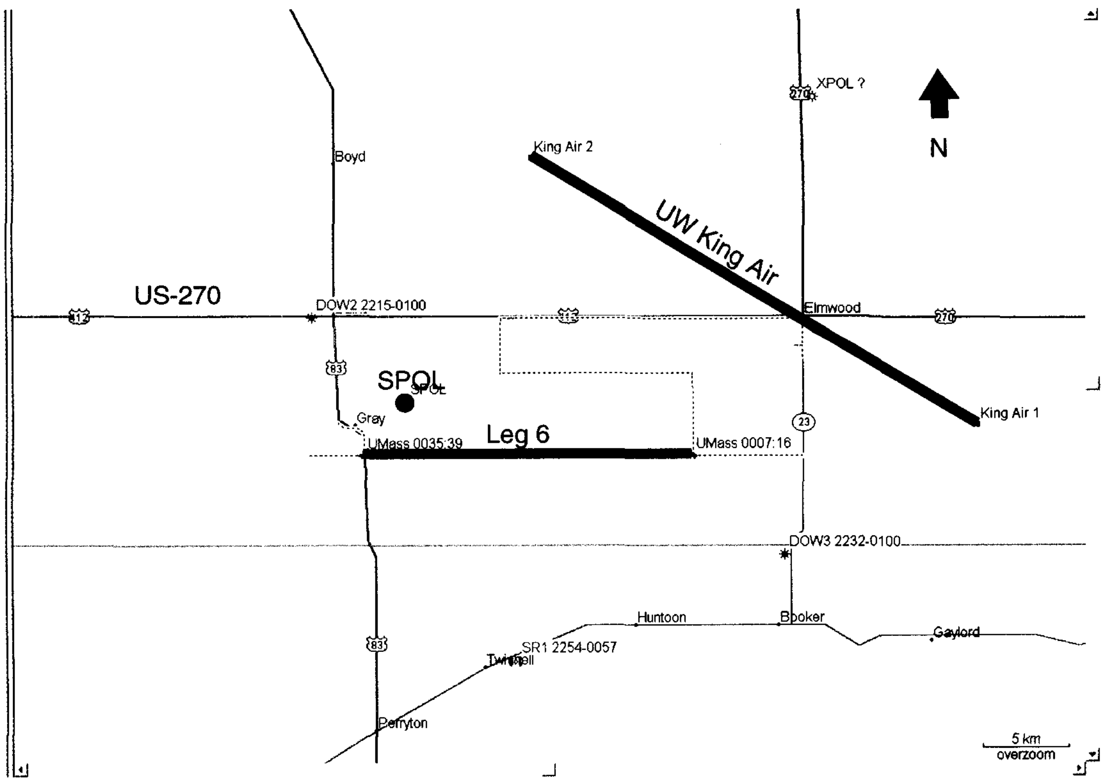

Figure 55 - A map of the leg 6 UMass W-band deployment (2007-2036 UTC). Distance scale located in the lower right hand corner. The thick red line denotes the path of the UMass rolling RHI deployment, from right to left (east to west). The thick blue line indicates the path of the UWKA radar (2345-2351 UTC) from right to left (east-southeast to west-northwest). The red dot labeled (SPOL) denotes the position of the SPOL radar at Homestead, OK.

a)

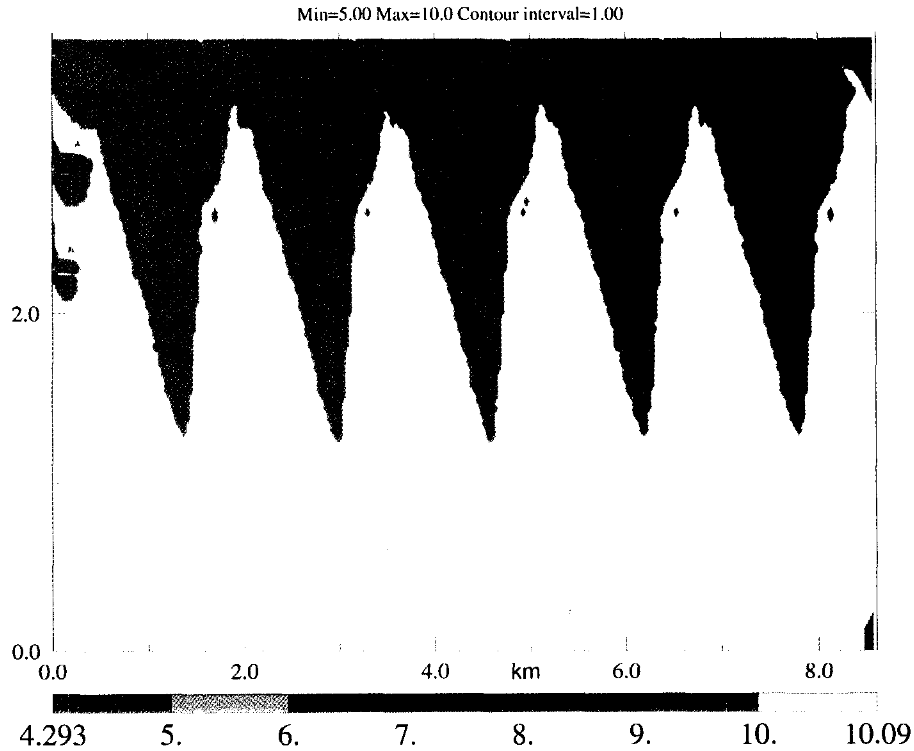

b)

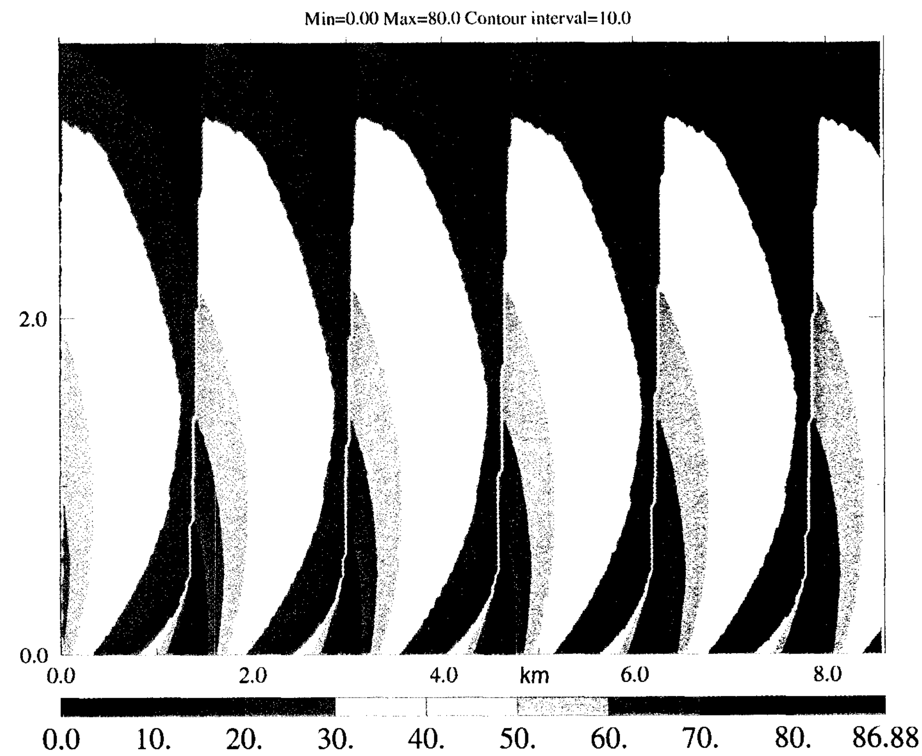

Figure 56 - a) Analysis *u*-component wind (m s^{-1}) and b) maximum look angle difference (deg) for the constant flow (u=10 m s^{-1}) OSSE with a truck velocity of 30 MPH and scan rate of 1.6 deg s^{-1}.

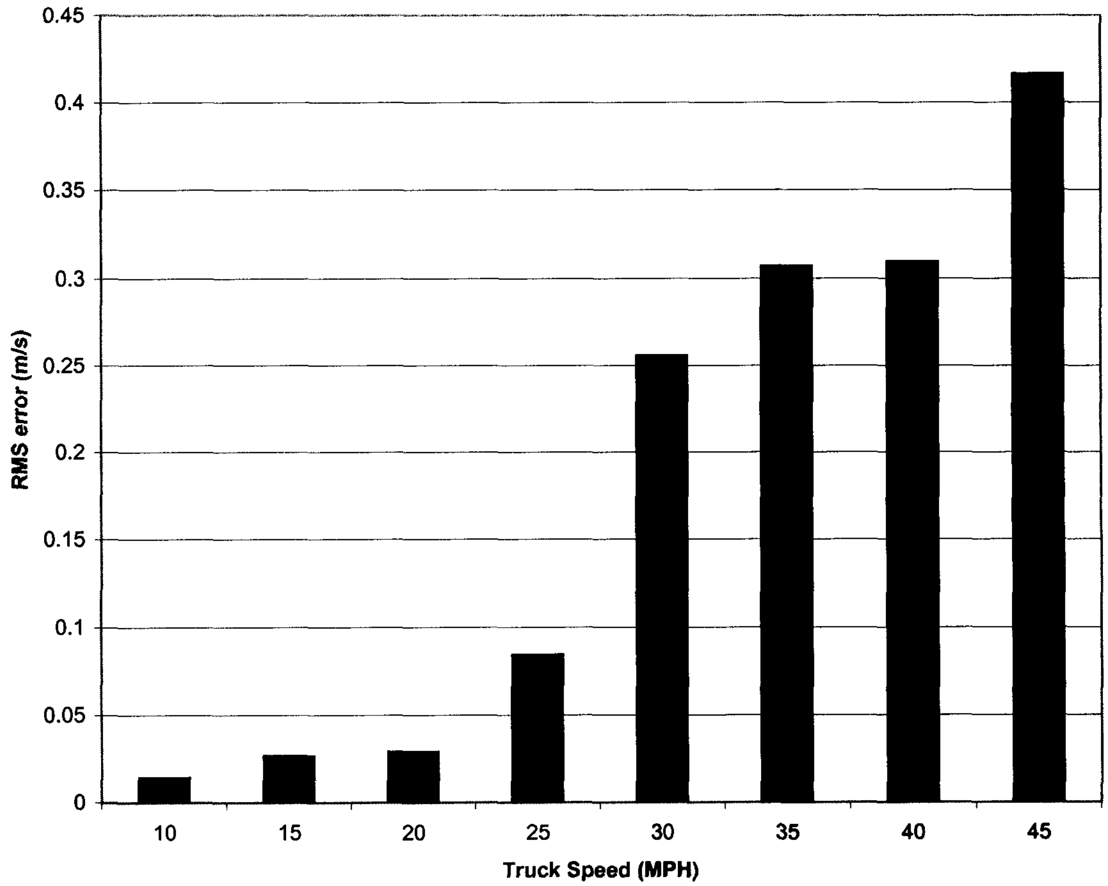

Figure 57 - Analytic constant flow OSSE RMS error (m s^{-1}) as a function of platform velocity (mph) for a fixed scan rate of 2.0 deg s^{-1}

a)

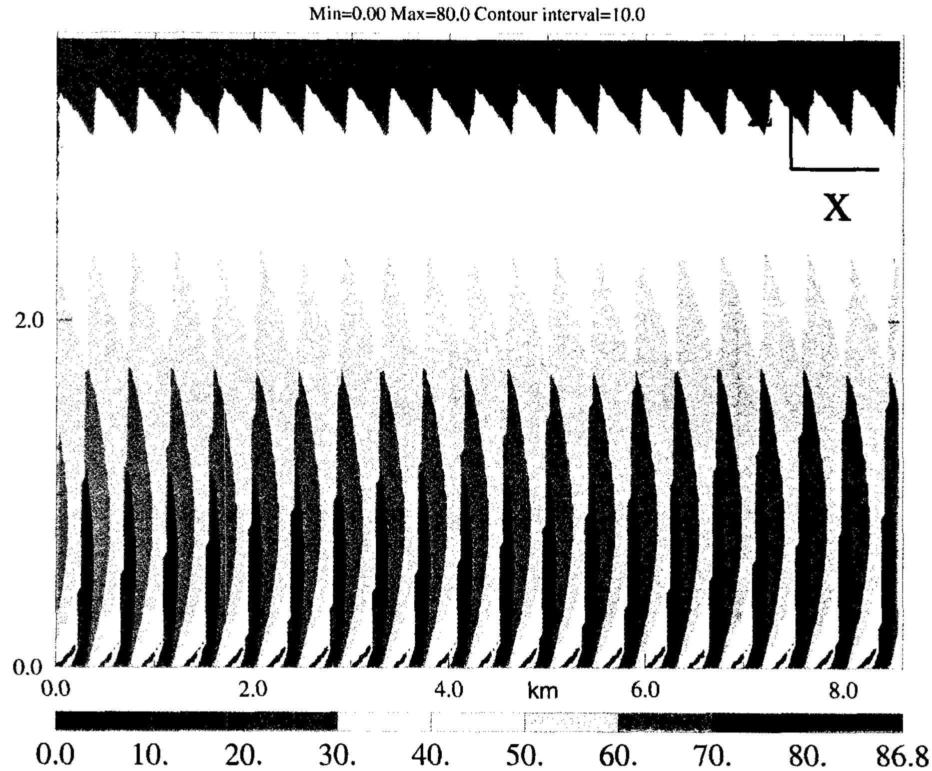

b)

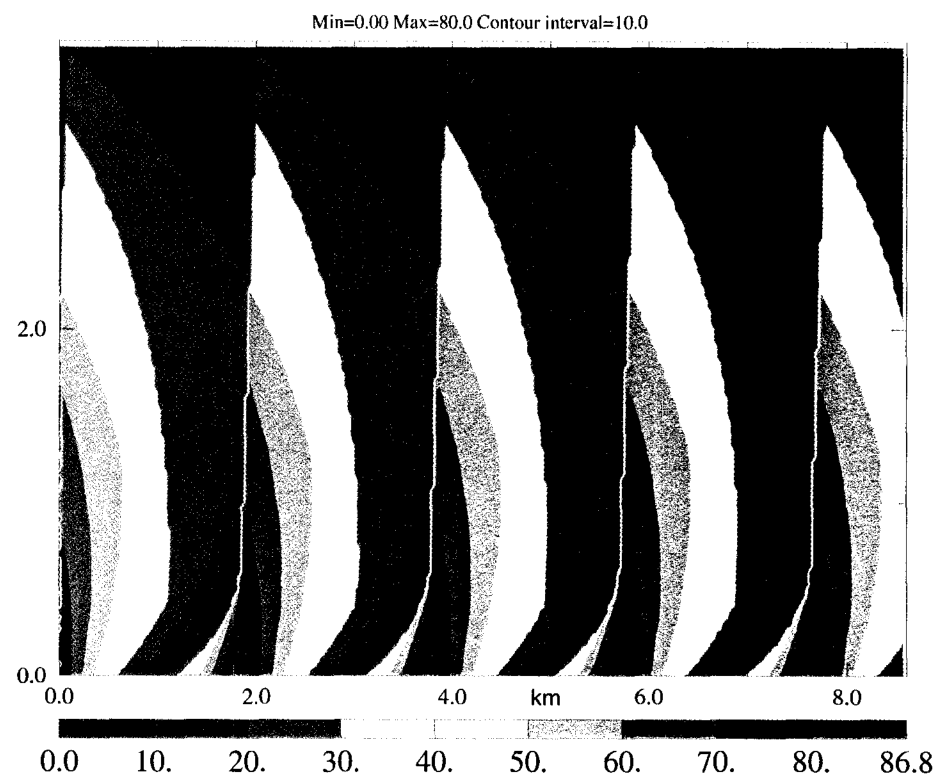

Figure 58 - Constant flow OSSE maximum look angle for a scan rate of 2.0 deg s^{-1} and a platform velocity of a) 10 mph (4.44 m s^{-1}) and b) 45 mph (20.0 m s^{-1}). The scales are indicated at the bottom of each figure. The truck is in motion from right to left. Horizontal and vertical distance scales are included.

a)

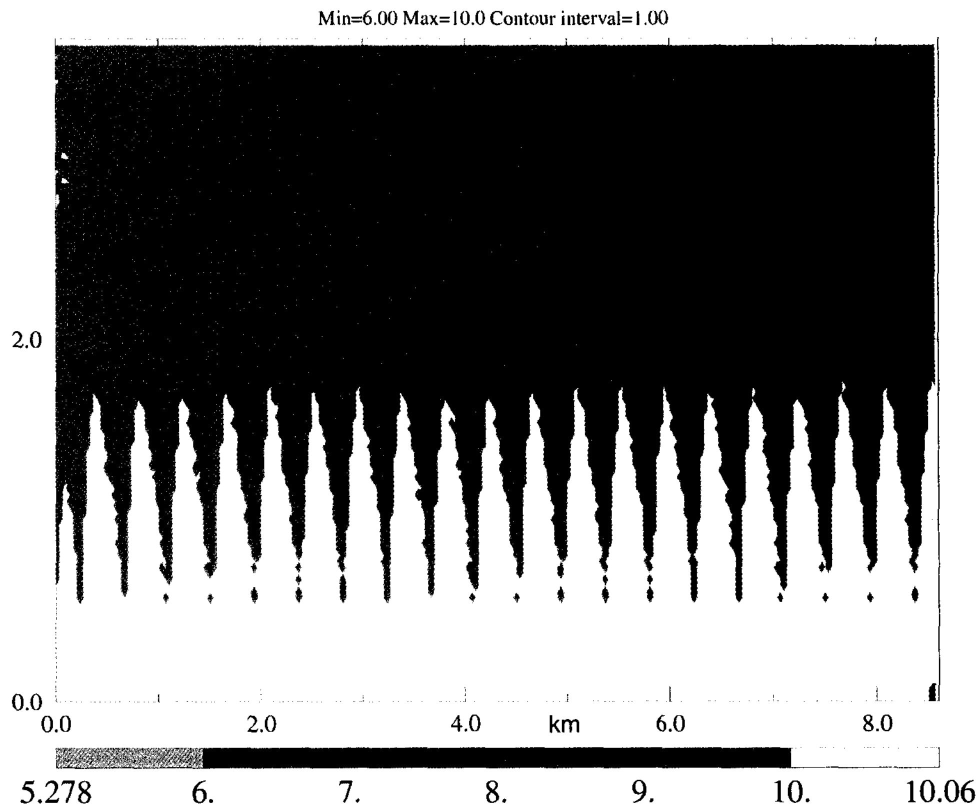

b)

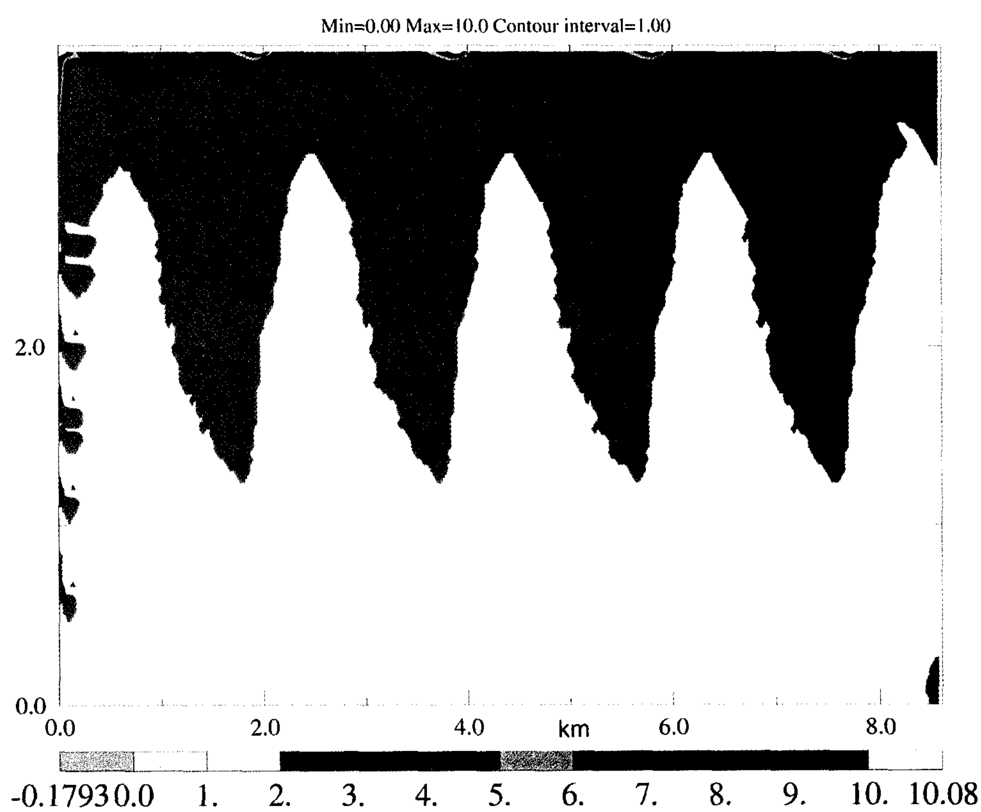

Figure 59 - As in Fig. 58, for the *u*-component wind.

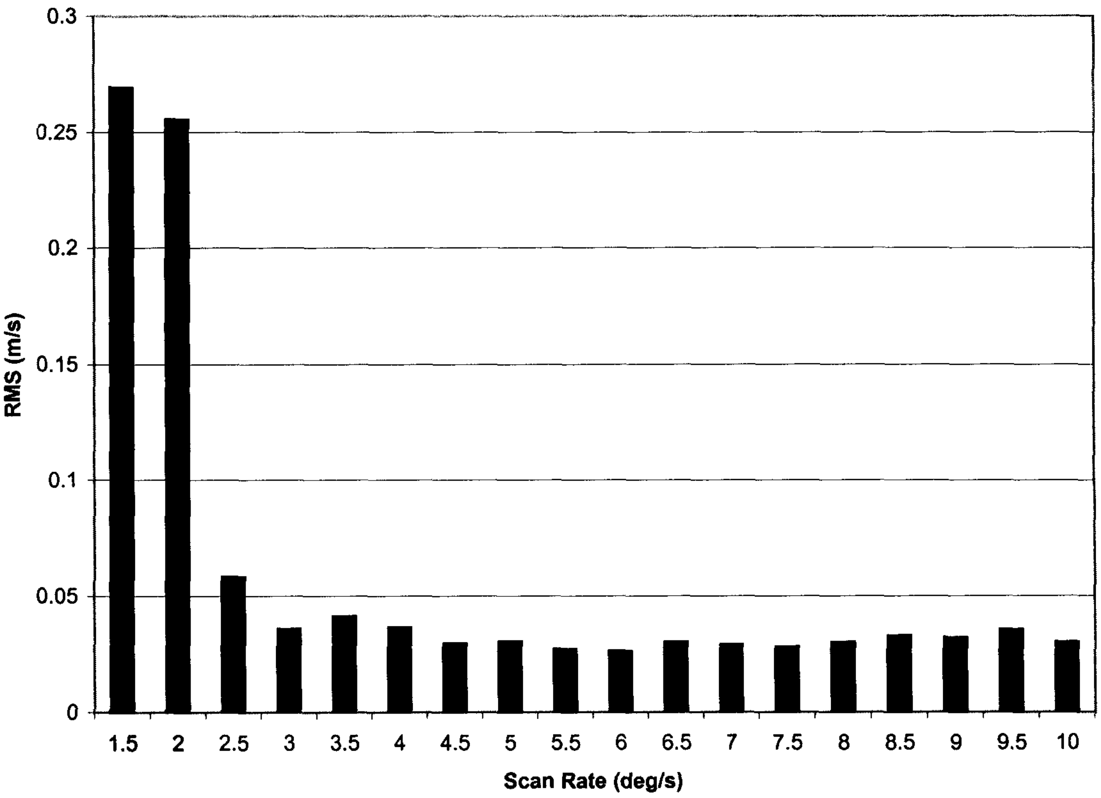

Figure 60 - Analytic constant flow OSSE RMS error (m s^{-1}) as a function of scan rate (deg s^{-1}) for a fixed platform velocity of 30 mph.

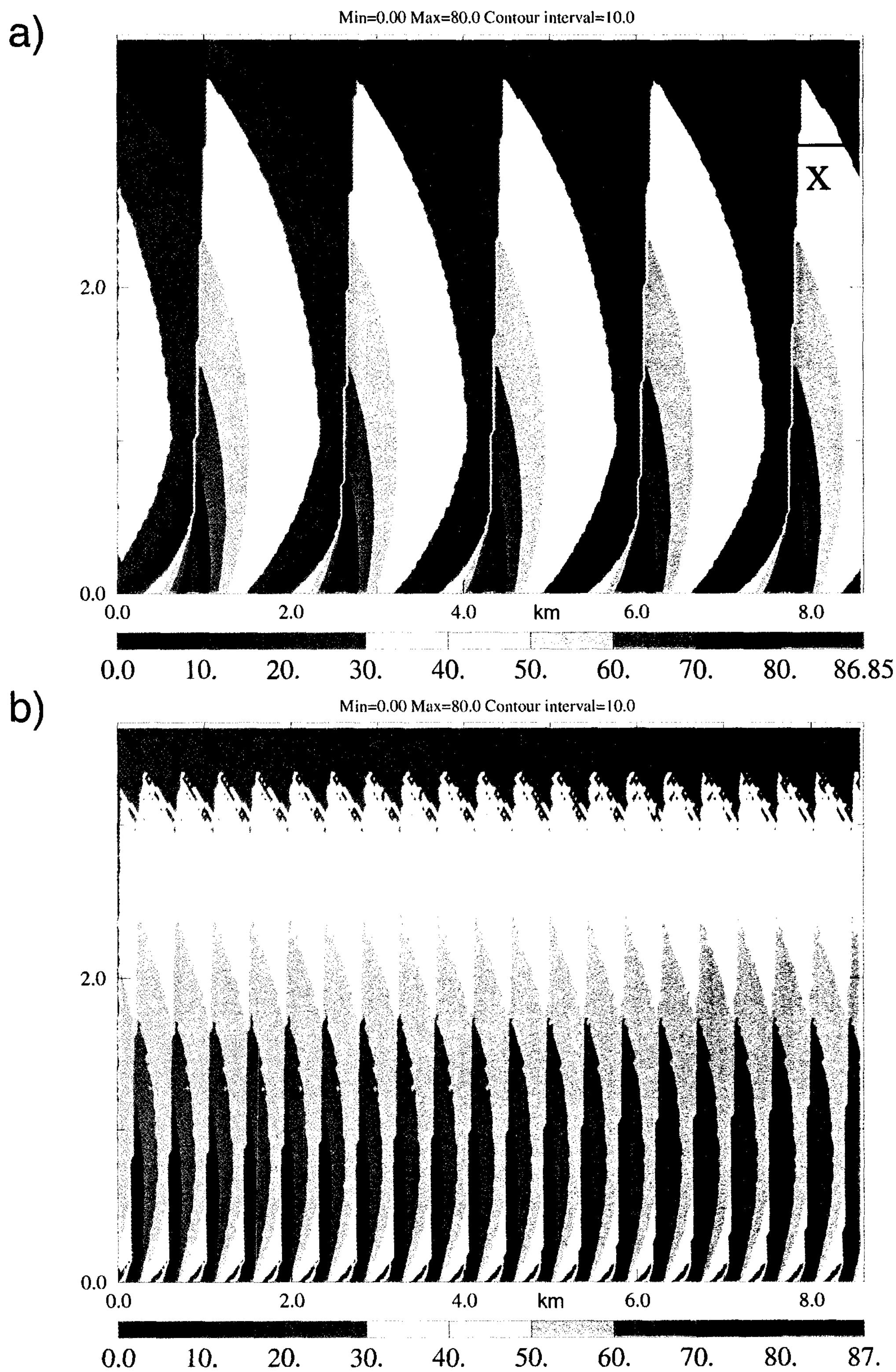

Figure 61 - Constant flow OSSE maximum look angle for a platform motion of 30 mph (13.33 m s^{-1}) and a scan rate of a) 1.5 deg s^{-1} and b) 6.0 deg s^{-1}. The scales are indicated at the bottom of each figure. The truck is in motion from right to left. Horizontal and vertical distance scales are included.

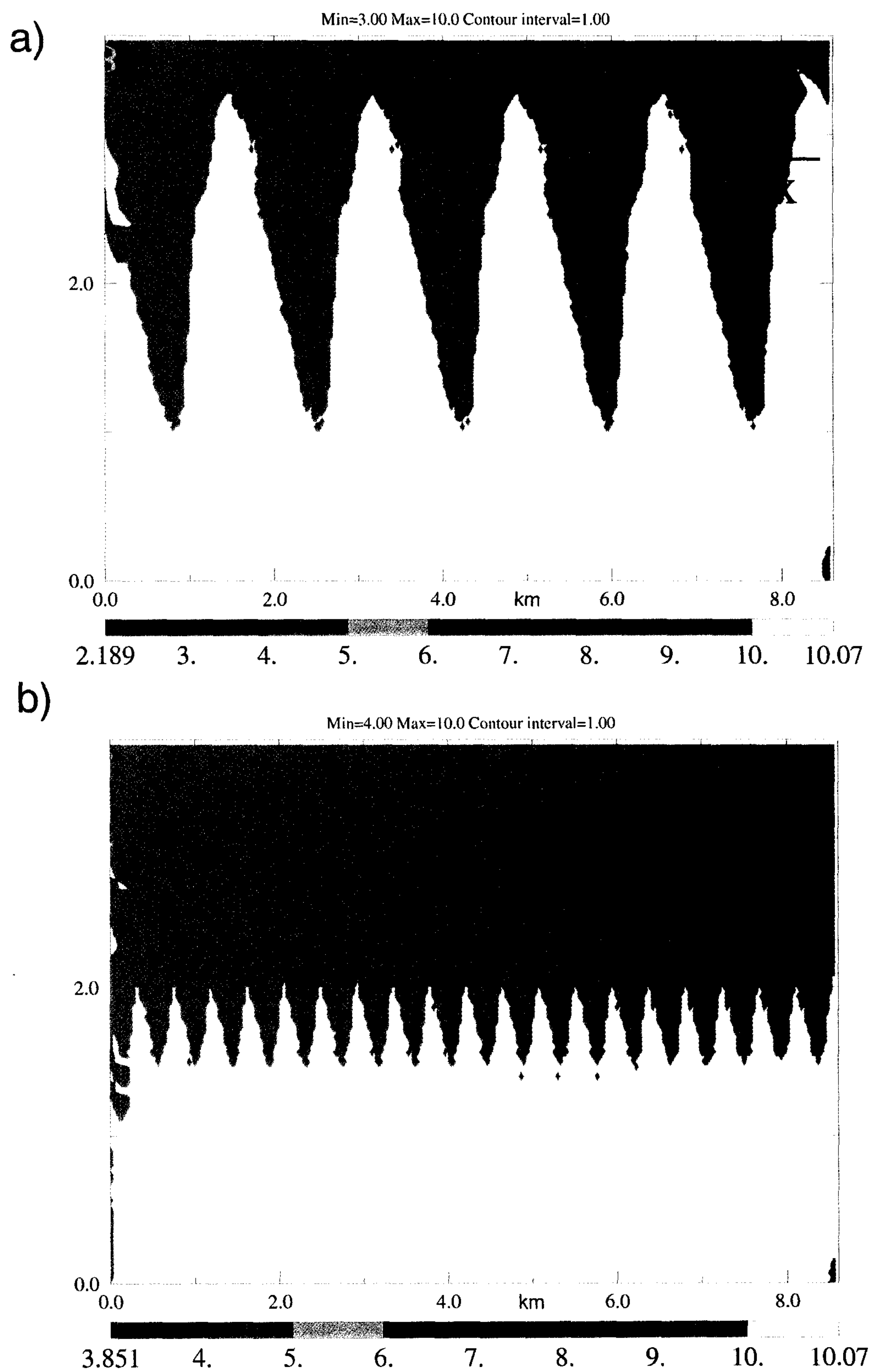

Figure 62 - As in Fig. 61, for the *u*-component wind.

a)

b)

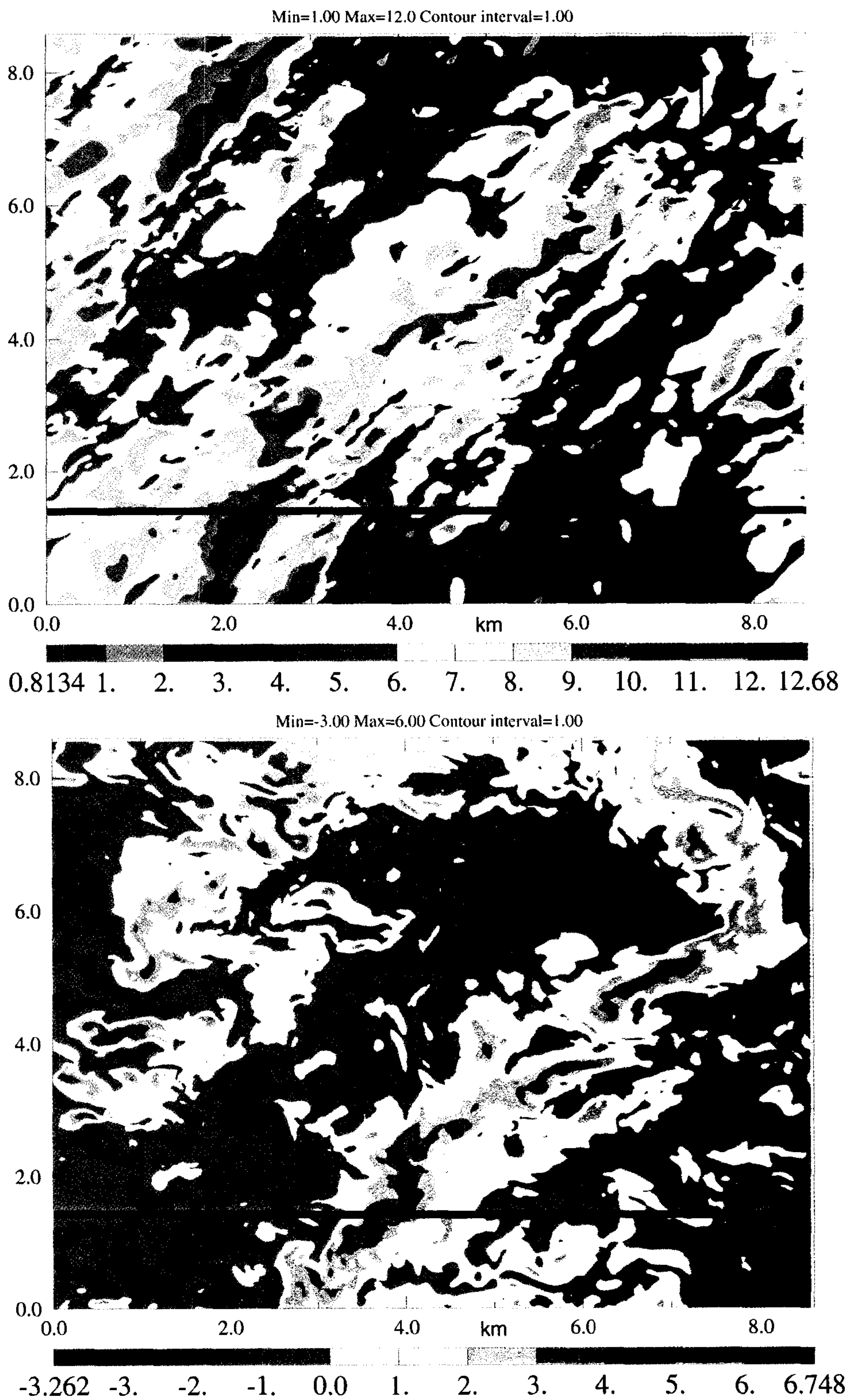

Figure 63 - LES plan images of a) u (m s^{-1}) at 90 m AGL and b) w (m s^{-1}) at 900 m AGL. Color scales are indicated at the bottom of each image. Horizontal distance scales are indicated. The blue line represents the plane of cross section for Fig. 64.

a)

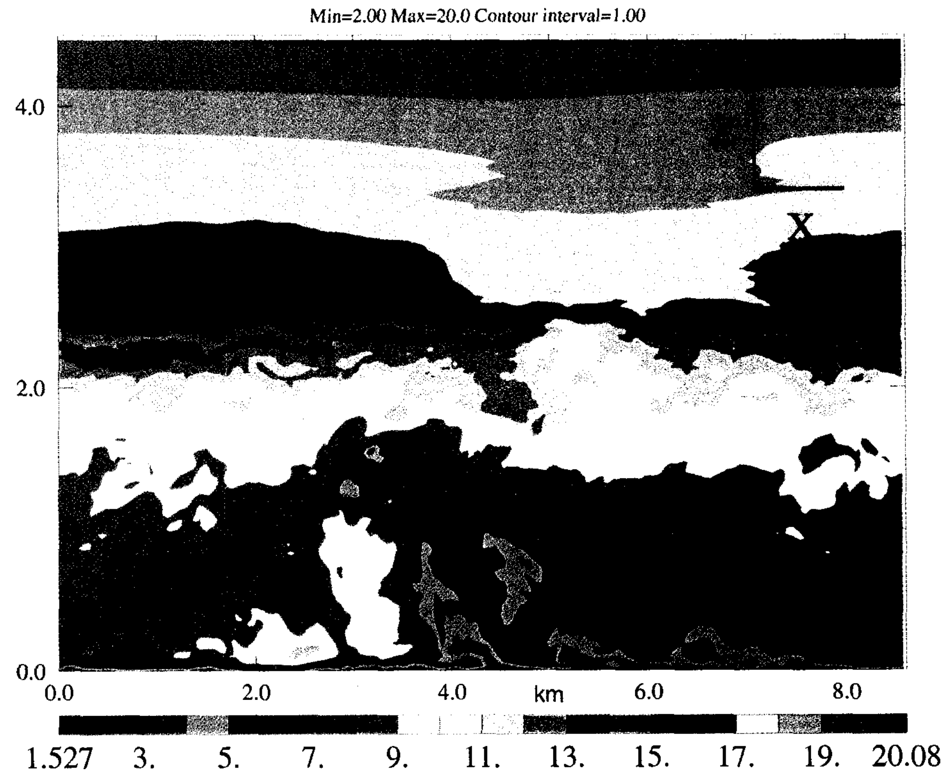

b)

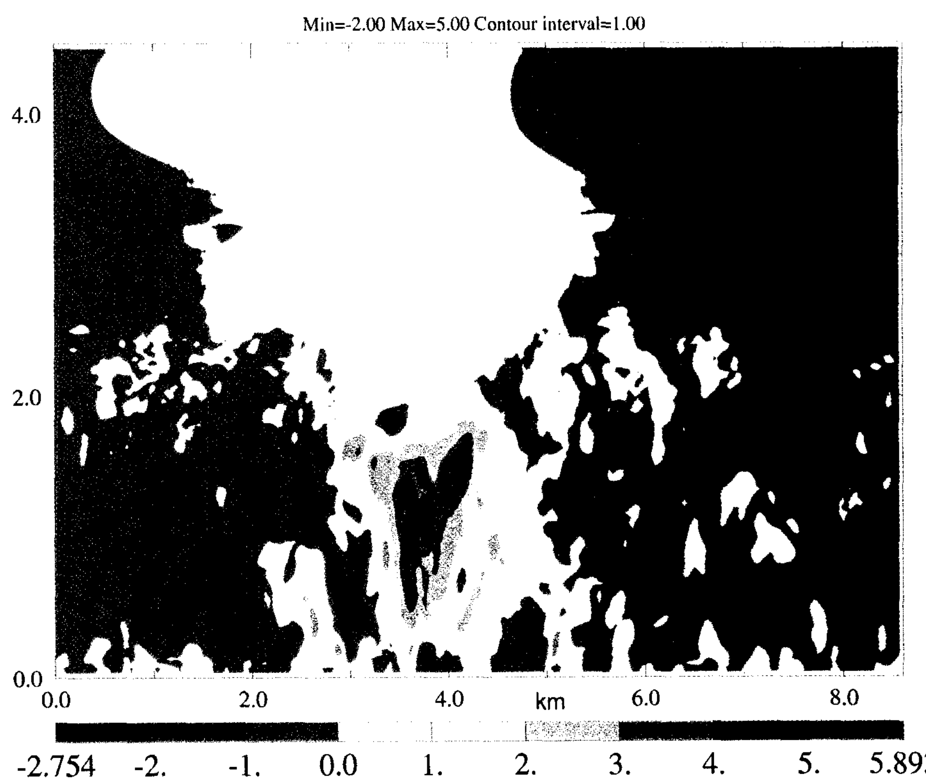

Figure 64 - LES cross sections of a) u (m s^{-1}) and b) w (m s^{-1}) along blue line in Fig. 63. Color scales are indicated at the bottom of each image. Horizontal distance scales are indicated.

a)

b)

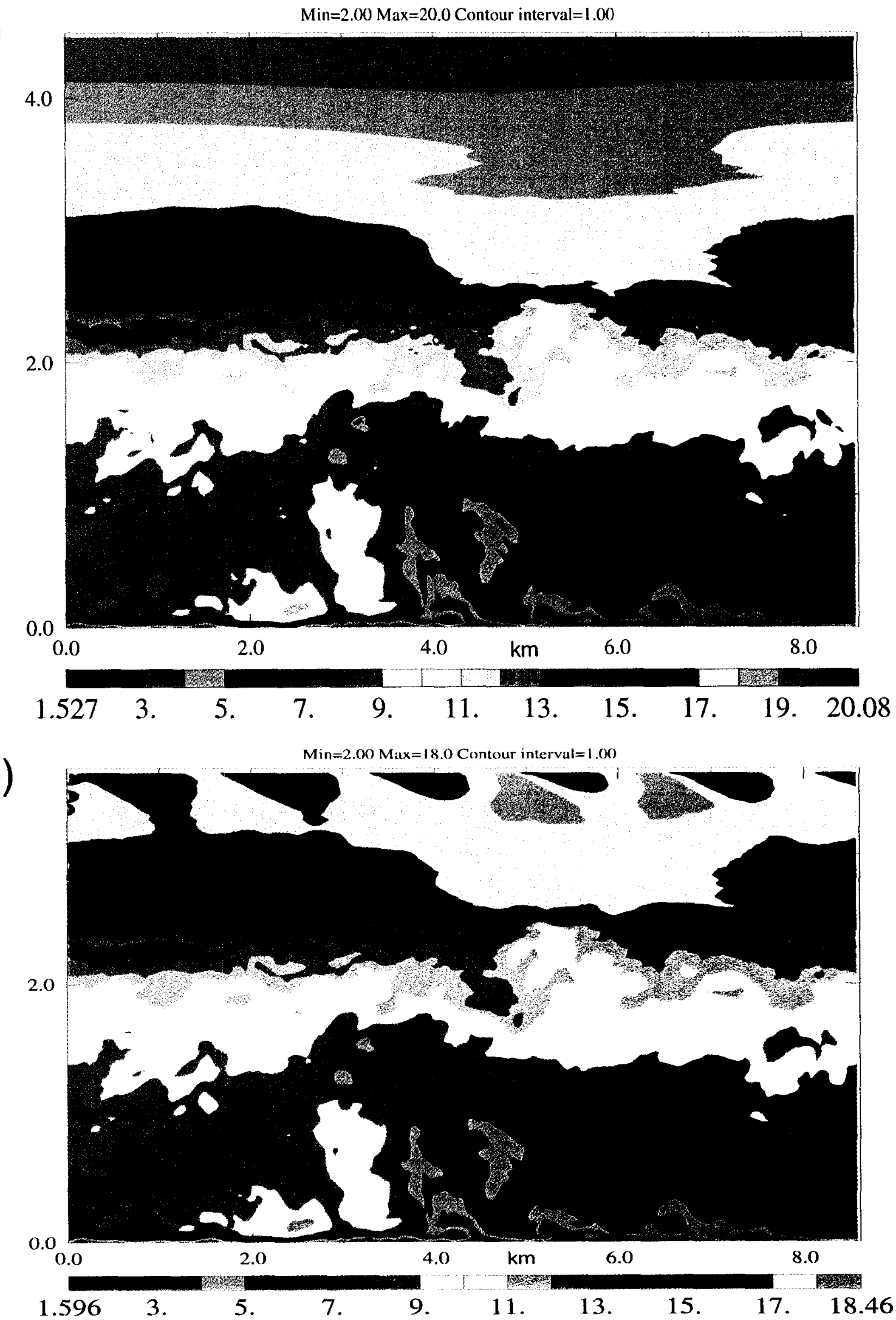

Figure 65 - a) LES cross-section of *u*-component wind ("truth") (m s^{-1}). b) OSSE *u*-component analysis (m s^{-1}) using a platform velocity of 30 mph and scan rate of 1.6 deg s^{-1}. Color scales are indicated at the bottom of each image. Horizontal and vertical distance scales are also provided.

a) b)

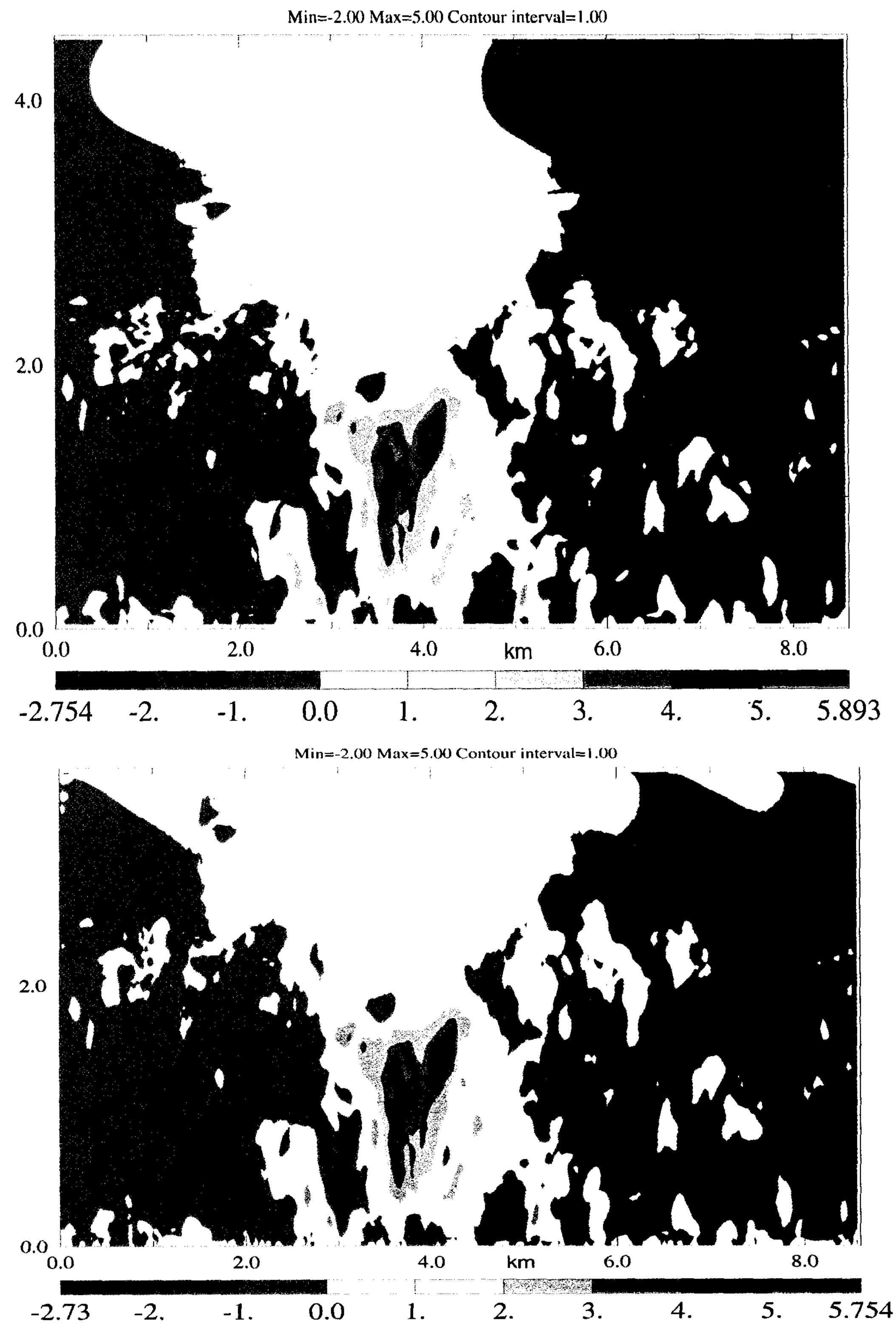

Figure 66 - As in Fig. 65, except for *w*-component wind (m s^{-1}).

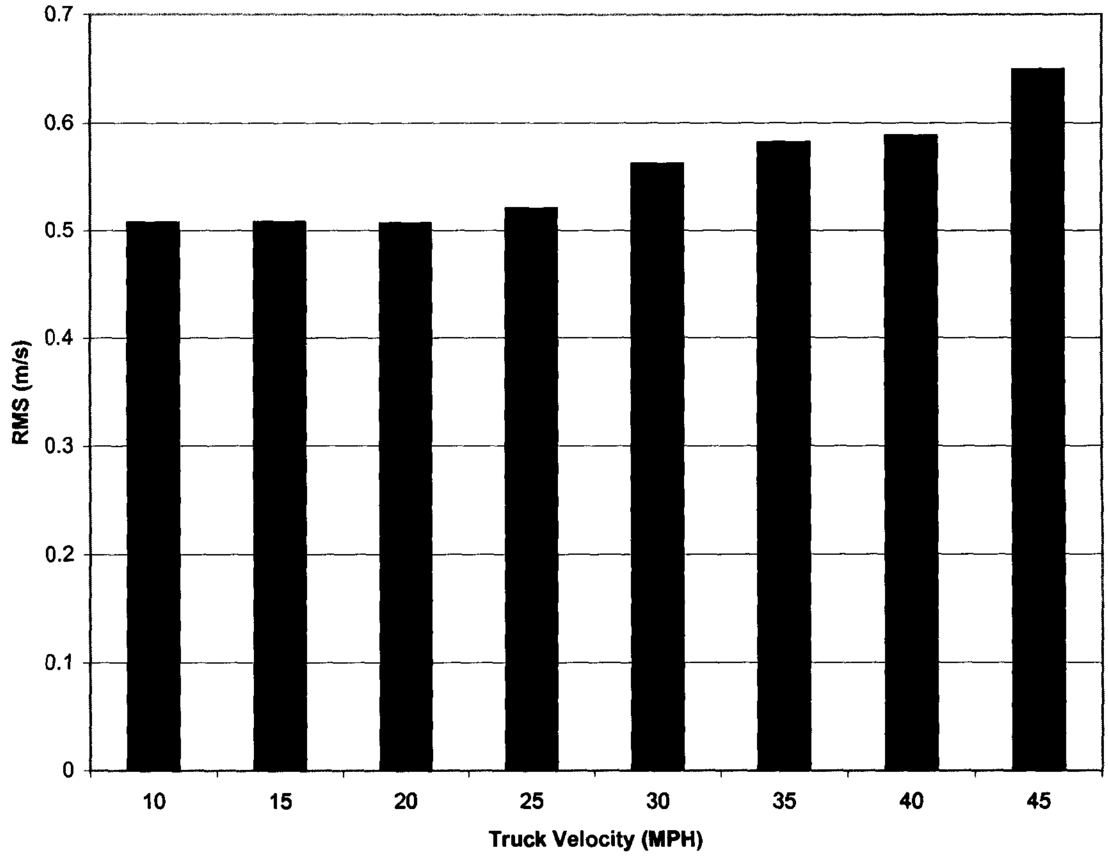

Figure 67 - LES OSSE RMS error (m s^{-1}) as a function of platform velocity (mph) for a fixed scan rate of 1.6 deg s^{-1}.

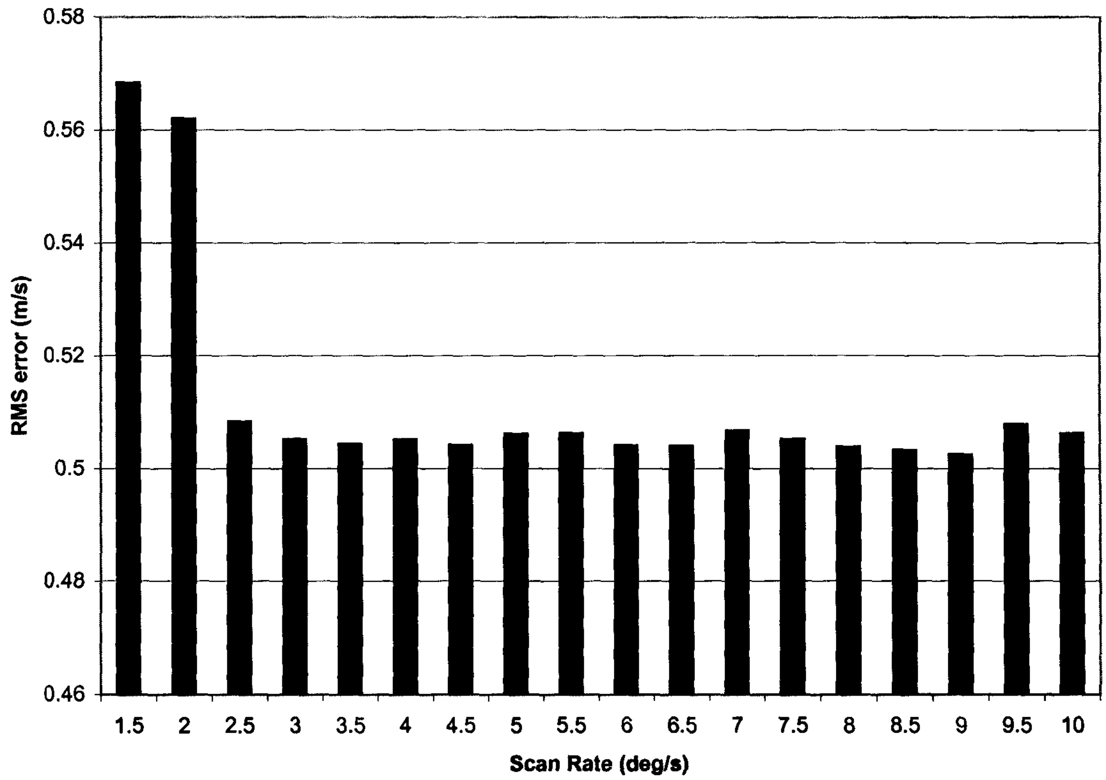

Figure 68 - LES OSSE RMS error (m s^{-1}) as a function of scan rate (deg s^{-1}) for a fixed platform velocity of 30 mph (13.33 m s^{-1}).

a)

b)

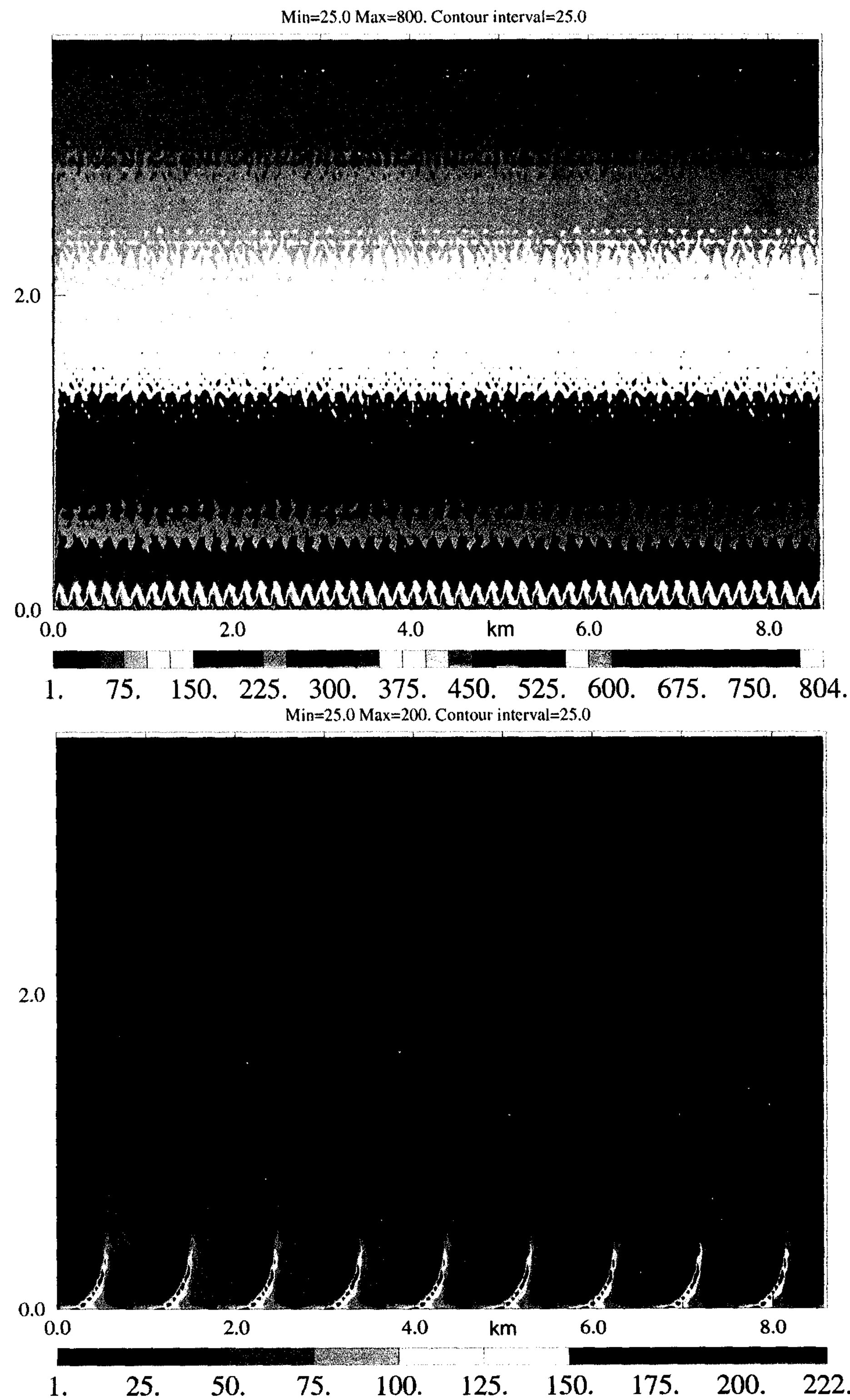

Figure 69 - Constant flow OSSE look count for a scan rate of 5.0 deg s^{-1} and a platform velocity of a) 10 mph (4.44 m s^{-1}) and b) 55 mph (24.44 m s^{-1}). The scales are indicated at the bottom of each figure. The truck is in motion from right to left. Horizontal and vertical distance scales are included.

a)

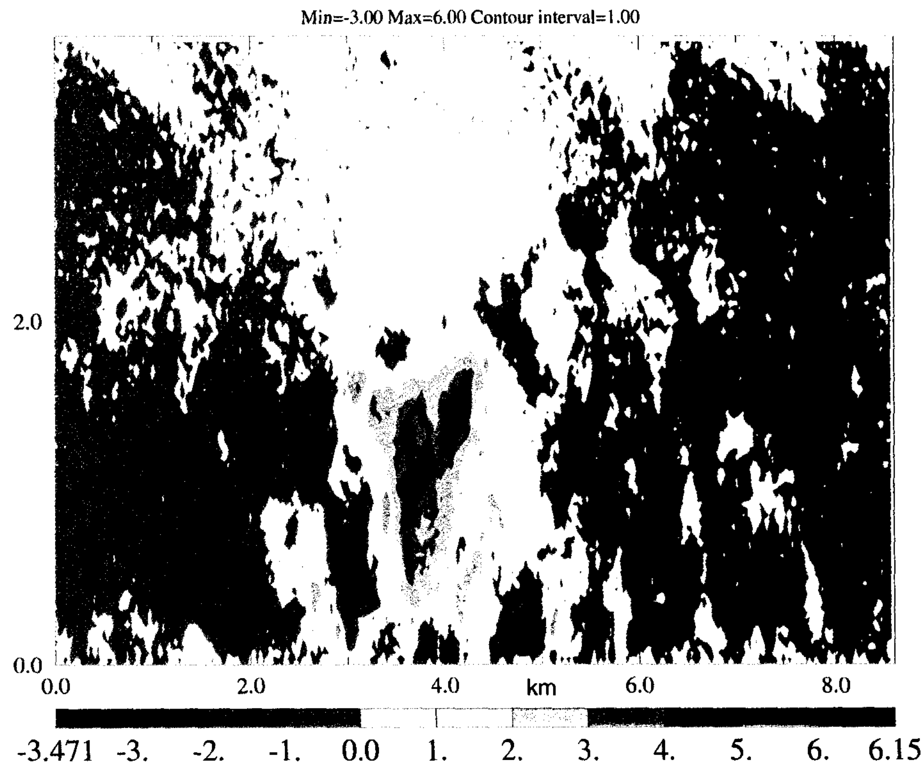

b)

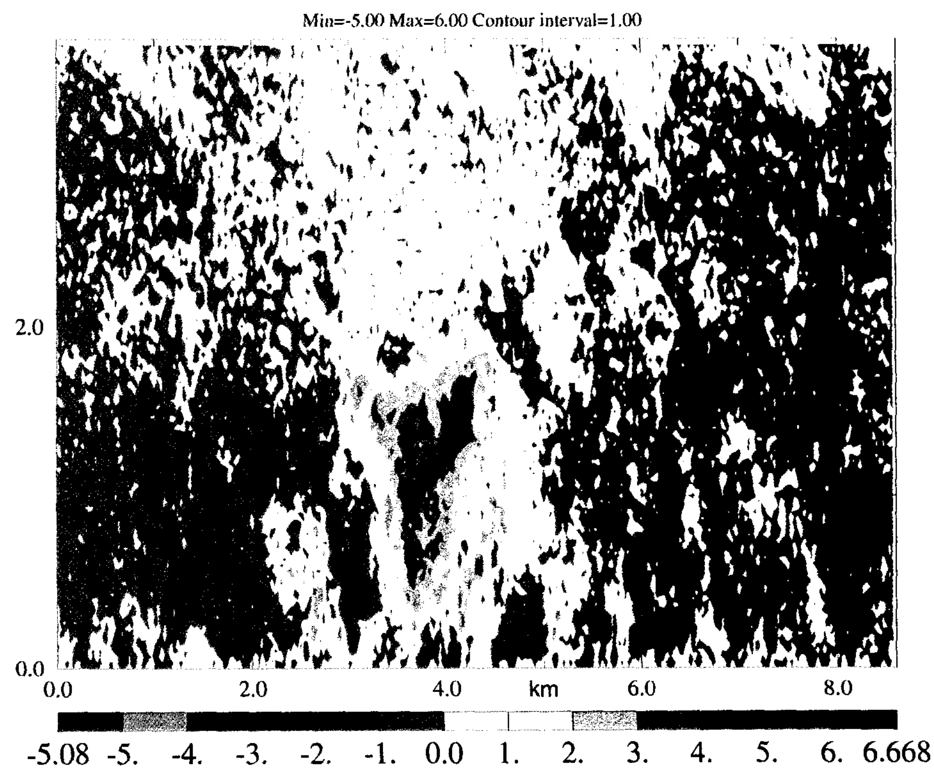

Figure 70 - LES OSSE analysis w-component wind (m s^{-1}) for a truck velocity of 30 mph (13.33 m s^{-1}), scan rate of 1.6 deg s^{-1} and an imposed Gaussian observational error of a) 1.0 m s^{-1} and b) 2.0 m s^{-1}. The "truth" field is shown in Fig. 66b.

a)

b)

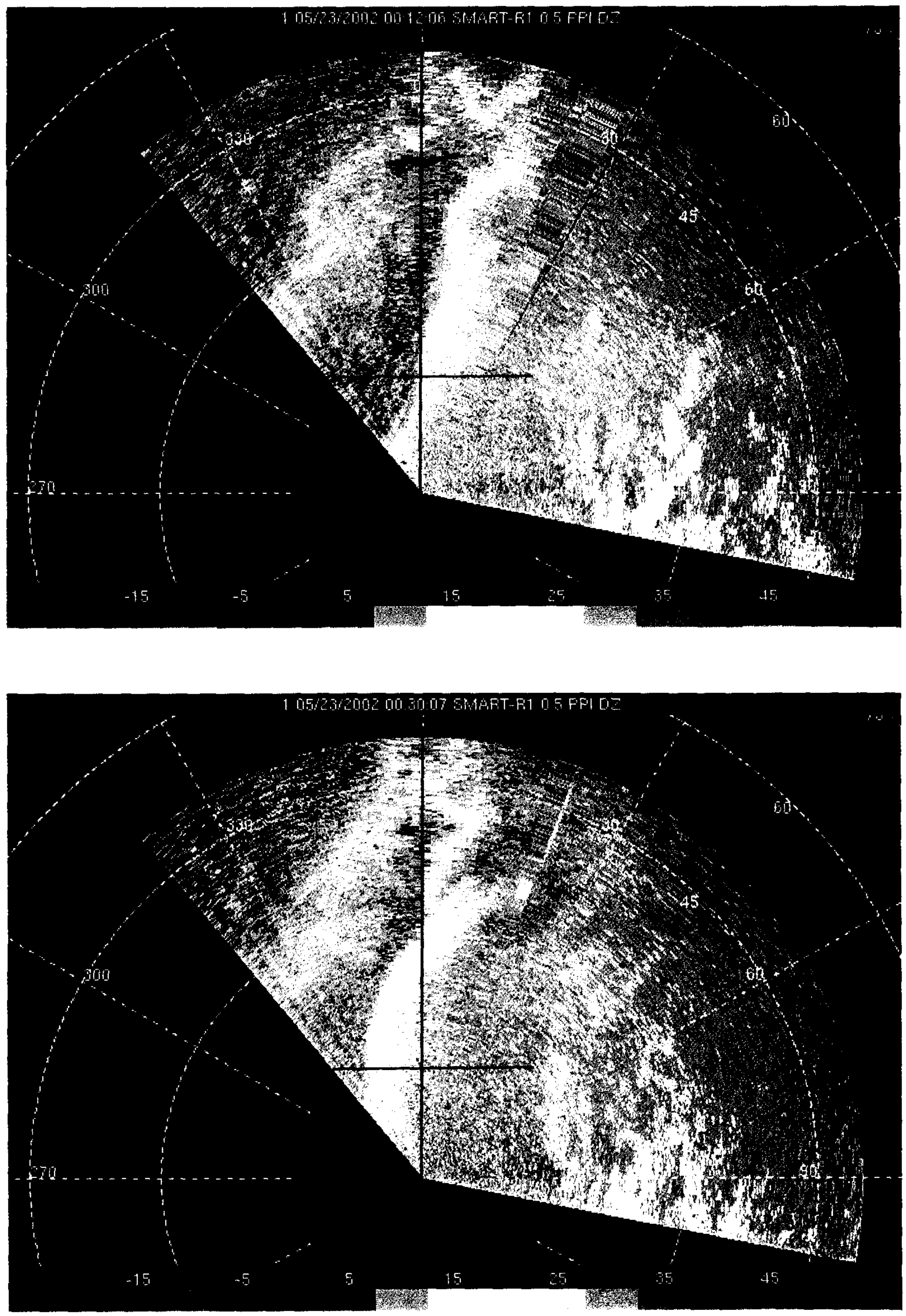

Figure 71 - SMART-R 0.5 degree reflectivity valid at a) 0012 UTC and b) 0030 UTC. The north radial is highlighted in black to show retrogression more clearly. The approximate path of UMass leg 6 (right to left) is shown in red.

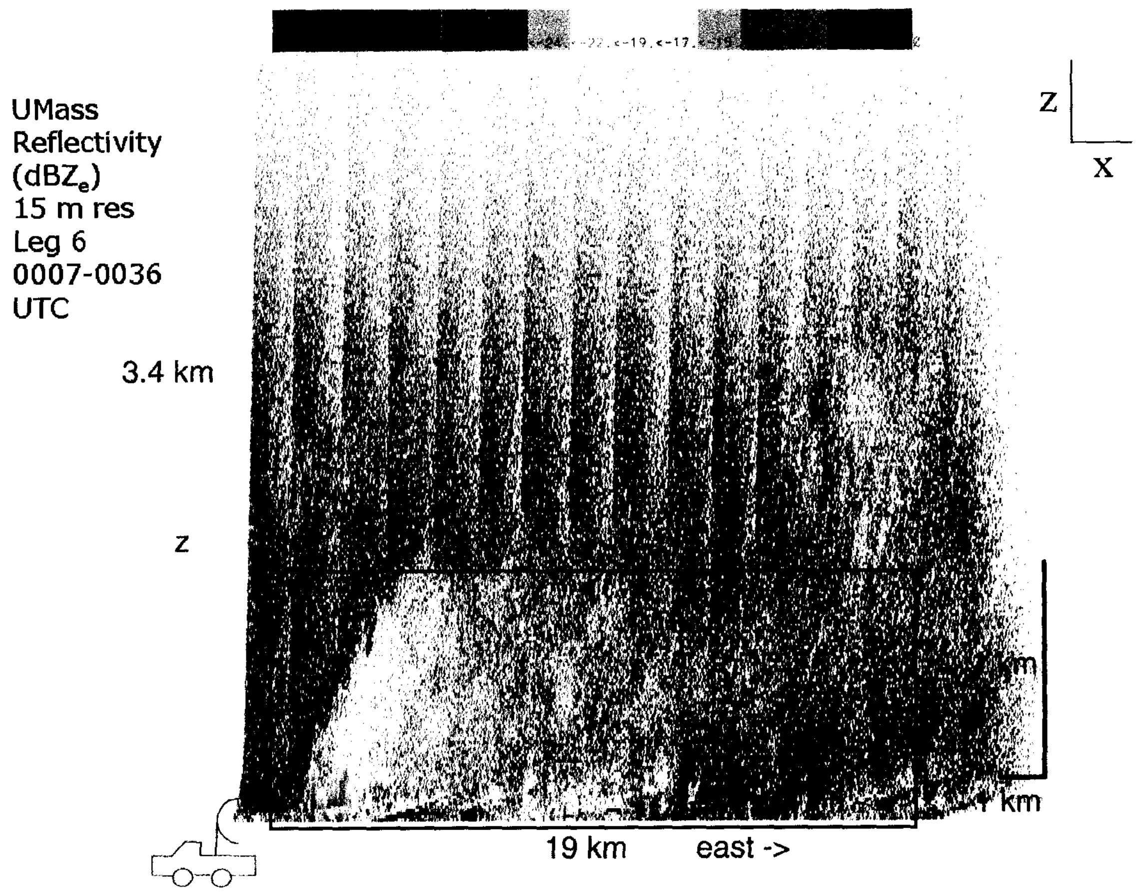

Figure 72 - An east-west display of composite reflectivity from UMass leg 6 (2007-2036 UTC). Horizontal and vertical distance scales are indicated in the lower right hand corner. The domain is approximately 19 km wide (east-west) by 3.4 km tall. The black box denotes the domain for analysis.

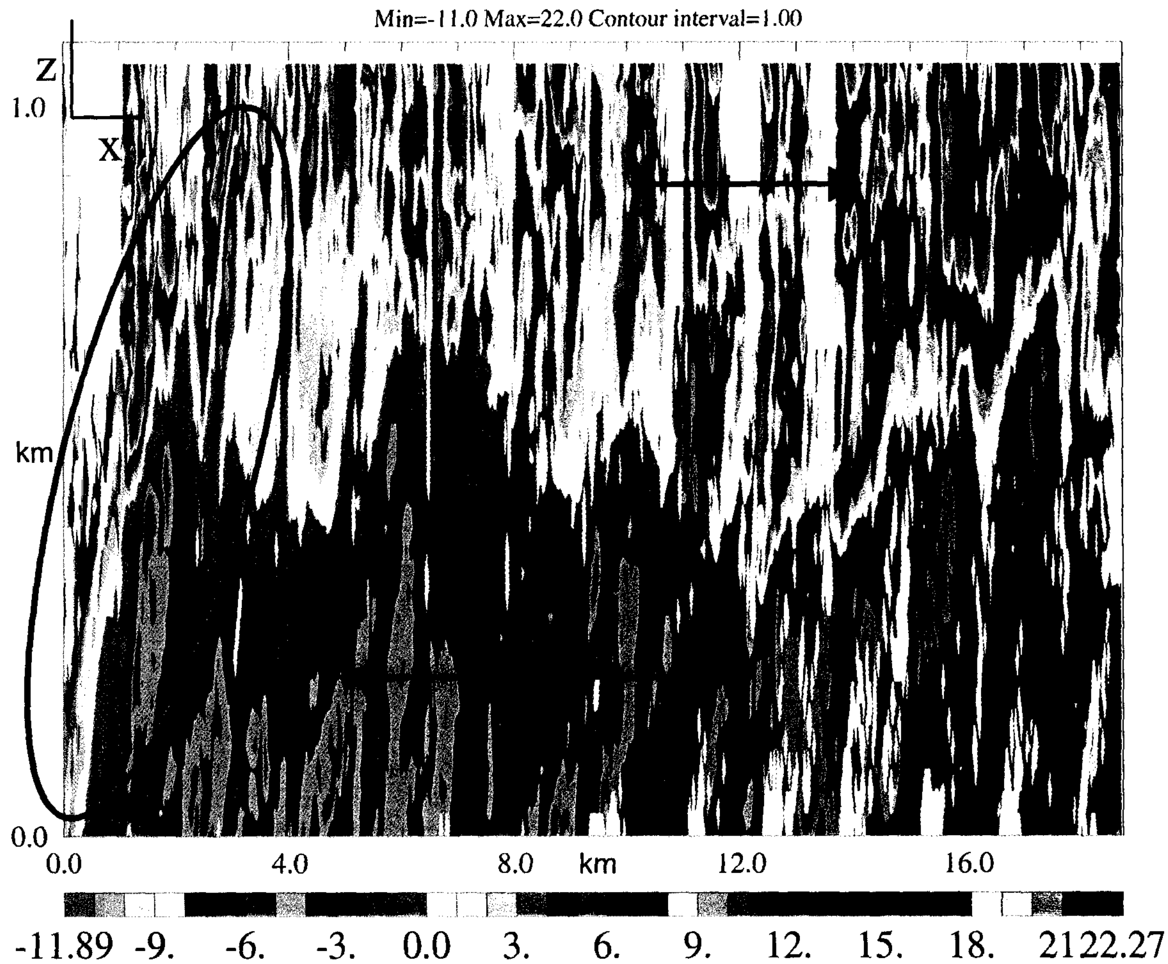

Figure 73 - U-component wind (m s^{-1}, contoured) and u/w wind vectors from the variational analysis of UMass leg 6. Horizontal and vertical distance scales are indicated. The oval encircles the DCZ, long arrows denote the easterly inflow to the DCZ at low levels and westerly return flow aloft. Note that the color scale folds at +12 m s^{-1}.

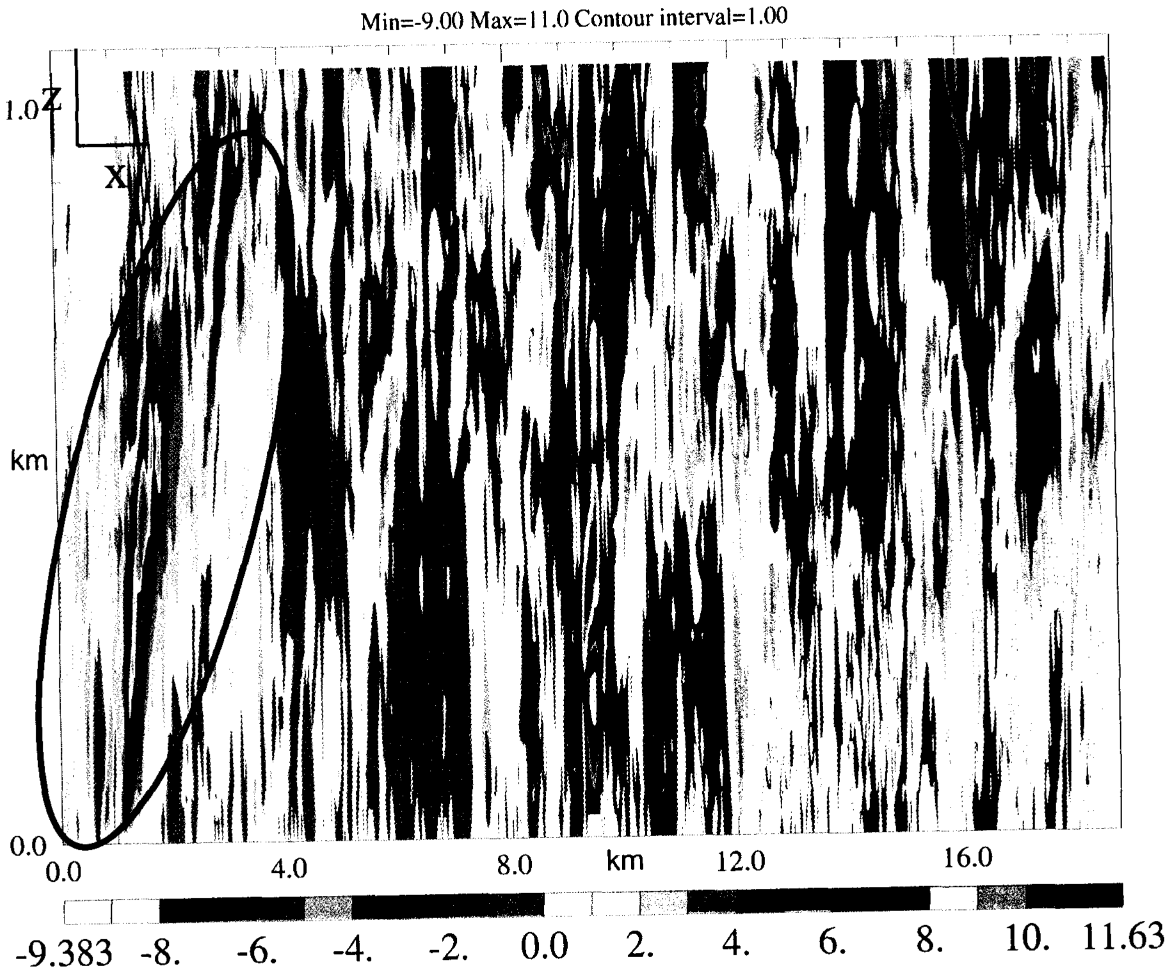

Figure 74 - as in Fig. 73, except for the *w*-component wind (m s^{-1}). Cool colors indicate descending motion, warm colors indicate ascending motion.

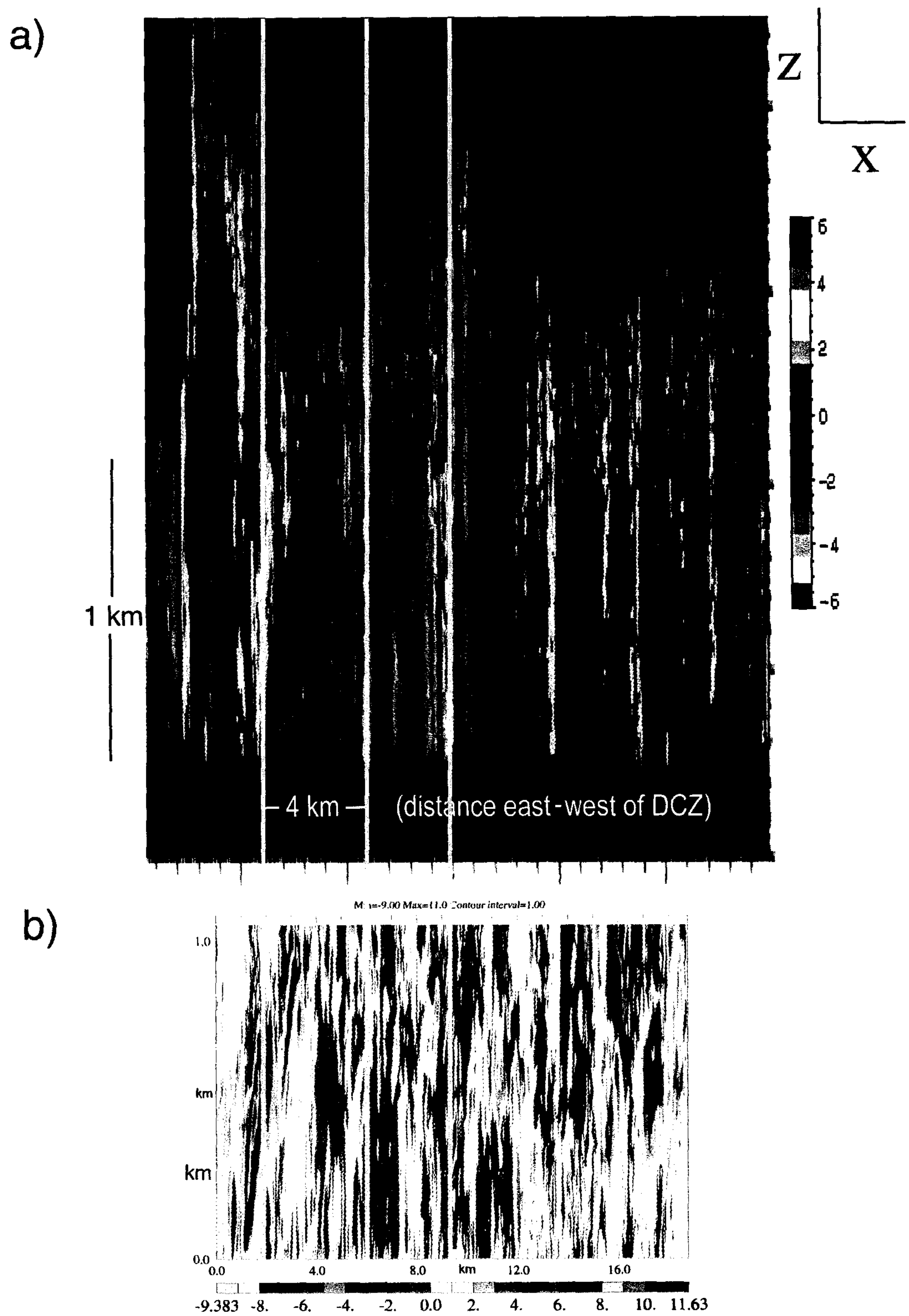

Figure 75 - a) UWKA vertical velocity (m s^{-1}, scale to right) from 2345-2351 UTC. b) UMass W-band vertical velocity (m s^{-1}, scale at bottom) as in Fig. 74. Both images represent approximately the same distance east-west from the primary (eastern) dryline, though separated in time.

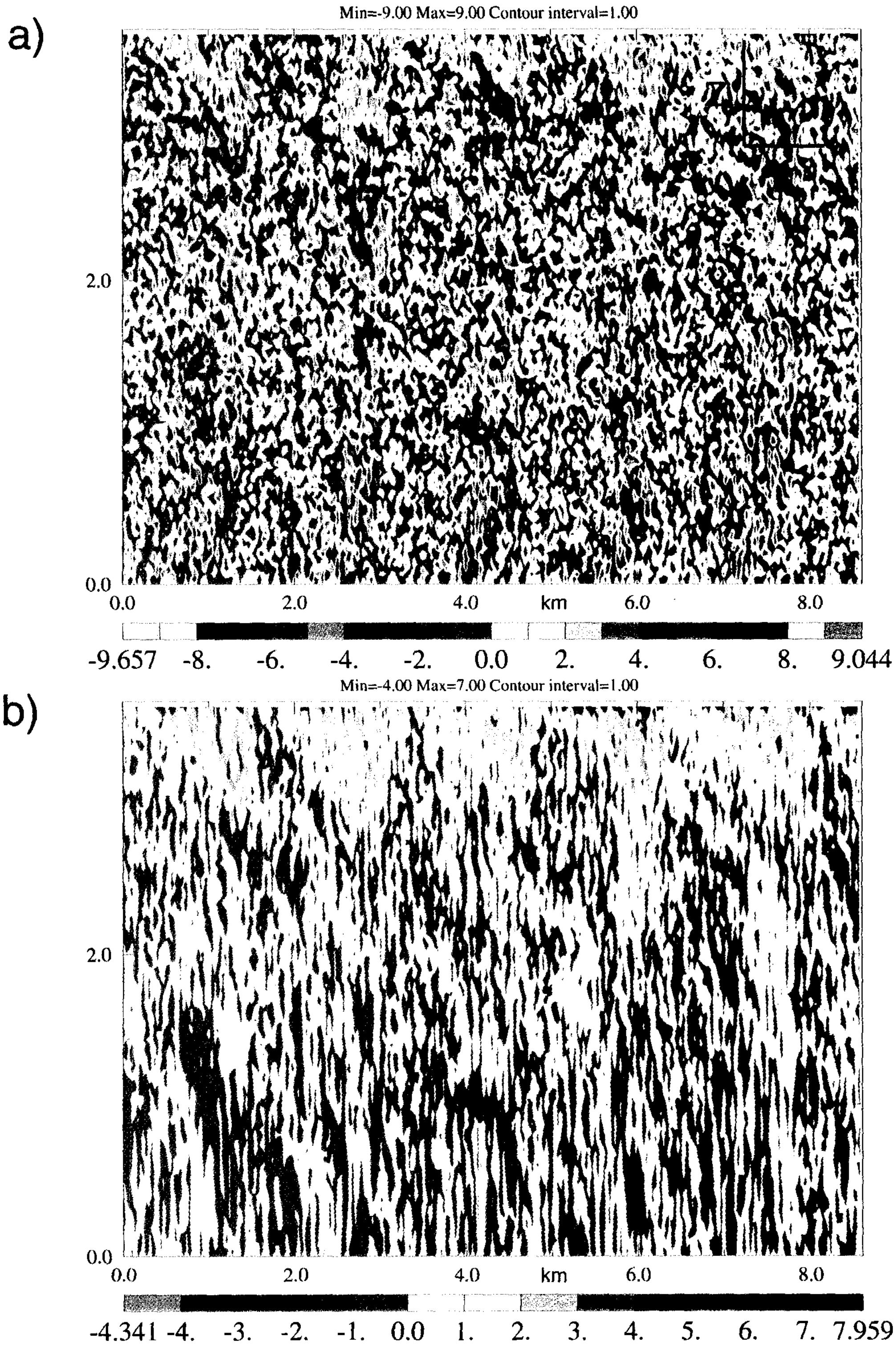

Figure 76 - Analyzed *w*-component wind (m s^{-1}) for the constant flow (u=10 m s^{-1}, w=0 m s^{-1}) OSSE using a platform velocity of 30 mph (13.33 m s^{-1}), scan rate of 1.6 deg s^{-1}, imposed Gaussian observational error of 6.0 m s^{-1} and an analysis β value of a) $\beta=(\Delta x)^2$ and b) $\beta=m(\Delta x)^2$, where m is the number of observations at each point in the analysis domain.

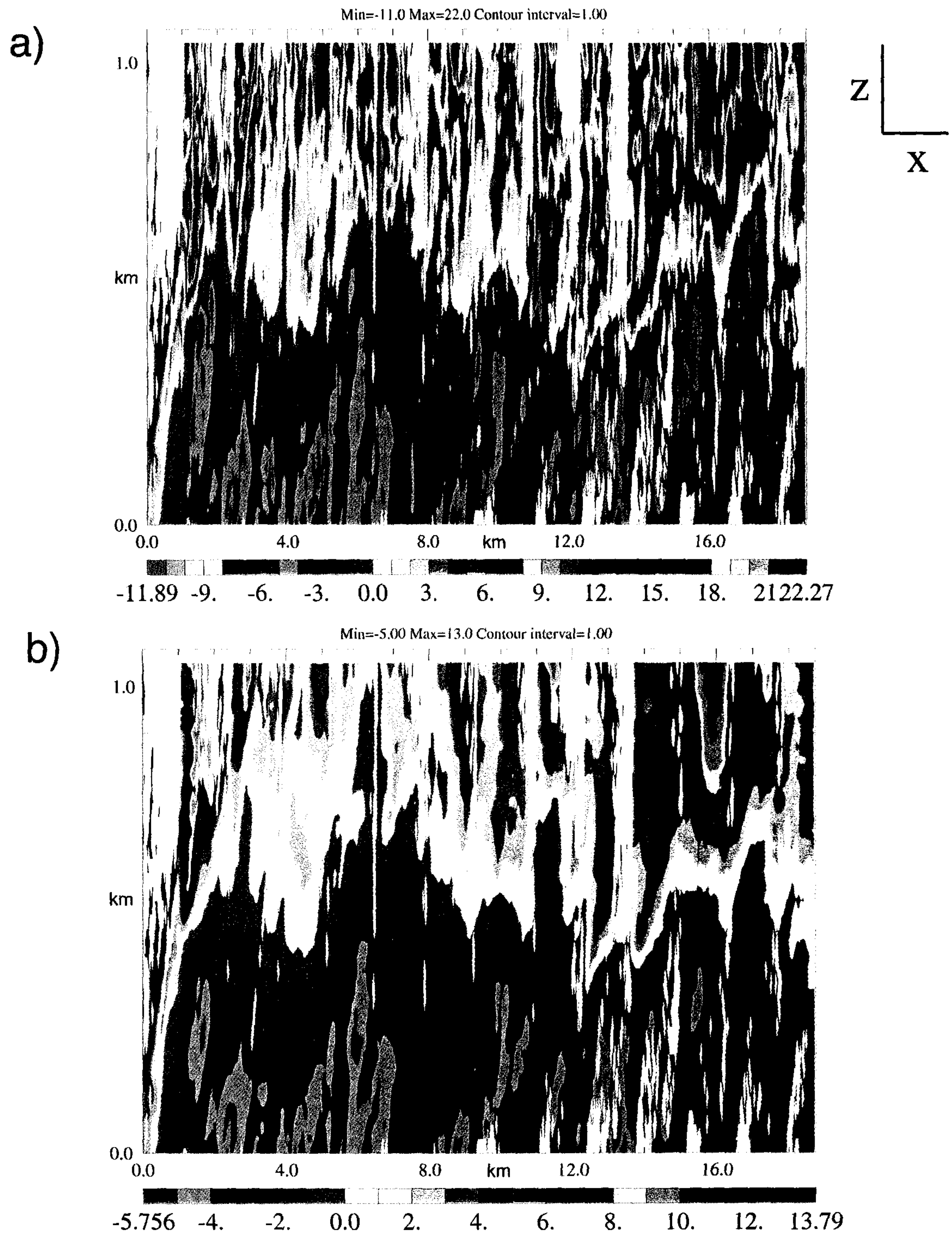

Figure 77 - Analyzed *u*-component wind (m s^{-1}) for UMass leg 6 using a) $\beta=(\Delta x)^2$ and b) $\beta=m(\Delta x)^2$, where *m* is the number of observations at each point in the analysis domain. Horizontal and vertical distance scales are indicated. Velocity scale is included at the bottom of each image.

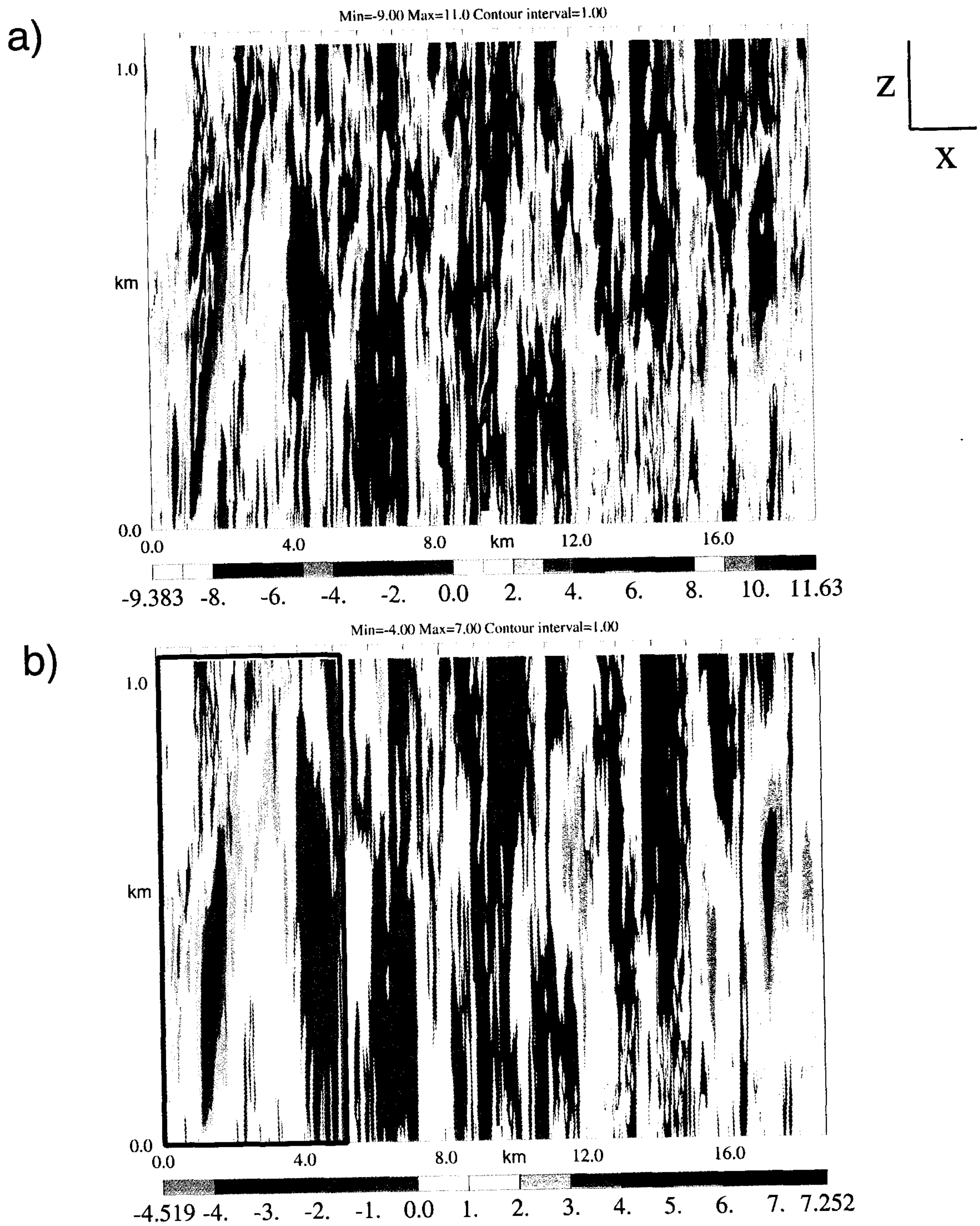

Figure 78 - As in Fig. 77, but for the *w*-component wind (m s^{-1}). The blue box in b) indicates the domain for Fig. 79.

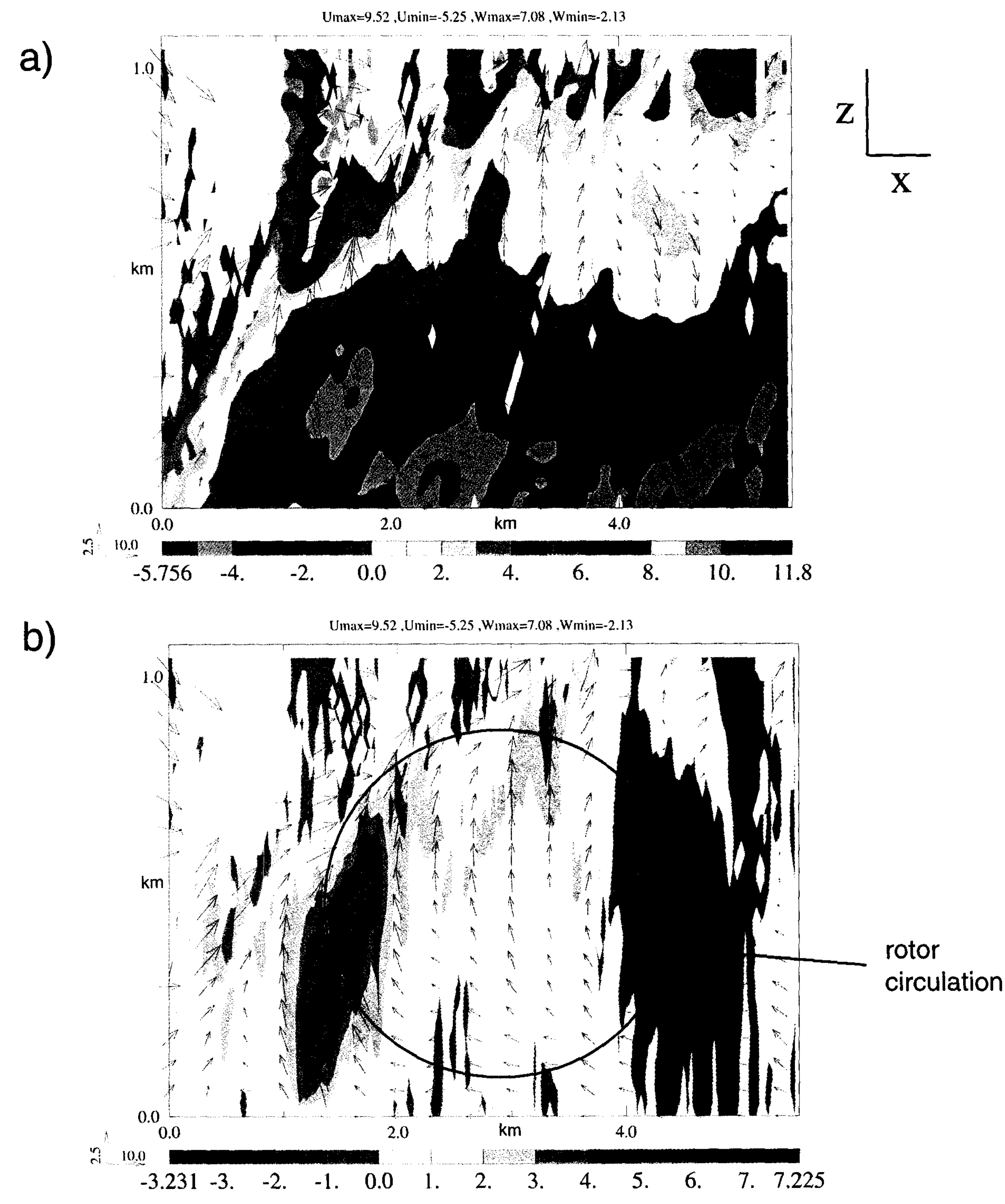

Figure 79 - Analysis a) *u*-component (m s^{-1}, contoured) and b) *w*-component (m s^{-1}, contoured) wind near the retreating dryline interface for UMass leg 6 (domain indicated in Fig. 78). Vectors represent *u*/*w* wind. Horizontal and vertical distance scales are indicated. Data-void areas represent points with less than 10 looks with the UMass radar. The location of the rotor circulation on the head of the DSC is indicated.

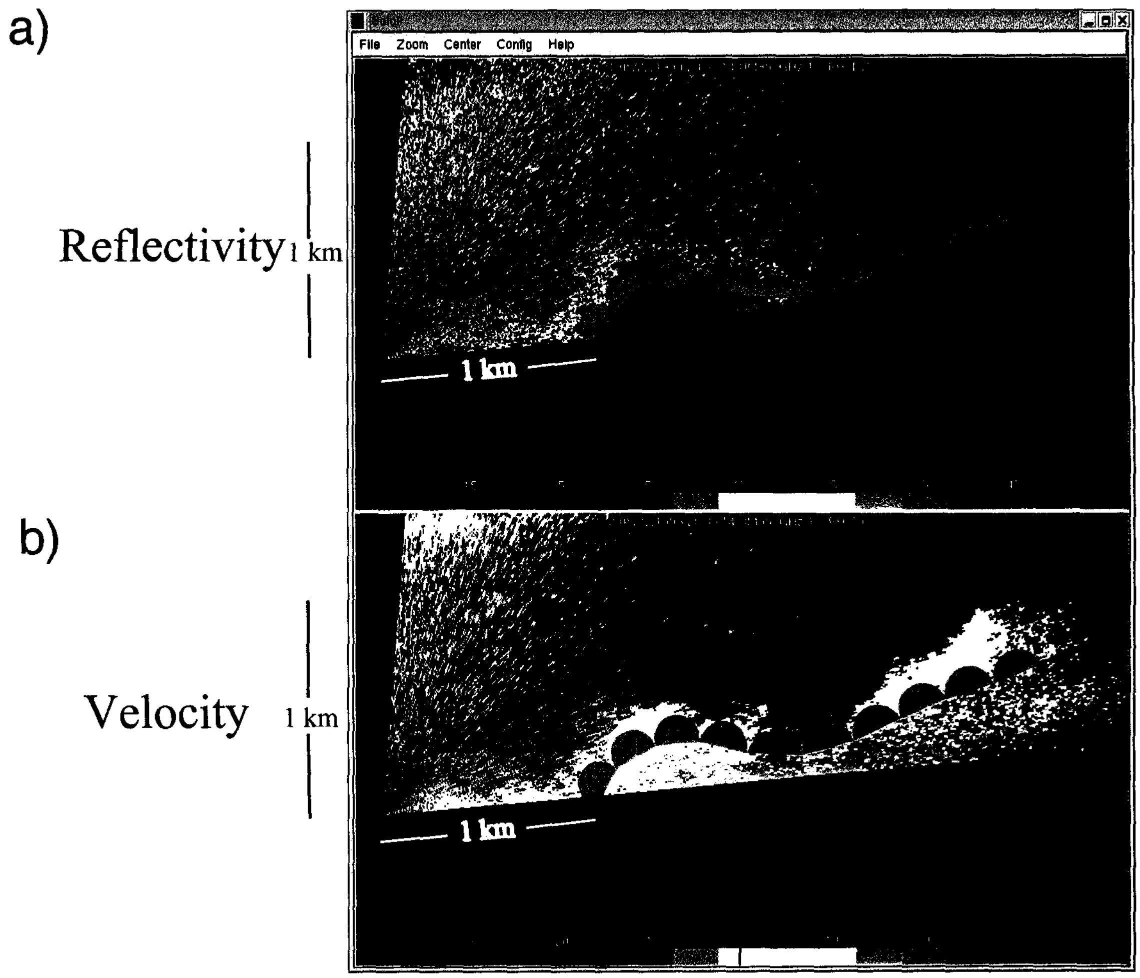

Figure 80 - SOLO display of a vertical sweep during UMass leg 6. Pictured is a) reflectivity (dBZ_e) and b) ground-relative radial velocity (m s^{-1}) of the retrograding dryline. Scales are located at the bottom of each figure. Vertical and horizontal distance scales are shown. Approximate dryline position indicated by the scalloped line.

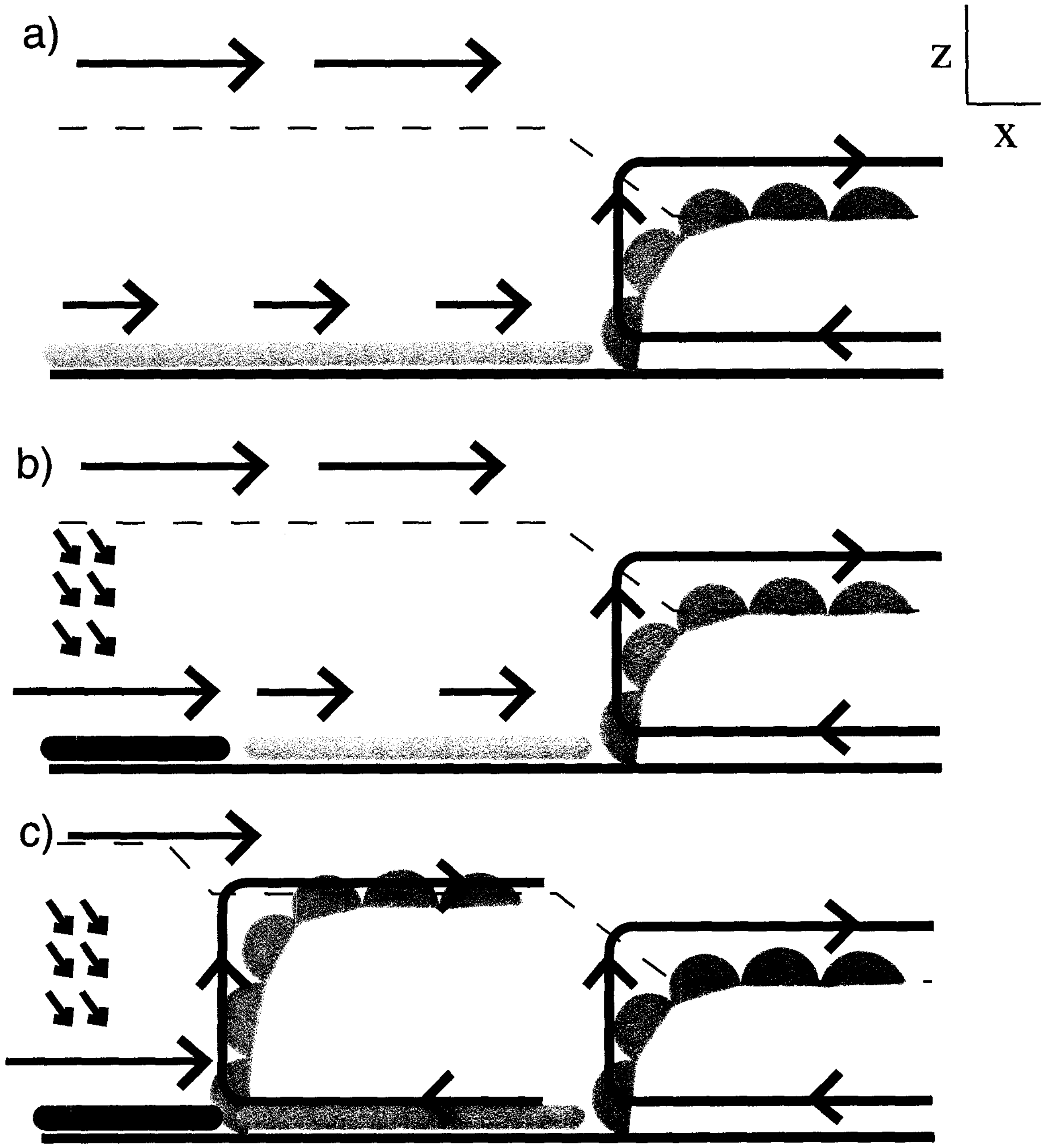

Figure 81 - Schematic of a hypothesis on ancillary dryline formation. Strong westerly momentum (a) is transferred to the surface via descending motion (b). The surface virtual temperature increases in this region driving an increasing horizontal virtual temperature gradient near the surface. A frontogenetical secondary circulation develops (c) parallel to the increased gradient, further sharpening the moisture gradient and establishing an ancillary dryline. In the diagrams, the scalloped line denotes the dryline positions. The dashed line denotes the top of the CBL.

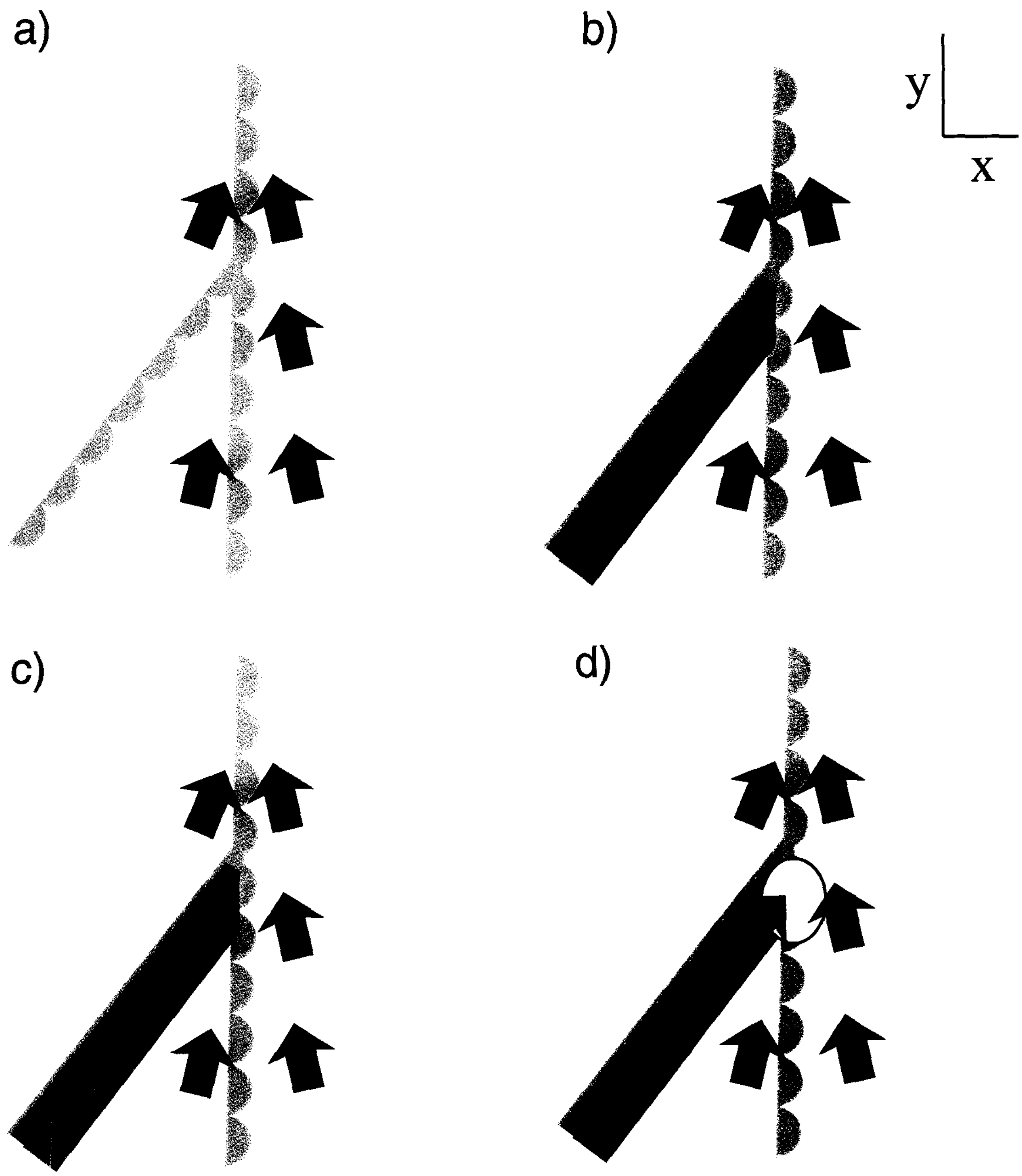

Figure 82 - Schematic of a possible convective initiation mechanism in a double-dryline environment (a). Forced descent to the east of the secondary dryline (b) transports westerly momentum down to the surface (c) increasing convergence along the dryline in select locations (shaded in yellow) to the south of the triple point (d). Scalloped lines indicate known drylines. Arrows represent surface winds. The blue(red) regions denote areas of ascent(descent) in the CBL.

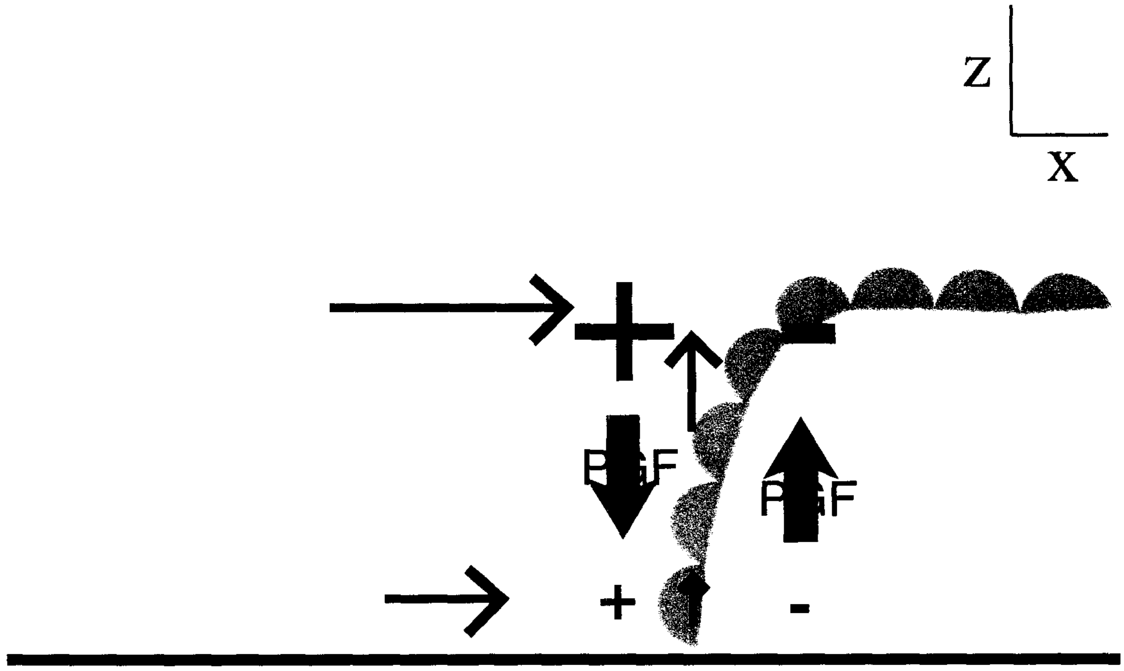

Figure 83 - Schematic of DCZ-shear interaction. Stronger positive perturbation pressure associated with stronger updraft aloft (in the DCZ) yields a downward-directed perturbation pressure gradient force. Such downward motion may be responsible for previously observed increases in westerly momentum in the CBL immediately to the west of the dryline (e.g., Atkins et al. 1998, Weiss and Bluestein 2002). The scalloped line indicates the dryline; the red "+"s denote perturbation pressure; the blue "-"s denote negative perturbation pressure.

Const flow OSSE (u=10 m/s, w=0 m/s)

Platform velocity (MPH)	Scan rate (deg/s) 0.1	0.5	1	1.5	2	2.5	3	3.5	4	4.5	5	5.5	6	6.5	7	7.5	8	8.5	9	9.5	10
1	x	x	x	x	x	x	x	x	x	x	x	x	x	x	x	x	x	x	x	x	x
5	x	x	x	x	x	x	x	x	x	x	x	x	x	x	x	x	x	x	x	x	x
10	x	0.163478	0.021779	0.015615	0.014327	0.011877	0.011714	0.011618	0.01111	0.011701	0.011697	0.011645	0.011613	0.012099	0.011504	0.010788	0.011975	0.011339	0.011672	0.012791	0.01062
15	x	x	0.218247	0.027186	0.026741	0.020057	0.018182	0.017316	0.015377	0.016719	0.014728	0.016491	0.016894	0.016765	0.015149	0.016647	0.016572	0.015152	0.016203	0.015385	0.022198
20	x	x	0.220123	0.171066	0.028975	0.030907	0.023886	0.023909	0.020266	0.020397	0.020158	0.019304	0.018654	0.01939	0.018938	0.021902	0.020917	0.021055	0.020165	0.024257	0.019112
25	x	x	x	0.280306	0.084321	0.032565	0.03599	0.028098	0.025252	0.025738	0.022666	0.024512	0.024771	0.024327	0.022922	0.024482	0.02533	0.027263	0.027753	0.026062	0.025887
30	x	x	x	0.269376	0.255431	0.058304	0.03589	0.041251	0.036323	0.029592	0.030377	0.027142	0.026237	0.030125	0.02901	0.028105	0.030046	0.032749	0.031951	0.035423	0.030031
35	x	x	x	x	0.306887	0.217493	0.058601	0.039341	0.042863	0.043238	0.032354	0.033453	0.034628	0.032124	0.033025	0.031382	0.034774	0.031846	0.038069	0.037363	0.038442
40	x	x	x	x	0.309242	0.302987	0.114135	0.06301	0.043753	0.047884	0.046879	0.038781	0.034246	0.039314	0.03579	0.037317	x	0.037831	0.042375	0.040749	0.036245
45	x	x	x	x	0.416308	0.338539	0.271958	0.106105	0.060887	0.048828	0.051297	0.053598	0.044436	0.041452	0.04234	0.042842	0.046456	x	x	0.0452	0.042572
50	x	x	x	x	x	0.337662	0.345371	0.264933	0.092007	0.061291	0.050445	0.055258	0.059248	0.05107	0.04607	x	x	0.051451	x	x	x
55	x	x	x	x	x	0.386582	0.365826	0.326462	0.142958	0.090331	0.062307	x	0.059073	0.064432	x	x	x	x	x	x	x
60	x	x	x	x	x	x	0.367254	0.366543	0.307179	x	x	0.063284	x	x	x	x	0.054573	x	x	x	x
65	x	x	x	x	x	x	x	x	x	x	x	0.088998	x	x	x	x	x	x	x	x	x
70	x	x	x	x	x	x	x	x	0.36754	x	x	x	x	x	x	x	x	x	x	x	x

Table 1 – RMS errors (m s^{-1}) for the constant-flow OSSE experiment as a function of scan rate (deg s^{-1}, columns) and platform velocity (mph, rows).

LES OSSE

Platform velocity (MPH)	Scan rate (deg/s)																				
	0.1	0.5	1	1.5	2	2.5	3	3.5	4	4.5	5	5.5	6	6.5	7	7.5	8	8.5	9	9.5	10
1	x	x	x	x	x	x	x	x	x	x	x	x	x	x	x	x	x	x	x	x	x
5	x	x	x	x	x	x	x	x	x	x	x	x	x	x	x	x	x	x	x	x	x
10	x	0.530195	0.508094	0.506518	0.507206	0.506379	0.5059	0.505265	0.505576	0.504359	0.506466	0.506698	0.505212	0.504428	0.507055	0.506471	0.504835	0.503974	0.50272	0.508463	0.506841
15	x	x	0.5469	0.506777	0.507757	0.506679	0.50558	0.505332	0.505485	0.504504	0.506173	0.506246	0.504501	0.504085	0.506315	0.505819	0.504279	0.50368	0.502518	0.508045	0.507164
20	x	x	0.547913	0.530805	0.506522	0.506073	0.504964	0.505138	0.505504	0.503731	0.505852	0.506798	0.504902	0.504586	0.506747	0.505551	0.504331	0.503409	0.502161	0.508107	0.506155
25	x	x	x	0.573073	0.520059	0.507048	0.504225	0.504633	0.505159	0.503358	0.506233	0.506412	0.50423	0.503727	0.50658	0.505669	0.504074	0.503465	0.502565	0.507552	0.50615
30	x	x	x	0.568358	0.562052	0.508268	0.505155	0.504319	0.505117	0.50415	0.506088	0.506238	0.504058	0.50395	0.506698	0.505183	0.503826	0.503217	0.502489	0.507866	0.506209
35	x	x	x	x	0.581818	0.546243	0.507481	0.504571	0.504864	0.50308	0.504836	0.505399	0.503305	0.50342	0.506462	0.505494	0.503332	0.503056	0.501976	0.507592	0.506852
40	x	x	x	x	0.588301	0.582948	0.53416	0.505448	0.505258	0.504913	0.50597	0.505761	0.503288	0.50289	0.505743	0.505409	x	0.502709	0.501678	0.508257	0.505874
45	x	x	x	x	0.648911	0.599579	0.563045	0.514544	0.506513	0.503948	0.507069	0.506367	0.504971	0.503471	0.505835	0.50568	0.504935	x	x	0.508297	0.506294
50	x	x	x	x	x	0.602979	0.604828	0.558171	0.510205	0.505038	0.505786	0.506846	0.504671	0.504567	0.506243	x	x	0.502639	x	x	x
55	x	x	x	x	x	0.627193	0.614608	0.588189	0.546739	0.507124	0.507527	x	0.50568	0.50544	x	x	x	x	x	x	x
60	x	x	x	x	x	x	0.617758	0.618402	0.570671	x	x	0.507298	x	x	x	x	0.504219	x	x	x	x
65	x	x	x	x	x	x	x	x	x	x	x	0.512327	x	x	x	x	x	x	x	x	x
70	x	x	x	x	x	x	x	x	0.627163	x	x	x	x	x	x	x	x	x	x	x	x

Table 2 – RMS errors (m s^{-1}) for the LES OSSE as a function of scan rate (deg s^{-1}, columns) and platform velocity (mph, rows).

LES OSSE (starting with vertical antenna)

Platform velocity (MPH)	Scan rate (deg/s)																				
	0.1	0.5	1	1.5	2	2.5	3	3.5	4	4.5	5	5.5	6	6.5	7	7.5	8	8.5	9	9.5	10
1	x	x	x	x	x	x	x	x	x	x	x	x	x	x	x	x	x	x	x	x	x
5	x	x	x	x	x	x	x	x	x	x	x	x	x	x	x	x	x	x	x	x	x
10	x	0.530515	0.507394	0.507143	0.507075	0.506826	0.506065	0.505065	0.506814	0.506652	0.506327	0.505579	0.506625	0.503443	0.505545	0.506513	0.507896	0.503818	0.508091	0.507667	0.507105
15	x	x	0.552391	0.506846	0.506789	0.507362	0.505933	0.504763	0.506531	0.506685	0.506323	0.50603	0.50684	0.502965	0.505901	0.50612	0.507202	0.503552	0.506121	0.507349	0.507224
20	x	x	0.548267	0.535249	0.506204	0.50668	0.5056	0.505116	0.506562	0.506495	0.505925	0.505586	0.505998	0.503011	0.505012	0.505987	0.507546	0.503249	0.507809	0.507176	0.506605
25	x	x	x	0.575315	0.520395	0.505972	0.506718	0.504459	0.505868	0.508343	0.505892	0.504556	0.505639	0.503448	0.505261	0.505757	0.507563	0.503088	0.50763	0.506799	0.506809
30	x	x	x	0.569102	0.569849	0.508467	0.505525	0.505529	0.506233	0.508057	0.505886	0.504811	0.506311	0.502702	0.505149	0.505808	0.507109	0.503095	0.507003	0.506609	0.506272
35	x	x	x	x	0.594682	0.551415	0.506754	0.505966	0.50668	0.508383	0.505193	0.505238	0.507449	0.503065	0.504809	0.505293	0.507079	0.502853	0.506767	0.506872	0.506603
40	x	x	x	x	0.589486	0.59502	0.540026	0.50703	0.505403	0.509453	0.506588	0.504157	0.505307	0.502207	0.504655	0.505688	0.506773	0.50292	0.507299	0.506192	0.505983
45	x	x	x	x	0.642704	0.612684	0.580627	0.514685	0.507891	0.50791	0.506592	0.506841	0.506228	0.502451	x	0.506094	0.506706	x	0.507798	0.506681	0.505587
50	x	x	x	x	x	0.606518	0.614417	0.566156	0.512661	0.509915	0.507088	0.504643	0.506878	0.503702	0.504726	x	x	0.504162	x	x	x
55	x	x	x	x	x	0.627808	0.631682	0.609278	0.558327	0.514073	x	x	0.506128	0.504118	0.506525	x	x	x	x	x	x
60	x	x	x	x	x	x	x	0.637737	0.588663	0.545554	x	0.508278	x	x	x	x	0.508383	x	x	x	x
65	x	x	x	x	x	x	x	x	x	x	x	0.509534	x	0.504421	x	x	x	x	x	x	x
70	x	x	x	x	x	x	x	x	x	x	x	x	x	x	x	x	x	x	x	x	x

Table 3 – RMS error (m s^{-1}) for the LES OSSE (with a start angle of 86 degrees elevation) as a function of scan rate (deg s^{-1}, columns) and platform velocity (mph, rows).

Difference from LES control											Scan rate (deg/s)										
Platform velocity (MPH)	0.1	0.5	1	1.5	2	2.5	3	3.5	4	4.5	5	5.5	6	6.5	7	7.5	8	8.5	9	9.5	10
1																					
5																					
10		0.00032	-0.0007	0.000625	-0.00013	0.000447	0.000165	-0.0002	0.001238	0.004293	-0.00014	-0.00112	0.001413	-0.00099	-0.00151	4.2E-05	0.003061	-0.00016	0.005371	-0.0008	0.000264
15			0.005491	6.9E-05	-0.00097	0.000683	0.000353	-0.00057	0.001046	0.004181	0.00015	-0.00022	0.002339	-0.00112	-0.00041	0.000301	0.002923	-0.00013	0.005603	-0.0007	6E-05
20			0.000354	0.004444	-0.00032	0.000607	0.000636	-2.2E-05	0.001058	0.004764	7.3E-05	-0.00121	0.001096	-0.00157	-0.00173	0.000436	0.003215	-0.00016	0.005648	-0.00093	0.00045
25				0.002242	0.000336	-0.00108	0.002493	-0.00017	0.000709	0.004985	-0.00034	-0.00186	0.001409	-0.00028	-0.00132	8.8E-05	0.003489	-0.00038	0.005065	-0.00075	0.000659
30				0.000744	0.007797	0.000199	0.00037	0.00121	0.001116	0.003907	-0.0002	-0.00143	0.002253	-0.00125	-0.00155	0.000625	0.003283	-0.00012	0.004514	-0.00126	6.3E-05
35					0.012864	0.005172	-0.00073	0.001395	0.001816	0.005303	0.000357	-0.00016	0.004144	-0.00035	-0.00165	-0.0002	0.003747	-0.0002	0.004791	-0.00072	-0.00025
40					0.001185	0.012072	0.005866	0.001582	0.000145	0.00454	0.000616	-0.0016	0.002019	-0.00068	-0.00109	0.000279		0.000211	0.005621	-0.00206	0.000109
45					-0.00621	0.013105	0.017582	0.000141	0.001378	0.003962	-0.00048	0.000474	0.001257	-0.00102		0.000414	0.001771			-0.00162	-0.00071
50						0.005539	0.009589	0.007985	0.002456	0.004877	0.001302	-0.0022	0.002207	-0.00087	-0.00152			0.001523			
55						0.000615	0.017074	0.021089	0.011588	0.006949			0.000448	-0.00132							
60								0.019335	0.017992			0.00098					0.004164				
65												-0.00279									
70																					

Table 4 – RMS error difference (m s^{-1}) between the LES OSSEs starting with a horizontal antenna (control) and a vertical antenna. Errors are presented as a function of scan rate (deg s^{-1}, columns) and platform velocity (mph, rows).

LES OSSE with Gaussian error ~ N(0,1 m/s)

Platform velocity (MPH)	Scan rate (deg/s)																				
	0.1	0.5	1	1.5	2	2.5	3	3.5	4	4.5	5	5.5	6	6.5	7	7.5	8	8.5	9	9.5	10
1	x	x	x	x	x	x	x	x	x	x	x	x	x	x	x	x	x	x	x	x	x
5	x	x	x	x	x	x	x	x	x	x	x	x	x	x	x	x	x	x	x	x	x
10	x	0.722067	0.689153	0.672386	0.678591	0.673356	0.672104	0.67304	0.668863	0.668638	0.671081	0.672822	0.66824	0.670383	0.672316	0.669924	0.67035	0.667067	0.667772	0.671211	0.670411
15	x	x	0.700074	0.685347	0.688436	0.683141	0.674095	0.669664	0.670166	0.677538	0.675871	0.674012	0.670308	0.666758	0.670076	0.668062	0.671883	0.672746	0.667897	0.672276	0.674443
20	x	x	0.716647	0.709835	0.690483	0.687241	0.683195	0.678762	0.680328	0.675674	0.680778	0.678496	0.680859	0.686696	0.683203	0.681998	0.681797	0.682595	0.679319	0.682019	0.681355
25	x	x	x	0.756078	0.721767	0.706295	0.70255	0.703358	0.698731	0.695082	0.701021	0.697794	0.695437	0.698943	0.69971	0.685068	0.693696	0.690076	0.694075	0.695188	0.69126
30	x	x	x	0.72887	0.729434	0.66977	0.669295	0.664427	0.666528	0.664781	0.665296	0.666043	0.660404	0.668759	0.659163	0.665656	0.666085	0.662439	0.661053	0.6664	0.657907
35	x	x	x	x	0.747649	0.694615	0.688827	0.679195	0.679675	0.675627	0.67883	0.675406	0.67673	0.675139	0.674885	0.679317	0.67141	0.673068	0.673411	0.671281	0.672173
40	x	x	x	x	0.776758	0.742949	0.72748	0.683283	0.689245	0.688337	0.690511	0.686942	0.681785	0.686421	0.686428	0.68298	x	0.685659	0.681224	0.690722	0.690172
45	x	x	x	x	0.821653	0.767948	0.751449	0.709142	0.698382	0.695439	0.695777	0.693788	0.691402	0.698727	0.692321	0.691487	0.693824	x	x	0.695119	0.693616
50	x	x	x	x	x	0.78365	0.76699	0.744808	0.706184	0.706557	0.71056	0.710217	0.695393	0.704852	0.707525	x	x	0.698326	x	x	x
55	x	x	x	x	x	0.807843	0.833634	0.766896	0.751207	0.713197	0.717858	x	0.704952	0.709383	x	x	x	x	x	x	x
60	x	x	x	x	x	x	0.779602	0.817865	0.759341	x	x	0.723362	x	x	x	x	0.715176	x	x	x	x
65	x	x	x	x	x	x	x	x	x	x	x	0.734855	x	x	x	x	x	x	x	x	x
70	x	x	x	x	x	x	x	x		x	x	x	x	x	x	x	x	x	x	x	x

Table 5 – RMS error (m s^{-1}) for the LES OSSE with Gaussian observational error as a function of scan rate (deg s^{-1}, columns) and platform velocity (mph, rows).